Doctoral Dissertation
Doctoral Program in Environmental Engineering (30^{th}cycle)

Investigation of the factors controlling hyporheic exchange at multiple spatial scales

By

Alice Caruso

******

Supervisor(s):
Prof. Fulvio Boano, Supervisor
Prof. Luca Ridolfi, Co-Supervisor

Doctoral Examination Committee:
Prof. Gonzalez-Pinzon Ricardo, Referee, University of New Mexico Albuquerque
Prof. Riml Joakim, Referee, KTH Royal Institute of Technology
Prof. Marion Andrea, University of Padova
Prof.ssa Butera Ilaria, Politecnico di Torino
Prof.ssa Tosco Tiziana, Politecnico di Torino

Politecnico di Torino
2018

Declaration

I hereby declare that, the contents and organization of this dissertation constitute my own original work and does not compromise in any way the rights of third parties, including those relating to the security of personal data.

Alice Caruso
2018

* This dissertation is presented in partial fulfillment of the requirements for **Ph.D. degree** in the Graduate School of Politecnico di Torino (ScuDo).

What makes a river so restful to people is that it doesn't have any doubt - it is sure to get where it is going, and it doesn't want to go anywhere else.

Hal Boyle

Alle persone che hanno sempre creduto in me e che mi hanno sostenuta
quando ero ad un passo dal rinunciare.

Acknowledgements

Ringraziamenti

Chi ha avuto modo di conoscermi e di starmi vicino nel corso di questi tre anni sa bene che non sono stati sicuramente anni semplici. Il percorso che mi ha portata fin qui è stato una marcia in salita e non certo in piano, e i momenti bui non sono mancati. Ho avuto, però, la grandissima fortuna di essere accompagnata e guidata durante il mio dottorato da due splendide persone, ancor prima che splendidi tutori. Per questo motivo il primo ringraziamento va a Fulvio Boano e Luca Ridolfi, che mi hanno seguita in questi tre anni, incoraggiandomi in ogni occasione e trasmettendomi i loro preziosi insegnamenti e la loro passione per lo studio e la ricerca. Non avrei potuto desiderare guide migliori di loro, dal punto di vista scientifico ma anche (e non meno importante) dal punto di vista umano.

Grazie ai miei colleghi, con cui ho condiviso, nel corso di questi anni, non solo innumerevoli ore lavorative, ma anche piacevolissimi momenti extra-Poli: dalle cene ai pranzi del mese, alle gite al mare e in montagna, al corso di arrampicata, e chi più ne ha più ne metta. In questi anni ho avuto la fortuna di coltivare delle amicizie vere e profonde, non certamente limitate alle pareti del Poli. Come ha detto una volta qualcuno, il DIATI ha una altissima concentrazione di persone meravigliose e qui ho trovato una seconda famiglia.

Grazie alla mia famiglia, a mia mamma, a mio papà e ad Edoardo, che mi hanno sempre sostenuto ed incoraggiato, ognuno a modo suo, ma tutti con l'unico e solo obiettivo di vedermi felice e serena, e di farmi superare i miei limiti e le mie paure. Grazie.

Grazie a tutte le persone che sono state fondamentali in questi anni e che continueranno ad esserlo nella mia vita. Grazie ai miei amici di sempre: Carla, Diana, Giulio, Marco, Francesca e Filippo; nonostante la distanza che ci separa so che loro ci sono sempre e basta alzare il telefono per superare ogni distanza fisica. Grazie ad Elena, per il suo affetto, il suo calore, il suo sostegno e la sua bontà; se al mondo esistessero più persone buone come lei, il mondo sarebbe sicuramente migliore. Grazie alle super amiche ”torinesi” di adozione, Giorgi, Giorgina, Miri e Fede, che hanno sempre contibuito a farmi sentire un po' più a casa, nonostante a volte la mancanza si sia sentita parecchio. Grazie ai miei zii, Mike e Marina, che non hanno mai mancato occasione per farmi sentire il loro affetto. Grazie a Silvi e Marta, che, anche se sono già state menzionate tra il mitico gruppo DIATI, meritano sicuramente una seconda menzione. Grazie a Rita, a Stefania G. e a tutte le persone che mi hanno aiutato in diverse occasioni. E grazie alle recenti e belle novità.

Infine, un ultimo grazie va a me, per non aver mollato. Posso dire che questo dottorato mi ha reso orgogliosa di me stessa e mi ha insegnato ad avere più fiducia e un po' più di autostima, che è il più grande insegnamento che potessi ricevere.

Abstract

Hyporheic exchange is the mixing between stream water and sediment pore water occurring vertically through the riverbed and laterally through the river banks. This mixing between water coming from the river and water coming from the aquifer, with very different physical and chemical characteristics, creates a unique environment in which important biogeochemical reactions occur and rich communities of microorganisms and macroinvertebrates flourish. The occurrence of the hyporheic exchange significantly influences the quality of the stream water and the nutrient cycling, playing a crucial role in hydrological, biogeochemical, and ecological processes. Although hyporheic fluxes are driven by the local morphology of the streambed, they are strongly affected by the large-scale groundwater system, which obstructs the penetration of stream water into the sediments and limits the intensity of hyporheic exchange. The present thesis aims to: i) investigate the role of the regional groundwater flow system on hyporheic exchange, analyzing the factors controlling the spatial variability of groundwater discharge patterns along the river corridor and ii) study the effect of microbial growth on exchange fluxes and nutrient reactions within the hyporheic sediments.

The work is divided into five Chapters. Chapter 1 presents a general overview on groundwater-surface water interactions, with a description of the multiple scales involved in these processes. The main aspects for which these interactions are important are recalled and a brief review on the modeling of river-aquifer interactions is presented. The attention is then focused on hyporheic processes, analyzing the main hydraulic and biogeochemical features characterizing these processes. The impact that the groundwater flow system has on these local processes is discussed. Finally, the main research topics investigated in the thesis are outlined.

In Chapter 2, the role of groundwater table structure at basin scale on the spatial patterns of groundwater discharge to the stream network and, consequently, on hyporheic exchange was investigated. Specifically, we determined the spatial structure of the groundwater upwelling along the stream network in order to investigate the effect of large-scale groundwater flow on local hyporheic flow velocity. A semi-analytical method for the estimation of the three-dimensional groundwater flow field was adopted, based on an approximation between the groundwater head distribution and the landscape topography. Results highlight that the complex topographic conformation of a basin determines a strong spatial variability of the groundwater flow field that, in turn, translates into a fragmentation of the hyporheic zone.

Chapter 3 is in line with the study developed in Chapter 2, looking at the groundwater-surface water interactions induced by large-scale hydrogeological characteristics. A more complex numerical model was adopted, allowing us to remove some simplifications on which the previous semi-analytical model was based on. The influence of some topographic and hydrogeological factors on determining the spatial variability of groundwater discharge patterns was investigated. Results indicate that the geological heterogeneity of the aquifer is the main control of river-aquifer exchange patterns and the structure of subsurface flow patterns is marginally affected by other modeling assumptions.

Chapter 4 shifts the focus on biogeochemical processes occurring at smaller scales and deals with the existing coupling between hydrodynamic processes, solute transport, and microbial metabolism within the hyporheic zone. A flow and reactive transport model was coupled with a microbial biomass model where two microbial components representing autotrophic (nitrifying) bacteria and heterotrophic (facultative anaerobic) bacteria were considered. The aim was to investigate how the filling of sediment pore space induced by biomass growth (i.e. *bioclogging*) alters hyporheic flow patterns and transformation rates of nitrogen, oxygen, and organic carbon within hyporheic sediments. Results show how the bioclogging-induced biogeochemical zonation of hyporheic zone strongly influences coupled nitrogen, carbon, and oxygen dynamics.

Finally, Chapter 5 presents general conclusions of the work.

Contents

List of Figures

List of Tables

List of Symbols

Latin Symbols

A_{pixel}	Area of a single raster cell
B	Width of the discharge area
b	Depth of the porous media in the biogeochemical model
B_{riv}	Width of the river in a cell in the numerical model
C	Conductance coefficient
c_i	Molar concentration of the i-th compound
c_{DOC}	Molar concentration of DOC
$c_{NH_4^+}$	Molar concentration of $\mathrm{NH_4^+}$
$c_{NO_3^-}$	Molar concentration of $\mathrm{NO_3^-}$
$c_{NO_3^-,lim}$	Molar limiting concentration for nitrate
$c_{O_2,lim}$	Molar limiting concentration for oxygen
c_{O_2}	Molar concentration of $\mathrm{O_2}$
D	Aquifer depth
d	Mean stream water depth
d_t	Maximum terrain rise
D_{50}	Median sediment diameter of the erodible bed

$\mathbf{D_m}$	Hydrodynamic dispersion tensor
D_{mol}	Molecular diffusion coefficient
f_i	Fraction of electrons consumed by the i-th reduction half-reaction
f_z	Cumulative flux per unit channel width
g	Gravity acceleration
H	Phreatic surface
$(h_m)_{i,j}$	Amplitude coefficients
h	Hydraulic head
h_0	Amplitude of sinusoidal hydraulic head distribution
h_{aq}	Head in the aquifer
h_{riv}	Water level (stage) in the river
$\mathbf{K}$	Hydraulic conductivity tensor
K	Homogeneous hydraulic conductivity
K_0	Hydraulic conductivity in absence of biomass
K_v	Hydraulic conductivity of the streambed material
K_x	Hydraulic conductivity along the x-direction
K_y	Hydraulic conductivity along the y-direction
K_z	Hydraulic conductivity along the z-direction
k_{d_a}	Autotrophic biomass die-off rate
k_{d_h}	Heterotrophic biomass die-off rate
k_{dune}	Bedform wavenumber
$k_{x,i}$	Wavenumber of the i-th harmonic in x-direction
$k_{y,i}$	Wavenumber of the i-th harmonic in y-direction

L	Total river length
l	Dimensional downstream distance
$\hat{l}$	Dimensionless downstream distance
L_h	Distance between hydrological boundaries
l_{dune}	Bedform wavelength
l_{pixel}	DEM resolution
L_{riv}	Length of a river reach through a cell in the numerical model
m	Thickness of the riverbed in the numerical model
N	Number of wavelengths in the x- and y-directions
n	Total porosity of the aquifer
n_e	Effective porosity
N_x	Number of harmonics in x-direction
N_y	Number of harmonics in y-direction
p	p-value
Q	Total dimensional groundwater discharge
Q_i	Groundwater discharge of each raster cell
$\mathbf{q}$	Darcy velocity vector
$\hat{q}$	Dimensionless Darcy velocity
q_0	Time scale for groundwater velocity
q_z	Groundwater upwelling
q_z^{simpl}	Vertical groundwater velocity in a simplified version of the numerical model
$q_{H,0}$	Hyporheic exchange flux in neutral conditions

q_H	Hyporheic exchange flux per unit bed area
$\mathcal{R}$	Recharge rate
R^2	Coefficient of determination
R_i	Consumption/production rate of the i-th compound
R_{DOC}	Reaction rate for organic carbon
$R_{NH_4^+}$	Reaction rate for ammonium
$R_{NO_3^-}$	Reaction rate for nitrate
R_{O_2}	Reaction rate for oxygen
t	Generic time
T_0	Time scale for groundwater flux
T_i	Dimensional travel time of each groundwater trajectory
$\hat{T}_i$	Dimensionless travel time of each groundwater trajectory
U	Mean stream velocity
u_0	Typical velocity scale for the hyporheic flow
v	Effective groundwater velocity
W	Volumetric flux per unit volume
X	Total biomass concentration
x	Coordinate axis
X_a	Autotrophic biomass concentration
X_h	Heterotrophic biomass concentration
y	Coordinate axis
Y_{DOC}	Growth yield for heterotrophic biomass
$Y_{NH_4^+}$	Growth yield for autotrophic biomass

z	Coordinate axis
z_H	Hyporheic zone depth
Z_{bot}	Elevation of the riverbed bottom

Greek Symbols

α_L	Longitudinal dispersion coefficient
α_T	Transversal dispersion coefficient
β_i	Ratio between the moles of transferred electrons per mole of oxidized DOC and the moles of electrons per mole of reduced compound in the i-th reaction
Δ	Maximum groundwater mounding
δ_{ij}	Kronecker's delta
η	Empirical coefficient
λ_{max}	Longest wavelength
λ_{min}	Shortest wavelength
$\lambda_{x,i}$	Wavelength of the i-th harmonic in x-direction
$\lambda_{y,i}$	Wavelength of the i-th harmonic in y-direction
μ_{DOC}	Reaction rate constant of DOC
$\mu_{NH_4^+}$	Reaction rate constant of NH_4^+
ρ_{q_z}	Autocorrelation function of the vertical velocity
ρ_{q_z}	Autocorrelation function
ρ_b	Sediment density
ρ_{X_a}	Density of autotrophic biomass
ρ_{X_h}	Density of heterotrophic biomass
τ	Tortuosity

θ	Sediment porosity
θ_0	Porosity in absence of biomass
ξ	Empirical coefficient

Other Symbols

$\mathcal{C}$	Correlation scale
∇	Laplacian

Acronyms

APM	Advective Pumping Model
$ARPA$	Regional Agency for Environmental Protection
DEM	Digital Elevation Model
GW	Groundwater
HZ	Hyporheic Zone
NV	Newer Volcanics
PB	Paleozoic Bedrock
QA	Quaternary Alluvium
SW	Surface water

Chapter 1

General Overview

1.1 An overview on groundwater-surface water interactions

Rivers are vital ecosystems since they gather and deliver water for human use (drinking, irrigation, etc.), supply hydroelectricity generation, provide the habitat for diverse fauna and flora, and support countless recreational and commercial opportunities. Not surprisingly, the economic value of river basins is estimated in billions of dollars [117]. As highlighted by a recent analysis conducted at global scale [204], however, rivers that serve 80% of the world's population are threatened by multiple human-induced stressors. The increasing occurrence of drought periods induced by climate changes and the progressive intensification of agricultural practices characterized by intensive irrigation and a widespread use of fertilizers are among the main factors threatening river ecosystems. These environmental stressors directly expose humans to health risks [186] and endanger the biodiversity of 65% of the world's river habitats putting thousands of aquatic wildlife species at risk [117].

A hazard trigger for water bodies is, for example, eutrophication, which consists of an excessive growth of plants and algae due to nutrient loads that may result in dissolved oxygen depletion causing die-offs of plants, fishes and aquatic organisms, the loss of biodiversity, and the emission of greenhouse gases [186]. Nutrients can derive from many sources, such as fertilizers, decomposition

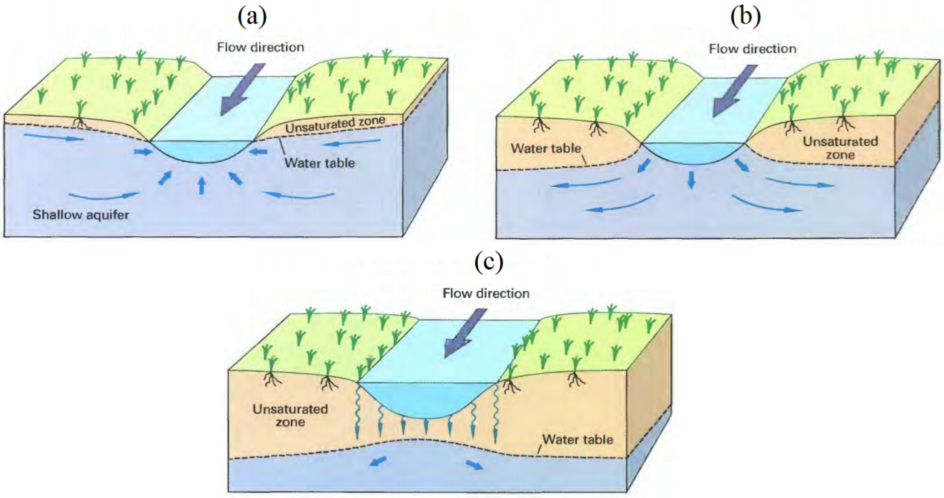

Fig. 1.1 Streams interact with groundwater in three basic ways: water from the aquifer flowing into the stream, i.e., gaining stream, panel (a); water from the river flowing into the aquifer, i.e., losing stream; or some combinations of both [209]. Losing streams can be either connected, i.e., fully saturated zone to water table, panel (b), or disconnected, i.e., separated from the ground-water system by an unsaturated zone, panel (c).

of plants and organisms, erosion of soil, sewage treatment plant discharges, and vegetation (e.g. from N-fixing plants). Among the nutrients, phosphorus and nitrogen are probably the two most widely discussed when it comes to water quality issues. The Water Framework Directive (WFD; 2000/60/EC) proposed by the European Union established a new integrated and comprehensive approach for the protection, management and sustainable use of water bodies with new and wide-ranging environmental goals, while progressively reducing or eliminating pollutants for the long-term protection and enhancement of the aquatic environment.

Most streams and rivers interplay wih groundwater and, therefore, the two compartments are strictly related. Similarly to riverine systyems, aquifers play an essential role for environmental health and for the economic and social development of the countries since they represent vital compartments for human activities (e.g., agriculture, energy production) and for many ecological and biogeochemical processes [126, 30, 177, 104]. Preserving the ecological integrity of rivers and aquifers is, therefore, a challenging and essential task.

Sustainable water quality management requires a holistic analysis of the water cycle and, in particular, of interactions among groundwater (GW) and surface water (SW), coupled to a deep understanding of pollutant fate in the riverine ecosystem. Groundwater interacts with surface water in a great variety of environments, ranging from lakes, steep mountain streams, lowland rivers, floodplains, wetlands, and oceans, with similar processes that take part in the chemical and biological cycling of nutrients. The present work focuses on the interaction between aquifers and rivers, that can take place in different ways as illustrated in Figure 1.1. The importance and the main characteristics of river-aquifer interactions will be discussed in the next sections, in conjunction with a review of the main studies and methodologies involving the prediction of GW-SW exchange fluxes.

1.1.1 Why study river-aquifer exchange?

Riverine and aquifer systems represent two environments with extremely different characteristics. On the one hand, rivers are characterized by a turbulent flow, considerable fluctuations of discharge and temperature, daylight-darkness cycles, and changing chemical conditions. In contrast, groundwater ecosystems exhibit more stable environmental conditions, with laminar flow, slight temperature variations and permanent dark conditions. The different properties of fluvial and groundwater ecosystems create a transitional environment characterized by unique characteristics that regulate exchange of water and solutes across the streambed. GW-SW interactions play an important role for the health of fluvial ecosystems, stream corridor restoration, and riparian zone management, therefore the protection of these two compartments is an essential element of water resources management.

The crucial zone where the connection among the subterranean and surface aquatic environments occurs is the GW-SW interface, known as hyporheic zone (HZ) (shown in Figure 1.2), which represents the transitional zone between these two different compartments. The hyporheic zone is the part of fluvial sediments beneath and adjacent to the river within which there is exchange of water between the stream and the subsurface, i.e., the hyporheic flow [25]. As reported in [20], 'hyporheic flow is commonly distinguished from groundwater flowing near rivers by its bidirectional nature, i.e., hyporheic flow is exchanged

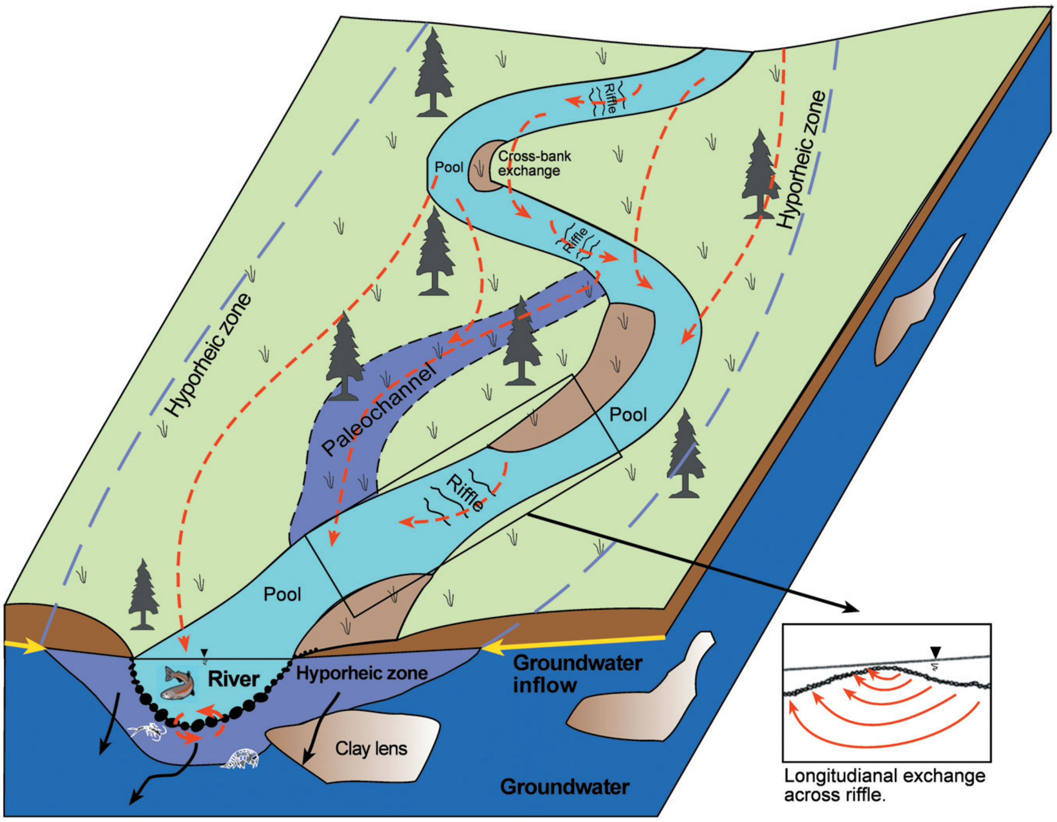

Fig. 1.2 Illustrative representation of a fluvial system and of its main components: surface, hyporheic, and groundwater flow domains [192]. Dashed red arrows indicate hyporheic exchange moving surface water into the surrounding alluvium and back to the river again. Hyporheic exchange is distinguished from far-field inflow of groundwater (yellow arrows) and from one way outflow of river water (i.e. flow paths that do not circulate water from the river and back again).

back and forth across the streambed interface whereas groundwater recharge or discharge is considered to travel unidirectionally over much longer distances'. The hyporheic zone is a dynamic ecotone characterized by strong chemical and temperature gradients that influence the fate of chemicals and organisms both at the interface and in the adjacent aquifer and stream environments [30, 94]. Processes occurring in the hyporheic zone will be focused in Section 1.2.

The increasing interest in studying hyporheic exchange has arisen from a number of ecological services provided by exchange processes. In fact, GW-SW exchange influences stream chemical and ecological conditions since it affects solute transport, chemical dynamics, and microbial activity [30, 104, 128, 202]. The transitional zone between surface water and groundwater is characterized by steep chemical and physical gradients with strong exchange of oxygen, carbon, and nutrients resulting in multiple microbially-mediated redox reactions and dense microbial and invertebrate community [176, 52, 123, 6]. Moreover, the connectivity among GW-SW systems stabilizes the baseflow of streams and controls spatial patterns of reaction zones and metabolic activities in streambeds [155, 19, 98, 124]. On the whole, river-aquifer interactions exercise a strong influence on the chemistry and the quality of both surface water and groundwater because the river-sediment interface hosts an intense biogeochemical activity, which affects nutrient cycling (e.g, organic carbon, nitrate and phosphate) [89, 99, 12, 6, 168] and contributes to the natural attenuation or removal of pollutants [107, 78, 174, 87].

Buss et al. [32] summarized the services provided by the hyporheic zone in the following points:

- controlling the flux and location of GW-SW exchange;
- providing an important zone for the cycling of carbon, energy and nutrients;
- providing a natural attenuation zone for certain pollutants by biodegradation, sorption and mixing;
- providing a habitat for a diversity of animal species, benthic and interstitial organisms, and supplying food for aquatic consumers;
- providing a spawning ground, a refuge for certain species of fish and a rooting zone for aquatic plants;
- attenuating river water temperature fluctuations;
- representing a location of sediment exchange.

In order to preserve the ecological integrity of groundwater and surface water systems it is therefore essential to assess the processes occurring in this critical zone, to estimate and to quantify water and contaminant fluxes throughout a catchment, and to implement strategies to protect the river ecosystem. Understanding the hydrologic and biologic processes that define the relationship between surface water and groundwater is essential to analyze the ecological effects of water resources management in a basin. The processes occurring at the interface of these environmental compartments have been studied in the last few decades, while the research was previously focused on processes occurring within either rivers or aquifers, separately. A multidisciplinary approach involving hydrology, biogeochemistry, and ecology has spread in order to better investigate the processes and dynamics of GW-SW interactions, focusing on the hyporheic region.

Groundwater fluxes at large scale have a strong impact on hyporheic fluxes at smaller scales. Specifically, rising or falling groundwater can constrain and reduce the circulation of water between the stream and the hyporheic zone, limiting the extent of the hyporheic zone and influencing biochemical processes that can occur within it. Therefore, the influence of GW-SW interactions at watershed scale on local hyporheic exchange and the resulting effect on nutrient cycling is another important aspect. This aspect will be analyzed in detail in the next subsections, together with a detailed description of the main aspects concerning hyporheic processes.

1.1.2 Multiple scales of GW-SW interactions

The hydrodynamic and biogeochemical GW-SW interactions are characterized by a wide range of spatial and temporal scales, which interact and determine a complex system where smaller flow cells (i.e., circulation structures) are nested inside larger flow cells [196, 33, 20]. The nested structure is a peculiar characteristic of the groundwater flow system. According to the classification adopted by Flipo *et al.* [70], based on an extensive literature review, five different scales can be identified (Figure 1.3):

- local scale (10 cm – 10 m): this is the scale of a single geomorphological unit (i.e., dunes, ripples). This is the scale referred to as hyporheic flow;
- intermediate scale (10 m – 1 km): this scale concerns the SW-GW flow pattern of a river reach;
- watershed scale (10 km^2 – 1000 km^2): this is the scale from which the river network is connected to its watershed and the resulting GW-SW interactions are associated to the hydrological cycle;

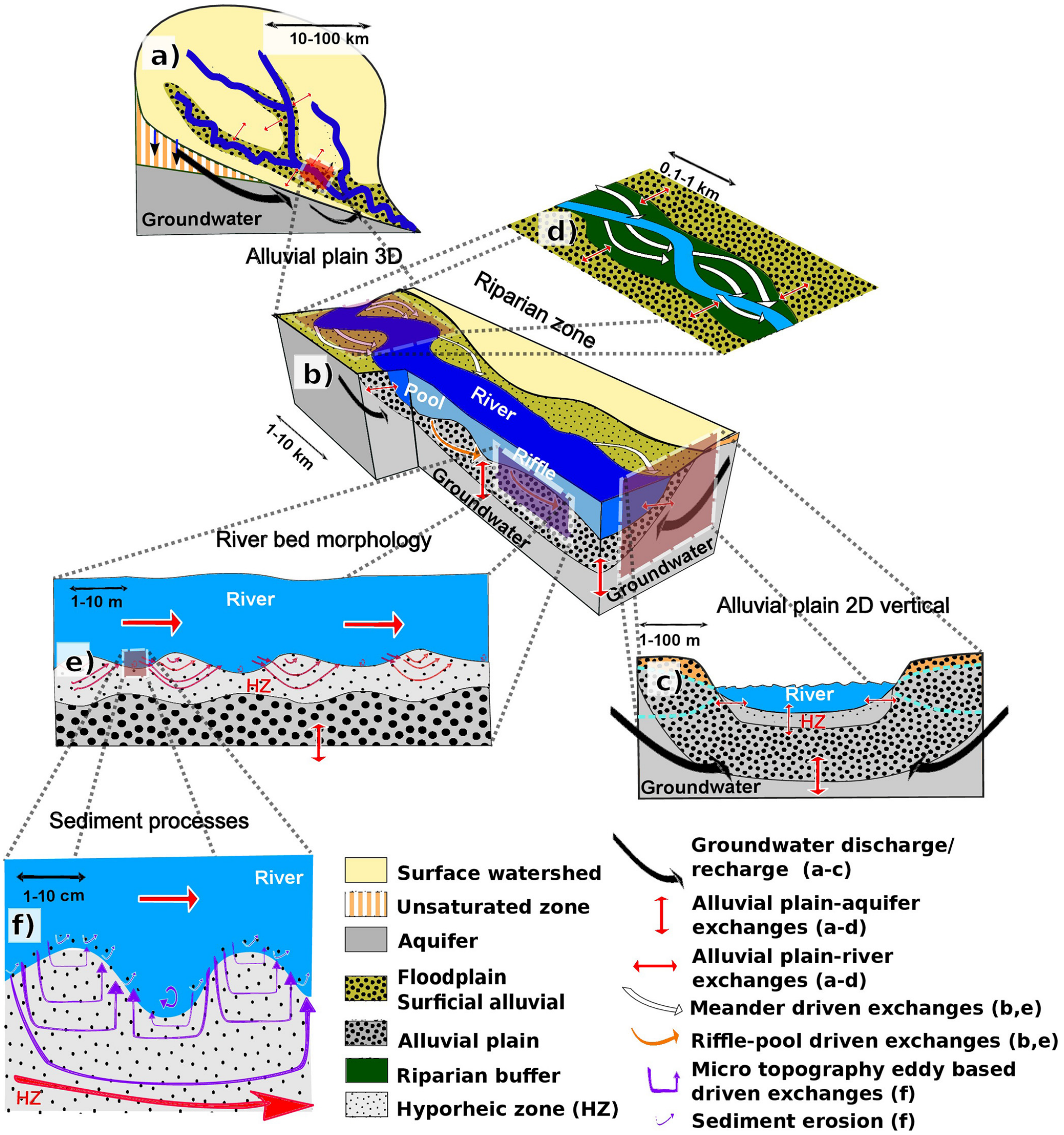

Fig. 1.3 Different scale involved in stream–aquifer interactions: (a) watershed-basin scale, (b) intermediate-reach scale, (c) cross section of the stream–aquifer interface (hyporheic zone), (d) meandered reach scale, (e) longitudinal hyporheic exchange, (f) water column–sediment interface scale. From Flipo *et al.* [70].

- regional scale (10000 km^2 – 10^6 km^2): this scale is related to water resources management, and it is the one for which the least is known about stream–aquifer exchange dynamics;
- continental scale ($> 10^6$ km^2): this scale is a collection of regional scale basins and differs from the regional scale because it considers climatic variations, taking into account a broad range of hydro-climatic conditions.

This classification will be adopted throughout the present work. It should be taken into account that the classification of scales is not unique but can vary on the basis of the application field and the terms "local", "small", "large", "regional", etc., have been used in different manner according to the specific use.

The different scales reflect the existence of multiple spatial scales characterizing landscape and river morphology (from the scale of a single geomorphological unit to the regional-watershed scale, Figure 1.4), which drive water flow within the catchment and control GW-SW interactions. Recent studies stress the complexity of the multi-scale processes taking place at the river-aquifer interface [153, 64, 184] but complete understanding of key interactions remains elusive [196, 214, 34, 130, 20].

An important parameter to analyze and describe river-aquifer interactions is the travel time, i.e., the time that the water takes to travel from the location where the precipitation infiltrates to a downstream location within a stream. Catchments exhibit a wide range of exchange timescales that play an important role for the biogeochemistry of the stream ecosystem and for nutrient cycling along the stream corridor [20]. In fact, longer and shorter flow paths have distinct roles for problems of nutrient transport and reactive processes, basically for two reasons: i) they may have infiltrated in different zones of the catchment with resulting physicochemical characteristics depending on the different land-use type and soil properties; ii) the time spent in the subsurface largely impacts the chemical reactions over the watershed and, thus, the downstream nutrient concentrations.

In order to analyze the broad spectrum of scales it is necessary to obtain substantial geomorphologic and fluid dynamic information that vary on the basis of the observed scale [20]. At local scale, the main properties controlling

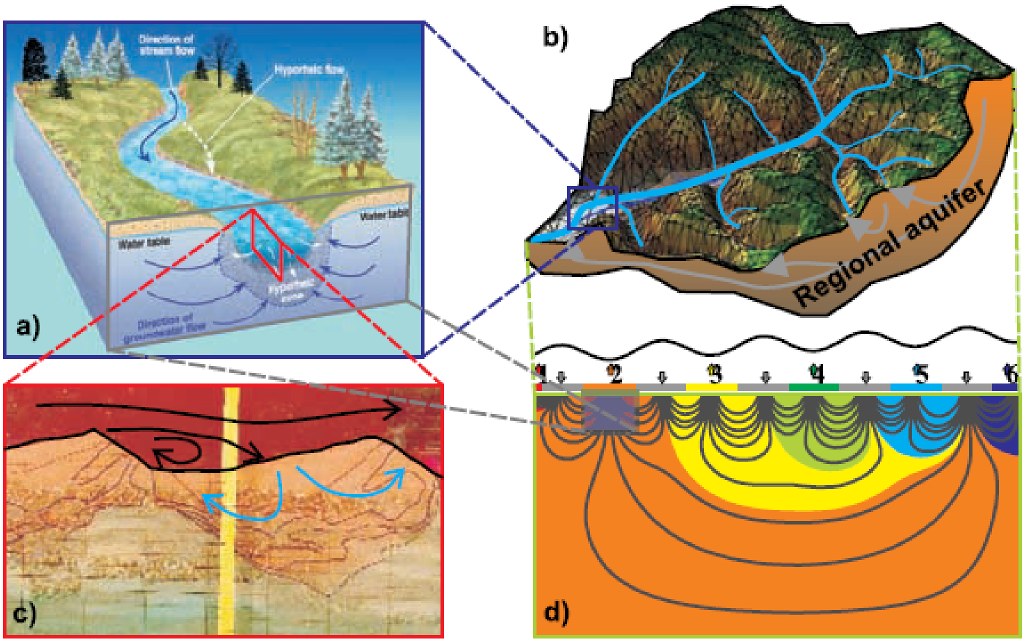

Fig. 1.4 Schematic raffiguration of GW-SW exchange across interfaces at nested scales from Cardenas [34]. (a) Exchange occurring at reach scale across sinuous channel deposits and bars (scales of meters to kilometers), (b) representation of a watershed, (c) vertical exchange due to river bedforms such as dunes and ripples (scales of centimeters to meters), and (d) topography-driven regional exchange (scales of kilometers to hundreds of kilometers).

GW-SW interactions are size and distribution of pores, shape and geometry of geomorphologic units, and connectivity of the aquifer substratum and riverbed [210, 8]. Experimental studies and field observations are generally used at local scale to describe physical properties and quantify physico-biochemical processes at the interface between surface water and aquifer. At reach scale, the involved parameters (geomorphological and topographic characteristics, hydraulic head gradients, etc.) show large spatial (and temporal) heterogeneity, and the fundamental processes become more difficult to analyze and describe since the complexity of the system increases [8]. Therefore, collecting a sufficient number of observations to describe the physical-chemical characteristics of the system becomes challenging and some generalizing predictive methods are convenient in order to exploit data or model parameters obtained from small areas for studying larger areas. Overall, a large amount of experimental and modeling studies exists at reach scales [18, 129, 170, 19]. Fewer studies, conversely, address GW-SW interactions at regional-watershed scale, which are rarely examined in experimental field studies. A common approach consists in transferring and upscaling properties, process descriptions and model parameters from studies carried out at local scales to larger scales [20, 8].

1.1.3 Modeling river-aquifer interactions

Aquifers and rivers were traditionally studied and managed as separate components of the hydrological system in most hydrogeological and ecological research studies [30, 25, 209], mainly because their physical and chemical characteristics are completely different. However, the growing demand for water resources accompanied by a reduction in water availability, mainly associated with climate change and increasing demand, led to a new perception of groundwater and surface water as a single resource and to a need for a more sustainable management of coupled GW-SW resources [26, 68]. Therefore, in the recent decades much attention has been paid to the GW-SW interactions [179, 177], widely recognising the strong connectivity between rivers and aquifers [18]. To date, many efforts have been made to elucidate the basic physical drivers of GW-SW water exchange and its connections with chemical and ecological processes [30, 89, 113] and different field methods and methodological approaches have

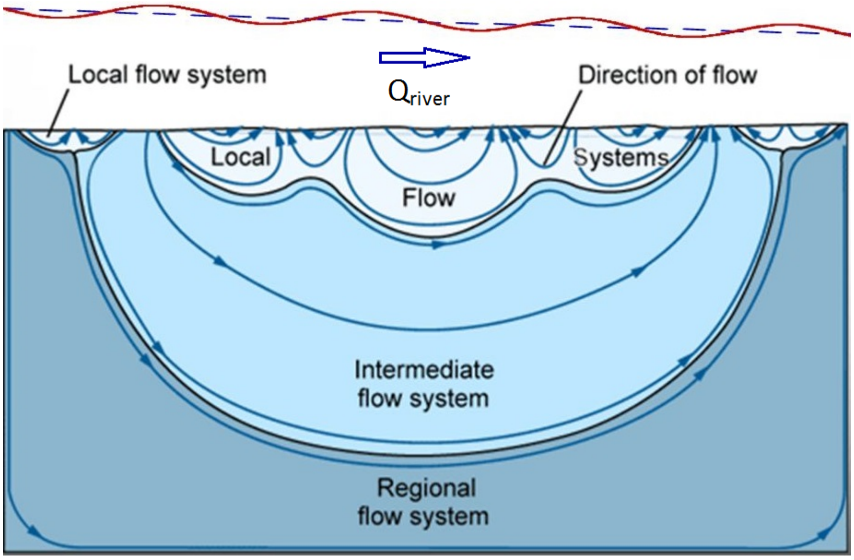

Fig. 1.5 Groundwater flow paths associated with the tree different orders of groundwater flow system: local, intermediate, and regional. Groundwater discharge into surface water system comes mostly from the local flow system. Figure from Winter [209].

been developed for estimating and the exchange fluxes between groundwater and surface water at various spatial and temporal scales.

A first elucidation about the mechanisms that drive the spatial patterns of GW-SW interactions was achieved through the early work by Tòth [195, 196], in which for the first time an analytical solution was developed. Tòth investigated groundwater flow in theoretical small drainage basins and examining the influence of factors like topography, geology and climate on groundwater flow system. The nested nature of groundwater flow systems was theoretically evidenced, identifying three distinct types of flow systems – local, intermediate, and regional (see Figure 1.5) - and identifying these factors as major controls for the formation of sub-flow systems of gravity-driven flow in a homogenous and isotropic groundwater basin. Notice that this flow system distinction is another example of the classification used in literature respect to that one proposed by Flipo *et al.* [70] and adopted in the present thesis.

The first numerical groundwater models were proposed by Freeze and Witherspoon [76, 74, 75]. They simulated three-dimensional steady state regional flow patterns in heterogeneous and anisotropic layered aquifer systems, investigating the effects of water table configuration, geological stratigraphy and variations in permeability. Further efforts were devoted to introduce unsaturated transient conditions [73], obtaining quantitative hydrographs of infiltration rates, water table depth, and stream base flow and predicting gmaximum basin yield as a function of withdrawals and recharge-discharge patterns in a hypothetical three-dimensional basin [219]. Mechanisms to simulate stream-aquifer relations and water exchange processes were included into the groundwater numerical models in the 1980s (e.g., [156]). Numerical models were firstly adopted with the aim of improving the management of water quantity and were then extended to link hydrologic dynamics at the GW-SW interface with ecological functions [89, 179] and biogeochemical processes [17, 106, 52].

Conventional groundwater models (e.g., MODFLOW, HYDRUS-2D, FE-FLOW) simulate GW-SW exchange processes without explicitly modeling the surface water component. For example, the MODular three-dimensional finite-difference groundwater FLOW (MODFLOW) model [135, 95], developed by the U.S. Geological Survey, considers GW-SW interactions through a streambed conductance factor that depends on river and bed characteristics and evaluates the exchange flux as a function of head differences between river stage and aquifer water levels. Fully integrated models (e.g., ParFlow, CATHY, HGS, OGS), conversely, simulate both SW and GW systems, including simultaneously SW (lakes, streams and wetlands) and subsurface water (unsaturated and saturated GW flow) in a single hydrological modeling scheme [1] and, therefore, they are more complex and require a greater amount of input data.

Together with the numerical modeling, SW-GW interactions have been investigated through statistical techniques based on monitoring data of groundwater levels and streamflow or through the analysis of environmental isotopes and geologic, hydrochemical and in situ physicochemical parameters [108]. However, although in the last few years robust methods have been developed to assess stream-aquifer exchanges at local scale, there is a fundamental necessity to propose innovative methodologies for calibration and validation of models simulating stream aquifer exchanges at regional-watershed scale [70, 120].

1.2 Hyporheic zone processes

1.2.1 What is the hyporheic zone?

The hyporheic zone is the transition region between the surface water and groundwater hydrological systems (Figure 1.2), characterized by an intense hydrodynamic exchange between river water and shallow groundwater and an intense biogeochemical activity and hence important for the health of the whole water systems. This transitional area is a key ecotone since it offers a habitat for benthic and interstitial microorganisms, supports a rich biodiversity in fluvial ecosystems, acts as a buffer zone for the attenuation of certain pollutants by biodegradation, sorption and mixing, and provides an important zone for biogeochemical cycling of carbon and nutrients [155, 19, 98, 20, 124].

The original use of the term “hyporheic” was found in the work of the ecologist Orghidan [146, 147], who described the GW-SW interface as a new habitat of subsurface waters containing a distinctive biotope [1], with peculiar physicochemical and biological conditions different from those characterizing streams and aquifers [103]. The adjective derives from the greek words “hypo” (i.e., “under”) and “rheos” (i.e., “flow”) to literally denote “under the flow”. The first surveys indicating the existence of a characteristic fauna living in near-stream alluvial deposits were carried out by Chappuis [42] and Angelier [3]. However, the distinction between groundwater and river ecosystems was ignored by most researchers until Orghidan [146] demonstrated through field studies that the fauna collected in the riverbed alluvium was a new biotope with both stream and aquifer physical and chemical characteristics.

---

[1] Area of uniform environmental conditions providing a living place for a specific biological community.

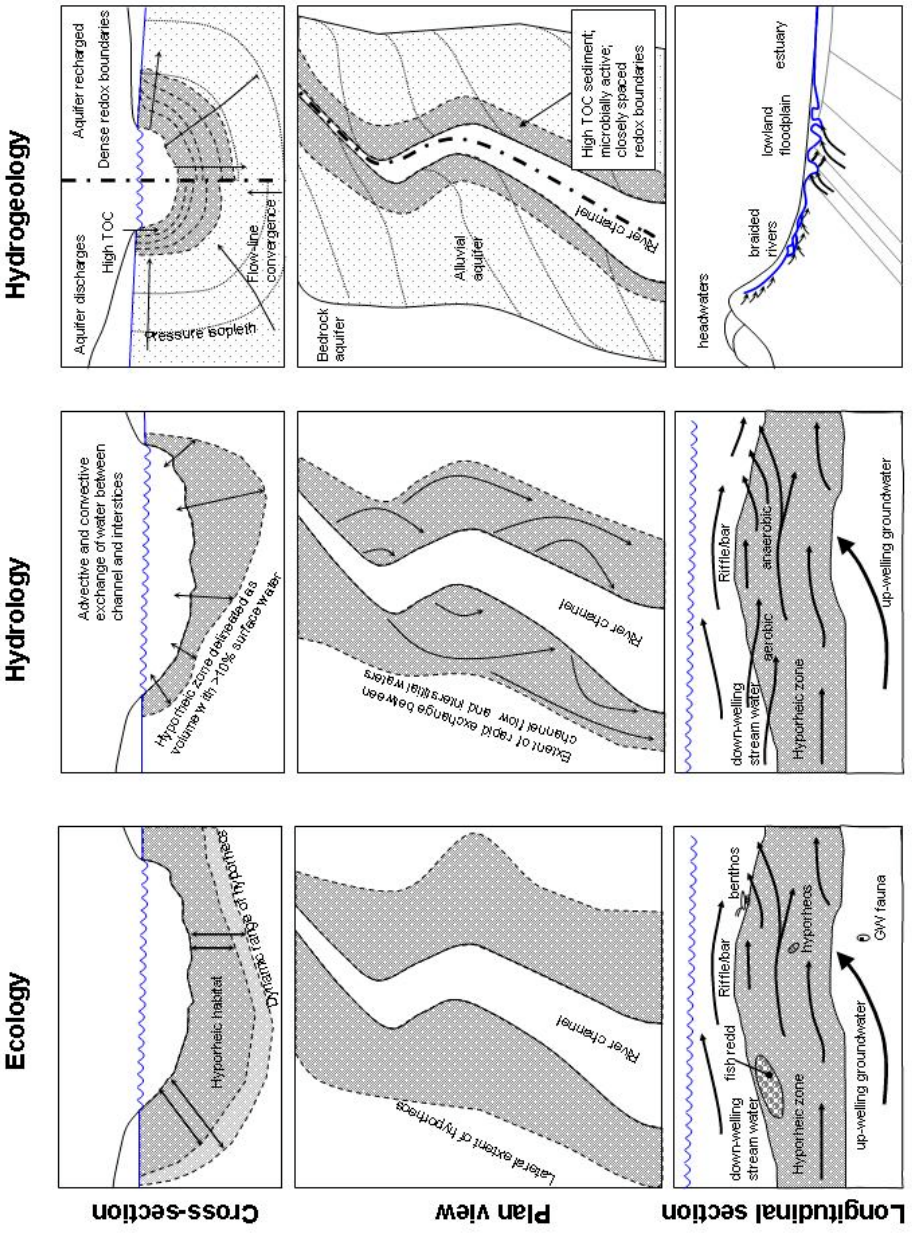

Fig. 1.6 Conceptual models of the hyporheic zone for ecology, hydrology and hydrogeology disciplines [175].

As dynamic and complex transitional zone between rivers and aquifers, the hyporheic zone is characterized by the simultaneous occurrence of multiple physical, biological, and chemical processes. For this reason, the study of this key ecotone is not related to a single discipline but it involves multiple scientific approaches (hydrology, hydrogeology, biogeochemistry, ecology, microbiology, etc.) necessary to investigate the multi-faceted nature of hyporheic zones. Therefore, the definition of hyporheic zone is not unique (Figure 1.6) but varies on the basis of the discipline in which the hyporheic processes are approached and studied [192, 5]. Hydrogeologists interpret the hyporheic zone as the upper part of an aquifer, belonging to the groundwater system, characterized by high organic matter concentrations and greater variety of microbial communities respect to the surrounding aquifer sediments [175]. To the hydrologist, by contrast, the hyporheic zone is considered as an extension of the river system and it is hydrologically defined as “a subsurface flowpath along which water recently from the stream will mix with subsurface water to soon return to the stream” [97]. In the geochemical field, the hyporheic zone is intended as a buffer in which the harmful impact of pollutants contained in groundwater on surface water is dampened. It is defined as the portion of sediments including between 10% and 98% of surface water and showing gradients of nutrients and dissolved gases [201]. Finally, ecologists look at the hyporheic interface as a refuge for fishes and aquatic organisms, a rooting zone for plants and a spawning ground for salmonids. The coexistence of characteristics typical of both groundwater and surface water environments entails the presence of hydraulic and chemical gradients leading to the development of a unique ecosystem.

Hyporheic exchange is a key process for a number of biochemical reactions since it reduces in-stream nitrate concentration by biological assimilation and denitrification and influences stream water quality and ecological conditions of stream ecosystem. An intense microbial activity characterizes the hyporheic zone: water-borne chemicals are, in fact, exchanged with the surrounding subsurface and transformed into oxidized or reduced substances by biogeochemical reactions mediated by different species of hyporheic microbiota. Microbial processes are influenced by water chemistry and transport mechanisms and, in turn, influence groundwater and surface water chemistry through important ecological services (e.g., degradation of nutrients and pollutants). Mechanisms governing solute transport and microbial processes within the hyporheic zone will be examined in detail in the following subsections.

1.2.2 Hyporheic flow and solute transport

Water exchanges through the streambed are mainly induced by variations in stream morphology, hydraulic permeability, and hydrological conditions and span a broad range of spatial scales (Figure 1.3) [127, 192, 184, 20]. The spatial variability of the hyporheic zone reflects on hyporheic residence times (i.e., the amount of time that a particle of river water spends within the hyporheic sediments, in contact with the groundwater environment, before re-emerging into the river), which range from seconds to tens of years and impact the hyporheic biogeochemical patterns [20, 116]. Bed topography basically defines the spatial scale of the hyporheic pathways (Figure 1.7). Small streambed geomorphologic features, such as ripples and dunes, give rise to short flow paths that reach shallow depths (centimeters or decimeters) with short residence times (e.g., from minutes to hours) [63, 149, 21], whereas longer flow paths infiltrating up to several tens, hundreds, or even thousands of meters [157] are driven by larger geomorphological features, like pool-riffle pairs, step-pool sequences, or meander bends, with longer residence times (from some days up to years) [116, 20]. Laterally, hyporheic mixing can be limited in small rivers confined by hillslopes or may extend deeply into the riparian zone (i.e., the horizontal extension can vary from hundreds of meters to more than a kilometer, [179]), including the wider floodplain and enhancing the formation of a vast habitat suitable for many microbial communities [180, 210, 178].

Flow interactions between streams and riverbed are responsible for solute transport within the sediments and play an important role in the ecology of the river environment. Reactive processes (e.g. chemical reactions or microbial growth) in the fluvial sediments depend on water flow and solute transport within the porous medium and are, thus, controlled by hydraulic properties of the granular material and presence of dissolved reactants or nutrients [41, 191]. These properties are in turn affected by solute transport and reactive processes and may change over time but, for the sake of simplicity, they are usually assumed as constant in describing and analyzing the interactions among rivers and aquifers. Different causes can induce a temporal variability, including

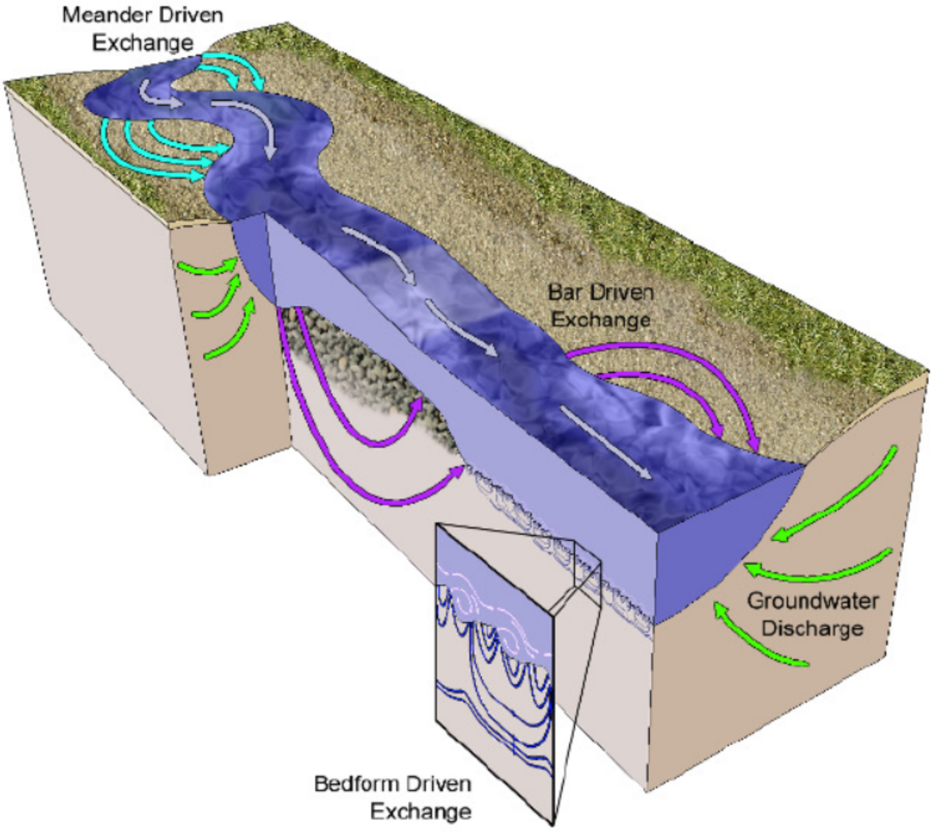

Fig. 1.7 Hyporheic flow patterns induced by different morphological features, i.e., ripples, dunes, bars, and meanders, and associated with different scales of stream topography. Complex interactions between these features and larger groundwater discharge/recharge pathways exist. From Stonedahl [184].

physical (e.g., particle deposition), chemical (e.g., dissolution or precipitation), microbial (e.g., production of gas by microorganisms or production of biomass), and thermal factors, influencing, for example, reaction rates.

Hyporheic exchanges have been studied and quantified adopting three main methods: physically-based models, stream transport models based on stream tracer tests, and field measurements. The first hydrodynamic model of hyporheic flow (APM, Advective Pumping Model) was proposed and experimentally validated by Elliott and Brooks [63, 62] although the river-sediment exchange induced by pressure variations was previously observed and discussed by Savant *et al.* [167]. The APM analyzes the exchange due to advective porewater flow (pumping) separately from the exchange resulting from trapping and release of porewater during bedform migration (turnover). The model assumes a sinusoidal head distribution at the bed surface that results from the interaction of the flow field with two-dimensional idealized bedforms (dune or ripple) and drives water through the sediments (see Figure 1.8). The shape of the head distribution used in the model was observed in experimental studies [65]. Starting from a Darcy groundwater flow model and an empirical formulation of the bedform-induced hydraulic head at the streambed interface, Elliott and Brooks derived an implicit analytical description of flow field and residence time distribution into a homogeneous porous bed induced by idealized bedforms.

The approach proposed by Elliott and Brooks [63, 62] considers only one scale of topography, ignoring the fractal natural of topography that leads to complex interactions between a wide range of scales. Many other available process-based models also focus on only one scale of topography, e.g., they either incorporate large-scale features such as meanders and bars while ignoring the finer details [19, 132], or they consider only small features like dunes and ripples [187, 37]. This limitation was overcome with the introduction of a physically based multiscale model proposed by Stonedahl et al. [184]. The two-dimensional bedform-induced pumping model for dunes and ripples was extended to three dimensions, integrating pore water flow field due to single-bedform with exchange induced by larger-scale topography such as bars and meanders through a spectral scaling approach [213]. This analysis showed that all scales of topographic features contribute to interfacial flux and residence time distributions, but that ripple and dune scales tend to both contribute more than and interact nonlinearly with meanders [184].

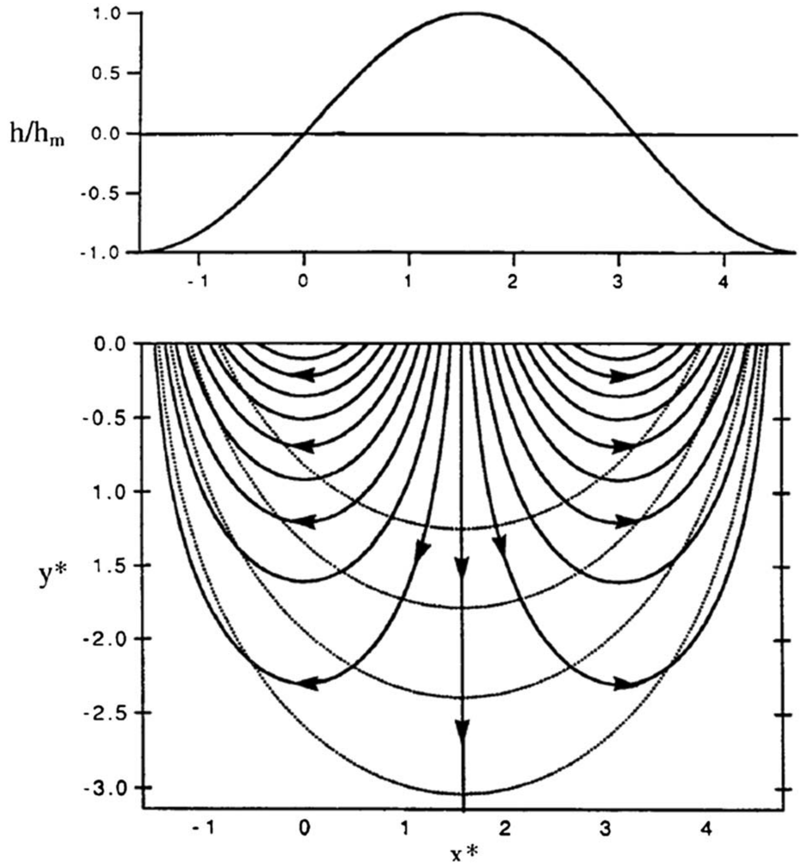

Fig. 1.8 Schematic representation of (top) sinusoidal head distribution adopted in the Advective Pumping Model for hyporheic flow below a stream bedform and (bottom) streamlines deriving from the flow field solution. From Elliott and Brooks [63].

The most widely used experimental approach for quantifying hyporheic exchange and characterizing transport properties is a stream tracer injection experiment combined with modeling of breakthrough curves [212, 205]. In a typical stream tracer study, a nonreactive solute tracer (e.g., chloride or bromide) is injected into the stream at a constant rate, and solute concentrations are monitored and sampled over time at downstream sampling stations [114]. The tracer-experiment data are then analyzed to estimate parameters not directly measurable and required in stream transport models for predictive purposes. These models, referred as phenomenological model, distinguish from the physically-based models because they do not focus on the physical principles governing the exchange flow and the water storage. Differently, these models aim to integrate at the reach scale the complex physical transport processes occurring at fine scales by calibrating the model to the results of a conservative solute tracer experiment conducted in the reach of interest [20]. Therefore, existing hyporheic models can be distinguished in physically based models and phenomenological models depending on the adopted approach and the provided information [20].

Since tracer experiment results are very sensitive to the experimental setup, as argued by Harvey and Wagner [96], the model parameters and the results achieved from the tracer tests for a particular system cannot be extended to another one with different characteristics. The history of in-stream tracer concentrations combined with solute transport simulations allows to quantify the physical parameters that characterize solute advection (which describes the rate at which the tracer moves downstream), longitudinal dispersion (which accounts for in-stream longitudinal mixing that cause the spreading of the peak solute concentration), lateral inflow of groundwater (which increases the rate of flow and dilutes the tracer), and storage zone exchange (which considers the transfer of solute between the active channel and dead or slowly moving zones in the stream or in the subsurface). The Transient Storage Model (TSM) proposed by Bencala and Walters [18] is the most commonly used model to analyze tracer data and to study hyporheic exchange, allowing to extract hyporheic residence times from breakthrough curves. Tracer concentrations are estimated using a differential equation that takes into account the variations associated with advection, dispersion, groundwater influx, and one or more storage zones, while hyporheic residence times are calculated from subsurface tracer data by monitoring the arrival time of the tracer at wells [200] or with surface water sampling [100, 205].

Conventional field methods for identifying zones of upwelling and downwelling and quantifying hyporheic exchange include direct measurements of hydraulic head gradients or hydraulic flux near the streambed interface from seepage meters and piezometers [59, 2, 164]. In situ measurements are very useful to characterize the site of interest and/or to calibrate two or three-dimensional numerical groundwater flow models. However, they are representative of very local conditions and realizing a number of point measurements suitable to represent the spatial variability of the topographical, hydraulic and physical characteristics of the sediments is extremely difficult or impossible and an upscaling is therefore necessary. Recently, a growing number of thermal applications dealt with innovative methodologies consisting in the measurement of temperature time series within the river or riverbed [101, 118, 102]. These techniques are advantageous since temperature sensors are easier to install in comparison to piezometers, as well as being cheaper.

1.2.3 Biogeochemical processes in the hyporheic zone

Flow interactions between rivers and riverbeds control solute fluxes and travel times that influence hyporheic habitat, microbial metabolism, and biogeochemical transformation rates. Hyporheic and surface water chemistry both depend on sedimentary microbial processes, which are in turn affected by chemistry of inflow water and porewater transport [89, 67, 114, 177, 20]. These processes have been shown to regulate the export and uptake of many stream-borne materials of high ecological significance, including nitrogen, phosphorus, organic carbon, and metals [140, 99, 77, 139, 217, 168]. Early models for microbial processes primarily relied on effective reach-scale parameterization of biogeochemical processes [141, 18, 140]. Recently, increasing process understanding and high-resolution observations have been used to develop spatially-explicit models for key biogeochemical processes – most notably hyporheic nitrogen cycling – at the scale of bedforms and other river channel features that drive hyporheic flow [19, 193, 6, 218].

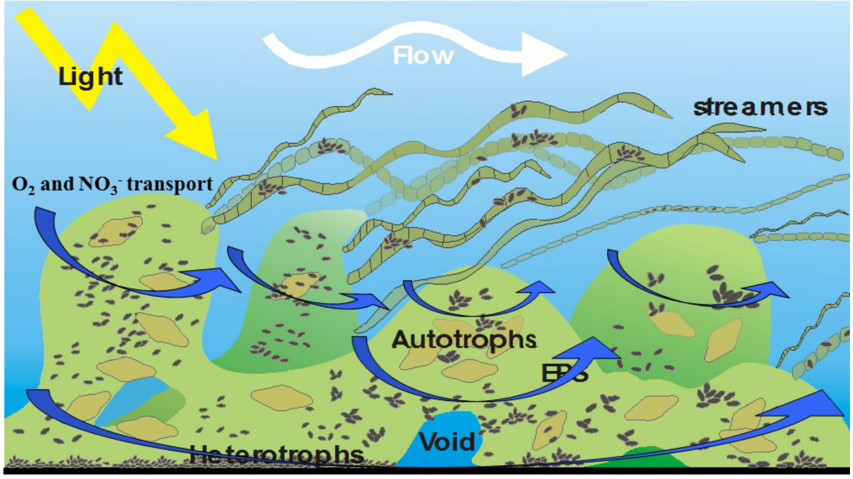

Fig. 1.9 Schematic diagram of hyporheic biofilm composed by heterotropic and autotrophic bacteria, which use oxygen and nitrate for their metabolism. Drawing by S. Arnon (www.civil.northwestern.edu).

The microbial metabolism is based on redox reactions that transform solutes in the sediments into oxidized or reduced substances: in particular, organic substances are used as electron donors with different electron acceptors (e.g., oxygen and nitrate) and ammonium is transformed to nitrate, with implications for the availability of N for plants and algae. These pore-scale transformations influence subsurface solute concentrations and, consequently, the chemistry of upwelling water and the water quality of the stream environment. Heterotrophic and autotrophic bacteria are commonly present within the fluvial sediments: heterotrophs are unable to synthesize their own food from inorganic substances and hence are dependent on external carbon sources while autotrophs obtain the organic carbon molecules (for cellular matter and energy storage) from inorganic compounds using light (photosynthesis) or chemical energy (chemosynthesis). Among chemolithoautotrophic microorganisms, a very important role is played by nitrifying bacteria which get their energy oxidating ammonium to nitrate (nitrification) under aerobic conditions.

The metabolism of these bacteria is essential for carbon and nitrogen cycles. Generally, heterotrophic bacteria can carry out both aerobic and anaerobic processes in function of the available quantity of dissolved oxygen in the water. In presence of sufficient oxygen, the organic substance is decomposed through aerobic respiration, while if there is a shortage of oxygen the heterotrophic bacteria rely on the denitrification, using nitrate as electron acceptor and

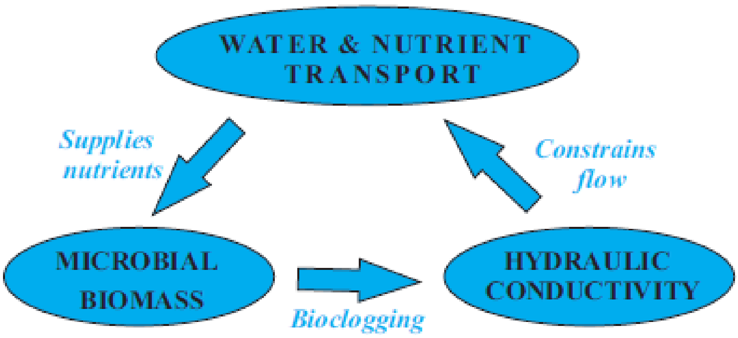

Fig. 1.10 Feedback between hydraulic conductivity, microbial growth and solute transport: hydrodynamic conditions determine and influence solute transport, which, in turn, controls biomass growth rate. Biomass accumulates within the sediment pore space and reduces water inflow and, consequently, penetration of nutrients into sediments, slowing down the own growth.

oxidizing the organic substrate. Overall, the streambed acts as a sink of DOC, oxygen, and ammonium, while nitrate shows a more complex behavior since it is subject to production and consumption reactions [5]. Regarding nitrate, in fact, the streambed can act as source or sink depending on whether nitrification exceeds denitrification, or *vice versa*. A critical controlling factor in establishing the behavior of the system is represented by the hyporheic residence time since it regulates which type of biogeochemical reaction prevails [218, 27]. In fact, for short residence times, oxygen concentration is sufficient to allow a net nitrification environment since it is not fully depleted along the hyporheic flowpaths. Under these conditions, it is therefore expected that the hyporheic zone acts as a net nitrate source through nitrification. Conversely, for long residence times, anaerobic conditions could occur, entailing the activation of the denitrification process. In this situation, the hyporheic zone could act as a net nitrate sink, reducing nitrate concentration in the river system and releasing N_2 concentration to the atmosphere.

Microbes also exert feedbacks on nutrient fluxes through the process of bioclogging (Figure 1.9), i.e. the reduction of water-filled pore volume and sediment permeability caused by biofilm growth and gas production [13, 50]. Microbial growth in streambed sediments primarily occurs in the form of biofilms that encapsulate sediment grains [11, 69]. Biofilm growth in porous media fills pore space, changes hydraulic properties of bed sediments over time, and diverts porewater flow in ways that regulate microbial growth and metabolism [185, 188, 29, 142, 150, 49]. Understanding the bioclogging process in porous media, therefore, involves the study of the coupling between water flow, solute transport, and microbial growth (Figure 1.10, [41]) but existing models generally do not consider feedbacks between microbial growth and porewater flow.

1.2.4 Effect of ambient GW system on hyporheic exchange

The multiple scales at which hyporheic exchange is commonly observed are small if compared with the watershed scales of groundwater fluxes within the aquifers. It is thus useful to distinguish small-scale hyporheic fluxes from the interactions induced by large-scale hydraulic head gradients in order to understand how these two different types of river-groundwater interactions affect each other. In fact, the exchange of water and solutes at the small scale typical of the hyporheic fluxes is strongly controlled by the upward or downward groundwater flow at larger scales.

The ambient groundwater flow diminishes hyporheic exchange (Figure 1.11) confining the portion of sediments in which these processes can occur and influencing stream nutrient cycling [215, 22, 23, 35, 4]. One of the most emblematic situations in which hyporheic and regional flows interact occurs when the river is in gaining conditions, i.e., it is fed by the aquifer. In this situation, the underlying groundwater flow system obstructs the penetration of stream water into the sediments, limiting the extent of the hyporheic zone and the magnitude of hyporheic flow paths [215, 22, 23, 71]. In order to analyze the hyporheic processes embedded within larger groundwater systems is therefore necessary to describe how the flow originating from the surrounding aquifer impacts exchange fluxes along the hyporheic corridor [38].

Understanding the role of large-scale hydraulic gradients on hyporheic exchange is extremely important for the health of fluvial ecosystems because of the implications for nutrient and other contaminants in river water and for the biogeochemical and ecological processes occurring along the river corridor [35, 199]. In fact, hyporheic exchange is highly variable along the river-aquifer interface [122, 28, 79] and this variability is induced, together with other

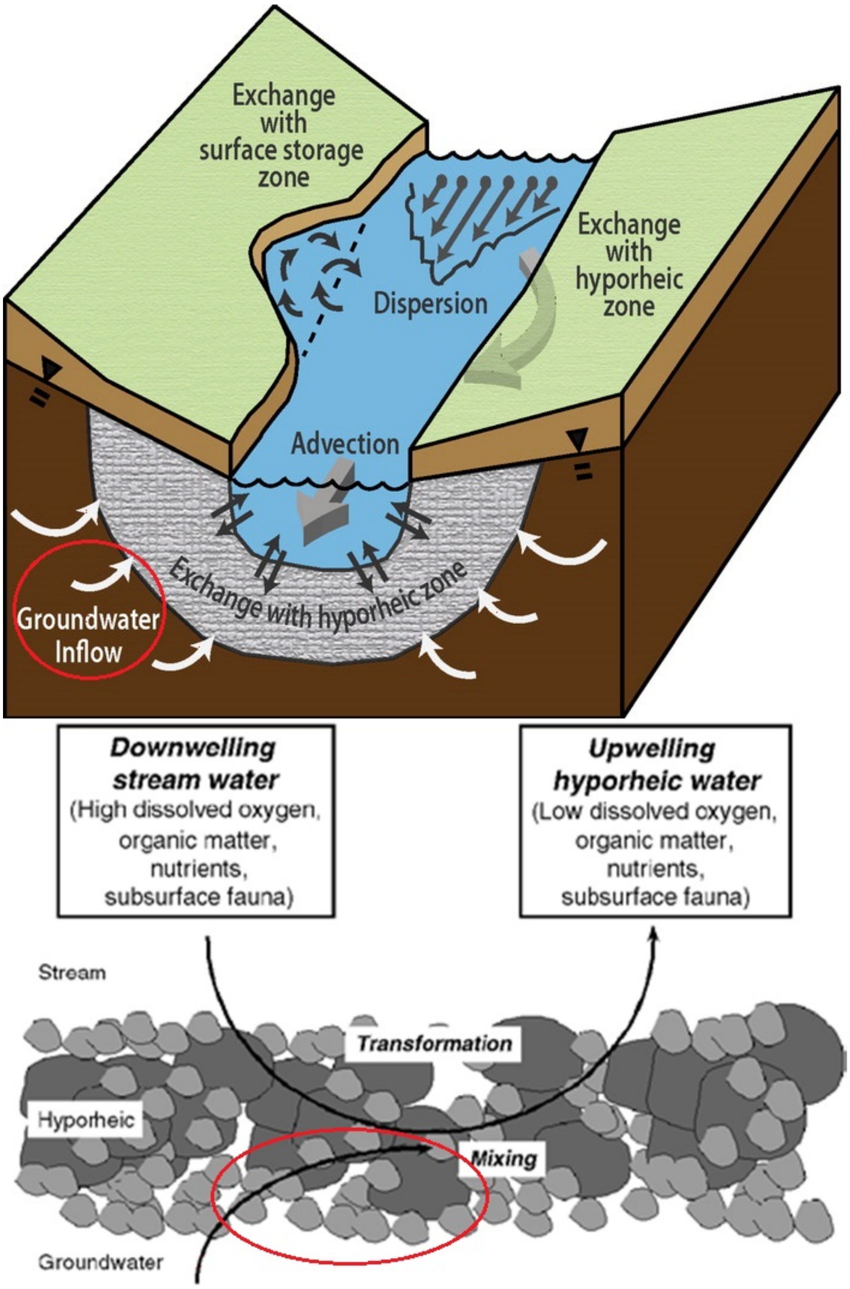

Fig. 1.11 Confinement effect of groundwater flow systems on hyporheic exchange. From Connor *et al.* [143] (upper figure) and Hancock *et al.* [94] (lower figure).

factors, by the complex structure of the groundwater flow system, which determines the intensity of the exchange with the surface system. The difficulty in estimating groundwater fluxes resides in the heterogeneity of hydraulic properties and geomorphological characteristics across a wide range of spatial and temporal scales [86]. This implies that GW-SW interactions in streams are not easy to measure with an extent and spatial resolution that allows for the characterization of groundwater discharge patterns at watershed scale. Therefore, there is still a lack of easily applicable and accurate methods to measure groundwater fluxes at the river-aquifer interface over long distances [120, 20].

Several numerical and field-based studies assess GW-SW interactions at large scale analyzing some specific aspects (hydrological stresses, aquifer heterogeneity, etc.). However, the role of the hyporheic zone in this interaction is not examined in detail in these studies [121, 83, 9, 81, 133]. Conversely, some modeling and experimental approaches were developed to specifically investigate the impact of large-scale river-aquifer interactions on the main properties of local exchange at various scales [36, 22, 23, 35, 198, 199, 71]. A first study was developd by Cardenas and Wilson [36], who expanded their previous work on the interactions between turbulent water column and underlying porous media modelled on dunes, including the effect of ambient groundwater discharge. Boano et al. [22, 23] investigated the influence of groundwater upwelling on bedform-induced hyporheic exchange developing a general simplified mathematical model (see Figure 1.12) and demonstrating how the large scale exchanges modify the shape and the residence time of hyporheic flow pathways. At the small scale of river bedforms, laboratory studies [71] were also performed, which assessed how increasing losing and gaining stream flow conditions reduce the hyporheic fluxes for a simple case of interaction with small geomorphological structures. Other analyses were conducted at larger scales. Trauth et al. [198, 199] showed by way of a 3D numerical model (which couples a fluid dynamics code to a groundwater flow model) that a reduction of the hyporheic exchange flow rate in pool-riffle stream is caused by ambient groundwater. The study also demonstrated how some biogeochemical reactions (aerobic respiration and denitrification) are influenced by variations of gaining and losing conditions. Cardenas [35] demonstrated via numerical modeling that the sinuosity-driven hyporheic exchange is affected by net gains/loses of water to the adjacent aquifer

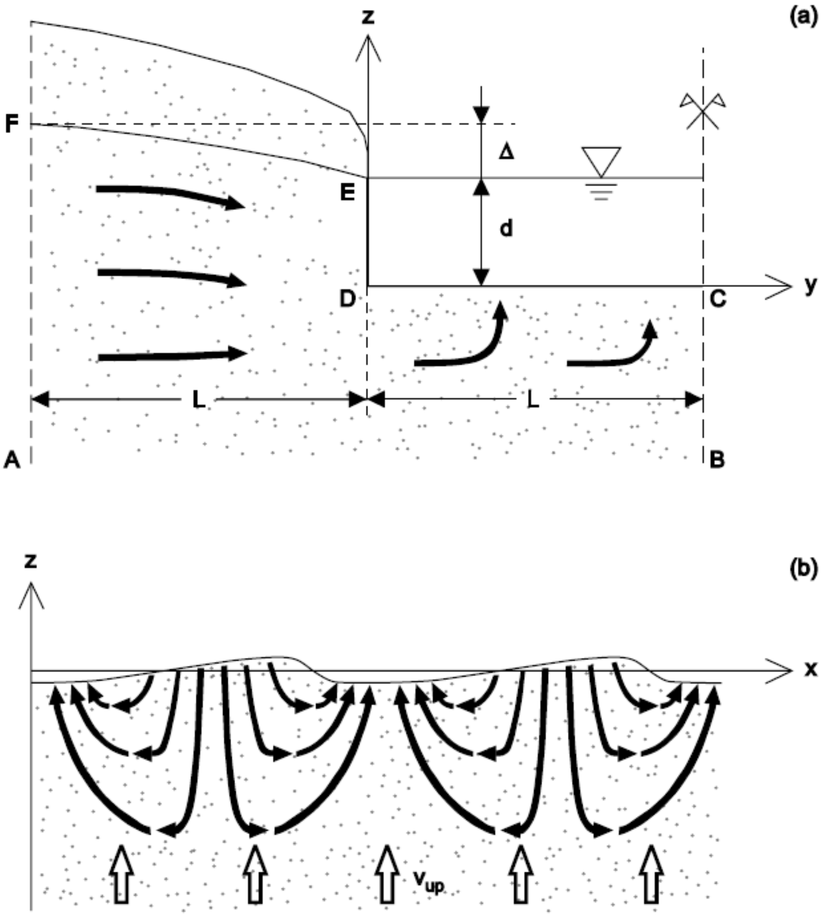

Fig. 1.12 Scheme of the model proposed by Boano *et al.* [22] to estimate the extent of the hyporheic zone taking into account the role of the groundwater discharge. The bold arrows qualitatively show (a) the large-scale exchange induced by the head difference between the groundwater table and the stream stage and (b) the bedform-induced hyporheic exchange.

similarly to the case of bed-form driven hyporheic zones. The work showed that the exponential reduction in hyporheic flux caused by gaining/losing conditions is more pronounced in straight channels than in sinuous channels. Gomez-Velez et al. [84, 85] proposed a multi-scale model to upscale the hyporheic exchange at the watershed scale. Hyporheic exchange in synthetic river networks was evaluated integrating the fluxes induced by single geomorphological features, obtaining a quantification related to the whole river system. Nevertheless, the influence of the upwelling component of regional groundwater flow was considered in a simplified way.

All the mentioned studies have provided some insights on the interactions between hyporheic exchange and groundwater flow at different scales. However, a clear and complete evaluation of how hyporheic fluxes interact with groundwater at watershed scale (generally 10-1000 km in extent) and are affected by the landscape structure is still missing [20, 71]. Such an evaluation is fundamental to predict the actual behavior of hyporheic exchange along the river network and its influence on nutrient cycling.

1.3 Motivations behind the study and outline of the thesis

The main issue of this dissertation is the investigation of the interactions between GW and SW at different spatial scales aimed at predicting biochemical reactions in river sediments and riparian zones. The main aims are essentially two: i) to estimate the upwellling and downwelling groundwater velocities along a river network in order to analyze the effect of groundwater flow system on hyporheic exchange at large scale, and ii) to study the coupling between water fluxes, nutrient reactions, and permeability variations due to microbial growth at small scale. The work is organized into three key research questions, the first two concerning the first task and the third one referring to the second task.

How much the watershed-scale groundwater discharge impacts dune-induced hyporheic exchange along the river corridor? More specifically, what is the role of the watershed topography on river-aquifer interactions and, consequently, on *hyporheic fluxes in a basin with a topography-controlled water table, i.e., in humid regions with low hydraulic conductivity?*

A clear and complete evaluation of how hyporheic fluxes interact with groundwater at the watershed scale and are affected by the landscape structure is fundamental to predict the actual behavior of hyporheic exchange along the river network and its influence on nutrient cycling. In Chapter 2, the impact of the regional groundwater flow on hyporheic fluxes is analyzed by investigating how these exchange fluxes vary along the river corridor. In this section, a semi-analytical model is adopted, based on some simplifications: first, the groundwater head distribution throughout the basin is obtained as an approximation of the landscape topography (i.e., the condition under which the water table does closely follow the topography is assumed) and secondly the case-study aquifer is considered as homogeneous and isotropic. Understanding how exchange fluxes vary along the river corridor is a first step to eventually analyze the consequences of hyporheic exchange on water quality and stream ecology at large-watershed scales.

Once the high spatial variability in GW-SW interactions induced by landscape topography in a homogeneous and isotropic aquifer at watershed scale has been established, is it possible to point out the main hydrogeological and topographic controls of GW discharge patterns? Can some factors be neglected in modeling and describing GW-SW interactions at regional-watershed scale?

Predicting the spatial patterns of river-aquifer interactions is challenging because of the strong spatial variability paired with the complexity in realizing field measurements with an appropriate resolution necessary to characterize this pronounced variability. Despite the significant advancements in the last years, realizing such field measurements remains difficult and not easily affordable. Therefore, the main factors controlling groundwater discharge patterns are not well understood. With regard to this, in Chapter 3, a numerical model is developed to simulate river-aquifer interactions in a catchment and investigate the dependence of exchange patterns on hydrogeological and topographic factors.

Shifting the focus on smaller scales (i.e., scales of single geomorphological units), how the microbial biomass growth within the sediment pore space controls the distributions of permeability and porewater flow and the micro-

bial transformation rates of coupled nitrogen, carbon, and oxygen dynamics in bedform-induced hyporheic zones?

It is well known that riverbed sediments host important biogeochemical processes that play a key role in sedimentary nutrient transformations, which are mediated by bacteria in the form of attached biofilms. However, the influence of microbial dynamics within the hyporheic zone is poorly understood. In Chapter 4, a hydrobiogeochemical model is presented in order to assess how biomass growth (heterotrophic and autotrophic bacteria) affects the transport and transformation of dissolved nitrogen compounds in bed form-induced hyporheic zones. The model is build on prior studies that represented the effects of hyporheic exchange flow, nitrogen dynamics, and heterotrophic and autotrophic metabolism, but they did not account for the consequences of this metabolism in biomass growth that fills pore space and alters hyporheic flow rates and patterns.

Chapter 2

Impact of landscape topography on hyporheic exchange at basin scale

The work described in this chapter has been previously published in a research article appeared in a peer-reviewed international journal [40].

2.1 Introduction

Among the interactions between surface water bodies and aquifers, hyporheic exchange has been recognized as a key process for nutrient cycling and contaminant transport. As discussed in Section 1.2.4, hyporheic exchange is strongly controlled by groundwater discharge since the groundwater flow system obstructs the penetration of stream water into the sediments and limits the extent of the hyporheic zone and the rate of the hyporheic fluxes [22, 23, 198, 71]. Our understanding of the impact of the regional groundwater flow on hyporheic fluxes is still limited because of the complexity arising from the multi-scale nature of these interactions. In fact, the impact of large-scale stream-aquifer interactions on small-scale exchange has generally been analyzed at local scales of a river reach, or even smaller. However, a complete comprehension of how hyporheic fluxes are affected by the groundwater system at watershed scale is still missing. Analyzing this influence is useful in order to predict the consequences of hyporheic exchange on water quality and stream ecology.

In this chapter, we investigate how the geometrical complexity of the water table at the watershed scale affects the spatial patterns of groundwater inflow fluxes in a river network and, in turn, hyporheic fluxes. Our aim is to provide a deeper understanding of how hyporheic processes are influenced by the ambient groundwater flow, examining the impact of groundwater structure at a large scale on the hyporheic fluxes. Focusing on catchments in humid regions, we consider a case in which the shape of the water table can be plausibly assumed to reproduce the one of the topographic surface [196, 93, 213]. Under these conditions, the complexity of the water table structure is a direct consequence of the topography complexity, i.e., the geometrical variations of the ground surface elevation spanning a wide range of spatial scales.

The main results show that the complex geometrical structure of the water table is itself able to entail a strong spatial variability of upwelling groundwater (i.e., groundwater upwards flow) along the river corridor and, consequently, of the confinement effect of the hyporheic zone. A statistical analysis of the spatial correlation of groundwater fluxes confirms the high variability of groundwater discharge to the river network. In addition, we evaluate the origin and the travel times of groundwater fluxes, which have important implications for the management of chemicals. Finally, we assess that both the groundwater fluxes into the river and the travel times of water pathways through the aquifer show a similar behavior when the analysis is limited to the only main river or extended to the whole river network.

2.2 Methods

2.2.1 Water table modelling and groundwater flow field

Characterising the groundwater table is fundamental in order to examine the groundwater flow field and the GW-SW water connection. Water table at large (regional to continental) scale can be classified as "topography-controlled" or "recharge-controlled" (see Figure 2.1), depending on the degree to which it is influenced by the topography [93, 82]. In this study, we considered the case of

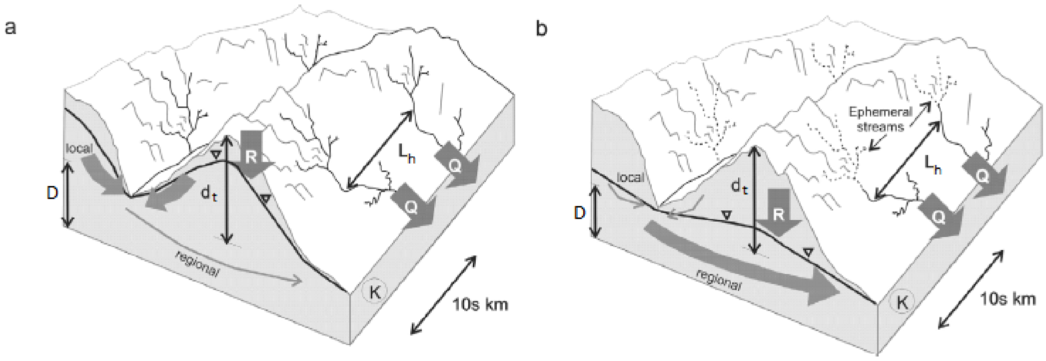

Fig. 2.1 (a) Low-permeable aquifer with topography-controlled water table and (b) highly permeable aquifer with a recharge-controlled water table. The variables (D, d_t, R, Q, K) are defined in the text. Modified from Gleeson *et al.* [82].

a water table that is controlled by the topography and that can be considered a subdued and smoothed version of the ground surface. This assumption has been largely employed in the literature in both seminal [196, 145] and recent [33, 214, 112] studies and asserts that the water table is fixed and the patterns of recharge and discharge areas are fixed as well. A different approach to groundwater modelling consists of imposing a recharge rate on the top of the aquifer and specifying the hydraulic head where streams interact with the aquifer; in this case, the water table is not prescribed [83].

This assumption allowed us to consider a water table derived from the topography ($H(x, y) = Z(x, y)$, where H is the phreatic surface and Z is the ground surface elevation), introducing a remarkable advantage as terrain elevation data are characterised by higher accuracy, higher resolution and easy accessibility in comparison to precipitation and evapotranspiration data [130]. The correctness of considering a water table that closely follows the shape of the ground surface will be tested in section 2.2.2 for our specific case. An orthogonal reference system was chosen, where x and y define the horizontal plane, while z is the vertical direction (positive upward). Here, $z = 0$ is defined as the lowest point of the water table in the catchment. In this system, the phreatic surface is denoted as $H(x, y)$.

In the present study, groundwater flow was analyzed under steady state conditions assuming that the groundwater surface was static and neglecting temporal variations. The basic governing differential equation for steady-state groundwater flow in a homogeneous and isotropic medium is the Laplacian

Fig. 2.2 Decomposition of raw data into Fourier components and reassembly into a topography function by summing the Fourier components. From Stonedahl [181].

equation given by $\nabla^2 h = 0$, where h is the hydraulic head of the groundwater [15]. In the two-dimensional case – where the transverse flow component is neglected – an exact solution of the subsurface flow field was obtained by Tóth [196] considering a spatially periodic (sinusoidal) head distribution applied over a flat bed that depicted the top boundary of the aquifer. Therefore, for the case of a flow field subject to a sinusoidal spatial pressure variation composed by a single harmonic, the solution of the subsurface flow field is known.

In order to use the abovementioned analytical solution, we modelled a domain bounded by two horizontal planes located at $z = 0$ and $z = -D$, where D is the finite depth of the aquifer. As boundary conditions, we considered a flat top surface at depth $z = 0$ where the head distribution described below is imposed (Dirichlet condition) and a no-flow boundary condition at the depth $z = -D$. Mathematically, these boundary conditions mean that $h(x, y, z = 0) = H(x, y)$ and $\partial h/\partial z|_{z=-D} = 0$, where $H(x, y)$ denotes the phreatic surface. Following the approach adopted in previous works [196, 220, 213], the water table can be decomposed into a sum of harmonics each with different amplitude and frequency. Since the Laplace equation is linear, the overall solution can be calculated as sum of the individual solutions related to the single harmonics (Figure 2.2). Starting from the simplification adopted in [196, 63] and using the superposition principle applied to potential Darcy groundwater flow, we adopted the approach proposed by Wörman et al. [213] which extended the two-dimensional solutions [196, 63] to three-dimensional domains and derived an analytical expression to determine GW-SW flows in three dimensions for an arbitrary topography, that is decomposed in a Fourier series. To this aim, we employed the codes "Spectop" and "Specvel" developed by Wörman et al. [213] for spectral analysis of the groundwater table.

The complexity in the subsurface flow pattern arises from the interaction between multiple scales characterizing the landscape topography. Each topographical feature, with a specific wavelength, most strongly affects the flow at a certain depth and the dominant wavelength increases with increasing depth [214]. The surface-subsurface water flux is dominated by a decreasing impact of topography with depth and with landscape wavelength. The interactions between shallow and deeper subsurface flows also explain the confinement effect of larger patterns of groundwater discharge and recharge in rivers (e.g., gaining vs. losing reaches) on spatial patterns and fluxes of water in streambeds (hyporheic exchange) [214]. The interfacial flux depends to some extent on all topographical scales in any point in the landscape, however it is likely to be dominated by smaller-scale topographic features. In fact, larger boundary head gradients are produced by smaller scale topographic features and, therefore, these smaller scales tend to mainly control river-aquifer flux in the fractal landscape [214]. The effects of the surface topography decay relatively rapidly, and the flows found at increasing depths must be induced by larger-scale topographic features.

The amplitude and wavelength of the head surface control the depth and spatial pattern of the exchange. In fact, higher-amplitude head variations drive deeper hyporheic flow, while shorter-wavelength head variations create more circulation cells with reduced path lengths and exchange times [192, 196]. The total pressure distribution on the streambed bottom is given by variations in (1) the elevation head (changes in bed elevation), (2) the static pressure head (changes in flow depth), and (3) the dynamic pressure head (changes in flow velocity and momentum). The relative importance of each of these pressure components changes with discharge, channel hydraulics, and bed topography. When the bedforms are only shallowly submerged, they strongly interact with the flow, creating spatial variations in velocity and dynamic pressure-head gradients that further enhance hyporheic exchange. As flow increases and submerges bed topography, the bedforms exert less influence on the water-surface profile, which becomes more uniform, reducing the spatial variation of static pressure and decreasing hyporheic exchange [192]. In contrast, dynamic pressure-head variations may increase or decrease with discharge, depending on bedform shape and whether flow separation (strong vorticity regions) occurs in the lee of the bedform.

The application of the described approach requires a spatial distribution of hydraulic head $H(x, y)$ to be prescribed. Digital elevation models (DEMs) are commonly used to depict the complexity inherent to a real landscape topography. Using topographic data provided by a DEM, landscape topography can be used as a proxy for the phreatic surface H:

$$H(x, y) = \langle h \rangle + \sum_{j=1}^{N_y} \sum_{i=1}^{N_x} (h_m)_{i,j} \sin(k_{x,i} x) \cos(k_{y,j} y) \tag{2.1}$$

in which $\langle h \rangle$ is areal mean value of the hydraulic head, N_x and N_y are the numbers of real harmonic functions applied in the x and y directions respectively, $(h_m)_{i,j}$ are the amplitude coefficients, $k_{x,i} = 2\pi/\lambda_{x,i}$ and $k_{y,i} = 2\pi/\lambda_{y,i}$ are the wave number, and $\lambda_{x,i}$ and $\lambda_{y,i}$ are the wavelength of the i-th harmonic in each direction. Hence, the periodicity of the water table was examined using a linear combination of harmonics encompassing a wide range of frequencies [213].

Using the above-mentioned boundary conditions and solving the Laplace equation, the three-dimensional head distribution is given by [213]

$$\begin{aligned} h(x, y, z) = \langle h \rangle + &\sum_{j=1}^{N_y} \sum_{i=1}^{N_x} (h_m)_{i,j} \cdot \sin(k_{x,i} x) \cos(k_{y,j} y) \cdot \\ &\cdot \frac{\exp\left(\sqrt{k_{x,i}^2 + k_{y,j}^2}\, z\right) + \exp\left(\sqrt{k_{x,i}^2 + k_{y,j}^2}\,(-2D - z)\right)}{1 + \exp\left(-2\sqrt{k_{x,i}^2 + k_{y,j}^2}\, D\right)} \end{aligned} \tag{2.2}$$

in which $-D \leq z \leq 0$, i.e., the solution is valid only below the plane where the sinusoidal head is applied. Each term of Eq. (2.2) represents a partial solution to the groundwater flow field related to a specific spatial scale and the relative contribution of each harmonic to the entire signal is provided by the amplitude of that harmonic.

The unknown variables of a Fourier series are the amplitude (or Fourier) coefficients and they can be determined by a least-square fitting of Eq. (2.1) to the given topographical dataset. The wave number can be selected arbitrarily, provided that they respect the constraints for possible wavelengths (i.e., periodicity equal to the domain size and frequencies smaller than the Nyquist frequency) [130]. However, it must be chosen so as giving an appropriate representation of the water table. An exemplary representation of a ground

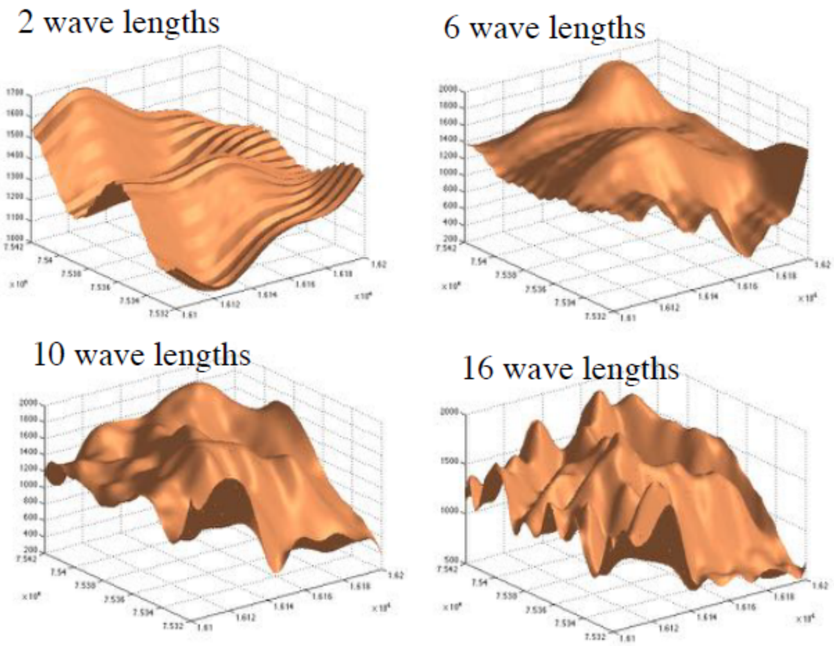

Fig. 2.3 Example of terrain approximation as number of increasing wavelengths. From Wörman.

surface as a function of different numbers of wavelength is given is Figure 2.3). To model the phreatic surface, the longest wavelength, λ_{max}, was chosen equal to the mean value of the domain lengths in the x and y directions, as suggested by Wörman [213]. The other wavelength values were calculated as sub-multiples of the longest one. As a result, the shortest wavelength, λ_{min}, was equal to the longest one divided by the number of wavelengths in each direction, i.e. $\lambda_{min} = \lambda_{max}/N$. In addition, we adopted isotropic harmonic functions so that $N_x = N_y = N$ and $\lambda_{x,i} = \lambda_{y,i} = \lambda_i$.

The analytical solution (2.2) was applied to evaluate the head distribution and, consequently, the subsurface velocity field over the whole domain as $\mathbf{q} = -K\nabla h$, where $\mathbf{q}$ is the Darcy velocity vector, and K is the hydraulic conductivity. Darcy velocity was divided by the soil porosity to obtain an effective velocity, v, of the water within the pores. Similarly to other works [33, 83], we considered a porous medium, with homogeneous and isotropic geologic conditions. While this assumption is not well representative of the real stratigraphy on an aquifer, our objective is to describe the general structure of river-aquifer interaction focusing on the hydraulic heterogeneity induced by the complexity of the water table shape. The value of hydraulic conductivity was chosen through a calibration procedure. For different values of hydraulic conductivity, the groundwater recharge (determined as the total vertical flux at $z = 0$ over the whole basin) was calculated and compared to the measured areal mean value for recharge. The value of K was changed until a good comparison between modeled and observed recharge was obtained.

2.2.2 Input data

In this section, the input data used to test the model are introduced, in conjunction with the description of the study area to which the data are related. The choice of a specific study area is not to be interpreted as a restriction of our analyses and results to a specific region. Rather, it is aimed to assess the impact of a realistic landscape topography on river-aquifer interactions, working with topographic data from a real catchment.

The method was applied on the Borbore catchment (44° 53' N; 8° 12' W), located in the Piedmont region, in the Northwestern part of Italy. The total area of the watershed is 506 km^2. The region has a continental climate, with a mean annual air temperature of 13 °C and the mean annual rainfall is 723 mm. The basin is located in a predominantly rural area, and the distribution of land use is 62.8% agricultural lands, 30.7% forest, 4.1% grasslands, 1.9% residential lands, 0.2% shrub land, 0.2% landfill, and 0.1% uncultivated land. The global data set of monthly irrigated and rainfed crop areas (MIRCA 2000, [154]) shows that the Borbore basin is almost entirely rainfed and the percentage of irrigated area is extremely low. Hence, seepage from irrigation canals is not an important source of recharge to shallow groundwater and has a minimal effect on groundwater levels and boundary conditions [66]. The elevation of the landscape ranges from 114 m to 544 m a.s.l., with a mean value of 232 m a.s.l. The annual average discharge of the Borbore river is about 9 m^3/s, that corresponds to a mean annual runoff of about 560 mm. This value was taken as reference value to calibrate the hydraulic conductivity. Information about the study area is provided by the Regional Agency for the Environmental Protection of Piedmont (ARPA), which confirms the absence of a significant irrigation system.

To represent the topography of the study area, we used a DEM with a resolution of 50 m (l_{pixel}= 50 m). A channel-threshold area method for extracting channel networks from DEMs was used. This method consists of specifying a critical support area that defines the minimum drainage area required to initiate a channel [138]. The impermeable layer was located at a depth D = 500 m under the lowest point of the water table, except where specifically indicated. As mentioned in section 2.2.1, detailed geological and geomorphological aspects are not here taken into account since the analysis of their influence goes beyond the scope of the present work in order to isolate the only impact of the water table geometry. The study area is composed mainly of successions of clays and sands and therefore is characterized by low permeability values, coupled to a relatively high precipitation rate. As discussed below, these hydrogeologic properties are compliant with the characteristics required for the validity of the topography-controlled water table assumption since they concur to cause a shallow water table.

2.2.3 Check of the topography-controlled water table assumption

The parameters required to evaluate the solution in equation (2.2) are here selected and the topography-controlled water table assumption is tested for the specific case. The differentiation of the water table into two types, i.e., topography- or recharge-controlled, depends on the aquifer properties and climate characteristics. Some criteria are suggested in the literature to check if the shape of the water table can be reasonably approximated by landscape topography. Haitjema and Mitchell-Bruker [93] proposed a dimensionless criterion to distinguish under what circumstances groundwater flow is controlled by landscape topography or when it is recharged-controlled. The former situation occurs in humid climates or regions with low topographic relief, where the recharge rate (precipitation) is sufficiently high relative to the infiltration capacity of the ground. In these areas, the groundwater table closely follows the topography. Conversely, in dry climates or regions with high relief, groundwater systems are characterized by deep groundwater tables and there is essentially no correlation between the shapes of the topography and of the water table.

First, we applied Haitjema's criterion [93] to evaluate the soundness of the hypothesis of topography-controlled water table in the study domain. This criterion is based on the evaluation of the following ratio

$$\frac{\Delta}{d_t} \simeq \frac{\mathcal{R} L_h^2}{8 K D d_t} \tag{2.3}$$

in which Δ is the maximum groundwater mounding (i.e., the maximum difference in elevation of the water table), d_t is the maximum terrain rise, $\mathcal{R}$ is the recharge rate, and L_h is the distance between hydrological boundaries. If the ratio Δ/d_t is less than 1, the groundwater circulation can be classified as recharged-controlled; if it is equal to or greater than 1, the phreatic surface is topography-controlled.

The previous criterion evaluates if the hypothesis of topography-controlled water table can be considered correct on the basis of landscape and climate properties averaged over the whole basin. When the water table is modelled as the sum of many harmonics, a more local perspective can be formulated to choose an appropriate number of wavelengths that takes into account that the groundwater surface undulation is certainly smoother and damped with respect to the landscape topography [63, 211]. Therefore, the number of wavelengths used in the Fourier series must be chosen in order to obtain a water table that is plausible and does not induce high-frequency oscillations which cannot exist in the real water table. The local elevation of the water table is governed by the balance between areal recharge and water flows, and this balance is governed by the following Poisson-like differential equation

$$\nabla^2 H^2 = 2\mathcal{R}/K. \tag{2.4}$$

The Laplacian of H^2 can be numerically calculated for each raster pixel of the groundwater table and compared with the threshold value $2\mathcal{R}/K$. If the condition $\nabla^2 H^2/(2\mathcal{R}/K) \leq 1$, is satisfied, the water table follows the topography at that point and the assumption is valid. As discussed in section 2.3 below, values slightly higher than unity will also be accepted provided they only occur in small parts of the catchment. Following this criterion, the phreatic surface was modeled by Eq. (2.1) using different numbers of harmonics N. Specifically, we started with a detailed description of the water table using a large number of harmonics, and we gradually eliminated some harmonics until Eq. (2.4) was verified for a large part of the points of the considered domain. It was observed that the area where the condition (2.4) was satisfied increased when a lower number of harmonics was used to model the phreatic surface. On the other hand, a low number of harmonics was insufficient to reproduce a plausible configuration of the water table and, consequently, of the river network. Therefore, a good compromise between these conflicting instances was searched, choosing a number of harmonics which respects both the requirements satisfactorily.

On the basis of the above considerations, we selected a number $N = 23$ ($N^2 = 529$ terms) of harmonics in each direction to use in the spectral solution given by Eq. (2.1). The condition $\nabla^2 H^2/(2\mathcal{R}/K) \leq 1$ was rigorously satisfied for about 55% of the domain points. In addition, about 95% of the domain points satisfied the condition $\nabla^2 H^2/(2\mathcal{R}/K) \leq 3$ and the whole study domain satisfied the condition $\nabla^2 H^2/(2\mathcal{R}/K) \leq 5$. The application of Eq.(2.4) at the scale of a single pixel (50 m) allowed us to eliminate steep local hydraulic gradients that are physically unrealistic. Hence, the chosen number of harmonics assured an appropriate modeling of the water table, with a good compromise between the absence of excessive undulations of the water table and the accuracy of the river network. The DEM of the study area and the water table obtained by the spectral representation are shown in Figure 2.4. The wavelengths of the phreatic surface range from $\lambda_{min} = 1.55$ km to $\lambda_{max} = 35.5$ km.

For the chosen value of N, the calibration procedure explained in section 2.2.1 has led to a homogeneous hydraulic conductivity of $3.2 \cdot 10^{-6}$ m/s. A value of porosity $n = 0.3$ which is consistent with the prevalent lithology (clay and sand, [105]) was set. Assuming L_h equal to the characteristic length of the study domain, the ratio $\nabla h/d_t$ in Eq. (2.3) is about 4, well above the unitary threshold. Therefore, according to the criterion stated by Haitjema and Mitchell-Bruker, the groundwater circulation in the study domain can be classified as topography-controlled.

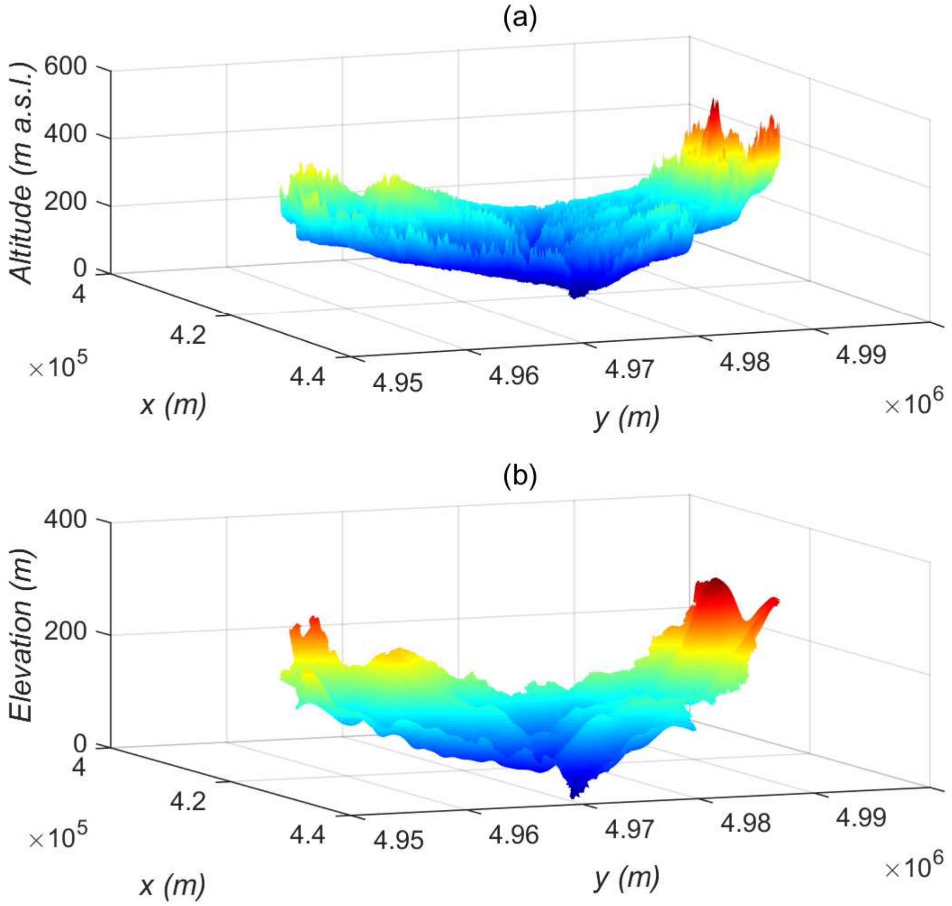

Fig. 2.4 (a) Landscape topography of the study domain according to the digital elevation model (DEM) with resolution 50x50 m. The coordinate system is WGS84/UTM. (b) Representation of the water table obtained by the spectral solution using a number of harmonics $N = 23$ in x- and y- direction. The elevation values are defined with respect to the plane $z = 0$ passing through the lowest point of the water table. Warmer colors indicate higher elevations.

2.2.4 Evaluation of exchange fluxes and groundwater pathway travel times

Once the water table was defined, the groundwater flow field was calculated over the whole domain as explained in section 2.2.1. The evaluation of the groundwater flow field allowed us to identify discharge and recharge areas in the study basin. Recharge zones are areas where the aquifer is fed by surface water from precipitation or rivers (vertical component of Darcy velocity $q_z < 0$). Conversely, discharge zones are areas where groundwater leaves the aquifer ($q_z > 0$), establishing effluent conditions and contributing to surface water supply. The distribution of recharge and discharge areas is strictly correlated to the configuration of the water table and significantly influences the structure of groundwater circulation [196, 10].

In order to quantify the impact of regional groundwater discharge on hyporheic exchange at smaller scales, the groundwater velocity was first estimated along the river corridor. Then, focusing on predicted hyporheic fluxes induced by bedforms [63], it was possible to evaluate the reduction of the size of hyporheic zone caused by groundwater upwelling through the relationship proposed by Boano *et al.* [22]

$$z_H = \frac{1}{k_{dune}} \log\left(\frac{q_z}{u_0}\right), \tag{2.5}$$

where z_H indicates the hyporheic zone depth, $u_0 = k_{dune} K_v h_0$ is a typical velocity scale for the hyporheic flow, $k_{dune} = 2\pi/l_{dune}$ is the bedform wavenumber, l_{dune} is the bedform wavelength, K_v is the streambed hydraulic conductivity, and h_0 is the amplitude of the hydraulic head profile determined by the presence of the bedform. This head difference is commonly evaluated as [63]

$$h_0 = 0.28 \frac{U^2}{2g} \left(\frac{h_{dune}/d}{0.34}\right)^r, \tag{2.6}$$

where U is the mean stream velocity, h_{dune} is the bedform height, d is the stream depth, g is the gravity acceleration, and r is an exponent equal to 3/8 if $h_{dune}/d < 0.34$ and 3/2 otherwise. The bedform geometry can be correlated to the flow and bed characteristics through the relations proposed by Julien and Klaassen [115] given as

$$h_{dune} = \eta d\left(\frac{D_{50}}{d}\right)^{0.3}, \quad l_{dune} = \eta\xi d, \tag{2.7a, b}$$

with D_{50} the median sediment diameter of the erodible bed and η and ξ empirical coefficients. The average values of these coefficients are equal to $\bar{\eta} = 2.5$ and $\bar{\xi} = 2.5$. Moreover, the hyporheic exchange flux per unit bed area, q_H, was evaluated following the theory proposed by Boano et al.[23] as

$$q_H = q_{H,0}\sqrt{1 - \left(\frac{q_z}{u_0}\right)^2} + \frac{q_z}{\pi}\arcsin\left(\frac{q_z}{u_0}\right) - \frac{q_z}{2}, \tag{2.8}$$

with $q_{H,0} = u_o/\pi$ the hyporheic exchange flux in neutral conditions [63].

The identification of the groundwater discharge areas requires some attention as the method overestimates the width of the upward groundwater flow zones around the river network (as it is shown later in 2.3.1). The reason is the lack of a specific boundary condition imposing the level of the phreatic surface equal to the river head where a river is present. To take into account that some trajectories ending near the river could actually feed the river either as runoff over hillslopes or as direct groundwater flow, we considered a strip of extension B located around and along the river. The discharge of each raster cell (pixel) belonging to this strip was calculated as $Q_i = q_{z,i} \cdot A_{pixel}$, where $q_{z,i}$ is the Darcy vertical velocity of the i-th cell and $A_{pixel} = l_{pixel}^2$, and Q_i was attributed to the closest river cell. To evaluate quantitatively the exchange fluxes between the aquifer and the main river, the total groundwater discharge related to each river cell was obtained by the algebraic sum of discharge to the river cells as $Q = \sum Q_i$, where the summation is extended to all cells within the delimited strip of width B. Following this criterion, groundwater discharge to the main river was quantitatively evaluated in terms of volumetric flow rate of exchanged water for each river cell. The cumulative flux per unit channel width defined as $f_z = \int_0^L q_z dl$, where L is the river length, was obtained integrating the value of the vertical velocity beneath the riverbed along the channel. This quantity gives an indication of the overall behavior of the river (i.e, gaining or losing depending on the positive or negative sign of f_z).

The spatial variability of groundwater upwelling along the river can be inferred from the autocorrelation function of the vertical velocity, ρ_{q_z}. Low values of the autocorrelation function indicate that values of ρ_{q_z} at points located at a given distance are not statistically correlated between themselves (generally it is assumed that a value $|\rho| < 0.2$ indicates an absence of correlation). In order to describe the correlation by varying the level of detail of the water table representation, we chose different values of the number of harmonics N. For each value of N, the value of hydraulic conductivity was conveniently calibrated (as illustrated in section 2.2.1) and the value of λ_{min} was modified. As previously explained, λ_{min} is a function of the number of harmonics, N, used to model the phreatic surface and it becomes smaller as the number of harmonics increases.

In order to assess the origin of the groundwater discharging to the river and the time spent in the aquifer, we calculated the groundwater flow trajectories by a particle tracking routine [166, 213]. Different infiltration areas in the basin can entail different physicochemical characteristics because of the effect of land-use type on soil properties. Moreover, longer flow paths and longer contact time with subsurface materials may influence the chemical characteristics of the receiving surface water. To identify inflow patterns of groundwater to the river, a single particle was placed at the $z = 0$ plane in each discharge cell (which represents the arrival cell for a pathway that feeds the river) within the considered area. The flow field was then reversed to track the streamline backwards. Therefore, the water particle positions were tracked along flow pathways and the location of groundwater discharge along the river network was determined. Finally, we evaluated the groundwater travel time, i.e., the time spent by a water parcel from its entrance into the soil to its discharge into a surface water body. The travel time T_i of each i-th trajectory was used to obtain the pathway travel time distribution. The modeled travel times are somewhat underestimated since the distance between the top of the domain and the water table is neglected. However, this underestimation is only relevant for short pathways, while it is negligible for the long times which characterize the tail of the probability density function.

In order to present results in dimensionless form and obtain their generalisation, we identified the characteristic scales (time scale T_0 and velocity scale q_0) of groundwater flow within the watershed and introduced a suitable normalisation. According to [63] and [149], the dimensionless travel time $\hat{T}_i$ of each flowpath can be expressed as

$$\hat{T}_i = \frac{T_i}{\frac{2\pi}{\lambda_{max}} \cdot \frac{K}{n} \cdot \frac{\Delta}{D} \cdot \tanh\left(\frac{2\pi D}{\lambda_{max}}\right)} = \frac{T_i}{T_0} \tag{2.9}$$

where λ_{max} and Δ are the maximum wavelength and the maximum difference in elevation of the water table, respectively, and T_i is the dimensional travel time relative to a trajectory starting from a generic cell. Similarly, the dimensionless Darcy velocity $\hat{q}$ can be evaluated as

$$\hat{q} = \frac{q}{\frac{\lambda_{max}}{2\pi} \cdot \frac{1}{K\Delta} \cdot \tanh^{-1}\left(\frac{2\pi D}{\lambda_{max}}\right)} = \frac{q}{q_0}. \tag{2.10}$$

Finally, the normalized groundwater discharge $\hat{Q}$ is obtained as

$$\hat{Q} = \frac{Q}{q_0 \cdot A_0}, \tag{2.11}$$

where Q is the dimensional groundwater discharge and $A_0 = B \cdot l_{pixel}$.

2.3 Results and Discussion

2.3.1 Flow field and exchange fluxes

Once the water table is modeled, the hydraulic head in each point of the domain is known. Therefore, flow velocity and direction at any depth and the overlying recharge can be completely determined by the equation $\mathbf{q} = -K\nabla h$. According to the direction of water flow, it is possible to distinguish between inflow conditions (negative vertical velocity, $q_z < 0$), where surface water contributes to subsurface flow, and effluent conditions (positive vertical velocity, $q_z > 0$), where groundwater drains into the river. Figure 2.5 shows the spatial distribution of recharge and discharge zones in conjunction with the values of vertical velocity in each point of the domain. For the steady state condition (i.e., average annual condition), it can be observed that the configuration of the discharge area agrees quite well with the structure of the river network. The spatial succession of recharge and discharge areas across a valley is due

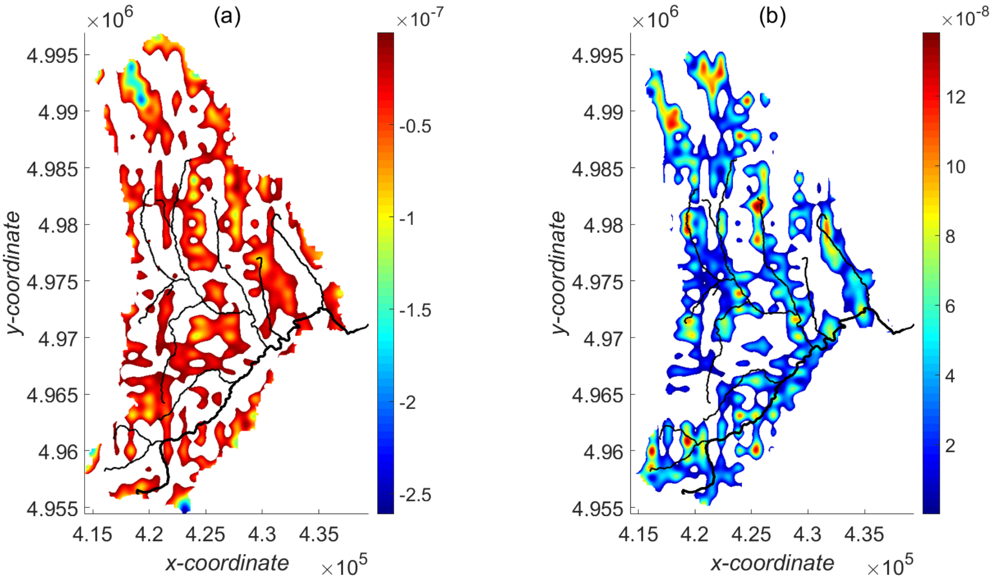

Fig. 2.5 Spatial distribution of recharge areas (a) and discharge areas (b) in the Borbore basin. The color scale indicates the values of vertical velocity [m/s] of groundwater. The river network is represented: the thicker line indicates the Borbore river, the thinner lines indicate its tributaries.

to the presence of flow systems at different scales and entails that water at close locations may have different origins and, consequently, different chemical properties [196].

The value of the vertical component of the groundwater velocity beneath the river bed indicates whether the river is gaining or losing. The overall behavior of the river and the confining effect of groundwater discharge on hyporheic exchange is here shown for the case of a groundwater discharge area of width equal to the river cell size (i.e., B = 50 m). This velocity value is represented in Figure 2.6a for the main river as a function of the dimensional downstream distance along the channel, l. Positive values represent water gaining river conditions and negative values represent losing river conditions. It should be noticed that water gains and losses are here estimated at the scale of hundreds of meters since the aim is assessing how the hyporheic fluxes are impacted by groundwater upwelling at basin scale. Therefore, Figure 2.6 does not consider the water exchange induced by river topography at a smaller scale, i.e., morphological units (such as bars, meanders, step-pools sequences, etc.), which also can affect the patterns of exchange flow and, consequently, the

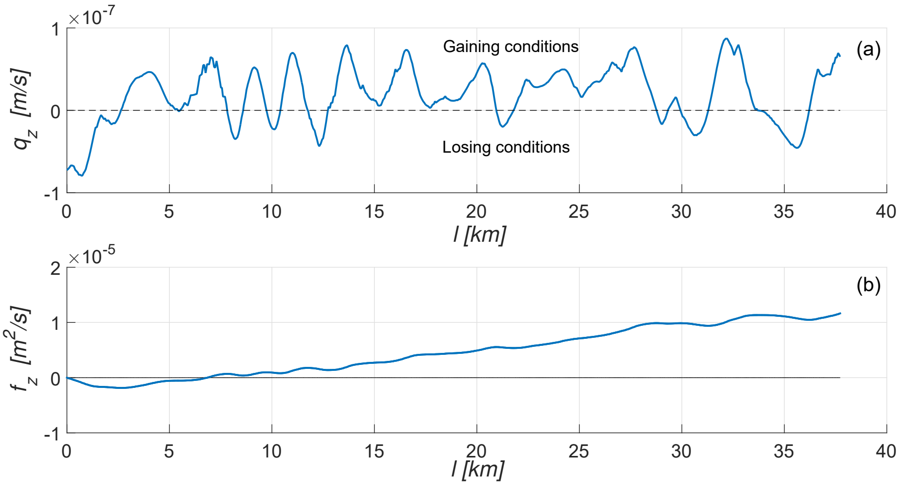

Fig. 2.6 Vertical velocity of groundwater discharge q_z [m/s] (a) and cumulative flux for unit width f_z [m^2/s] (b) as a function of the dimensional downstream distance l along the main river for $B = 50$ m. Positive and negative values of vertical velocity indicate river gaining and losing conditions, respectively.

transport of nutrients and contaminants. As it is possible to observe in Figure 2.6b, which depicts the cumulative flux per unit channel width f_z defined in section 2.2.4, along the river $f_z = \int_0^x q_z dl$ the net GW-SW exchange flux is positive, i.e., most of the river is gaining. However, there are also some reaches where the river recharges the aquifer (i.e., losing flow conditions).

The confinement effect of groundwater discharge on hyporheic exchange is exemplified for two representative river reaches (in upstream and downstream areas of the basin) under gaining conditions. For these reaches, the vertical extent of the hyporheic zone (see Figure 2.7) and the rate of the hyporheic flux (see Figure 2.8) were evaluated through the relationships (2.5) and (2.8), respectively. The stream characteristics of the reaches were evaluated on the basis of data provided by ARPA, resulting in medium characteristic values given by $(\bar{d}, \bar{U})$=(0.45 m, 1.10 m/s) for the upstream reach and $(\bar{d}, \bar{U})$=(0.95 m, 0.95 m/s) for the downstream reach. The bedform geometry was calculated using Eq. (2.7) obtaining $(\bar{h}_{dune}, \bar{l}_{dune})$=(0.1 m, 2.80 m) for the upstream reach and $(\bar{h}_{dune}, \bar{l}_{dune})$=(0.15 m, 5.95 m) for the downstream reach. The calibrated hydraulic conductivity value was used, and the median grain size $D_{50} = 10^{-4}$ m, which corresponds to a fine sand, was assumed. The hyporheic zone depth ranges from 0.20 m to 1.30 m in the upstream reach and from 0 m to 1.5 m in the downstream reach. Similarly, the hyporheic fluxes range from $7 \cdot 10^{-9}$

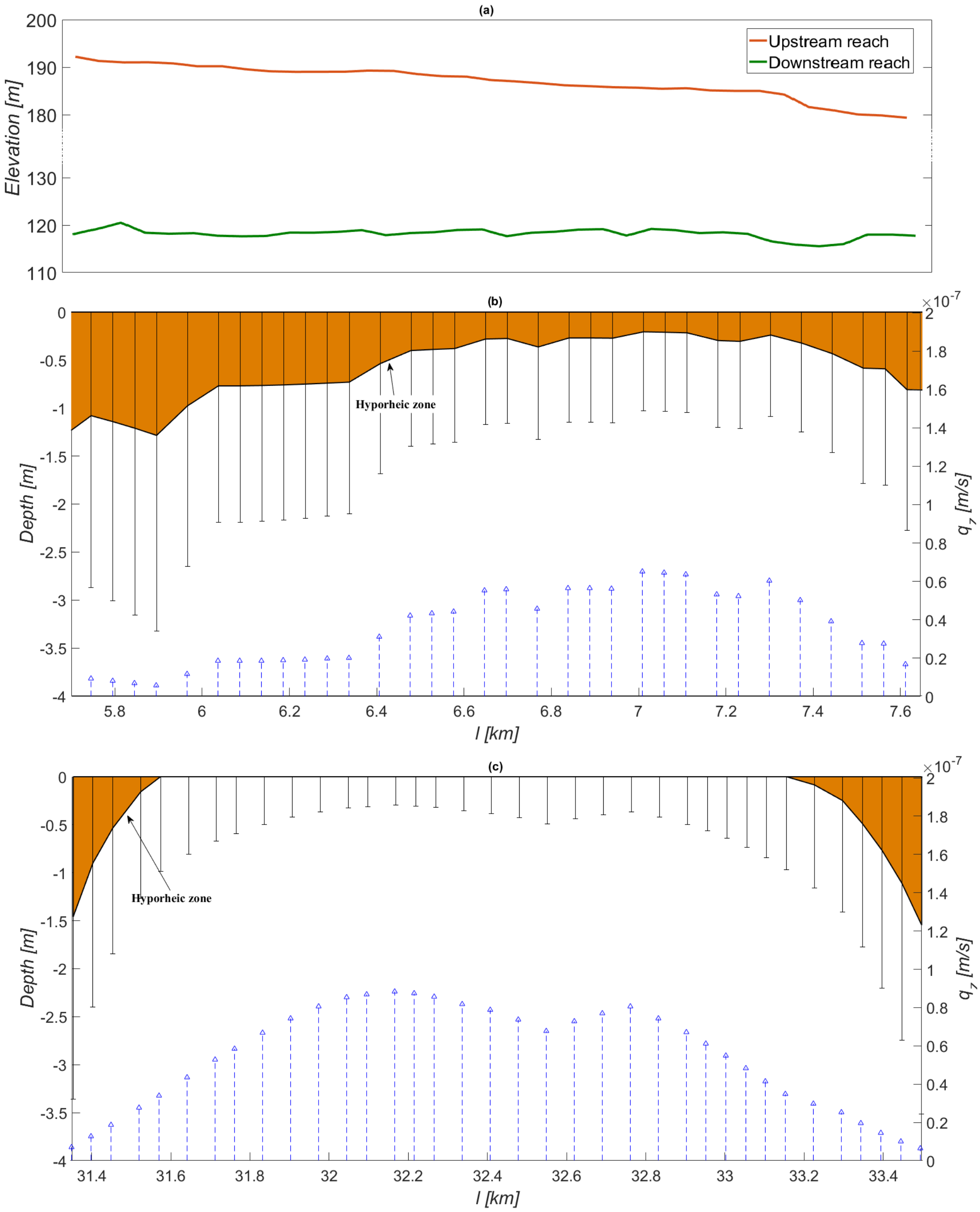

Fig. 2.7 Longitudinal variations of bed topography (a) and hyporheic zone depth (left vertical axis) for an upstream (b) and a downstream (c) gaining reach for average hydraulic and morphodynamic parameters. Error bars represent maximum variations induced by the considered ranges of U, d, h_{dune}, and l_{dune}. The arrows indicate the intensity of groundwater upwelling for $B = 50$ m (right vertical axis).

m/s to $3 \cdot 10^{-8}$ m/s in the upstream reach and from $7.4 \cdot 10^{-9}$ m/s to 0 in the downstream reach. Overall, it can be observed that high upwelling velocities counteract the penetration of the river water in the streambed sediments, reducing the depth (Figure 2.7) and the intensity (Figure 2.8) of hyporheic exchange and sometimes preventing the development of bedform-induced flow. In fact, the flow from the stream to the hyporheic zone is totally suppressed when groundwater upwelling flux is equal or higher than the hyporheic exchange flux and this happens in a large part of the downstream reach. Therefore, we can state that the vertical extent and the intensity of hyporheic exchange are highly variable since they reflect the variability of the groundwater upwelling. The amount and depth of solute exchange with the river will consequently be influenced by the variation in groundwater input.

In order to make the results more general and representative, we assessed how hyporheic exchange is expected to be influenced by the variability of the hydraulic and morphological features of the stream. Specifically, a variation of ±10% was adopted for the flow parameters (i.e., $d = \bar{d} \pm 10\%$ and $U = \bar{U} \pm 10\%$). Moreover, the dune height defined by Eq. (2.7a) was varied considering $0.8 < \eta < 8$, as observed in [115]. A range of dune lengths was then calculated imposing a ratio $h_{dune}/l_{dune} = 5 - 10\%$ [216]. In this way, $h_{dune} \in [0.03$ m, 0.31 m$]$ and $l_{dune} \in [0.27$ m, 6.17 m$]$ were obtained in the downstream reach, while $h_{dune} \in [0.04$ m, 0.52 m$]$ and $l_{dune} \in [0.45$ m, 10.41 m$]$ in the downstream reach. The maximum variation of the hyporheic zone depth for the considered parameter ranges is shown by the bars in Figure 2.7. High and long dunes increase the hyporheic zone depth. The dune size exerts a stronger influence on hyporheic zone depth than the flow characteristics. Variations of the hydromorphological features also affect the rate of the hyporheic exchange, which is found to be highest for the smallest bedforms that correspond to the shallowest hyporheic zones.

The autocorrelogram of the vertical velocity shown in Figure2.9 provides information about the spatial variability of groundwater discharge. It is plotted as a function of a normalized downstream distance, $\hat{l} = l/\lambda_{min}$, in order to identify the spatial scale that characterizes the variability in exchange fluxes and to obtain a generalized result that is valid regardless of the watershed size. It can be observed that the spatial correlation decreases to small values ($|\rho| < 0.2$) at a dimensionless distance comparable to the unit value (always in

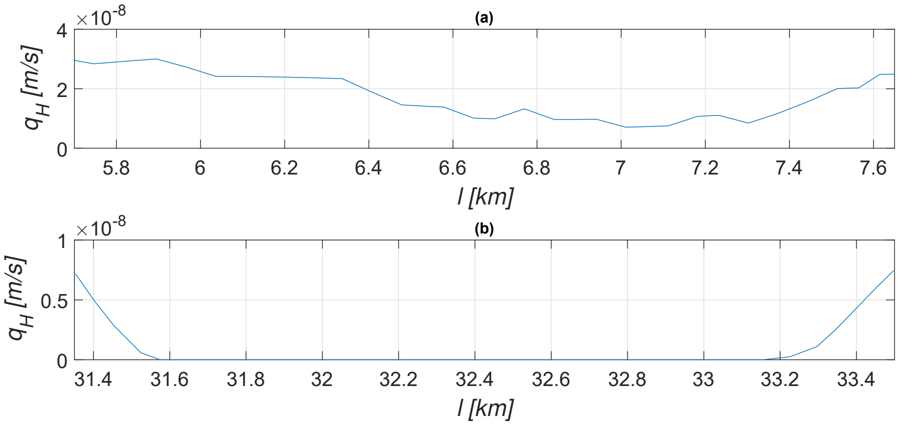

Fig. 2.8 Hyporheic flux per unit bed area in (a) an upstream and (b) a downstream reach in gaining conditions. Hyporheic exchange flux is evaluated by Eq. 2.8 considering the value of groundwater upwelling velocity obtained for $B = 50$ m.

the range 0.5-1.5), and it remains low except for some short reaches in which $|\rho|$ is slightly higher than 0.2. Therefore, the typical correlation scale, $\mathcal{A}$, is approximately equal to λ_{min}, i.e., $\mathcal{C} = \mathcal{O}(\lambda_{min})$. This means that the vertical velocities related to river reaches (i.e., pixels) more distant than λ_{min} are statistically uncorrelated. The only correlation could be obtained for $\hat{l} \leq 1$, i.e., for reaches closer than λ_{min}. However, λ_{min} represents the resolution with which the water table is modeled, hence it is not possible to consider results obtained for $l < \lambda_{min}$ ($\hat{l} < 1$) as reliable because the observed correlation is at least partially determined by the periodicity of the smallest harmonic function. This result indicates that the vertical exchange velocity is essentially uncorrelated along the Borbore river since for $l > \lambda_{min}$ a significant correlation does not exist and for $l < \lambda_{min}$ results are not truly reliable. Introducing more spatial scales and describing in greater detail the water table, the autocorrelation scale of the vertical velocity as a function of the dimensional downstream distance is reduced and more complexities arise in the phreatic surface representation. Hence, the smaller scales lead to less correlation over space and entail a more complex description of the groundwater flow field.

In Figure 2.5 (b) we showed that wide upward groundwater flow areas exist, which largely extend around the stream channel. However, considering that this result is at least in part a consequence of the hypothesis of topography-controlled water table, as explained in section 2.2.3, it is reasonable that the

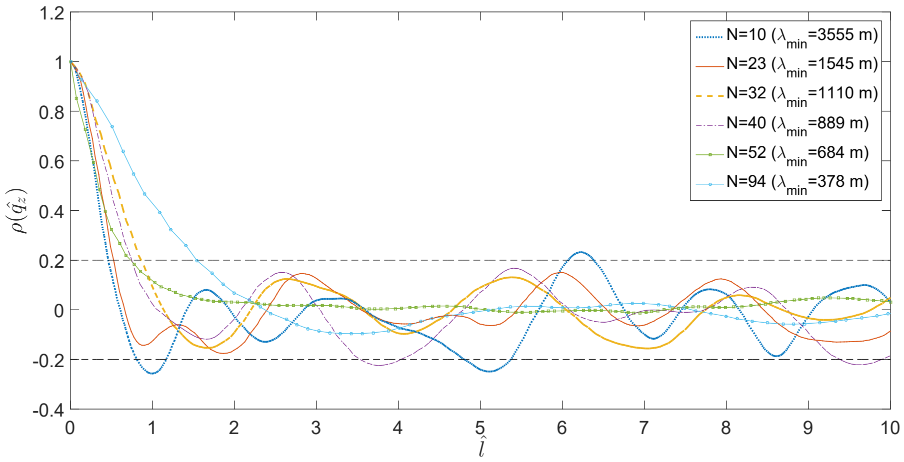

Fig. 2.9 Autocorrelogram of the vertical velocity ρ_{q_z} as a function of the dimensionless downstream distance $\hat{l} = l/\lambda_{min}$ for different values of the number of harmonics N used in the spectral solution (2.2).

actual groundwater discharge is limited to the streambed. Considering three different values of the discharge area width, $B=50$ m, $B=200$ m and $B=1000$ m, we evaluated how the spatial pattern of the groundwater discharge into the river varies with the size of this contributing area since the actual width of this strip is uncertain.

Figure 2.10a shows the groundwater discharge into the main river for the three different discharge areas of width equal to $B=50$ m, $B=200$ m and $B=1000$ m (i.e., the only river cells in the first case and a distance of 100 m and 500 m on each side of the river in the other two cases). The figure reveals the presence of a strong spatial variability of the groundwater discharge along the river. This variability is expected to influence the river-hyporheic zone exchange, enhancing the formation of different environmental conditions along the river ecosystem. The spatial distribution of groundwater discharge shows more peaks for the larger width of the contributing area and a smoother behavior for the narrower band. However, the high degree of irregularity observable in all cases indicates that the exchange between the river and the aquifer can be quite different even among adjacent reaches along the stream. Field and numerical studies frequently found similar high variability in the intensity and also in the direction of exchange fluxes [122, 28]. In our specific case, this strong spatial variability is attributable uniquely to the complex

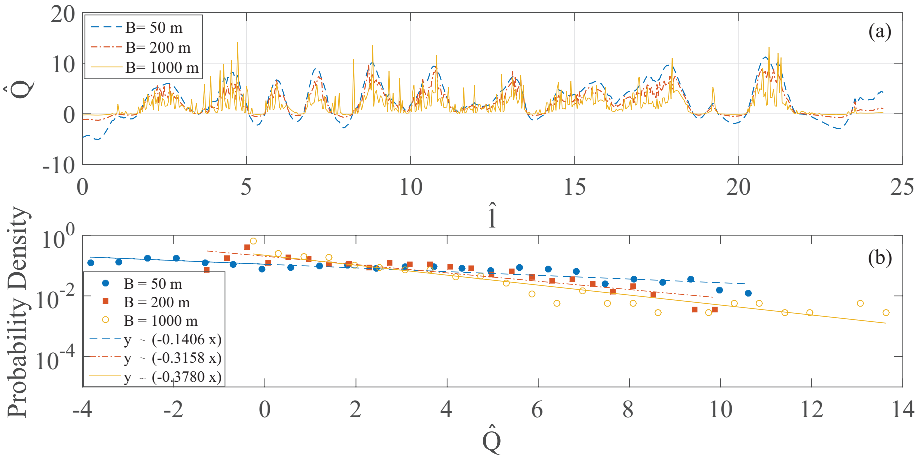

Fig. 2.10 Profile of the dimensionless groundwater discharge, $\hat{Q}$, to the main river (a) and probability density function of the groundwater discharge (b) for three different extension of the area feeding the river.

multiscale groundwater flow field induced by watershed topography since other factors (such as heterogeneity of the aquifer geology, river bed morphology, etc.) are not included here. Among the several potential causes of natural variability in a river-aquifer system, the geometrical structure of the water table is therefore able to induce heterogeneity in exchange fluxes along the river. From this result, it can be inferred that groundwater upwelling acts quite irregularly in confining the hyporheic fluxes, as is observable also in Figs. 2.7 and 2.8. This implies that there is no typical scale imposed by groundwater upwelling, i.e., a scale equal or greater than the minimum scale used to model the phreatic surface does not emerge. Consequently, this heterogeneity will reflect on the extension of the hyporheic zone and on all processes linked to the hyporheic fluxes (such as chemical reactions, biogeochemical and ecological processes, etc.), which in turn will not be characterized by a typical scale imposed by upwelling.

The probability density function of exchange discharge between the river and the aquifer is represented in Figure 2.10b for the three examined cases. It can be observed that the values are well modeled by an exponential tail (straight lines in Figure 2.10b, $R^2 = 0.70$ for $B = 50$ m, $R^2 = 0.79$ for $B = 200$ m and $R^2 = 0.87$ for $B = 1000$ m). Moreover, the three examined cases give very similar results: this means that the adopted normalization allows us to

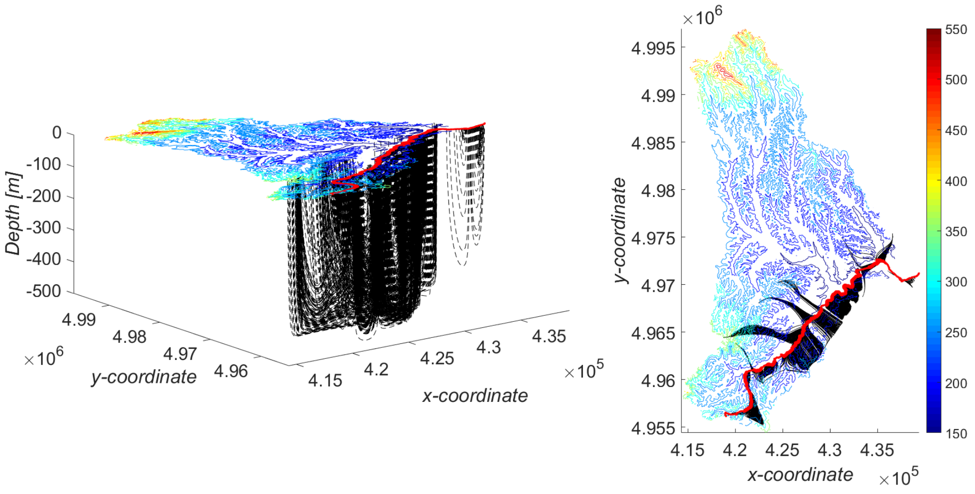

Fig. 2.11 Results from particle tracking simulation in 3D (a) and 2D (b) view. The black lines depict the groundwater pathways that discharge in the main the river. The color scale indicates the topography elevation (m asl).

eliminate substantially the dependence on the dimensional parameters and to obtain a general result.

2.3.2 Flow trajectories and residence times

The evaluation of groundwater pathways and travel time distribution is initially limited only to the main river in order to identify the areas of the basin directly feeding the main river by groundwater discharge. The streamlines were calculated for two different values of depth of the impermeable layer, $D = 500$ m and $D = 1000$ m, in order to investigate the influence of this parameter on the travel times. In addition, the three different contributing areas of width $B = 50$ m, $B = 200$ m and $B = 1000$ m were considered. Figure 2.11 shows the groundwater pathways feeding the main river obtained for $D = 500$ m and $B = 200$ m. It can be detected that only part of the whole basin feeds the base flow of the main river (Borbore river). In fact, the main stem of the river network is fed by groundwater deriving from a limited area of the catchment and the upper reaches of the watershed are only indirectly connected to the main stream. In the represented case, the length of the trajectories ranges from 5 m to 10 km, with a mean value of 2 km. The wide distribution of

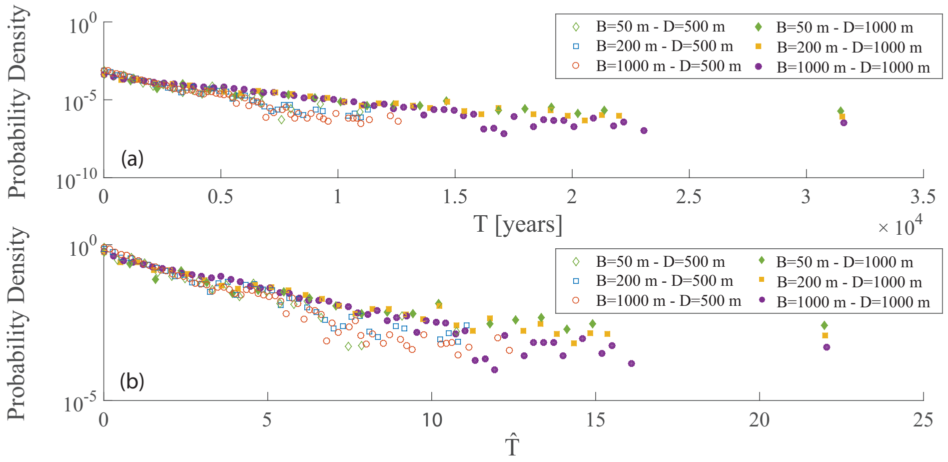

Fig. 2.12 Probability density functions of travel times, calculated using the particle tracking method. Distributions of travel times in dimensional (a) and dimensionless (b) form. The dimensionless time, $\hat{T}$, is defined in (2.9). Simulations are performed for two different depths of the impermeable layer, $D = 500$ m and $D = 1000$ m, and three different widths of the contributing area, $B = 50$ m, $B = 200$ m and $B = 1000$ m.

flow path lengths is the result of the superposition of flows induced by various topographic features, as observed in different studies [214, 184].

The travel time of each trajectory was calculated and the probability density function for each simulation is reported in Figure 2.12, in dimensional (Figure 2.12a) and dimensionless (Figure 2.12b) form. It can be observed that the travel time distribution follows an exponential decrease ($R^2 = 0.85 - 0.94$), similar to the structure of the discharge distribution. This result is consistent with other works on humid catchments with similar geological settings [83, 92], which show how the exponential behaviour of the travel times distribution is characteristic of groundwater flow at the catchment scale within homogeneous aquifers with uniform recharge. However, other studies [214, 33] found residence time distributions with power-law tails. This difference can be explained considering the aspect ratio of the domain. Specifically, when the aquifer is sufficiently deep ($\tanh(2\pi D/L) \simeq 1$), the influence of the impervious bottom on the flow field is limited, while when the domain is shallow enough so that $\tanh(2\pi D/L) \ll 1$, the influence of the bottom is relevant. In this work, the impermeable bottom layer is relatively shallow in comparison with the longitudinal extension of the study domain, i.e., $D/L \ll 0.02 - 0.03$ from which $\tanh(2\pi D/L) \simeq 0.1 - 0.2$. In particular, the presence of a shallow bottom

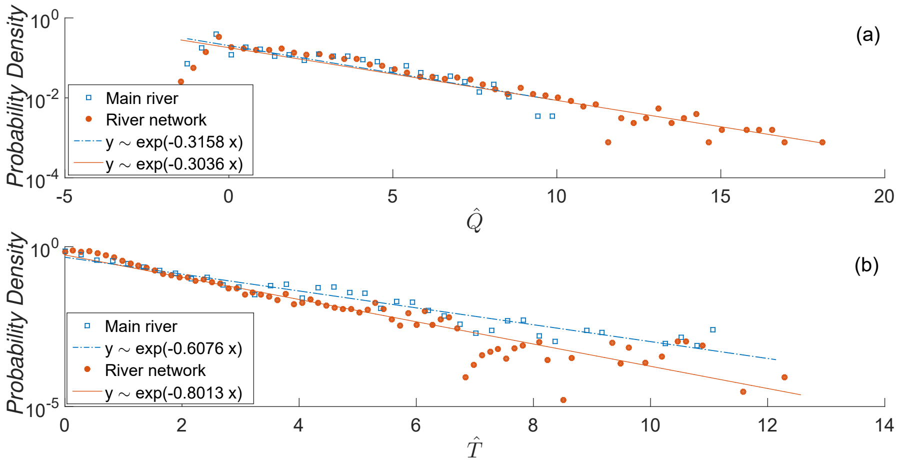

Fig. 2.13 Comparison between groundwater flow results for the main river and the whole river network. Probability density function of groundwater discharge (a) and of travel times (b) are reported in dimensionless form.

prevents the presence of the previously long and deep streamlines, which are confined to the shallow parts of the aquifer. This causes shorter trajectories and shorter residence times and leads to the observed exponential tailing, eliminating the very long trajectories that are responsible of a power-law tailing behavior. In addition, the exponential behavior of the travel time distribution can be explained considering the hypothesis of homogeneous aquifer since the aquifer heterogeneity is among the main factors that entail a power law distribution.

As for the discharge Q^*, the results suggest that the adopted normalized scale allows us to obtain a general behavior since dimensionless curves are similar regardless of the values D and B. The dimensional results show that a deeper aquifer results in longer travel times, while the width B has no relevant effect.

Finally, the analysis of groundwater discharge and water pathways was extended to the whole river network. The simulations were carried out for $B = 200$ m and $D = 500$ m. Figure 2.13a depicts a comparison of the probability density function of groundwater discharge between the cases in which only the main river and the whole river network are considered. A similar comparison was also implemented for the travel times and is shown in Figure 2.13b. It can be observed that the exponential model is preserved and the behaviour is very similar. Therefore, the results can suggest a fractal nature of GW-SW exchange, as discussed in [214]. The fractal behavior of exchange fluxes is a direct consequence of the fractal geometry of mountain and river topographies. This has been shown by several studies, which have demonstrated that residence times of water and solutes follow a fractal distribution both in river networks and in the hyporheic zone underlying stream channels [163, 119, 91]. Therefore, although the subsurface water flow paths differ markedly in length, depth, and duration of the subsurface flow, being the results of the interaction of a wide range of spatial and temporal scales, they exhibit a self-similar behavior [214]. This implies that the contribution of gaining and losing fluxes induced by river topography at smaller (unresolved) scale would likely not alter the scaling behavior of the system due to self-similarity property.

2.4 Concluding Remarks

Landscape topography is one of the major factors that control the interaction between GW-SW waters, since it is the dominant driver for groundwater movement at large scales. A study of the role of topographic complexity in controlling river-aquifer exchange has been presented in this chapter. We have focused on the effects induced by the ground surface structure, considering a simplified system composed by a homogeneous and isotropic aquifer.

The connectivity between the river and the aquifer has many important ecological and environmental effects on the fluvial ecosystem, because it affects the quality and quantity of surface and subsurface water. The GW-SW interface is a crucial point for biogeochemical pathways and nutrient cycling rates, since it controls the flux of groundwater solutes discharging into rivers, and *vice versa*. Studying GW-SW interactions at large scales is useful to identify the zones of a catchment that are most important in determining where groundwater is discharging into the river and where attenuation of groundwater pollutants at the GW-SW interface might reduce the concentration of pollutants in river water.

The analysis of a simplified real case study has demonstrated how the river-aquifer interaction is influenced by landscape topography, which induces spatial heterogeneity in groundwater discharge to the river. Groundwater discharge exhibits substantial spatial variations induced by the complex structure of the water table, even among adjacent reaches along the river. This result suggests that groundwater upwelling related to a river reach should be modeled as a spatially fluctuating variable when an analysis at smaller scales is implemented. We have observed that a more detailed description of the water table entails a reduction of the spatial correlation scale of exchange fluxes since the representation of the phreatic surface becomes more complex. Overall, a lack of autocorrelation of the vertical exchange velocity along the river is evidenced. An exponential behavior has been found both for groundwater discharge and travel time distribution.

The geomorphological complexity of landscape and river topography results in a corresponding fractal nature of the subsurface flow patterns at a wide range of spatial scales. The subsurface flow patterns, in fact, exhibit a self-similar behavior when different scales are considered. A self-similar distribution is also characteristic of the residence times over a wide range of temporal scales. This peculiar behavior has been shown and studied in several studies [213, 214] and it has been confirmed by the present analysis. The fractal nature of surface-subsurface fluxes of water and solutes is important in applications ranging from microbial ecology to nutrient dynamics to contaminant transport [214].

This study represents an important step in conceptualizing how the structure of a regional aquifer influences groundwater upwelling, which, in turn, defines and constrains hyporheic exchange by limiting the extent of the hyporheic zone. The strong impact of groundwater discharge at the reach scale on hyporheic fluxes at smaller scales influences the exchange of water and solutes between the river and the hyporheic zone. Therefore, the source of spatial complexity in hyporheic fluxes is not only the geomorphological complexity of the river but also the topographic structure of the whole basin. The landscape structure substantially affects the groundwater flow field, which plays a key role in defining the depth and the intensity of the hyporheic exchange since it confines and embeds the hyporheic zone. These results represent a complement existing frameworks which analyze the consequences of hyporheic exchange on water quality and stream ecology at large watershed scales.

The analyses developed in this work to fulfill the aims of the study are independent of the specific approach used to obtain the water table and could be implemented using more refined (but computationally demanding) numerical methods, obtaining similar qualitative results, since they are due to the intrinsic complexity of the groundwater table. Future efforts will be devoted to increasing the complexity of the system and to verifying the impact of factors such as geological variability on the results, as we will see in the following chapter. It is expected that the inclusion of other factors of natural complexity will further complicate the spatial patterns of exchange fluxes. In fact, other factors could contribute to the strong spatial heterogeneity in fluxes observed in various field studies. Therefore, the main finding regarding the almost random confinement of the hyporheic zone would be confirmed also in a more complex system.

Chapter 3

Controlling factors of watershed-scale spatial patterns of exchange flux

The work described in this chapter is currently under finishing and improvement with the aim of producing a research article in a peer-reviewed international journal.

3.1 Introduction

GW-SW interactions in streams are not easily measured in most locations, especially not with an extent and spatial resolution that allow for the characterization of groundwater discharge patterns at watershed scale. Therefore, there is still a lack of easy and accurate methods to measure groundwater fluxes at the river-aquifer interface [120, 20]. Despite the significant advancements in recent years, obtaining high resolution field measurements remains hence difficult and not easily accessible. Therefore, it is important to develop refined techniques for modeling groundwater-river interactions, because a deeper understanding of the main factors that control the spatial patterns of groundwater discharge at large-catchment scale could improve the prediction of exchange fluxes.

The focus of this chapter is to analyze and characterize the factors that dominate the patterns of groundwater upwelling and downwelling intensity. Specifically, the aim is to better identify the processes and the structures affecting groundwater patterns and understand the link with external controls to make more reliable predictions of exchange flux. In order to do this, a numerical model of GW-SW interactions is developed at a site that is well characterized relative to its hydrology and geology. The spatial patterns of groundwater discharge and recharge over the river network under different hydrogeological approximations are analyzed, predicting the intensity of groundwater fluxes along the river corridor and examining the factors that largely influence these patterns.

The results indicate that the heterogeneity of the aquifer and the spatial distribution of lithological units play the most important role in determining the spatial variability of groundwater inflow fluxes in a river network. Conversely, it seems that a detailed description of the spatial variability of recharge pattern and of other hydrological factors (e.g., parameters describing the stream channels) is less relevant to reproduce a plausible characterization of GW-SW interactions along the river corridor. The level of detail used to describe the topographic structure of the watershed also display a certain impact on determining the pattern of GW-SW flow interactions, highlighting the influence of land surface topography on the spatial patterns of groundwater inflow fluxes, as already evidenced in the previous study [40].

3.2 Model

3.2.1 Case study and data collection

Here the focus is on the Jackson Creek watershed, a rapidly urbanizing watershed located in the outer northern suburbs of Melbourne, in the Australian state of Victoria (Figure 3.1a). The headwaters of Jackson Creek and its tributary streams begin in the Macedon Ranges with the creeks cutting deep narrow channels through the basalt plains (Figure 3.1b) [197]. Jackson Creek is a predominantly agricultural catchment with growing urban centers and it plays a significant role in water supply for domestic, agricultural and industrial use for the surrounding area [197]. The catchment has a highly modified hydrology due to water harvesting at Rosslynne Reservoir, from which a water flow in Jackson Creek is provided in support of environmental goals and downstream water supply. The riparian zone is highly degraded in most reaches, with widespread willow infestation and only limited native vegetation [208]. The elevation ranges between 17 m a.s.l. and 1018 m a.s.l (Figure 3.1b). The region has a temperate climate, with distinctly dry and warm summers [24]. The mean annual air temperature is about 20 °C and the mean annual rainfall is 586 mm. Rainfall was significantly lower during the Millennium Drought (1997 to 2009).

Groundwater is present in two main aquifer systems, the Quaternary Alluvium (QA - sediment deposits of sand, silt, and gravel) aquifer system and the Newer Volcanics (NV - basalt) aquifer system [51]. Underlying these aquifer systems is the less permeable regional Paleozoic Bedrock aquifer (PB - sandstone, black shale, black and grey silt-stones). The QA aquifer system is a shallow and unconfined aquifer that is highly connected to the surface water network [51]. The NV aquifer system is an unconfined to semi-confined rocky aquifer of variable thickness in which groundwater flows move through the fractured rocks at spatially variable flow rates in both regional and intermediate flow systems and discharges into waterways where the water table intersects the creek [51]. The regional PB aquifer (basement) conveys significantly less water than NV and QA and it is not considered significant in terms of regional groundwater because of its low permeability [51]. The NV and the underlying PB dominate the geology beneath Jackson Creek (Figure 3.1c, [60]). Recharge to the aquifer is predominantly from direct infiltration of rainfall, where the aquifer outcrops, or via discharge from streams, where pressure levels are below the stream stage height (i.e., losing conditions) [207].

Groundwater is critical to this site in providing baseflow in low flow periods and sustaining permanent refuge pools during drought for both the alluvium zone and basalt zone. Field groundwater data are lacking in the area but the topographic and geological configuration of the aquifer suggests that groundwater discharge varies along the river corridor [60]. Where the section of the creek is more incised and surrounding landscape steeper it is likely that the creek is alternating between gaining and losing. Moreover, a few bores were recently installed along Jackson Creek in order to assess gaining and losing reaches (personal communication provided by Sarah Gaskill, Melbourne Water, 2017).

In this study, we considered the Upper Jackson Creek catchment, from the Rosslynne Reservoir to the confluence with Riddells Creek (Figure 3.1, area highlighted in red). This study area was chosen because the area upstream of the reservoir is geologically dominated by the bedrock formation, which has a low importance for the groundwater system since infiltration is very low. Another reason to study this portion of the catchment is that the area is slated for rapid development, so understanding the role of GW-SW interactions could be important for anticipating future urban impacts on critical habitat (including species such as the platypus) in the creek and downstream nutrient inputs to the ecologically sensitive Port Phillip Bay. The total area of the study catchment is 65 km^2 and the study reach predominantly consists of basalt crops. An observation borehole is present within the study area (Gisborne, downstream of Rosslynne Reservoir; WGS 1984/UTM Zone 55S - 5848688 N, 286587 E).

To determine the topographic characteristics of the study area we used the 30 m ASTER GDEM (Advanced Spaceborne Thermal Emission and Reflection Radiometer Global Digital Elevation Model, retrievable through NASA JPL database) implemented in ArcGIS (v. 10.3, ESRI, Redland, California). The topographic elevation within the catchment is represented in Figure 3.2a, together with the channel network extracted from the DEM through a channel-threshold area method [138] and used for building the river boundaries in the model. The elevation of the landscape ranges from 285 m a.s.l to 641 m a.s.l.

As geological layers describing the different hydrostratigraphic units, we used the ArcGIS raster (with spatial resolution equal to 100 m) provided by SAFE project [56]. Hydrogeological map series and aquifer information were collected in order to provide a 3D aquifer stratigraphic map - extending from the top of the youngest Quaternary aquifers to the top of the relevant hydrogeological basement unit (the oldest formations, [57]). A state-wide interpreted stratigraphic borehole database containing approximately 20.000 interpreted bore samples was provided for the project. The stratification of the different geological units and the disposition of the different materials within the aquifer is shown more clearly through the three geological cross

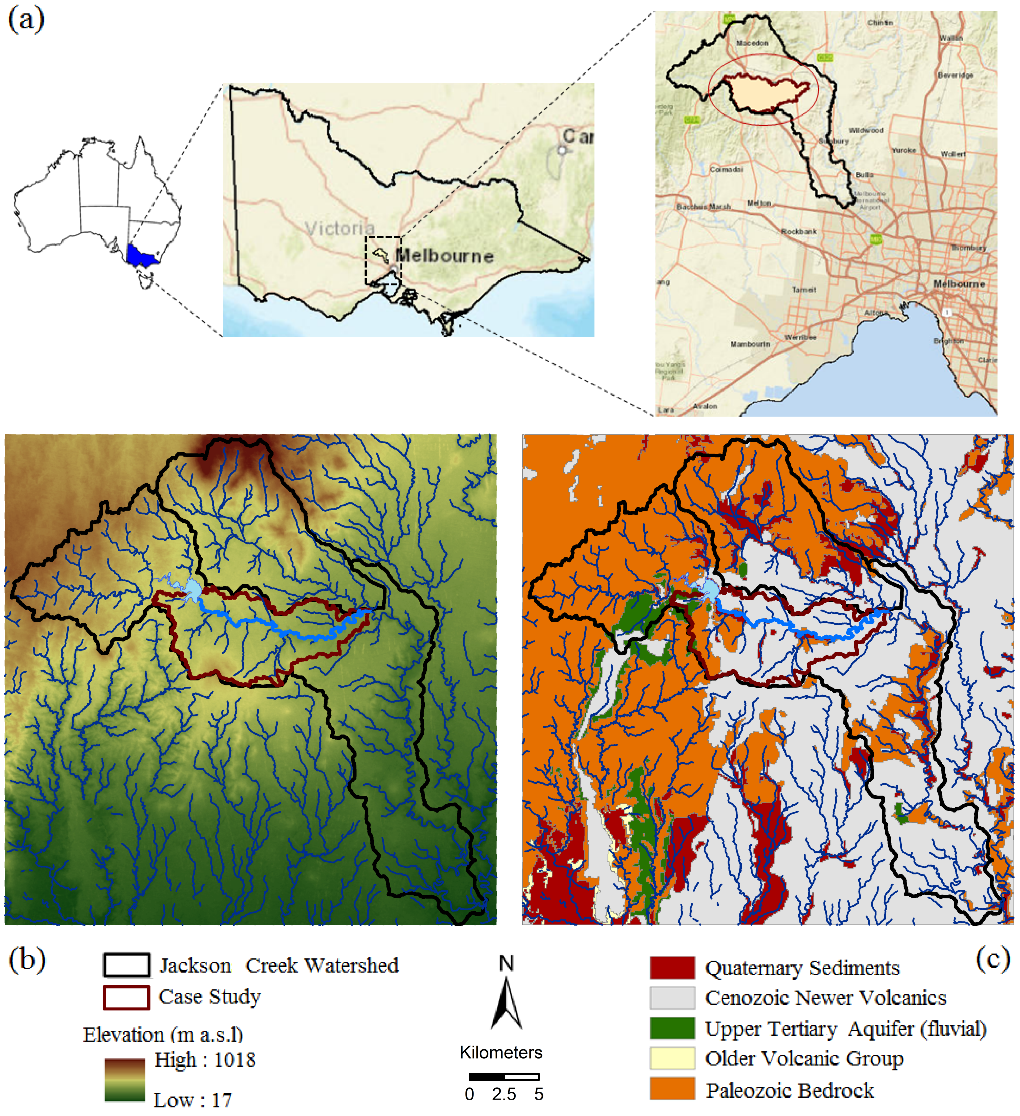

Fig. 3.1 (a) Location, (b) elevation and (c) outcrop geology of the Jackson Creek watershed. The thick black line indicates the whole Jackson Creek catchment while the thick bordeaux line indicates the study area. The river network is represented in blue. The thicker blue line indicates the main river.

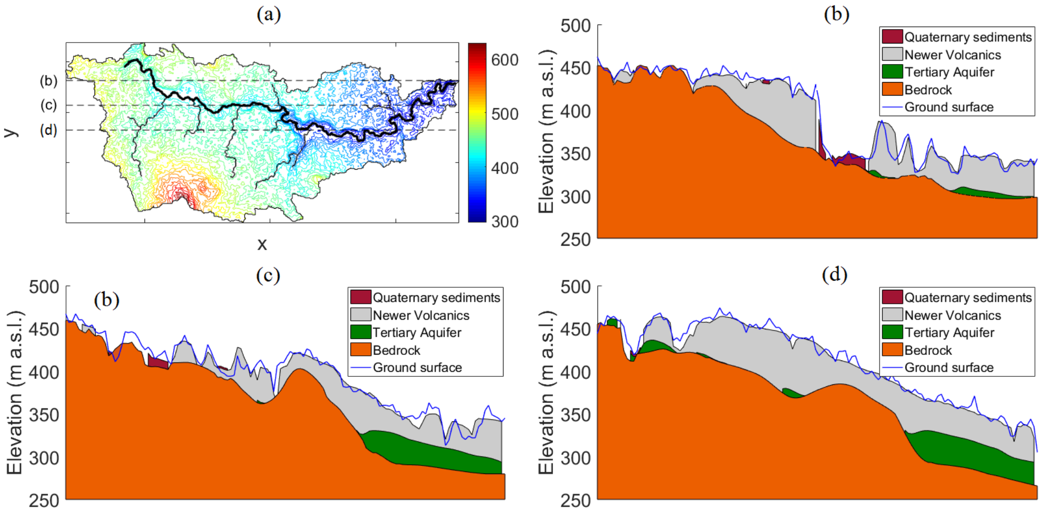

Fig. 3.2 (a) Digital Elevation Model (DEM) of study area (with a resolution of ≃ 30 m). The coordinate system is WGS84/UTM Zone 55S. Warmer colors indicate higher elevations. The river network is represented; the thicker line indicates the main creek. (b) - (d) Geological cross sections indicated in panel (a) and showing the stratification of the different geological units.

sections represented in figures 3.2b-3.2d (position of these sections is indicated in Figure 3.2a). The dominant surface geology in the catchment is NV, as visible from the cross sections and in the outcrop geology represented in Figure 3.1c. Bedrock outcrops mainly occur in the western part of the basin and in other isolated areas, while the QA are common close to the streams and dominate the floodplains along the river network within the catchment.

Rainfall data for Australian territories are available from the Australian Government Bureau of Meteorology (BOM), and they are useful in identifying longer-term variations in Australia's rainfall patterns. Figure 3.3 shows the average annual rainfall (with spatial resolution of about 5 kilometers) over the period from 1946 to 2005 in the Jackson Creek catchment. To model the groundwater recharge starting from rainfall data, we used the spatially variable values of infiltration calculated using the Department of Sustainability and Environment Victoria EnSym (Environmental Systems Modelling Platform) developed to improve understanding about the impacts that actions such as revegetation and riparian management have on the landscape [80, 90]. EnSym takes as input daily weather (rainfall and pan evaporation) and irrigation recharge (derived from a series of plant growth models) to produce a near

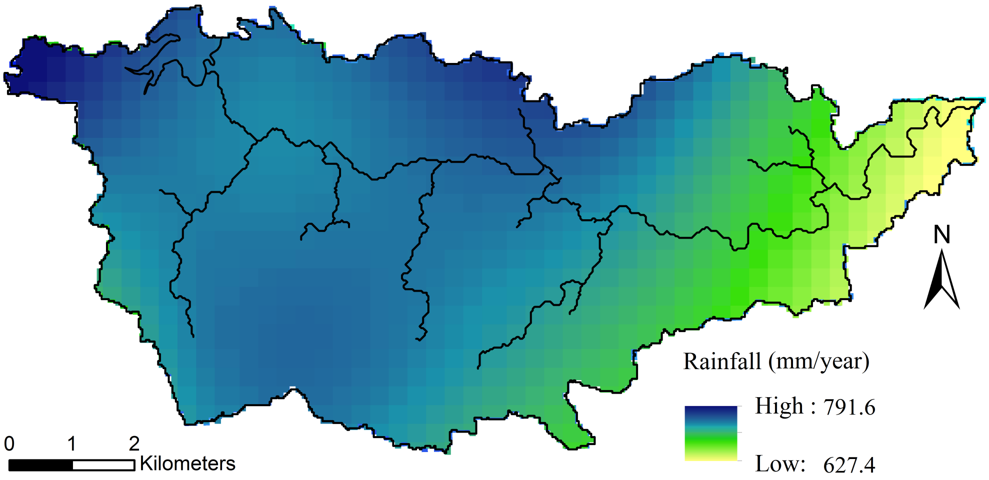

Fig. 3.3 Average annual rainfall over the period from 1946 to 2005 in the study area. Blue colors indicate areas where the precipitation is high; yellow colors indicate areas where the precipitation is low.

surface water balance for a number of different land use types [54]. It excludes river/stream/channel/reservoir leakage. Documented withdrawals and licensed domestic extractions (e.g., for irrigation purposes) in the study area are orders of magnitude lower than inflow to the stream network and, therefore, negligible [197]. Daily spatial recharge was determined subtracting the calculated surface runoff from the total daily precipitation and irrigation. Water infiltrating into the soil can then be removed by evapotranspiration, lateral flow and downward flow if the water input rate exceeds the field capacity and the layer below is not saturated [80]. The applied recharge is therefore based on soil moisture balance and actual evapotranspiration calculations. Specifically, we used the long term average recharge calculated for the period from January 1957 to December 2005 for the state of Victoria.

3.2.2 Model implementation

We simulated groundwater flow within the study catchment under different hydrogeological conditions. Two GIS based computer softwares, ESRI ArcMap 10.3 and MODFLOW Flex 2015.1, were employed. ArcMap provided the spatial editing tools needed to generate the spatial boundaries of the model, the stream network and the aquifer characteristics in the area of interest.

MODFLOW Flex utilized this spatial information to model the hydrogeological conditions and to simulate groundwater flow in the study area, through the discretization of the domain by a finite difference grid and the resolution of the groundwater governing equations with numerical methods under appropriate boundary conditions. A deformed grid was adopted, with the top and bottom of the model layers following the elevation of the horizons used to describe and construct the geology of the study area. The model domain was split into 253 rows and 554 columns, with each cell having the same resolution of the DEM (1 arc-second that in metric coordinates is approximately equal to 30 m). The simulations were performed in steady-state conditions, assuming that the phreatic surface refers to an average annual configuration and thus not considering temporal changes in the groundwater flow field.

The groundwater flow was modeled through the use of the 3-D groundwater flow equation in a heterogeneous and anisotropic medium under steady-state conditions that assumes the following expression:

$$\frac{\partial}{\partial x}\left(K_x\frac{\partial h}{\partial x}\right)+\frac{\partial}{\partial y}\left(K_y\frac{\partial h}{\partial y}\right)+\frac{\partial}{\partial z}\left(K_z\frac{\partial h}{\partial z}\right)+W=0 \tag{3.1}$$

where K_x,K_y, and K_z are values of hydraulic conductivity along the x, y, and z coordinate axes (where x and y define the horizontal plane in an orthogonal reference system, while z is the vertical direction, positive upward), h is the hydraulic head, W is the volumetric flux per unit volume representing sources and/or sinks ($W < 0$ for flow out of the groundwater system, and $W > 0$ for flow into the system), and t is the time. The governing equation (3.1) was numerically solved for the hydraulic head, under appropriate boundary conditions.

Aquifer characteristics were assigned to the different geological layers and the values of hydraulic conductivity in the three direction (K_x, K_y, K_z), effective and total porosity (n_e and n respectively) of various soil, and rock types are indicated in Table 3.1. Hydraulic conductivity values were assigned based on pre-existing published studies involving pump tests where available or on the lithology where field records are not available [55]. The modeled outcrop geological zonation is represented in Figure 3.4a. The numerical model included a four layer representation (one layer for each geological unit) of the three dimensional regional geology. The elevation of the top of each layer was defined using the geological rasters previously described. The Paleozoic Bedrock was simulated using a flat bottom at 200 m a.s.l., deep enough that the groundwater flow field is not influenced. The vertical stratification of the different hydrostratigraphic layers is visible in Figure 3.4b that shows the 3D domain modeled in MODFLOW.

Table 3.1 Input values to the model regarding soil and lithology: hydraulic conductivity in the three directions, K_x, K_y, K_z, effective porosity, n_e, and total porosity, n.

Geological Unit	$K_x = K_y$ (m/s)	K_z (m/s)	n_e (-)	n (-)
Quaternary Sediments	1.16×10^{-4}	1.16×10^{-6}	0.14	0.30
Newer Volcanics	2.90×10^{-5}	2.90×10^{-6}	0.14	0.30
Tertiary Aquifer	5.80×10^{-6}	5.80×10^{-7}	0.14	0.30
Bedrock	1.16×10^{-7}	1.16×10^{-8}	0.14	0.30

Boundary conditions were specified to all external boundaries of the model. A ”river” boundary condition (head-dependent flux) was prescribed along the stream network previously extracted through a specific tool in ArcMap and for the part of the reservoir within the domain of the model. A ”recharge” boundary condition was assigned to the uppermost active layer in each model cell. Finally, a ”no-flow’ boundary condition was prescribed to all lateral limits and to the bottom of the model.

The MODFLOW River Package input file required the following information for each grid cell containing a river boundary: river stage (i.e., the free water surface elevation of the surface water body), riverbed bottom elevation (i.e., the elevation of the bottom of the seepage layer - bedding material - of the surface water body), and the conductance (i.e., a numerical parameter representing the resistance to flow between the surface water body and the groundwater caused by the riverbed) [95]. The total exchange flow Q (L^3/T) between the river and the groundwater system was calculated as

$$\begin{cases} Q = C(h_{riv} - h_{aq}) & h_{aq} \geq Z_{bot} \\ Q = C(h_{riv} - Z_{bot}) & h_{aq} < Z_{bot} \end{cases} \tag{3.2}$$

where C is the hydraulic conductance of the river-aquifer interconnection, h_{riv} is the water level (stage) in the river, h_{aq} is the head in the aquifer in the cell underlying the river reach, and Z_{bot} is the elevation of the riverbed bottom. The conductance is defined as $C = K_v B_{riv} L_{riv}/m$, where K_v is the vertical hydraulic conductivity of the riverbed material, B_{riv} is the width of the river in the cell, L_{riv} is the length of a reach through a cell, and m is the thickness of the riverbed [95]. The river-aquifer interconnection was hence represented assuming that head losses between the river and the aquifer occur across the riverbed layer (i.e., no substantial head loss occurs between the bottom of the riverbed layer and the grid model cell representing the underlying aquifer). Further, MODFLOW assumes that the water level does not drop below the bottom of the riverbed layer and the underlying model cell remains fully saturated [95]. Stream bottom elevations in each river cell were set at the same elevation as the modeled ground surface, which is based on DEM data, while stream stages were derived assuming a river depth of 0.5 m for the main river and of 0.1 m for the tributaries. River length of each reach was automatically evaluated by MODFLOW on the basis of the length of the polyline defining the stream reach in each cell. The other numerical values of the input parameters for river boundary condition are indicated in Table 3.2. The river bed hydraulic conductivity was set equal to the value of vertical hydraulic conductivity of the Quaternary sediments, which is a dominant geological unit along the river channels, as observable in Figure 3.4b.

Table 3.2 Input parameters for river condition: riverbed thickness, m, river width, B, water depth, d, and riverbed conductivity, K_v.

	m (m)	B_{riv} (m)	d (m)	K_v (m/s)
Main river	0.5	5	0.5	1.16×10^{-6}
Tributaries	0.5	1	0.1	1.16×10^{-6}

The diffuse recharge estimates were evaluated with a spatial resolution of 100 m and are represented in Figure 3.4c. The spatial recharge distribution shows a variation pattern with an average rate equal to 94.1 mm/year and a standard deviation of 15.8 mm/year. The areas where the bedrock outcrops coincide with the areas with low infiltration rate, as physically expected. In fact, in bedrock outcrop areas, the low permeability of the basement bedrock, the relatively steep topography and the dense vegetation cover result in relatively low recharge and deep water table with steep gradients, even if the rainfall is high [90], as it is visible comparing figures 3.3 and 3.4c.

3.2.3 Estimation of river GW discharge and identification of GW basins

The head values obtained from MODFLOW as main output were then used for the evaluation of the 3D groundwater flow field applying the Darcy law expressed as $\mathbf{q} = -\mathbf{K}\nabla h$, where $\mathbf{q}$ is the Darcy flux vector, and $\mathbf{K}$ is the hydraulic conductivity tensor. The total exchange flow from Equation 3.2 was divided by the river surface area to calculate the vertical exchange flux (q_z) between the river and groundwater. The values of this flux allow us to distinguish between inflow and outflow conditions along the river network. According to the adopted reference system, the vertical flow velocity is positive if the exchange flux occurs from the aquifer to the river (e.g., gaining conditions) and is negative if the exchange flux occurs from the river to the aquifer (e.g., losing conditions). Stream reaches throughout the study area were then mapped as gaining or losing.

The three-dimensional groundwater flow field was then used to implement a particle tracking procedure with the aim of identifying the groundwater sub-basins, i.e., the subdivision of the aquifer into discrete units that feed different points of the river network. A grid of 13054 points was created starting from the DEM points and increasing the raster resolution of a factor equal to 2.5. These points were used as starting points from which groundwater flow pathlines were tracked to their discharge location using the MODPATH code [151]. MODPATH is a MODFLOW post-processing program that generates groundwater flow pathways (i.e., particle paths and travel times) based on MODFLOW output files and specified aquifer porosity (see Table 3.1). The stream network was divided in sub-reaches where each tributary represents a separate reach, while the main river was discretized in correspondence of the confluence points with the tributaries (for a total number of 14 river reaches which correspond to the same number of sub-basins). Using the output

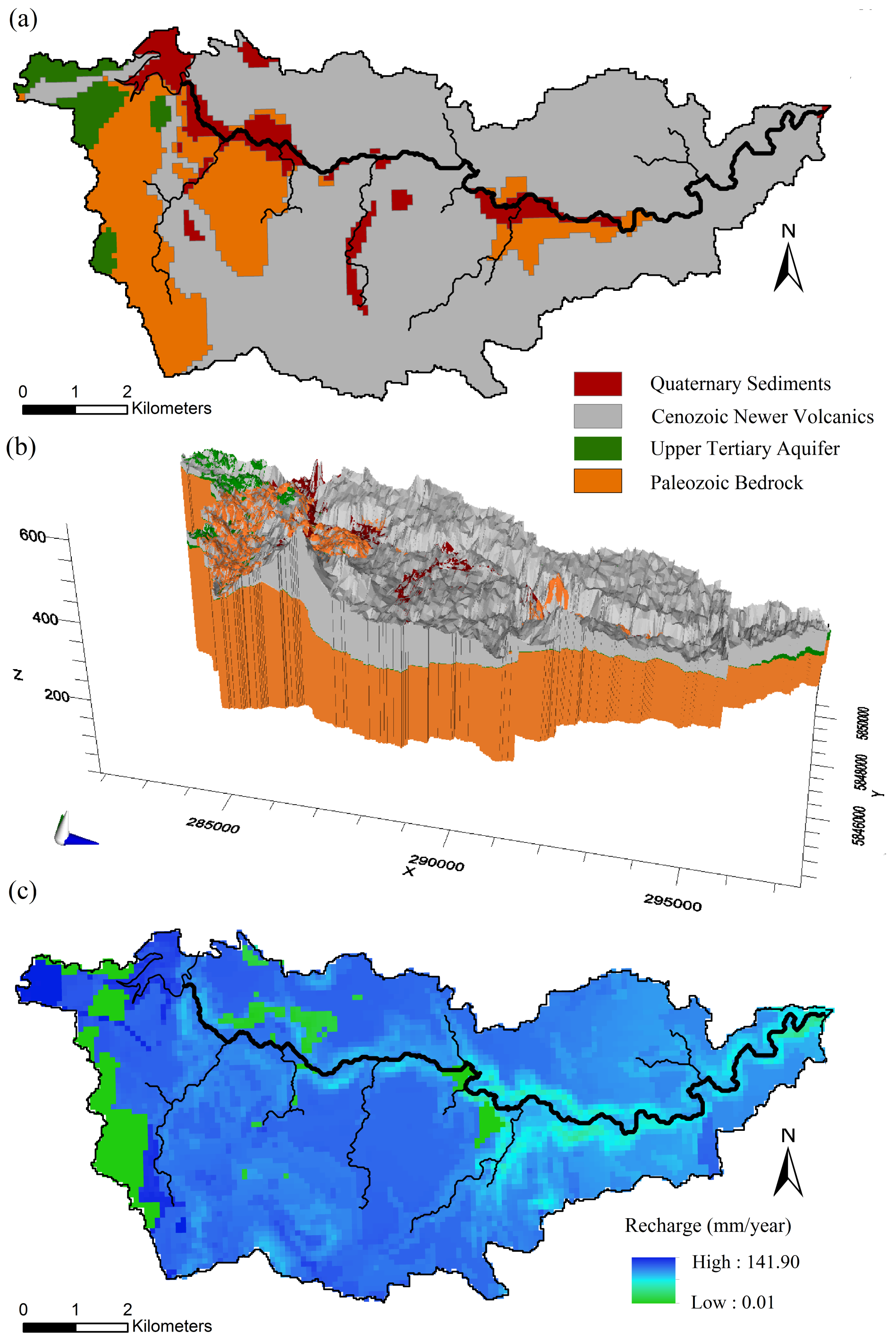

Fig. 3.4 Model development: (a) modeled outcrop geology, (b) 3D domain created in Visual MODFLOW Flex that shows the geological stratification in the study area and (c) spatially variable recharge applied as boundary condition in the uppermost active layer of the model. The thicker black line in panels (a) and (c) indicates the main river.

obtained from ModPath, the aquifer was then subdivided into hydrogeological sub-basins based on groundwater flow patterns. The groundwater sub-basins were characterized by identifying the areas of the catchment that directly feed the same river reach. The subdivision of the basin into groundwater sub-basins allowed us to better analyze the compartmentalization of groundwater system and the distribution of groundwater fluxes. Understanding the hydrogeological compartmentalization of an aquifer is of critical importance since it basically controls how different parts of the aquifer are hydraulically connected, and in what direction, groundwater fluxes distribute and move within a basin, determining specific preferential pathways [137, 83].

3.2.4 Sensitivity analysis of drivers of river groundwater discharge patterns

The previously described model represents the most general and complete case we simulated. Starting from this case, we also simulated different systems in order to identify the main controls of exchange flux patterns. As potential drivers of river-groundwater exchange we considered: a) the spatial variability of the groundwater recharge; b) the structure of the river network (specifically, the variation of the river width and the river stage); c) the topographic landscape structure (in particular, the influence of the spatial scales that characterize the ground surface); d) the geologic heterogeneity of the aquifer (specifically, the stratification of the different geological units and the spatial variability in hydraulic conductivity). The main influential factors were studied considering the complete model and systematically turning off one or more of the attributes described above in order to analyze a simpler system and evaluate the effect of those attributes on the spatial distribution of losing and gaining fluxes over the catchment. Therefore, the present sensitivity analysis concerns some specific factors investigated as limit cases while potential threshold behaviors are not studied.

The effect of the spatial variability of groundwater recharge was examined simulating a system with an uniform value of recharge applied in each surface cell ("Constant Recharge Case"). For the uniform value, we chose the average value (equal to 94.1 mm/year) of the spatial distribution. The resulting total volume of water entering into the soil is about equal in the cases with spatially variable and uniform recharge but the flux infiltrating through the surface of a single grid cell is quite different. The aim is to understand how the recharge distribution pattern influences the groundwater motion in the different hydrogeological units and the structure of groundwater pathways.

In the general case, stream parameters of secondary channels were distinguished from those of the main stream (see Table 3.2) in order to represent the river network as realistically as possible. The influence of the structure of the stream network was analyzed considering a river boundary condition with constant values of river stage and river width across the whole stream network ("Constant River Parameters Case"). In such case, for the tributaries these parameters were assigned the same values chosen for the main channel. The aim is to observe how the global behavior of the groundwater flow system is influenced by the size and characteristics of the river network.

Another factor under investigation was the impact of the spatial scales used to represent the topographic surface of the catchment. Land surface topography, in fact, strongly impacts groundwater flow and river-aquifer exchange patterns, as demonstrated by several studies [196, 213, 40]. Therefore, the influence of the topography is an important factor to investigate since it could influence the results. In order to observe the effect of small scale heterogeneity in the topography, the ground surface (represented by the DEM) was smoothed ("Smoothed Ground Surface Case") by applying a low-pass filter and removing the smaller spatial scales (i.e., higher frequencies). The effect of this filtering is observable in Figure 3.5: panel (a) represents the ground surface of the catchment according to the DEM while panel (b) represents the corresponding smoothed version. It is clearly visible the absence of short wavelengths with high frequency in the second version of the landscape topography. Panel (c) shows the one-dimensional surface roughness power spectrum for the non-smoothed and smoothed surface topography in x- and y-directions. The power spectra are calculated for each line profile and are then averaged to obtain a unique spectrum in each direction. It can be noted that the spectra related to non-smoothed and smoothed landscape topography overlie for low frequencies and long wavelengths (green curves in x-directions and red curves in y-directions), while they deviate for high frequencies and short wavelengths, highlighting the cutting of the smaller scales represented by short wavelengths.

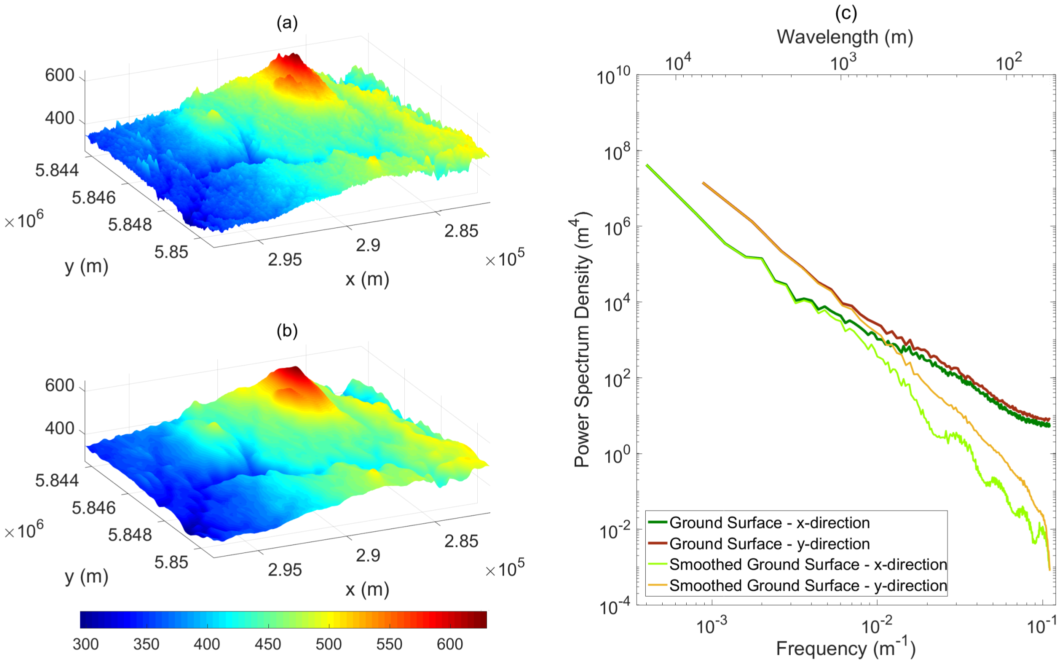

Fig. 3.5 (a) Landscape topography of the study domain according to the digital elevation model (DEM). (b) Smoothed version of ground surface. (c) Surface roughness power spectrum of non-smoothed and smoothed ground surface in x- and y-directions. Frequency (lower axis ticks) increases to the right, and wavelenght (upper axis ticks) increases to the left.

Finally, the effects of geological stratification and aquifer heterogeneity were investigated, considering (1) a geologically simplified system ("Simplified Geology Case") and (2) a homogeneous system ("Homogeneous Case"). The first system was obtained removing the Tertiary Aquifer unit and extending the Newer Volcanic layer up to the top of the basement layer. In this way, we evaluated how the behavior of the system changes when a rougher - but still detailed - geological structure is considered. The last case was represented by a homogeneous aquifer with constant values of hydraulic conductivity equal to the values assumed for the Newer Volcanic layer (Table 3.1), that represents the main geological unit within the aquifer. Notice that we focused on variations of hydraulic conductivity at scales comparable with the scales of the typical groundwater flowpaths (few kilometers) and we did not consider heterogeneity at smaller scales. However, variations at scales much smaller than the typical scales of groundwater flowpaths entail only a dispersion effect and do not result in preferential flowpaths. Therefore, the structure of the groundwater sub-basins should not be altered by these smaller scale variations.

As previously highlighted, the study area is lacking field data useful for the calibration and validation of the model. The only borehole existing within the study area has been installed recently and the monitoring data provide an average level over the monitored period (October 2016 to June 2017) of about 412.2 m (personal communication provided by Sarah Gaskill, Melbourne Water, 2017). This is in agreement with the value of 415.8 m obtained by the complete simulation in the corresponding cell. In fact, this error is 1 % of the range of simulated hydraulic heads in the catchment and, therefore, it is acceptable. The "Complete Case" is the case that we expect to reproduce most correctly the actual exchange fluxes. It must be considered that although the model is not well validated due to the absence of field data, our results are independent from a full validation since our aim is to observe how the patterns of groundwater exchange velocity vary when a local sensitivity analysis (in the sense of parameter space) is performed and different hydrogeological conditions are considered.

3.3 Results and Discussion

3.3.1 Groundwater flow field and exchange flux

In order to quantify stream-aquifer interactions, we look at the groundwater discharge-recharge along the stream in terms of exchange flow per unit area. Figure 3.6 shows the values of the vertical component of the groundwater velocity beneath the stream bed along the stream network for the different simulated systems. The maps highlight whether the river is gaining (positive values, blue colors) or losing (negative values, red colors). Different gradations of these two colors indicate the intensity of the exchange flux. Table 3.3 indicates the fraction of gaining and losing cells over the total number of river cells for each simulation and shows quantitatively the difference in gaining and losing conditions along the river network when different modeling assumptions are made. It can be observed that the main river is alternating between gaining and losing, as suggested by the geomorphological configuration of the catchment in previous studies [60]. Moreover, the patterns of exchange fluxes are very similar among the different scenarios; the only system that shows a substantially different behavior is the “Homogeneous Aquifer Case”, where the losing conditions increase considerably along the tributaries, while the main stem becomes more gaining. This can be explained considering a higher value of the average hydraulic conductivity of the domain in comparison with the heterogeneous case, that entails a drop in the water table. According to equations (3.2), the total exchange flux between the river and the aquifer is directly proportional to river width and river stage. Therefore, water exchange fluxes along the tributaries will be higher when increased values of width and stages are considered (“Constant River Parameters Case”). Finally, another observation that emerges from the results is related to the strong influence of the structure of the river network. The spatial patterns of groundwater recharge and drainage can be strongly affected by the position of the stream network within the catchment. The position of a stream in its river network, in fact, determines if a reach receives groundwater, loses water into the aquifer, or it is neutral. In this study, we considered a single level of detail in the representation of streams in the model and this could be explain the stability of GW-SW exchange flux patterns, at least partially. Future investigations could

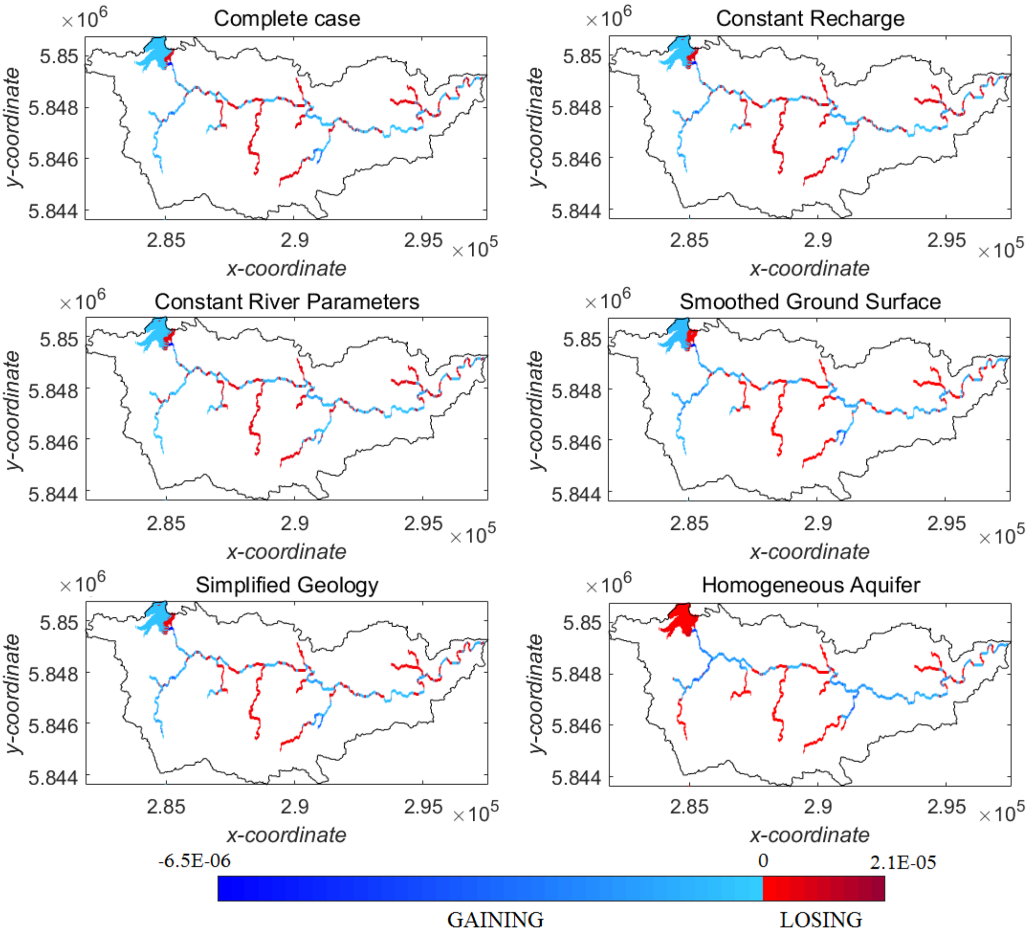

Fig. 3.6 Intensity of vertical exchange velocity q_z(m/s) for different simulations. Gaining and losing conditions are represented in blue and in red, respectively. Deeper colors indicate higher intensity of exchange flows.

be conducted to analyze the effect of capturing different levels of representation of the stream network.

Figure 3.7a represents the vertical exchange velocity q_z (m/s) as a function of the position along the main channel for the different cases. Positive values represent water gaining river conditions and negative values represent losing river conditions. The exchange velocity behavior is very similar for most of the cases, with the exception of (i) the “Homogeneous Case”, as already noted in the previous figure, and (ii) the “Smoothed Ground Surface Case”. In this latter case, the vertical exchange velocity shows a more regular pattern, with less oscillations, due to the fact that a narrower range of spatial scales is driving GW-SW interactions. Table 3.4 shows some statistical parameters (i.e., mean

Table 3.3 Percentage of gaining and losing river cells for different simulations. The amount in parentheses indicates the variation of the percentage fraction of gaining and losing river cells respect to the reference case (“Complete Case”).

	Losing conditions (%)	Gaining conditions (%)
Complete case	32.6	67.4
Constant Recharge	33.0 (+0.4)	67.0 (-0.4)
Constant River Parameters	31.6 (-1.0)	68.4 (+1.0)
Smoothed Ground Surface	34.7 (+2.1)	65.3 (-2.1)
Simplified Geology	33.7 (+1.1)	66.3 (-1.1)
Homogeneous Aquifer	72.4 (+39.8)	27.6 (-39.8)

value and standard deviation) of vertical exchange velocity along the main river for the different simulations. The only case with meaningfully different values is the “Homogeneous Case”, for which the prevalence of gaining conditions can be observed: the mean value of q_z is about three times the value obtained for the other cases since the increase of losing conditions along the tributaries is compensated by a more gaining main reach. Moreover, the standard deviation of q_z for the “Smoothed Ground Surface Case” is lower than the other cases, indicating a reducing dispersion of exchange flux values.

The degree of change among the different sets of vertical exchange velocity data is examined graphically through the box plots represented in Figure 3.7b, that highlight the associated variability. The vertical exchange velocities show almost equal distributions for most cases, with very similar values of median and mean. The only exception is the “Homogeneous Case”, which exhibits more variability in the statistical parameters. In order to quantitatively compare these differences, we ran a statistical test (two-tailed t-test) and the results highlight that the “Homogeneous Case” is the only case statistically different from the other cases ($p < 0.05$).

A more detailed quantification of the variability of the modeled exchange velocity under different hydrogeological conditions is represented in Figure 3.8. The scatter plots show the comparison between the vertical exchange flow per unit area obtained at each river cell for the complete model, q_z^{compl}, and for each simplified system, q_z^{simpl}. The different series of exchange velocity

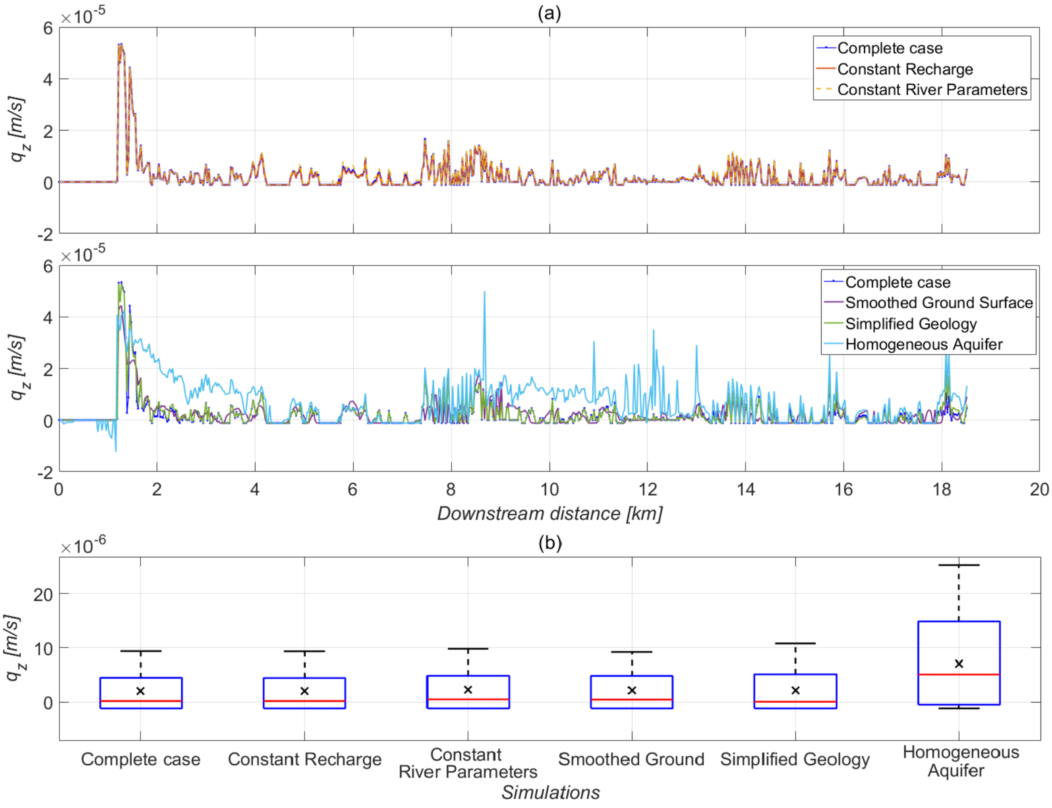

Fig. 3.7 (a) Exchange vertical velocity along the main river and (b) boxplots of the vertical exchange fluxes for different simulations. Quantiles are determined in correspondence to 5, 25, 50, 75 and 95% of the numerical data. The cross markers indicate the mean value of each series.

values compare well for the simulations with constant recharge, constant river parameters and simplified geology: in fact all points are most closely aligned along the 1:1 line of best fit with limited scatter, as confirmed by the values of the coefficient of determination, R^2. The smoothed-ground surface case shows a lower correlation (with R^2 equal to 0.5695), while the R^2 value of the homogeneous system (very close to zero) indicates the total lack of correlation, highlighting that there does not exist a meaningful relationship between the two variables, i.e., the exchange velocity estimated for the homogeneous system is substantially different from the values estimated with the full model. Moreover, it can be observed that the “Homogeneous Case” tends to overestimate the values of groundwater inflow/outflow, while in the “Smoothed Ground Surface Case” there is the presence of both over/underestimation clusters.

The discrepancy that emerges from the scatter plot for the “Smoothed Ground Surface Case” was not distinctly visible through the boxplots. This means that the total fluxes occurring in the system are nearly equal in both the “Smoothed Ground Surface Case” and the “Complete Case”, so the average behavior of the system is unchanged. However, the dispersion highlighted by the scatter plot indicates the presence of local variations of gaining and losing conditions induced by local variations of ground and riverbed elevations. These variations of elevation entail a shift from gaining to losing (and *vice versa*) conditions at specific points, with a resulting redistribution of exchange fluxes within the aquifer. This result confirms the relevance of topographic description of the study area in determining local river-aquifer interaction patterns since the landscape topography is among the main factors that influence groundwater flow [40].

Overall, we can state that the similarity between the structure of groundwater discharge patterns under different hydrogeological conditions – with the exception of the homogeneity condition – represents a significant result since it shows how a detailed description of some hydrological factors has a marginal effect on the structure of subsurface flow patterns.

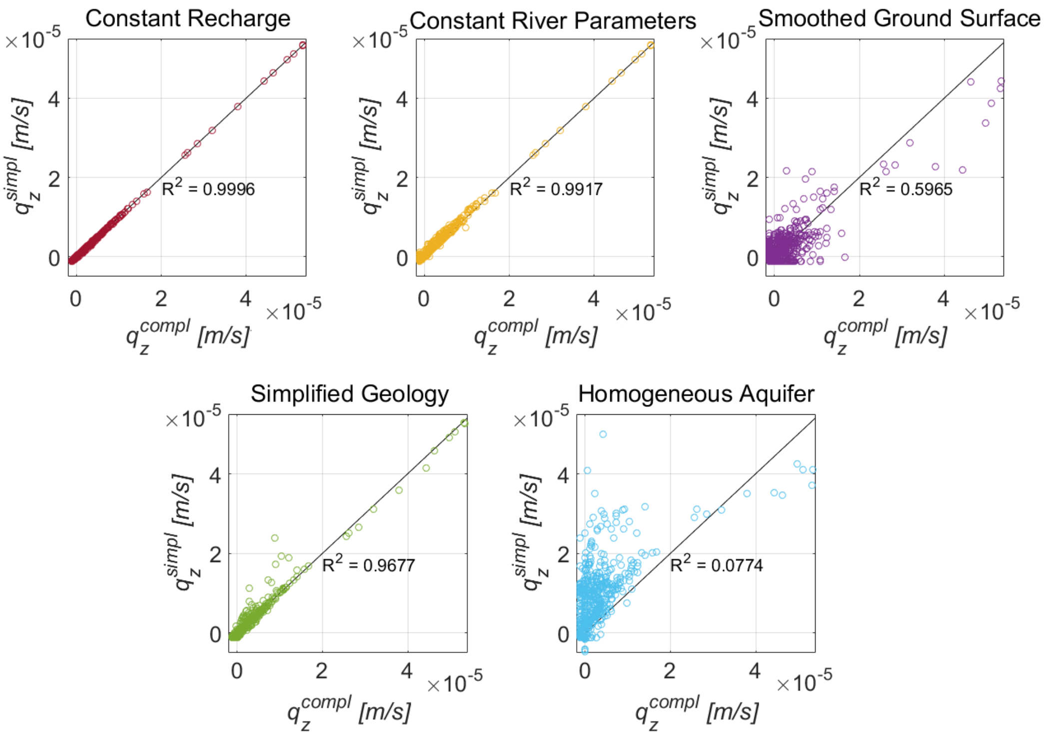
Constant Recharge

Constant River Parameters

Smoothed Ground Surface

Simplified Geology

Homogeneous Aquifer

Fig. 3.8 Comparison of the vertical exchange flux per unit of length obtained for the complete system, q_z^{compl}, and for each simplified system, q_z^{simpl}. The R^2 indicates the coefficient of determination between the two estimates.

Table 3.4 Statistical parameters of vertical exchange velocity along the main river for different simulations. The values in parentheses indicate the percent variation with sign respect to the reference case ("Complete Case").

	Mean Value (m/s)	Std Deviation (m/s)
Complete case	$2.10 \cdot 10^{-6}$	$6.07 \cdot 10^{-6}$
Constant Recharge	$2.08 \cdot 10^{-6}$ (-0.9%)	$6.06 \cdot 10^{-6}$ (-0.2%)
Constant River Parameters	$2.36 \cdot 10^{-6}$ (+12.5%)	$6.15 \cdot 10^{-6}$ (+1.3%)
Smoothed Ground Surface	$2.17 \cdot 10^{-6}$ (+3.3%)	$5.20 \cdot 10^{-6}$ (-14.3%)
Simplified Geology	$2.20 \cdot 10^{-6}$ (+4.8%)	$6.17 \cdot 10^{-6}$ (+1.6%)
Homogeneous Aquifer	$7.02 \cdot 10^{-6}$ (+243.3%)	$8.59 \cdot 10^{-6}$ (+41.5%)

3.3.2 Groundwater sub-catchments

In order to better understand the similarities among the exchange flow patterns, it is useful to identify features of the aquifer that mainly influence the structure of the groundwater flow field and the subsurface pathways. Figure 3.9 represents the groundwater sub-basins that identify the part of the basin from which the groundwater flow arrives at different reaches of the river network. The fraction of points belonging to each groundwater sub-basin on the total number of simulated pathways is indicated in Table 3.5 for each case. The already noted similarity in groundwater discharge patterns is confirmed by the structure of groundwater sub-basins. It can be observed that GW sub-catchments drained by each river segment are relatively stable for most considered cases. Specifically, the compartmentalization of the aquifer and, thus, of the groundwater flow system can be considered as the cause of similarity of the different exchange flux patterns. In fact, the aquifer can be divided into discrete compartments that maintain the same structure under different simplifying assumptions of the model, with the exception of the homogeneous aquifer simplification.

The spatial distribution of recharge rates seems to be a minor control of groundwater pathways. This means that groundwater flow patterns show a configuration that is intrinsically linked with the topographical and geomorphological structure of the aquifer while it is not strongly affected by the spatial distribution of recharge. The only case in which the compartmentalization of the aquifer is quite different is the "Homogeneous Aquifer Case", in which the increase of losing river reaches entails a different redistribution of groundwater resources and subsurface pathways. Therefore, the main variations in hydrogeological sub-basin patterns are ascribable to different discharge zone spatial distributions, that may significantly modify the structure of groundwater circulation. These results indicate that geology and topography of the aquifer dictate the structure and the distribution of groundwater fluxes within hydrogeological basins, providing key controls in defining the degree of compartmentalization of the aquifer.

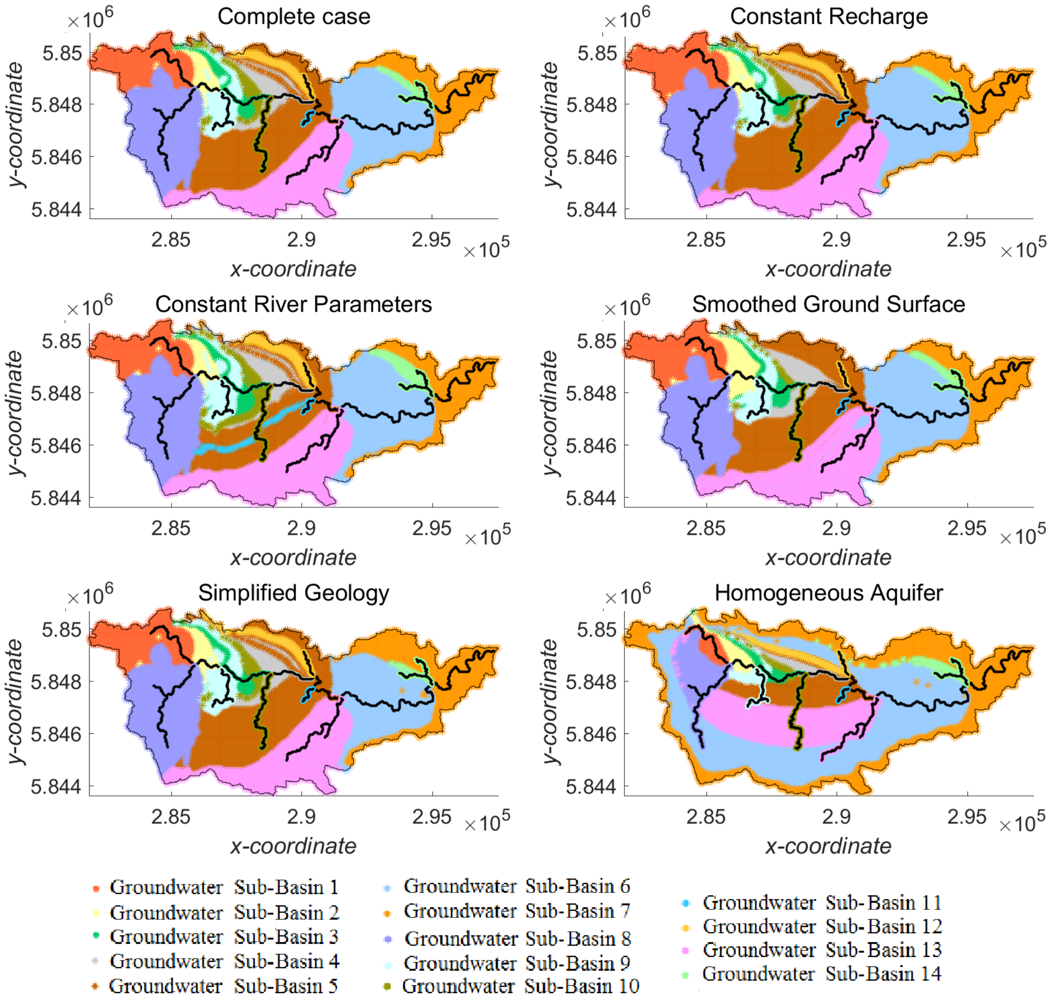

Fig. 3.9 Groundwater sub-basins for different simulations. Each color evidences the part of basin that directly feed the correspondent reach of the river network. The subdivision is indicated by the legend.

Table 3.5 Percentage of points in each groundwater sub-basin for different simulations. The values between parenthesis indicate the variation, in percentage, of points belonging to each basin compared to the complete-reference case.

	Basin 1 (%)	Basin 2 (%)	Basin 3 (%)	Basin 4 (%)	Basin 5 (%)
Complete case	8.22	2.39	2.55	6.08	20.28
Constant Recharge	8.58 (+0.36)	2.43 (+0.04)	2.46 (-0.09)	5.47 (-0.61)	21.37 (+1.09)
Constant River Parameters	8.09 (-0.13)	2.27 (-0.12)	3.42 (+0.87)	6.14 (+0.06)	15.26 (-5.02)
Smoothed Ground Surface	8.76 (+0.54)	3.93 (+1.54)	2.58 (+0.03)	5.69 (-0.39)	19.43 (-0.85)
Simplified Geology	8.40 (0.18)	2.27 (-0.12)	2.54 (-0.01)	5.96 (-0.12)	20.47 (+0.19)
Homogeneous Aquifer	1.96 (-6.26)	2.22 (-0.17)	1.80 (-0.75)	2.28 (-3.80)	9.40 (-10.88)
	Basin 6 (%)	Basin 7 (%)	Basin 8 (%)	Basin 9 (%)	Basin 10 (%)
Complete case	18.36	9.07	14.05	3.34	0.85
Constant Recharge	18.30 (-0.06)	9.14 (+0.07)	13.63 (-0.42)	3.13 (-0.21)	0.74 (-0.11)
Constant River Parameters	18.17 (-0.19)	8.45 (- 0.62)	14.39 (+0.34)	3.54 (+0.20)	1.40 (+0.55)
Smoothed Ground Surface	19.91 (+1.55)	9.31 (+0.24)	12.55 (-1.50)	2.45 (-0.89)	0.28 (-0.57)
Simplified Geology	16.54 (-1.82)	11.14 (+2.07)	13.93 (-0.12)	3.39 (+0.05)	0.77 (-0.08)
Homogeneous Aquifer	41.53 (+23.17)	20.22 (+11.15)	0.49 (-13.56)	0.87 (-2.47)	0.29 (-0.56)
	Basin 11 (%)	Basin 12 (%)	Basin 13 (%)	Basin 14 (%)	
Complete case	0.00	0.95	13.48	0.37	
Constant Recharge	0.00 (-)	1.05 (+0.10)	13.44 (-0.04)	0.36 (-0.01)	
Constant River Parameters	0.58 (+0.58)	1.30 (+0.35)	15.80 (+2.32)	1.19 (+0.82)	
Smoothed Ground Surface	0.00 (-)	0.00 (-0.95)	14.65 (+1.17)	0.46 (+0.09)	
Simplified Geology	0.00 (-)	0.97 (+0.02)	13.47 (-0.01)	0.15 (-0.22)	
Homogeneous Aquifer	0.00 (-)	0.75 (-0.20)	13.14 (-0.34)	0.65 (+0.28)	

3.3.3 Comparison with a regional-national scale model

The Department of Sustainability and Environment of Victorian Government developed a three dimensional groundwater flow model of the entire Port Phillip Catchment Management Area (CMA) [80]. The Port Phillip study represents part of a state-wide program aimed at producing groundwater models for each CMA in Victoria to assess the impact of land use change on depth to water table and stream baseflows. This is a very large scale model (the total modeled domain covers an area of around 12800 km^2), with a maximun spacing of 200 meters (cell size) and a six layer representation of the three dimensional regional geology [80]. The adopted approach consisted in conceptualizing the multi-layered aquifer system present within the Port Phillip CMA followed by development and calibration of a steady state groundwater model. The first phase was followed by the construction and calibration of a multi-layer transient groundwater model of the Port Phillip CMA [80]. This model was developed with different aims compared to the present study. Nevertheless, a comparison between our model and the Port Phillip CMA groundwater model is useful in order to analyze if a rather simple model is able to reproduce the results obtained by a more complex, detailed and calibrated model relative to gaining and losing conditions along the stream network.

Figure 3.10 shows the comparison of the two models (blue and red points and cross markers refer to Port Phillip CMA groundwater model). The comparison reveals a good agreement, especially along the main stem of Jackson Creek, with the exception of very few points. The comparison is slightly worse for some tributaries, for which the lack of interaction is not always reproduced by our model. However, this can be explained considering that in the Port Phillip CMA groundwater model the river network is modeled through the MODFLOW stream package rather than the alternative river package used in our model. In the stream package, the modeled baseflows are routed through the defined network and the stream cells are de-activated when the modeled groundwater levels are beneath the streambed and there is no baseflow from upstream cells, being classified as no-interaction cells. Differently, river package does not take into account the amount of flow in the river itself and the exchange flux in each cell is calculated based on the stage in the river specified by the user and the model calculated head in the boundary cell adjacent to the river cell [95]. For

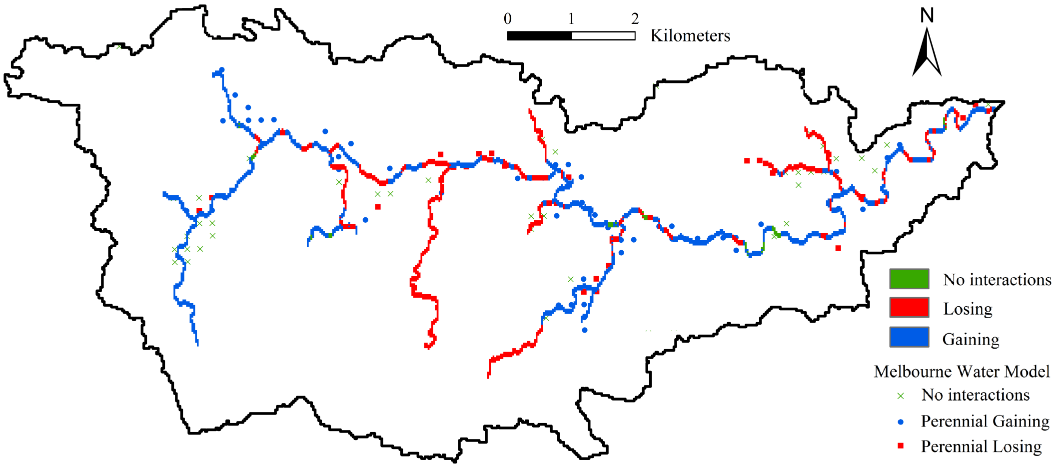

Fig. 3.10 Comparison among the results of our model and the results obtained by the Port Phillip CMA Groundwater Model in terms of gaining and losing conditions.

this reason, we classified as reaches with no interactions those reaches where the value of vertical velocity falls below a threshold value, chosen equal to 5% of the mean value. Therefore, the different classification of tributaries visible in Figure 3.10 can be partially attributed to this arbitrary choice. The other minor differences are expected considering that the two models have different spatial resolutions (30 m vs 200 m) and different study domains and settings, which can influence the general pattern of river-groundwater exchange. In fact, we have observed that the DEM resolution can locally influence and modify the position of gaining and losing points.

3.4 Concluding Remarks

In the work presented in the previous chapter [40], an analytic solution was used to solve the groundwater flow field and to investigate how the geometrical complexity of the water table affects the spatial patterns of groundwater inflow fluxes in a river network. The previous semi-analytical approach presented some limitations due to the hypothesis of topography-controlled water table, which approximates the phreatic surface with a smoothed version of the ground surface. This assumption can be considered valid only in specific regions, where the recharge rate (precipitation) is sufficiently high relative to the infiltration capacity of the ground. Therefore, the approach developed previously can not be applied indifferently to every type of catchment and topography. Moreover, in the present study the numerical model allowed us to analyze the effect of aquifer heterogeneity while the analytical solution of the groundwater flow field was valid for homogeneous conditions. Therefore, this new numerical approach certainly overcomes the constraints imposed by the previous analytical approach, at the expense of a greater computational cost.

The present work highlights the relevance of describing the geological and morphological structure of a catchment in order to model the GW-SW exchange patterns along the river corridor. This result implies that the spatial distribution of groundwater inflow strongly differs from basin to basin because it depends on the complex hydrogeological settings of each aquifer. The assumption that landscape topography can help to determine the groundwater flow field is, in fact, plausible only in homogeneous aquifers in humid regions. A detailed description of geological stratification and aquifer heterogeneity thus plays a key role in describing the intensity and the direction of river-groundwater interactions along the stream network. Moreover, it emerges that the spatial scales describing the landscape topography locally have an influence in determining the patterns of gaining and losing conditions within a catchment, although not impacting the global behavior of the groundwater system. Conversely, an accurate description of the spatial variability of the boundary conditions (specifically, groundwater recharge and river network) does not have a substantial effect on influencing groundwater discharge patterns. In fact, the behavior of the river system in terms of gaining and losing conditions is well reproduced also assuming uniform values of the parameters describing these boundary conditions. Therefore, a simplified description of these parameters results adequate for our modeling purposes.

Understanding the main controls of the patterns of river-aquifer exchange velocity at watershed scale is important in order to collect the data necessary to well describe and analyze river-groundwater interactions in a certain area. A lack of available data is often a major hurdle to conducting this type of analyses. Overall, it is possible to conclude that even a rough description of the geological structure of an aquifer is required to adequately predict gaining and losing conditions along the river network since the aquifer heterogeneity is a major controlling factor. However, considering that aquifer heterogeneity is very difficult to predict, the estimation of GW-SW interactions derived without such knowledge should be treated with considerable caution.

A correct and accurate modeling of surface-subsurface water exchange at the regional and continental scales is challenging because of the complexity of the water exchange dynamics and of the multi-scale processes taking place at the stream–aquifer interface [152, 182, 70]. Therefore, some simplifications and assumptions are unavoidable. In the present work, surface water–groundwater exchange are simulated with an approach based on a conductance factor using the MODular three-dimensional finite-difference groundwater FLOW (MODFLOW) model [135, 95]. The streambed conductance factor relies on a linear relationship between river stage and aquifer water levels. Some authors considered this relationship too simplistic [148, 165, 58]. The conductance model implicitly formulates the hypothesis of a vertical water flux between surface water and groundwater whatever the mesh size. Moreover, it usually assumes an equivalent homogeneous riverbed for the definition of the conductance value, which can imply estimation errors in the exchanged water fluxes compared to a more realistic heterogeneous riverbed [70]. This inconvenience could be bypassed if the model was appropriately calibrated with regard to the connection/disconnection status, obtaining slight estimation errors [110, 70].

Another limitation concerns the fact that MODFLOW makes the assumption of saturated flow between a stream and the underlying aquifer, appropriately accounting for saturated flow. The unsaturated flow, otherwise, is accounted by making some simplifying assumptions. When the aquifer head is above the bottom of the streambed (i.e., saturated conditions), MODFLOW assumes that the exchange flux through the streambed in proportional to the difference betweeen the river stage and the aquifer hydraulic head [72]. If the aquifer head drops below the bottom of the streambed, MODFLOW assumes that the seepage becomes a function of the water level in the streambed and of the bottom elevation, indipendent from the aquifer head [72]. The conductance model is able to simulate connected or disconnected systems but it remains appropriate for disconnecting streams only when the GW table elevation is deep [31]. Otherwise the model leads to estimation errors for disconnecting systems [70]. The assumption of fully saturated conditions is often not valid across a riverbed and the importance of unsaturated flow on stream-aquifer exchange has been stressed and analyzed in several studies [72]. In fact, unsaturated flow transforms streams from constant head boundaries to constant flux boundaries, impacting not only the quantity of stream recharge but also biogeochemical transformations. Therefore, the effects of unsaturated flow should be considered in future analyses.

Another problem faced by MODFLOW approach is that the geometry of the river is lumped into a single value and the river stage is assumed to remain constant throughout a given stress period within the model despite many factors (i.e., hydropower generation) can contribute to a spatial and temporal variation of water levels. Therefore, more detailed information and data at the regional scale would be helpful, together with a method that enables more realistic representations of the river geometry in order to consider also the floodplain. The low number of temporal and spatial measurements of aquifer head and stream stage, in fact, remains one of the biggest challenges [173, 171].

Finally, it should be considered that the present analysis is not valid when the Darcy's law is not more applicable. This is the case of aquifers in carsic formations, characterized by splitting rocks, wide fractures, and subsurface channels. In fact, fractures, splits and cavities can be much more larger than the scale of analysis, and, in these conditions, the medium cannot be considered continuous and the flow pathways would change considerable. Heterogeneity variations here considered, thus, represent some exemplifying cases and do not cover all the range of real conditions that can be occur in a real aquifer. Future research should be devoted to extend the analysis to other complexity factors.

The present model looks at the GW-SW interactions induced by large-scale characteristics of the aquifer, i.e., water gains and losses at the scale of tens of meters. Therefore, our results do not include the effect of local characteristics of the riverbed that provoke river-aquifer exchange at small scales (tens of centimeters or few meters). However, hyporheic exchange induced by local variations of hydraulic conductivity in riverbed sediments or small scale morphologies, such as dunes, bars, riffles and pools, are in turn impacted by groundwater upwelling at basin scale. Therefore, small-scale river-aquifer interactions are not independent from large-scale exchange but, on the contrary, modulate them. Among the other limitations of our model, it is important to remember that we do not take into account seasonal and annual fluctuations of the groundwater table depth, that could convert some gaining reaches into losing reaches, and *vice versa*.

An obvious extension of our work presented here would involve examining how various human induced changes to the hydrology of the watershed (such as urbanization) and shifting climate (such as prolonged droughts) affect the gaining/losing patterns observed here, and how these patterns in turn influence stream water quality through hyporheic exchange [88, 4].

Chapter 4

Effect of bioclogging on hyporheic biogeochemistry in river dunes

Part of the work described in this chapter has been previously published in a research article in a peer-reviewed international journal [39].

4.1 Introduction

Riverbed sediments host important biogeochemical processes that play a key role in nutrient dynamics. Sedimentary nutrient transformations are mediated by bacteria in the form of attached biofilms. For their metabolic activity, hyporheic microbes rely on water-borne solutes that are supplied by water exchanged with the nutrient-enriched stream. An important aspect to take into consideration to study microbial processes within the hyporheic zone is the feedback that microbes exert on nutrient fluxes through the process of bioclogging. Bioclogging is the reduction of water-filled pore volume and sediment permeability caused by biofilm growth and gas production. Unfortunately, the present understanding of the influence of microbial metabolic activity on the hydrochemical conditions in the hyporheic zone is poorly understoond since it is limited by the difficulty of data collection within streambed sediments. Furthermore, available models capture the effects of hyporheic exchange flow in microbial metabolism and biogeochemical transformation [6, 218, 150], but they do not consider the consequences of the resulting biomass growth in filling pore space, reducing streambed porosity and permeability (bioclogging), and larger-scale feedbacks on rates and patterns of hyporheic exchange flow.

In this chapter, we present a new hydrobiogeochemical model to assess how the growth of heterotrophic and autotrophic biomass affects the transport and transformation of dissolved nitrogen compounds in bed form-induced hyporheic zones. The aim is to investigate how the bioclogging phenomenon influences the biogeochemical and hydrodynamic processes since the biomass growth induces a reduction of the sediment permeability and porosity, with a direct consequence on GW-SW exchange fluxes and nutrient transport. The model simulates coupling between porewater fluxes, reduction in permeability associated with microbial growth, and heterotrophic and autotrophic metabolism of nitrogen, oxygen, and organic carbon.

The results show how coupling of physical and biological processes regulates spatial distributions of microbial guilds that drive hyporheic nitrogen transformation, the associated heterogeneity in hyporheic flow and hydrological properties (porosity, permeability), and the resulting hyporheic nitrogen transformation rates. The system eventually attains an equilibrium between permeability reduction and microbial metabolism that yields shallow hyporheic flows in a region with low permeability and high rates of microbial metabolism near the stream-sediment interface. Our model demonstrates how the bioclogging caused by microbial growth can constrain rates and patterns of hyporheic fluxes and microbial transformation rate in many streams.

4.2 Hydraulic and Biogeochemical model

4.2.1 Model description

In this study, we provided a new model that captures the effects of multiscale coupling and feedback processes resulting from hyporheic microbial metabolism and growth. We build on prior models that represented the effects of hyporheic exchange flow, nitrogen dynamics, and heterotrophic and autotrophic metabolism, but did not account for the consequences of this metabolism

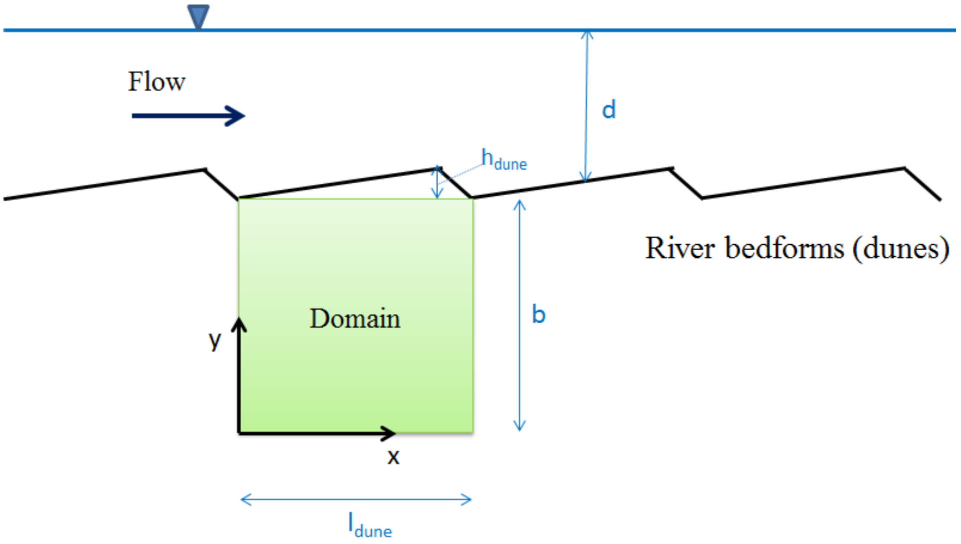

Fig. 4.1 Sketch of the study system: a turbulent current with average flow velocity U and water depth d flows over a river bed with periodic dunes with height h_{dune} and length l_{dune}. The study domain is represented by a single dune and the porous media below it of depth b. The adopted reference system is represented.

in biomass growth that fills pore space and alters hyporheic flow rates and patterns. Hyporheic exchange flow, nutrient dynamics, and heterotrophic and autotrophic hyporheic nitrogen metabolism were simulated for baseflow conditions in a low-gradient sand-gravel bed stream, with moderate in-stream nutrient concentrations and no carbon limitation on nitrogen metabolism.

The study system is depicted in Fig. 4.1 and consists of a turbulent water stream with mean water depth d and average velocity U flowing over a periodic dune-shaped river bed composed by granular material with homogeneous and isotropic properties. The streambed is formed of two-dimensional asymmetric dune-like bedforms which repeat periodically with triangular shape, amplitude h_{dune} and wavelength l_{dune}. Due to the morphological periodicity, a single dune and the corresponding porous media below it (depth b) were considered. The physical and chemical properties of the stream and the hydraulic properties of the sediments were assumed to be known. As $b \gg h_{dune}$ was assumed, it follows that the stream-sediment interface can be approximated as a horizontal plane in order to model the hyporheic flows in the sediments [63]. The domain of the mathematical problem, thus, results to be a vertical rectangle b x l_{dune}. A Cartesian reference system was adopted, where x and y represent the streamwise and upward coordinates, respectively, and the axis origin was located on the left corner of the domain bottom.

4.2.2 Hyporheic flow field and pressure distribution

We considered a modeling approach of the hyporheic exchange based on the formulation proposed by Elliot and Brooks [63], adopting a pressure variation induced by stream flow over bedforms well approximated by a sinusoidal distribution (4.2). Two key exchange mechanisms, “pumping” and “turnover”, drive the advective flow of water across a dune streambed: the former is due to the pressure variations over the bedforms induced by the movement of pore water into and out of the bed, the latter occurs as moving bedforms trap and release interstitial fluid [63]. In this work, we assumed that the dunes are not moving, neglecting water fluxes induced by turn over.

Water currents flowing over small-scale topography, such as dune-like bed forms, logs and boulders, result in high pressure areas upstream of the irregularity, where flow detaches, or low-pressure areas downstream, where flow reattaches [192, 169]. These dynamic head variations at the GW-SW interface cause circulation of water within the sediments. High- or low-pressure areas represent outflow and inflow areas, respectively (see Fig. 4.2). The periodicity of the bedforms entails that a discharge area is present also upstream of the considered dune, induced by the previous bedform. Therefore, the dune effect can be described through a hydraulic head distribution with a sinusoidal variation applied over a flat bed

$$h = h_0 \sin\left(\frac{2\pi}{l_{dune}}x - \frac{\pi}{2}\right), \tag{4.1}$$

with h_0 the head amplitude, l_{dune} the dune length and x the coordinate in the flow direction. The value of head amplitude h_0 reported by Elliott and Brooks [63] and based on experiments by Vittal et al. [203] and Shen et al. [172] is the following

$$h_0 = 0.28\frac{U^2}{2g}\left(\frac{h_{dune}/d}{0.34}\right)^r, \tag{4.2}$$

where g is the gravity acceleration and r is an exponent equal to 3/8 if $h_{dune}/d < 0.34$ and 3/2 otherwise.

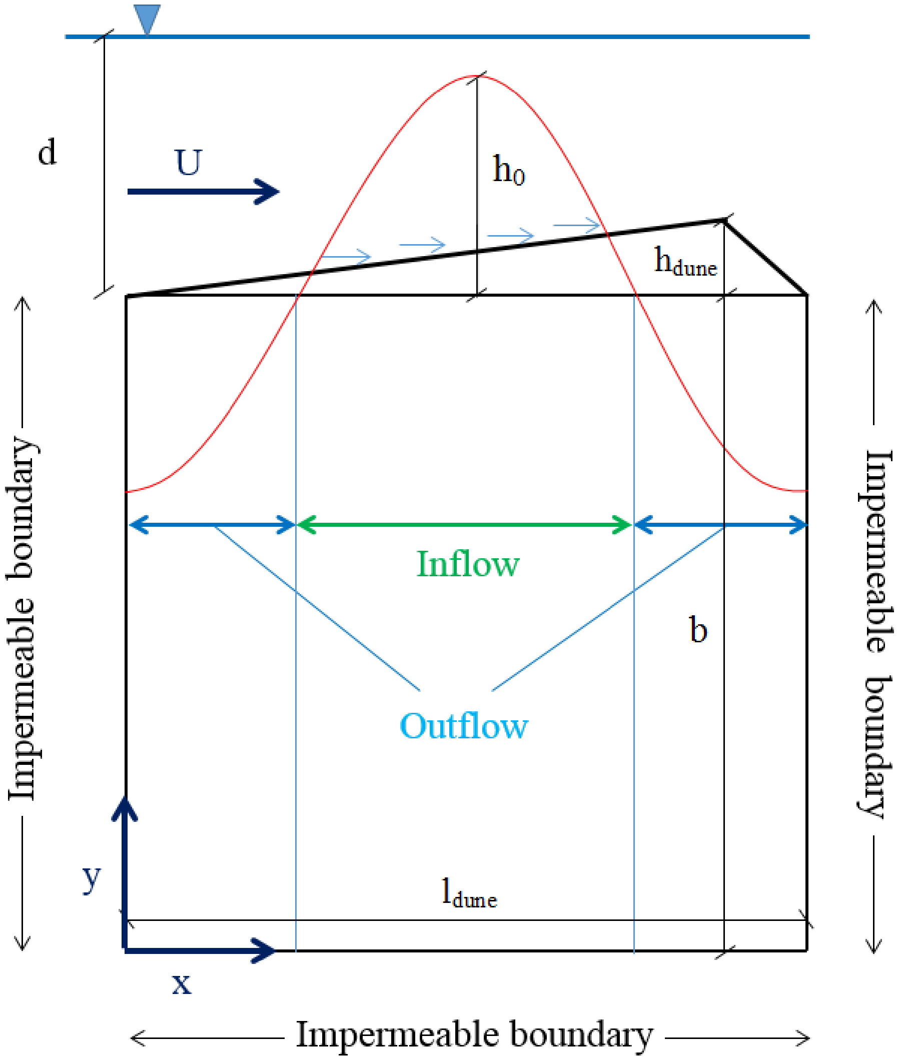

Fig. 4.2 Modeling scheme. The head distribution over a river dune is well approximated by a sinusoidal variation. The head amplitude h_0 is a function of dune height h_{dune}, average flow velocity U and water depth d. The pressure and the velocity boundary conditions for the stream water turbulent flow over the streambed are indicated. The model domain represents an asymmetrical stream dune of length $l_{dune} = 1$ m, height $h_{dune} = 0.01$ m. In the simulations, the water depth d and the stream velocity U are 0.16 m and 0.7 m/s, respectively.

The Darcian flow induced in the sediments by the pumping process [63] was described by

$$\frac{\partial \theta}{\partial t} - \nabla \cdot (K \nabla h) = 0, \tag{4.3}$$

where $\theta(x, y, t)$ is the soil porosity, $K = K(\theta)$ is the hydraulic conductivity, and $h(x, y, t)$ is the hydraulic head distribution. We assumed that dunes are not moving and the turnover mechanism was therefore neglected. The Darcy velocity was given by $\mathbf{q}(x, y, t) = -K\nabla h$. Porosity was described as a function of the total biomass concentration $X = (X_h + X_a)$ in the sediments

$$\theta\left(X\right) = \theta_0 - \frac{X_h}{\rho_{x_h}} - \frac{X_a}{\rho_{x_a}}, \tag{4.4}$$

where X_h and X_a represent the concentration (biomass per total soil volume) of heterotrophic and autotrophic biomass, respectively, and ρ_{X_h} and ρ_{X_a} are the relative densities (bacterial mass per biofilm volume), that are considered constant. The subscript 0 refers to the no biomass condition. Therefore, the porosity varies in time as a function of biomass growth and decay. Hydraulic conductivity was assumed to depend on porosity according to a power law, $K = K_0(\theta/\theta_0)^j$, where the exponent is set $j = 3$. In this way, the feedback between spatio-temporal bacteria biomass dynamics, the hydraulic properties of sediments, and the hyporheic flow field was established.

The biomass growth rate decreases gradually as a function of the nutrient concentration within the sediments and stops when the biomass occupies the whole void space and the porosity reaches the zero value. The flux of solutes is strictly correlated to the permeability of the riverbed and, hence, to the porosity. Therefore, the study problem is based on a coupled system between the variables of the model. This formulation was used to capture the effects of microbial growth filling hyporheic pore space and it has been found to robustly describe both physical and biological clogging processes that fill pore space by deposition and growth on grain surfaces and accumulation of deposits that bridge grain contacts. This is a multiscale formulation that captures the effects of microscale deposition, biofilm cluster growth, and pore-filling on upscaled bulk permeability. Both modeling (e.g.,[46, 185, 190, 188]) and experimental (e.g.,[111, 43, 45]) studies have adopted a power-law relation, with the exponent ranging from 2 to 4, to model clogging process caused by biofilm growth in porous media under different assumptions (e.g., heterogeneous porous media characterized by a random distribution of pore radii, different specific patterns for microbial growth, etc.). The clogging formulation used here has also been applied for clogging of porous media by colloid deposition, but the reason for this is that this formulation has proven to be surprisingly robust for many kinds of clogging processes, including bioclogging and particle clogging [189, 44]. Essentially, this formulation appears to provide a good description for many processes that fill pores in granular porous media, most likely because the fundamental growth of both biological and mineral colloidal deposits is similar – initial deposition on grain surfaces, followed by formation of small aggregates (particle aggregates or biofilm clusters), bridging of pore throats, and later general filling of pore space [190, 48, 194]. Equation (4.4) shows that biomass growth reduces the porosity of the bed and, consequently, the permeability, influencing the solute transport within the sediments and limiting nutrient availability for microbial metabolism.

A power-law relationship between the hydraulic conductivity and the porosity has been initially used in simple models (e.g., [46]) that estimate changes in porous media properties induced by biomass accumulation under some simplifying assumptions (pore connectivity in one dimension, no specific patterns for microbial growth, pores with uniform dimension, etc.). However, the power-law relationship has been then confirmed by more advanced studies (e.g., [185, 191]), where some additional processes are introduced (heterogeneous porous media with pore radius randomly extracted from a log normal distribution, different patterns of microbial growth, etc.). For modeling porous media biomass, Clement *et al.* [46] used an approach very similar to our approach, where the porosity reduction is expressed as a function of the biomass concentration as $\theta = \theta_0 - X/\rho_x$ (analogous to Eq. 4.4 in our model) and the change of relative hydraulic conductivity is related to the change of relative porosity through a power-law relation expressed as $K/K_0 = (\theta/\theta_0)^j$, where the exponent is equal to about 3 (j=19/6), in line with our model. Porosity and permeability profiles are confirmed by column simulations of biologically reactive flow, verifying the validity of the analytical model. Suchomel *et al.* [185] used a network model (i.e., the pores are modeled as a random network of interconnected pipes) to simulate the accumulation and the detachment of bacteria and EPS in porous media, analyzing the variation of flow properties

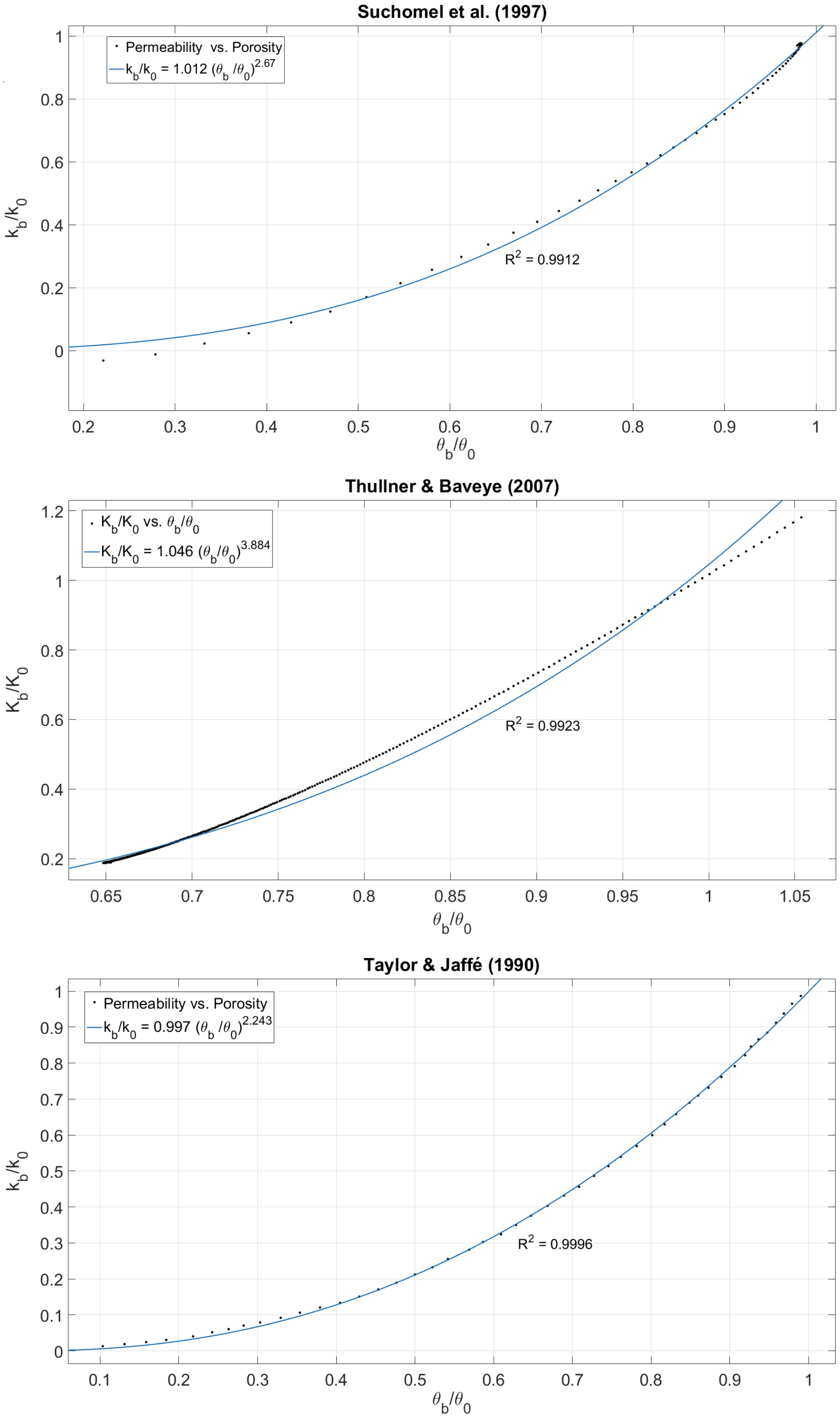

Fig. 4.3 Exemplifying relationships between permeability reduction and porosity reduction used in previous studies [185, 188, 111].

and rate parameters in two- and three- dimensional networks. Extrapolating the relationship between normalized permeability and porosity for two-dimensional base case and for specific values of the other parameters of the model, we have obtained $K/K_0 = \alpha(\theta/\theta_0)^j$, where α=1.012 and j=2.67 (see Figure 4.3). Similar relationships describe the dependence between the permeability and the porosity for the three-dimensional case and for other sets of parameters. Similar relationships describe the dependence between the permeability and the porosity for the three-dimensional case and for other sets of parameters. This confirms the validity of a power-law relation to model the permeability reduction induced by bioclogging effect.

One of the more interesting and challenging features of biofilms is they do not simply fill pore space, but close pore throats and reduce, but not eliminate, connectivity as there can be actual flow through the films themselves. Concerning this issue, the model we have developed is based on current observations and models of biofilm growth, which have found that transport through biofilms is several orders of magnitude slower than transport through the surrounding pore fluid (e.g., [53, 158]). The challenge with an upscaled model is that the exact biofilm configuration cannot be explicitly represented, and each element contains a mixture of pore fluid, biofilm biomass, and solid sediment grains. The assumption we use is that the upscaled effect of biomass pore filling can be adequately represented by a power-law relationship for biofilm biomass. This assumption is justified based on the results of prior experimental and modeling studies of both bioclogging and particle clogging. Note the exact same process occurs in both bioclogging and particle clogging. For particle clogging, particle deposits in the pore space are not completely solid, and instead have an internal porosity associated with microscale packing of the deposited colloids. While detailed in situ observations are not available for bioclogging, they are available for particle clogging, and it has been demonstrated that flow through these microporous deposits can be ignored in flow simulations [43, 45]. The mechanism of this is the same in colloidal deposits and biofilms – while there is certainly fluid motion within microporous materials, the permeability is orders of magnitude lower than the bulk permeability of the porous medium, and can therefore the internal permeability of the clogging deposits be ignored in upscaled simulations.

Thullner and Baveye [188] first examined bioclogging in porous media alleviating the restriction of an impermeable biofilm and modeling the flux through the biofilm. They showed that the prediction of biomass accumulation in the pores is underestimated when the biofilm permeability is neglected, at least in cases when porosity is reduced so much that biofilm permeability contributes significantly to water and nutrient transport. However, our simulations display a reduction of hydraulic conductivity of one order of magnitude ($K_0 = 10^{-3}$ m/s and $K \simeq 1.5 \cdot 10{-}4$ m/s), that corresponds to a decrease of the porosity of about 50%. This means that the biogeochemical system is far from the condition in which the porosity tends to zero and the flux through the biofilm could become significant since the porous space is entirely occupied. Moreover, the results of Thullner and Baveye [188] indicate that the patterns of hydraulic conductivity reduction induced by an increase of biomass volume are qualitatively similar for both permeable and impermeable biofilms. Therefore, neglecting the actual flow through the biofilms does not affect the qualitative characterization of the influence of microbial metabolic activity on the hydrochemical conditions and nutrient transformations within the hyporheic zone.

The boundary conditions for the stream water turbulent flow over the streambed, equation (4.3), are: no flux on the lateral and lower boundary ($\partial h/\partial x|_{x=0,l_{dune}} = 0$ and $\partial h/\partial y|_{y=0} = 0$) and dune-induced sinusoidal head on the upper boundary, $h|_{y=b} = h_0 \sin(2\pi x/l_{dune} - \pi/2)$.

4.2.3 Solute transport and biogeochemical reactions

A multicomponent reactive transport model was used to predict solute fluxes and concentrations in the hyporheic zone. Four key solutes were considered: dissolved organic carbon (DOC), oxygen (O_2), ammonium (NH_4^+), and nitrate (NO_3^-). The formaldehyde (CH_2O) was chosen to represent the DOC substance. This species is usually selected as the representative DOC compound for numerical simulations or field investigations (e.g., [109, 6]) for its simple chemical structure and because it can be a degradation product of more complicated DOC compounds. The chemical (convective and dispersive) transport and reaction in the sediments were described as

$$\theta \frac{\partial \theta c_i}{\partial t} + c_i \frac{\partial \theta}{\partial t} - \nabla \cdot (\mathbf{D_m} \nabla c_i) + \mathbf{q} \cdot \nabla c_i = R_i, \tag{4.5}$$

where $c_i(x, y, t)$ is the molar concentration of each compound (i = DOC, O_2, NO_3^-, NH_4^+), $\mathbf{D_m}$ is the hydrodynamic dispersion tensor [6] and $R_i(x, y, t)$ is the consumption/production rate of i. The hydrodynamic dispersion tensor has components [16]

$$\theta D_{ij} = (\alpha_L - \alpha_T) \cdot \frac{q_i q_j}{|\mathbf{q}|} + \delta_{ij} \cdot (\alpha_T |\mathbf{q}| + \theta \cdot \tau D_{mol}), \tag{4.6}$$

where $i, j = x, y$, α_L and α_T are the longitudinal and transversal dispersion, respectively, τ is the tortuosity, δ_{ij} is the Kronecker's delta and D_{mol} is the molecular diffusion coefficient. Longitudinal transport is usually more pronounced than transverse transport, therefore the values of the dispersivities α_L and α_T range in the interval $\alpha_t/\alpha_l = 1/20 \div 1/5$. Molecular diffusion is much smaller than hydrodynamic dispersion and it can be neglected.

The model includes three biochemical reactions: aerobic respiration, denitrification, and nitrification (see Table 4.1). The first two processes are heterotrophic and are generally induced by facultative dentirifying organisms in streambed sediments, while the third is autotrophic and is usually attributed to specific Authotrophic nitrifying bacteria, such as *Nitrosomonas* and *Nitrospira* [134, 109]. The DOC represents the electron donor and oxygen (aerobic respiration) and nitrate (denitrification) represent the electron acceptors, respectively. The autotrophic micro-organisms transform ammonium into nitrate through the nitrification, in which the ammonium is used as electron donor and the oxygen as electron acceptor. Aerobic respiration and nitrification start simultaneously, while denitrification only takes place in anoxic conditions, i.e., when oxygen concentration falls under a limiting value $c_{O_2,lim}$. The nitrate is produced by the nitrification and is used by heterotrophic bacteria as reagent in anaerobic conditions. Therefore, the autotrophic micro-organisms supply nitrate to the heterotrophic micro-organisms, which is used when the oxygen is lacking. Under anoxic conditions, in fact, the nitrification reaction stops. Hence, the two species of micro-organisms are in competition for the oxygen consumption necessary both for the aerobic respiration and for the nitrification, but also for space occupation, as indicated by Eq. 4.4.

Reaction rates for organic carbon and ammonium were modeled as first order in soil porosity, chemical concentration, and heterotrophic biomass adopting

Table 4.1 List of the reactions considered in the simulations.

Reaction type	Reaction	β
Aerobic respiration	$CH_2O + O_2 \longrightarrow CO_2 + H_2O$	1
Denitrification	$5CH_2O + 4NO_3^- + 4H^+ \longrightarrow 5CO_2 + 2N_2 + 7H_2O$	0.8
Nitrification	$NH_4^+ + 2O_2 \rightarrow NO_3^- + 2H^+ + H_2O$	-

the approach proposed by Hunter et al. [109]:

$$R_{DOC} = -\mu_{DOC}\theta X_h c_{DOC}(f_{O_2} + f_{NO_3^-}), \tag{4.7}$$

$$R_{NH_4^+} = -\mu_{NH_4^+}\theta X_a c_{NH_4^+} c_{O_2}, \tag{4.8}$$

where μ_{DOC} and $\mu_{NH_4^+}$ are reaction rate constants. Notice that the DOC consumption stops when oxygen and nitrate are depleted, because of the term $(f_{O_2} + f_{NO_3^-})$, while the rate of reaction of nitrification depends on the concentration of both ammonium concentration and oxygen. In the previous reaction rates, f_{O_2} and $f_{NO_3^-}$ describe the delayed activation of the aerobic respiration and denitrification in function of oxygen and nitrate concentrations and are equal to [109, 6]:

$$f_{O_2} = \begin{cases} \frac{c_{O_2}}{c_{O_2,lim}} & \text{if } c_{O_2} < c_{O_2,lim} \\ 1 & \text{if } c_{O_2} \geq c_{O_2,lim} \end{cases} \tag{4.9}$$

and

$$f_{NO_3^-} = (1 - f_{O_2}) \cdot \begin{cases} \frac{c_{NO_3^-}}{c_{NO_3^-,lim}} & \text{if } c_{NO_3^-} < c_{NO_3^-,lim} \\ 1 & \text{if } c_{NO_3^-} \geq c_{NO_3^-,lim}, \end{cases} \tag{4.10}$$

where $c_{O_2,lim}$ and $c_{NO_3^-,lim}$ are the molar limiting concentrations for oxygen and nitrate. These concentrations define conditions under which aerobic respiration and denitrification rates become linearly proportional to c_{O_2} and $c_{NO_3^-}$, respectively. When the global oxygen concentration (i.e., the average value in a computational element) falls below the value set as limit concentration, the aerobic reactions can continue until the oxygen concentration reaches the zero value and the different reactions coexist (i.e., when $0 < c_{O_2} < c_{O_2,lim}$ both aerobic respirations and denitrification occur). Thus, denitrification occurs only when the oxygen concentration is lower than the limiting value $c_{O_2,lim}$. Our model considers simple threshold values to define reaction dominance but actually the coexistence of both aerobic (respiration and nitrification) and anaerobic (denitrification) reactions is considered and, thus, the transition between aerobic and anaerobic conditions does not occur instantaneously but through a transitional phase. This behavior reflects the concept according to there can exist local aerobic zones within each computational element also when the average oxygen concentration is below a limit value. Therefore, the fact that the model fixes threshold values to define reaction dominance does not entail that there exist a net transition from one type of reaction to another type. Similarly to other reactive transport models [131, 7], the influence of pH variation on reaction kinetics was considered to be negligible and thus omitted from the model, due to the buffering in the hyporheic zone.

Since oxygen is involved both in nitrification and aerobic respiration, its reaction rate was modeled as

$$R_{O_2} = \beta_1 f_{O_2} R_{DOC} + 2R_{NH_4^+}. \tag{4.11}$$

Finally, nitrate is a byproduct of nitrification but it is also consumed by heterotrophic bacteria by denitrification. This yields the net nitrate transformation rate:

$$R_{NO_3^-} = \beta_2 f_{NO_3^-} R_{DOC} - R_{NH_4^+}. \tag{4.12}$$

The terms β_i ($i = 1$ for oxygen, $i = 2$ for nitrate) represents the ratio between the moles of transferred electrons per mole of oxidized DOC and the moles of electrons per mole of reduced compound in the i-th reaction, and f_i is the fraction of electrons consumed by the i-th reduction half-reaction. Values of β_i are indicated in Table 4.1.

Similar to hydraulic head boundary conditions, no chemical flux conditions were set on the lower and lateral domain boundaries. At the upper boundary (i.e., the stream-sediment interface), concentrations were assumed equal to those in the stream at all times – i.e., $c_i|_{y=b} = c_{i,s}$, where subscript s refers to the stream. The same values were also set as chemical initial conditions throughout the hyporheic zone.

4.2.4 Microbial biomass model

Bacteria were modeled using a growth-death model based on the metabolic processes described in equations (4.7)-(4.12), i.e., facultative denitrifying bacteria consume DOC by aerobic respiration and denitrification, while autotrophic bacteria consume ammonia and produce nitrate by nitrification. Our analysis neglected the sorption and considered the biomass as a continuous film attached to the grain surface, which is not transported. The died cells are instantaneously removed and are not used by micro-organism as a source of organic matter. Net microbial growth was therefore simulated as:

$$\frac{\partial X_h}{\partial t} = Y_{DOC}|R_{DOC}| - k_{d_h} X_h, \tag{4.13}$$

$$\frac{\partial X_a}{\partial t} = Y_{NH_4^+}|R_{NH_4^+}| - k_{d_a} X_a, \tag{4.14}$$

where Y_{DOC} and $Y_{NH_4^+}$ are growth yields and k_{d_h} and k_{d_a} are biomass die-off rates. This is a standard formulation for biomass growth in pore spaces that has been shown to adequately represent biomass in complex system geometries, such as reactor [160, 158, 150]. Initial conditions were spatially homogeneous, with $X_{h,0} > X_{a,0}$ (subscript 0 denotes $t = 0$) because autotrophic bacteria grow more slowly and are less numerous than the heterotrophic ones [144, 125, 61].

4.2.5 Simulation conditions

Using the approach described in the previous section, numerical simulations were carried out to investigate how the microbial growth controls the distributions of permeability, exchange flow and nutrients. For this purpose, we employed a numerical code in COMSOL Multiphysics®, a finite element solver that uses a finite-volume approach [47]. A non-uniform mesh was adopted, with a higher node density near the bed surface, where the spatial gradients are higher (Figure 4.4a). Specifically, 100 structured layers of quadrilateral elements were generated along the top boundary of the domain, while a free meshing technique generating an unstructured mesh was used to create triangular elements of size ranging from 0.01 m to $2.0 \cdot 10^{-5}$ m in the remaining part of the domain, for a total number of 35064 elements. In order to analyze the behavior of the system at different depths, we considered several points differently arranged within the domain at which we observed the temporal variation of each variable of interest, understanding how microorganism growth is affected by the distance from the stream-bed interface. The position of the observation points is indicated in Figure 4.4b.

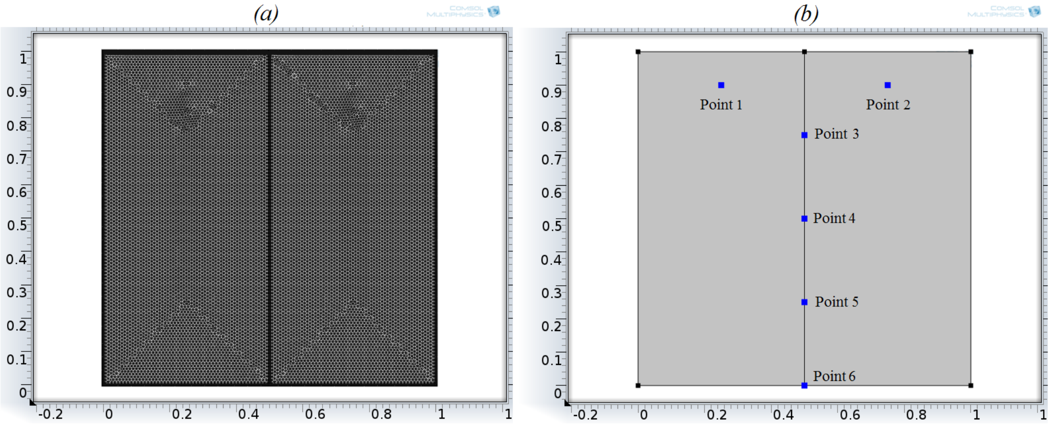

Fig. 4.4 (a) Mesh and (b) localization of observation points.

Table 4.2 Hydrodynamic Model Parameters

	Value
Mean stream velocity U (m/s)	0.7
Stream depth d (m)	0.16
Head amplitude h_0 (m)	0.017
Hydraulic conductivity K_0 (m/s)	10^{-3}
Porosity θ_s (-)	0.3
Sediment density ρ_b (kg/m ^{3})	1400
Longitudinal dispersivity α_L (m)	0.002
Transverse dispersivity α_T (m)	0.0002
Molecular diffusion coefficient D_{diff} (m ^{2}/s)	$1 \cdot 10^{-9}$

We simulated low flow conditions in a stream with coarse sediments and no DOC limitation on nitrogen metabolism. A flow with velocity $U = 0.7$ m/s and depth $d = 0.16$ m was considered. The streambed has a hydraulic conductivity $K_0 = 10^{-3}$ m/s (characteristic of well-sorted coarse sands to gravels) and a porosity $\theta_0 = 0.3$ and is covered by bedforms with wavelength $l_{dune} = 1$ m and height $h_{dune} = 0.1$ m [115]. The depth of the domain is $b = 1$ m hence the ratio between h_{dune} and b allowed us to approximate the domain as a flat bed on which

Table 4.3 Solute in-stream concentrations, initial values of biomass and reaction parameters

	Value	Unit
c_{DOC}	40	mg/l
c_{O_2}	10	mg/l
$c_{NO_3^-}$	1	mg/l
$c_{NH_4^+}$	0.05	mg/l
X_{h_0}	$5 \cdot 10^{-3}$	kg/m^3
X_{a_0}	$5 \cdot 10^{-6}$	kg/m^3
First reaction rate per unit biomass μ_{DOC}	0.001	$\frac{m^3}{mg_{X_h} \cdot d}$
Second reaction rate per unit biomass $\mu_{NH_4^+}$	0.0001	$\frac{m^6}{mg_{X_a} \cdot mg_{O_2} \cdot d}$
Decay coefficient k_{d_h}	1	$1/d$
Decay coefficient k_{d_a}	1	$1/d$
Conversion factor Y_{DOC}	0.16	$\frac{mg_{DOC}}{mg_{X_h}}$
Conversion factor $Y_{NH_4^+}$	0.16	$\frac{mg_{NH_4^+}}{mg_{X_a}}$
Biofilm density ρ_{X_h}	1	kg/m^3
Biofilm density ρ_{X_a}	1	kg/m^3

a sinusoidal head variation with amplitude $h_0 = 0.017$ m was imposed. The hydrodynamic parameters of the model are shown in Table 4.2. We assumed $\alpha_t/\alpha_l = 1/10$ (e.g., [6]), setting the longitudinal dispersivity $\alpha_l = 2 \cdot 10^{-3}$ m (e.g., a few grain diameters [14, 6]). Solute initial concentrations were set equal to the in-stream solute concentrations, shown in Table 4.3, together with the initial values of biomass and the reaction parameters. Parameters describing microbial growth and metabolism were chosen based on values reported by previous studies of heterotrophic and autotrophic biofilm growth [162, 159, 206, 136]. Notice that the values of hydraulic conductivity of riverbed sediments in conditions of absence of biomass and the values of in-stream solute concentrations (DOC and nitrogen concentrations) will be varied in Sections 4.3.2 and 4.3.3 in order to test their influence on the behavior of the system.

4.3 Results and Discussion

4.3.1 Typical behavior of the system

The temporal evolution of spatial patterns in permeability, porewater flow and biomass is shown in Figure 4.5. Steady state conditions are reached at $t = 50$ d. Sediment permeability is progressively reduced at streambed surface owing to microbial growth induced by the nitrogen, carbon, and oxygen in the exchange flow. The hydraulic conductivity progressively decreases over time (Figure 4.5, first row), eventually reaching a steady equilibrium configuration. The pattern of hyporheic exchange flow also changes substantially over time (Figure 4.5, second row) due to the clogging induced by bacterial growth, which blocks flow at depth and confines it to the near-surface zone. Figure 4.6 shows the stratification of the domain in terms of hydraulic head: the pore occlusion produces a general head loss in the domain. This head loss reflects on the flow conditions. Only the shallow portion of the domain still has high values of pressure and is therefore affected by higher flow. The results show how coupling between biofilm-induced clogging, hyporheic flow, and microbial metabolism leads to an equilibrium between permeability reduction and biomass growth characterized by sharp fronts. The homogeneous stream sediments display a strong heterogeneity at steady state, with significant hyporheic flow confined only in the shallow portion of the domain where high rates of bacterial growth occur. Therefore, the dynamics of sediment porosity, biomass concentration and hydrodynamic flow are highly related, and the bioclogging process strongly limits the extent of hyporheic exchange.

The pattern of hydraulic conductivity is very similar to the one of heterotrophic biomass, indicating that permeability is governed by the distribution of heterotrophic denitrifying organisms. The strong stratification of heterotrophic bacteria with depth in time can be observed in row 3 of Figure 4.5. Owing to faster growth rate, heterotrophic bacteria outcompete autotrophic nitrifiers (Figure 4.5 row 4) for oxygen and space, confining autotrophs to a thin layer near the sediment-water interface. In this layer, strong spatial gradients of ammonium and oxygen concentration are observed. Thus, total microbial biomass and bioclogging are both dominated by heterotrophic bacteria, and the permeability of the sediments is primarily dependent on

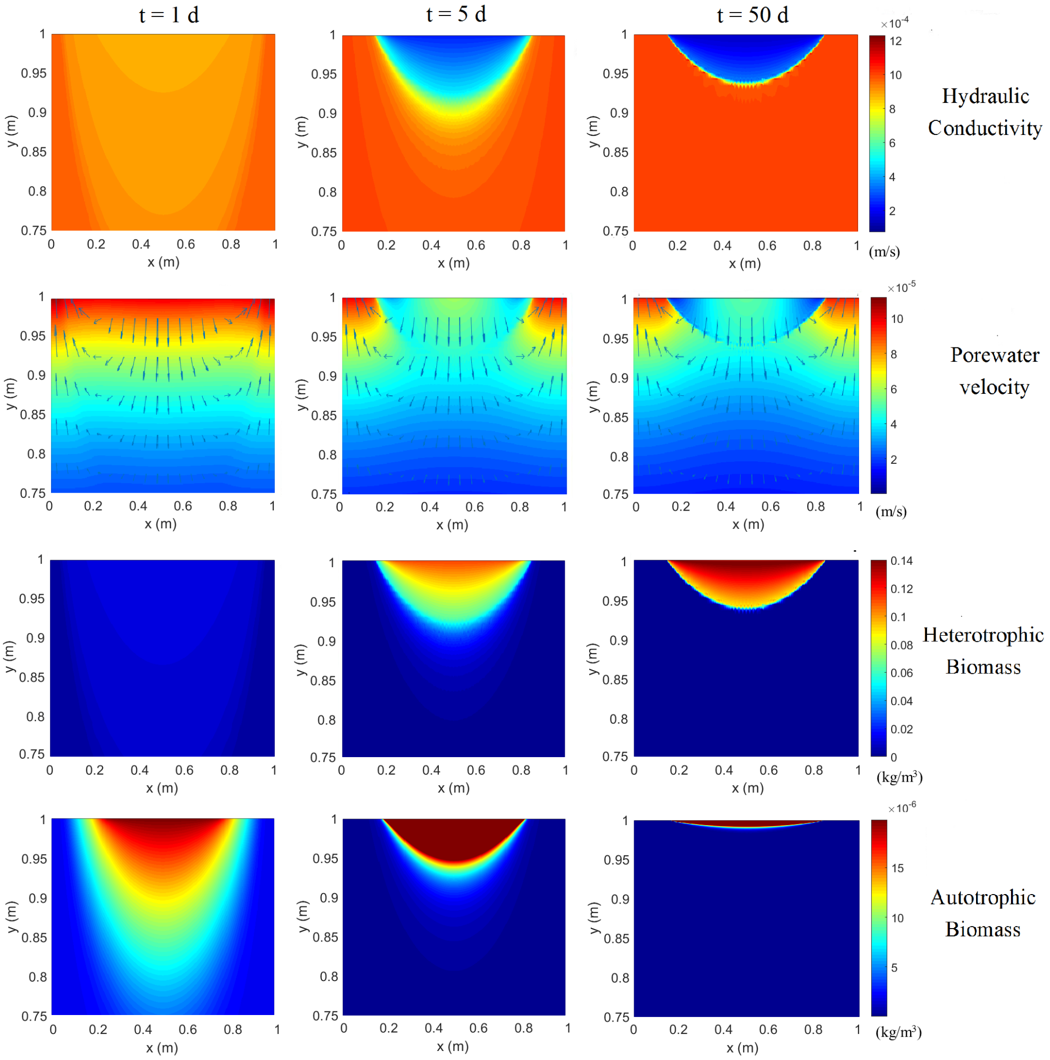

Fig. 4.5 Temporal evolution of spatial patterns in (a) permeability, (b) porewater flow and (c) heterotrophic and (d) autotrophic biomass at short time (first column, $t = 1$ d), in the transient (second column, $t = 5$ d) and at the steady state (third column, $t = 50$ d). Warmer colors indicate higher values of the variables. The arrows in panel (b) indicate the flow direction. Notice that the y-axes have been exaggerated to evidence the patterns.

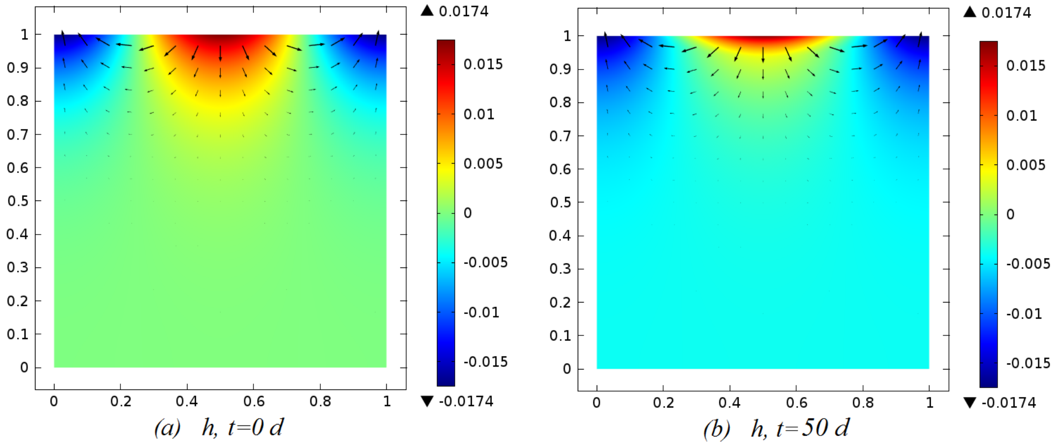

(a) h, t=0 d

(b) h, t=50 d

Fig. 4.6 Spatial distribution of the hydraulic head h (m) (a) at the initial time ($t = 0$ d) and (b) at the steady state ($t = 50$ d). The arrows indicate the direction and the intensity of the flow.

concentration of heterotrophic biomass within the pore space. The coexistence between nitrifying and denitrifing bacteria is analyzed in [161], showing that the nitrifiers are forced deeper in the biofilm. However, the clogging mechanism is not included in the system and this could explain the different behavior. At steady state (last column of Figure 4.5), two distinct regions can be identified within the sediments: a shallower zone, characterized by advective flux, rapid solute transport, and high rates of microbial metabolism, and a deeper region that is characterized by very slow flow, nutritional depletion, and little microbial growth. This shows that both penetration of nutrients and microbial metabolism in the sediments are eventually limited by bioclogging, which induces a very strong heterogeneity within the domain, restricting hyporheic exchange, nutrient transformation, and microbial metabolism to a thin region near the sediment-water interface.

For each time reported in Figure 4.5, we evaluated the total hyporheic exchange flux by integrating the downward component of Darcy velocity along the stream-bed interface ($y = 1$ m) defined as

$$q_H = \int_0^{l_{dune}} \frac{|q_y|}{2} dx. \tag{4.15}$$

Moreover, we calculated the total biomass and the total rates of consumption of DOC, oxygen, nitrate and ammonium by an integration over the whole domain.

Table 4.4 Values of porewater flow, biomass concentrations per unit stream width and reaction rates at different times.

	t = 1 d	t = 5 d	t = 50 d
q_H $[m^2/s]$	$3.16 \cdot 10^{-5}$	$2.41 \cdot 10^{-5}$	$2.24 \cdot 10^{-5}$
X_h $[kg/m]$	$4.10 \cdot 10^{-3}$	$4.15 \cdot 10^{-3}$	$3.41 \cdot 10^{-3}$
X_a $[kg/m]$	$3.38 \cdot 10^{-6}$	$4.12 \cdot 10^{-6}$	$3.32 \cdot 10^{-5}$
R_{DOC} $[kg/(m \cdot s)]$	$2.61 \cdot 10^{-7}$	$2.91 \cdot 10^{-7}$	$2.47 \cdot 10^{-7}$
R_{O_2} $[kg/(m \cdot s)]$	$2.27 \cdot 10^{-7}$	$2.42 \cdot 10^{-7}$	$2.25 \cdot 10^{-7}$
$R_{NO_3^-}$ $[kg/(m \cdot s)]$	$1.41 \cdot 10^{-8}$	$2.36 \cdot 10^{-8}$	$1.80 \cdot 10^{-8}$
$R_{NH_4^+}$ $[kg/(m \cdot s)]$	$1.79 \cdot 10^{-10}$	$3.18 \cdot 10^{-10}$	$2.41 \cdot 10^{-9}$

The results are presented in Table 4.4 and are referred to unit stream width. Hyporheic flow decreases over time as a result of an increase of microbial biomass and consequent filling of pore space in the sediments. The heterotrophic and autotrophic biomasses initially grow and then decrease. The microorganisms begin to decay when the stratification effect is more pronounced and the nutrient inflow coming from the river does not reach the deeper area of the streambed. The reaction rates show a similar behavior of the biomass, with an initial increase followed by a reduction.

Figure 4.7 represents the spatial patterns in DOC, O_2, NO_3^-, NH_4^+ and microbial biomass under steady conditions. The spatial distributions of solutes and biomass concentrations show clear stratification. Distributions of key microbial functional guilds are controlled by the extent of penetration of electron acceptors from the stream. Specifically, the spatial extent of heterotrophic and autotrophic biomass is controlled by the penetration of nitrate and oxygen, respectively. The electron donors (DOC and NH_4^+) are not fully depleted, indicating that metabolism is limited by delivery of electron acceptors (nitrate and oxygen) from the water column. Strong coupling between heterotrophic metabolism, microbial growth, and permeability causes a very sharp front at the maximal extent of nitrate penetration, which can be seen to co-occur in the patterns of heterotrophic biomass (Figure 4.7d), nitrate (Figure 4.7c), permeability (Figure 4.5 row 1), and porewater velocity (Figure 4.5, row 2). The sharp interface for heterotrophic growth co-occurs with the penetration of nitrate and not oxygen because these organisms are facultative, and oxygen

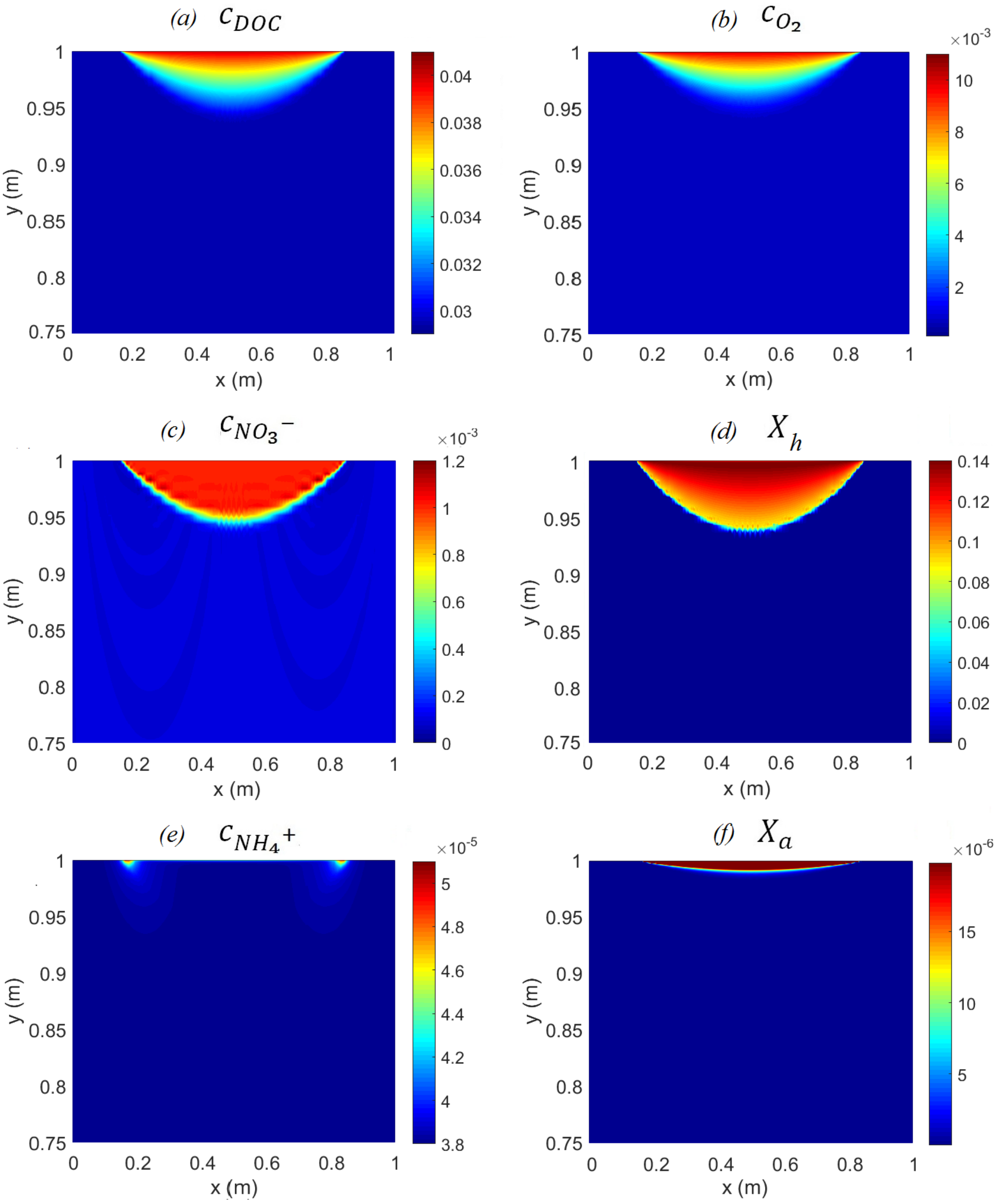

Fig. 4.7 Expanded view of the spatial distributions of microbial biomass and chemical constituents near the sediment-water interface at steady-state: (a) DOC, (b) O_2, (c) NO_3^-, (d) heterotrophic biomass, (e) NH_4^+ and (e) autotrophic biomass. All concentrations are expressed in kg/m^3

is preferentially depleted before nitrate near the sediment-water interface. Therefore, the spatial distribution of the concentrations of DOC, O_2, and NO_3^- are most strongly influenced by heterotrophs, which occlude the pores and prevent the infiltration of nutrients to deeper sediments. Conversely, the ammonium concentration is essentially controlled by autotrophic biomass, which survives only in a very thin layer near the streambed surface where the oxygen concentration is sufficient for the growth of both species. The ammonia concentration is very low in the deeper part of the domain, owing to the low porewater fluxes into this part of the domain and the rapid metabolism of ammonia in the region of high autotrophic nitrification just under the sediment-water interface.

These results suggest that an equilibrium between nutrient exchange and microbial metabolism arises from feedback among biomass growth, reduction of permeability, and reduction of nutrient fluxes. When equilibrium is reached, two distinct zones are found: first, a superficial zone with lower hydraulic conductivity since the nutrient availability is sufficient to allow the survival of a high amount of biomass, that occupies most of the porous space; secondly, a deeper zone with higher hydraulic conductivity, where the nutrient flux is low due to consumption by microorganisms in the superficial zone, and the biomass is not able to survive. Between these two areas, a transitional zone is present, where hydraulic conductivity, biomass and nutrient concentrations vary sharply. The reduction of the hydraulic conductivity in the shallower zone prevents the supply of nutrients and substrates to the deeper zone, causing the biomass to die off and eventually restoring the hydraulic conductivity of the open granular sediment bed.

The temporal evolution of solute and biomass concentrations at different depths (see Figure 4.4b for the position of the points within the domain) is illustrated in Figure 4.8. Notice that the curves relating to points 1 and 2 are overlapped since the points are at the same depth and specular respect to the center of the domain. Moreover, the assigned boundary conditions guarantee a perfect symmetry in the behavior of the system. The results in Fig. 4.8e-f show that both heterotrophic and autotrophic biomass grow up in the whole domain during the first days (1-5 days depending on the distance from the stream-bed interface). For longer times, the biomass begins to die off since the flux infiltration is prevented by pore occlusion induced by bioclogging.

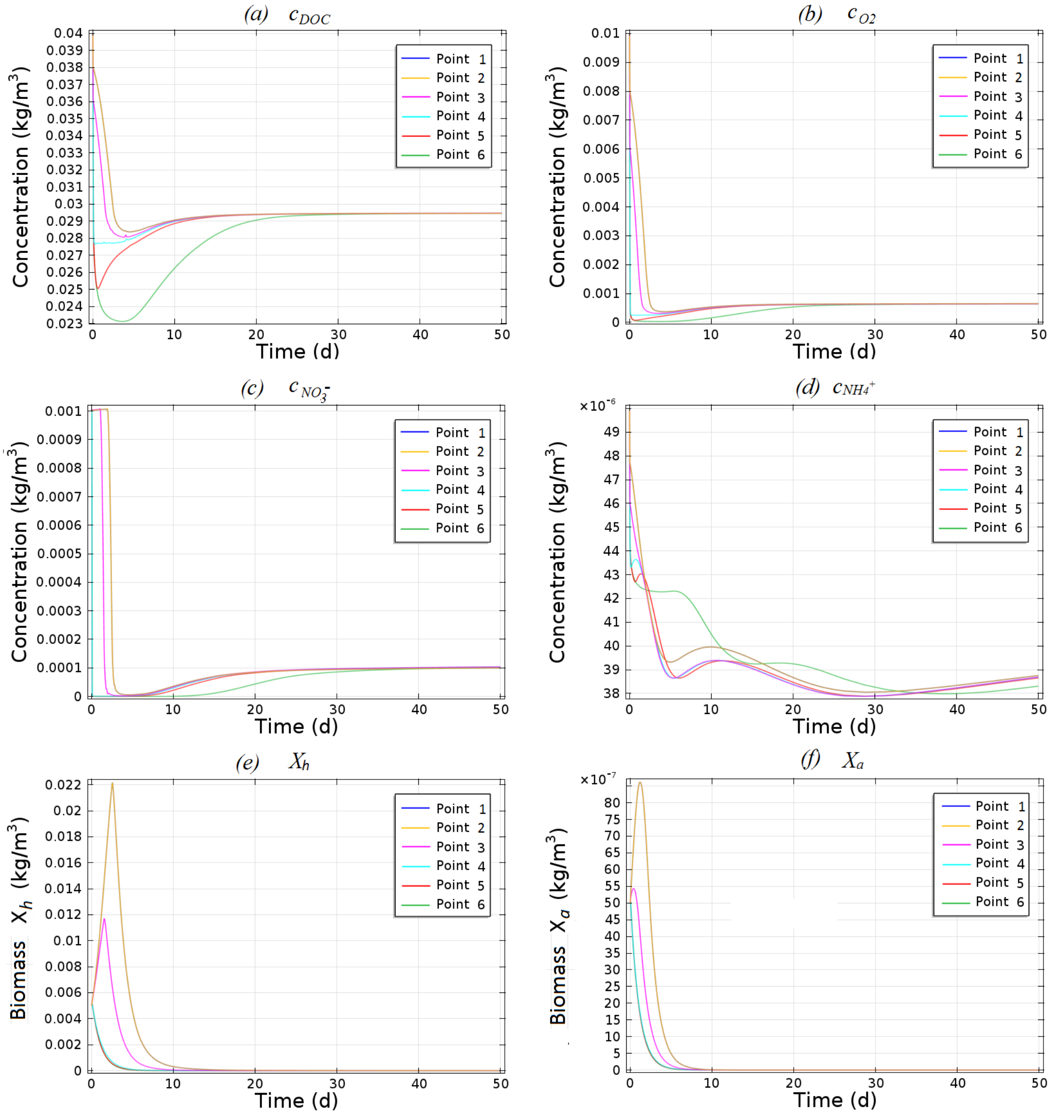

Fig. 4.8 Time behavior of solute concentrations (a) c_{DOC}, (b)c_{O_2}, (c) $c_{NO_3^-}$, (d) $c_{NH_4^+}$, (e) heterotrophic biomass X_h, and (f) autotrophic biomass X_a. The position of the points within the domain is indicated in Figure 4.4b.

The part of the domain where the biomass largely decreases is the deeper zone, farthest from the sediment-water interface, where the reduction of the flux is more pronounced, while the biomass remains alive in a thin layer near the stream-bed interface (upper part of the domain). Bacterial growth is accompanied by a notable reduction of solute concentrations (Figs. 4.8a-d) because microorganisms use the nutrients for their metabolism, synthesizing new biomass. The nutrient deficiency causes a slowdown of the metabolism, resulting in a progressive death of bacteria. The temporal variation of solute concentration is characterized by a minimum: the decrease due to bacterial growth is followed by a slight increase corresponding to microbial death. At the steady state, the concentration of nutrients reaches a stable value, lower than the initial value. Regarding nitrate concentration, this means that the streambed acts as a net sink of nitrate. Since we are considering a system with no DOC limitation on nitrogen metabolism, the denitrification can advance without restrictions, leading to nitrate reduction. The steady-state is reached at the latest in the lower part of the domain, more slowly affected by the processes that occur in the surface.

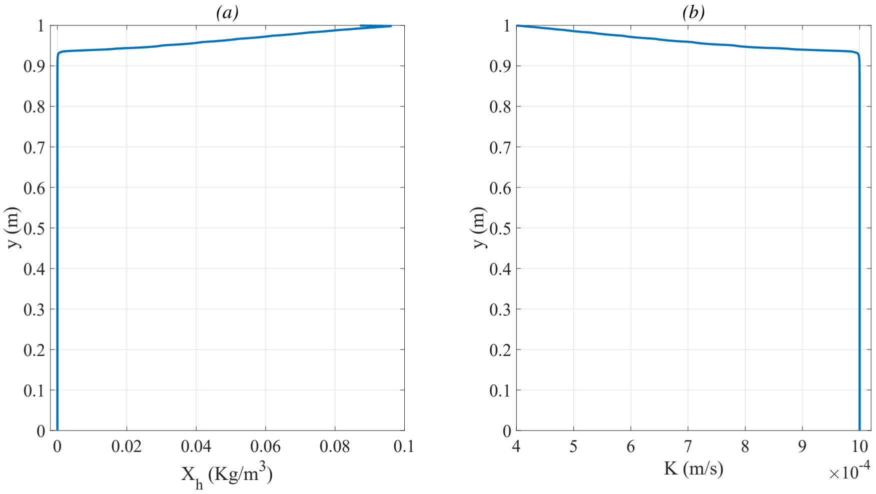

Fig. 4.9 Vertical profiles of (a) averaged heterotrophic biomass and (b) averaged hydraulic conductivity. The steady state is here considered. The heterotrophic biomass growth induces a strong reduction of the hydraulic conductivity.

The bioclogging process induced by biomass growth strongly influences the hydraulic conductivity within the riverbed. Figure 4.9 shows the average vertical profile of heterotrophic biomass together with the vertical profile of average hydraulic conductivity at the steady state – the variables are averaged along the x-direction. It is evident that the hydraulic conductivity of the sediments primarily depends on heterotrophic biomass concentration while the effect of autotrophic biomass is almost negligible because of the higher quantity of heterotrophs. This is confirmed by the vertical profiles of X_e and K that result perfectly specular, indicating the reduction of porosity (and hydraulic conductivity) due to heterotrophic growth. The X_e-profile shows the front depth of heterotrophic bacteria. It can be observed that the front is very sharp and the concentration of biomass shifts from the maximum value to the null value in few centimeters. Where the biomass grows, the hydraulic conductivity is lower than the initial value, while it increases up to the value in absence of biomass where the biomass dies off.

4.3.2 Impact of stream water quality

The role of DOC in the river ecosystem is here investigated. To this aim, we analyzed the behavior of systems with different stream DOC concentrations, implementing (i) a first set of simulations where stream DOC concentration was the only changing parameter (Cases 1-5, see Table 4.5) and (ii) a second set of simulations where the ratio between stream DOC and nitrogen concentrations was kept constant (i.e., c_{DOC} increases similarly to the previous set of simulations while the ratios $c_{NO_3^-}/c_{DOC}$ and $c_{NH_4^+}/c_{DOC}$ are constant; Cases 6-10, see Table 4.6). Stream DOC concentration varies from 21 to 40 mg/l in both sets of simulations, while NO_3^- and NH_4^+ vary from 1.0 to 1.9 mg/l and from 0.05 to 0.095 mg/l, respectively (see Table 4.5 and Table 4.6). Notice that the system analyzed in Section 4.3.1 corresponds to Case 5.

Figure 4.10 illustrates the trend of heterotrophic and autotrophic biomass concentrations as a function of stream DOC concentration. For increasing values of stream DOC concentration, the heterotrophic bacteria show a similar growing behavior up to a certain value of DOC concentration, followed by either a decay behavior (only DOC variation) or a saturation behavior (DOC and nitrogen variation). In spite of an increasing stream DOC concentration, therefore, biomass concentration undergoes a reduction or reaches a limit value. This behavior can be explained considering the bioclogging phenomenon: a greater amount of dissolved organic carbon entails a rise in heterotrophic metabolism since heterotrophic microorganisms have a higher quantity of substrate to feed and grow. However, this process is not monotonic because an excessive growth of biomass can induce an occlusion of the upper sediments, preventing the bacteria in the deeper part of the riverbed to receive the nutriment necessary to survive and, consequently, causing their death.

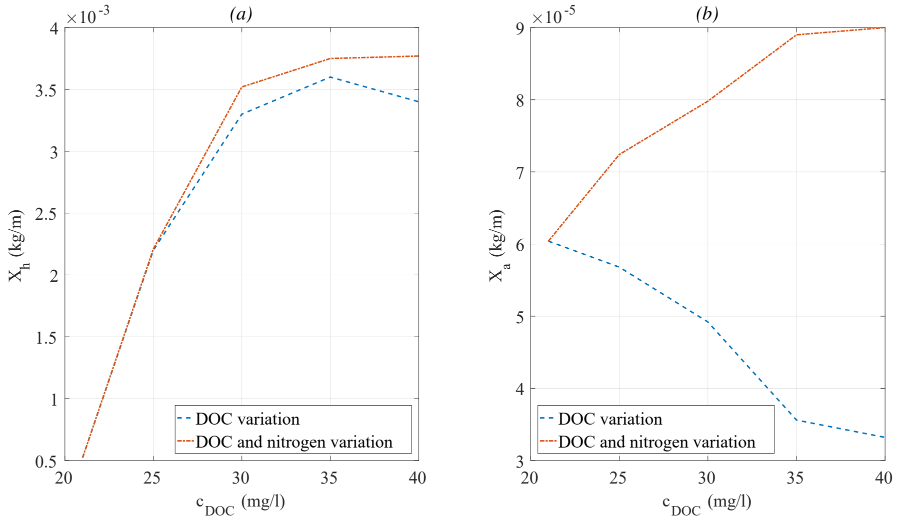

Fig. 4.10 Spatial integration values over the whole domain of (a) heterotrophic and (b) autotrophic biomass as a function of DOC concentration in the stream. The blue line is referred to only in-stream DOC variation, while the red one is referred to both in-stream DOC and nitrogen variation.

Autotrophic biomass shows a different behavior when only stream DOC concentration and both stream DOC and nitrogen concentration vary (see Figure 4.10). The concentration of autotrophic bacteria decreases for higher values of stream DOC concentration when the stream nitrogen concentration is constant and increases for higher value of stream DOC concentration when the stream nitrogen concentration is increased. In the first case, an increase in stream DOC concentration entails that the heterotrophic bacteria have available a greater amount of nutriment respect to the autotrophic bacteria and, therefore, win the competition for the occupancy of the pore space. In the second case, both heterotrophic and autotrophic biomass grow since a higher stream concentration of $c_{NH_4^+}$ improves the efficiency of the nitrification reaction, with a consequent increase of autotrophic biomass.

Table 4.5 and Table 4.6 display the values of reaction rates and biomass concentrations – integrated over the whole domain – for each value of stream DOC and nitrogen concentration at the final time (steady state). The reactions rates show the same non-monotonic behavior of the biomass concentrations, indicating more reactive bacteria for increasing stream solute concentrations until a limit value is reached. In addition, the value of front depth of heterotrophic biomass (i.e., the maximum depth of the riverbed sediments at which

Table 4.5 Areal integrated values of biomass concentrations and reactions rates per unit stream width at the steady state for systems with different DOC concentration in the stream ($K_0 = 10^{-3}$ m/s). Front depth indicates the maximum depth at which the heterotrophic biomass survives within the domain.

Case -	c_{DOC} mg/l	X_h kg/m	R_{DOC} $kg/m \cdot s$	X_a kg/m	$R_{NH_4^+}$ $kg/m \cdot s$	Front depth m
1	21	$5.22 \cdot 10^{-4}$	$3.65 \cdot 10^{-8}$	$6.04 \cdot 10^{-5}$	$4.37 \cdot 10^{-9}$	0.70
2	25	$2.20 \cdot 10^{-3}$	$1.61 \cdot 10^{-7}$	$5.68 \cdot 10^{-5}$	$4.11 \cdot 10^{-9}$	0.57
3	30	$3.30 \cdot 10^{-3}$	$2.41 \cdot 10^{-7}$	$4.92 \cdot 10^{-5}$	$3.56 \cdot 10^{-9}$	0.22
4	35	$3.60 \cdot 10^{-3}$	$2.60 \cdot 10^{-7}$	$3.56 \cdot 10^{-5}$	$2.65 \cdot 10^{-9}$	0.10
5	40	$3.41 \cdot 10^{-3}$	$2.47 \cdot 10^{-7}$	$3.32 \cdot 10^{-5}$	$2.41 \cdot 10^{-9}$	0.07

Table 4.6 Areal integrated values of biomass concentrations and reactions rates per unit stream width at the steady state for systems with different DOC and nitrogen concentrations in the stream ($K_0 = 10^{-3}$ m/s). Front depth indicates the maximum depth at which the heterotrophic biomass survives within the domain.

Case -	c_{DOC} mg/l	$c_{NO_3^-}$ mg/l	X_h kg/m	R_{DOC} $kg/(m \cdot s)$
6	21	1.0	$5.22 \cdot 10^{-4}$	$3.65 \cdot 10^{-8}$
7	25	1.2	$2.21 \cdot 10^{-3}$	$1.59 \cdot 10^{-7}$
8	30	1.4	$3.52 \cdot 10^{-3}$	$2.53 \cdot 10^{-7}$
9	35	1.7	$3.75 \cdot 10^{-3}$	$2.71 \cdot 10^{-7}$
10	40	1.9	$3.77 \cdot 10^{-3}$	$2.93 \cdot 10^{-7}$

Case -	$c_{NH_4^+}$ mg/l	X_a kg/m	$R_{NH_4^+}$ $kg/(m \cdot s)$	Front depth m
6	0.050	$6.04 \cdot 10^{-5}$	$4.37 \cdot 10^{-9}$	0.70
7	0.060	$7.24 \cdot 10^{-5}$	$5.22 \cdot 10^{-9}$	0.55
8	0.071	$7.98 \cdot 10^{-5}$	$5.75 \cdot 10^{-9}$	0.28
9	0.083	$8.90 \cdot 10^{-5}$	$6.44 \cdot 10^{-9}$	0.16
10	0.095	$9.00 \cdot 10^{-5}$	$7.31 \cdot 10^{-9}$	0.15

heterotrophic biomass receives nutriment and can survive) is reported in the tables for each case. A decreasing value of the front depth for increasing values of DOC concentration is observable, when the values of biomass concentration and reaction rates start to drop. This can be explained considering the bioclogging phenomenon, that entails a filling of the pore space due to the biomass growth with consequent reduction of the front depth. In fact, in Case 5 a reduction of heterotrophic biomass – respect to the other cases – occurs despite an increase of stream DOC concentration since the occlusion induced by bacteria in the upper part of the sediments causes the death of the biomass in the deeper sediments.

An interesting parameter to analyze the hydrodynamic aspect of bioclogging process is the total flux across the river-bed interface (Eq. 4.15), that is represented in Figure 4.11 as a function of stream DOC concentration for both sets of simulation (Cases 1-5, panel on the left, and Cases 6-10, panel on the right). In the same figure, we show the concentration, integrated over the whole domain, of heterotrophic biomass – that mainly induce the bioclogging process – in order to better investigate the dependence of hyporheic flow on the distribution of microorganisms. Both variables are made dimensionless by their initial value ($t = 0$ d). It can be observed that the exchange flux decreases when the DOC concentration increases, showing an opposite behavior respect to the biomass concentration. This can be explained considering that a greater concentration of biomass induces a greater reduction of hydraulic conductivity and, consequently, of pore water flux.

Figure 4.12 represents the comparison among the hydraulic conductivity profile along the y-direction for Cases 1-5 (panel on the left) and Cases 6-10 (panel on the right). The values of hydraulic conductivity are averaged along the x-direction and are referred to the steady state. The results show that for higher DOC concentrations the gradients of hydraulic conductivity are stronger since the biomass is confined to a thinner layer near the sediment-water interface (the front depth decreases, see Table 4.5 and Table 4.6) and, therefore, the hydraulic conductivity rapidly varies in the upper part of the domain where the microorganisms manage to survive. The value of hydraulic conductivity in conditions of absence of biomass ($K_0 = 10^{-3}$ m/s) is, therefore, reached at decreasing depths for increasing values of stream DOC concentration. The occlusion process of the upper sediments due to microbial growth, which prevents the survival of the bacteria in the deeper part of the riverbed, is evident from the strong gradients of hydraulic conductivity profiles. Results show that this effect increases for higher values of stream DOC concentration, since more heterotrophic biomass is present in a smaller portion of sediments

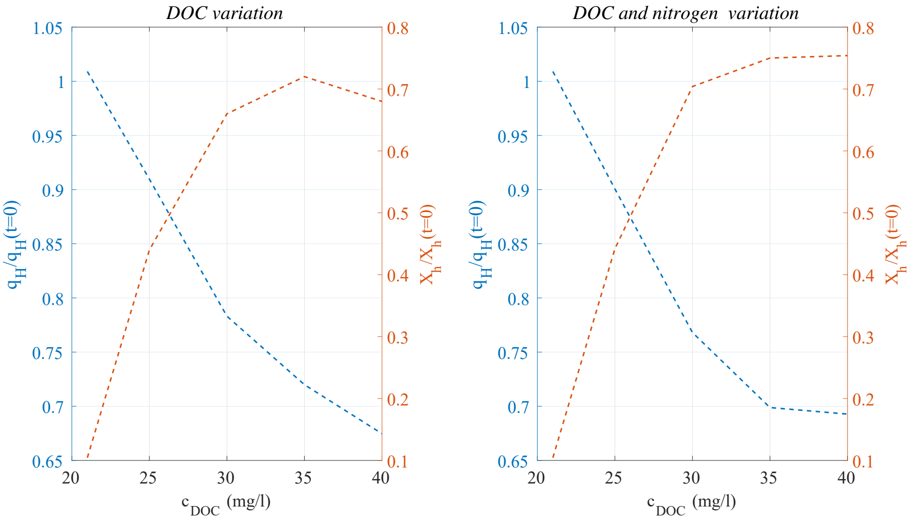

Fig. 4.11 Flux across the river-bed interface and heterotrophic biomass over the whole domain for increasing DOC concentration in the stream at the steady state. Both variables are made dimensionless by the value at the time $t = 0$ d. Panel on the left is referred to Cases 1-5 (only in-stream DOC variation) while panel on the right is referred to Cases 6-10 (in-stream DOC and nitrogen variation).

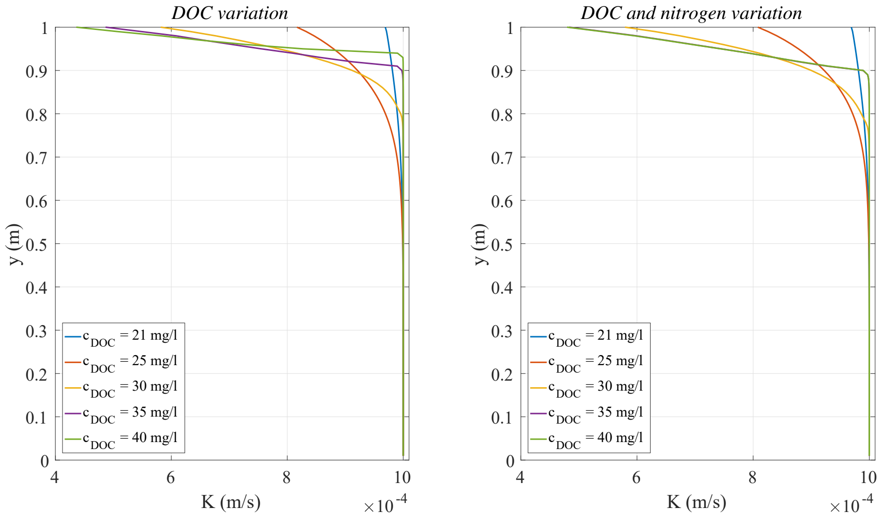

Fig. 4.12 Vertical profiles of hydraulic conductivity averaged along the horizontal direction for increasing stream DOC concentration at the steady state for only stream DOC variation (Cases 1-5, panel on the left), and for both stream DOC and nitrogen variation (Cases 6-10, panel on the right).

(higher values of heterotrophic biomass concentration and shallower portions of sediments in which the biomass can survive, see Table 4.5 and Table 4.6).

4.3.3 Impact of hydraulic conductivity

In this section, we examined the role of sediment properties, specifically permeability of the sediments, considering systems with different granulometry, i.e., different values of hydraulic conductivity in absence of biomass (K_0). Starting from the configurations with variation of stream DOC concentration (Cases 1-5 in Section 4.3.2), we simulated a system with same hydraulic and biogeochemical characteristics, but different value of K_0. Specifically, we considered a lower value of hydraulic conductivity in absence of biomass, equal to $K_0 = 10^{-4}$ m/s (riverbed composed by medium sand), with respect to the value considered in the system analyzed previously, $K_0 = 10^{-3}$ m/s (riverbed composed by coarse sands to gravel). Simulated systems with stream DOC concentrations increasing from 21 mg/l to 35 mg/l and $K_0 = 10^{-4}$ m/s are indicated here below as Cases 11-14 and represents the corresponding of Cases 1-4 with a lower value of hydraulic conductivity. Notice that the case with $c_{DOC} = 40$ mg/l, corresponding of Case 5, is missing because of convergence problems during the numerical resolution of the governing equations.

Table 4.7 Areal integrated values of biomass concentrations and reactions rates at the steady state for systems with different DOC concentration in the stream ($K_0 = 10^{-4}$ m/s). Front depth indicates the maximum depth at which the heterotrophic biomass survives within the domain.

Case -	c_{DOC} mg/l	X_h kg/m	R_{DOC} $kg/m \cdot s$	X_a kg/m	$R_{NH_4^+}$ $kg/m \cdot s$	Front depth m
11	21	$9.83 \cdot 10^{-5}$	$6.78 \cdot 10^{-9}$	$1.80 \cdot 10^{-5}$	$1.30 \cdot 10^{-9}$	0.40
12	25	$3.56 \cdot 10^{-4}$	$2.53 \cdot 10^{-8}$	$1.72 \cdot 10^{-5}$	$1.25 \cdot 10^{-9}$	0.25
13	30	$5.26 \cdot 10^{-4}$	$3.78 \cdot 10^{-7}$	$1.58 \cdot 10^{-5}$	$1.15 \cdot 10^{-9}$	0.08
14	35	$5.66 \cdot 10^{-4}$	$4.10 \cdot 10^{-7}$	$1.19 \cdot 10^{-5}$	$8.90 \cdot 10^{-10}$	0.03

Table 4.7 displays the values of reaction rates and biomass concentrations integrated over the whole domain and front depth of heterotrophic biomass in Cases 11-14. A direct comparison with the coarser-sediment system is represented in Figure 4.13, which shows the values of heterotrophic and autotrophic biomass concentration over the whole domain as a function of stream DOC concentration for the different values of hydraulic conductivity in absence of biomass. We can observe that the behavior of the system is unchanged, with

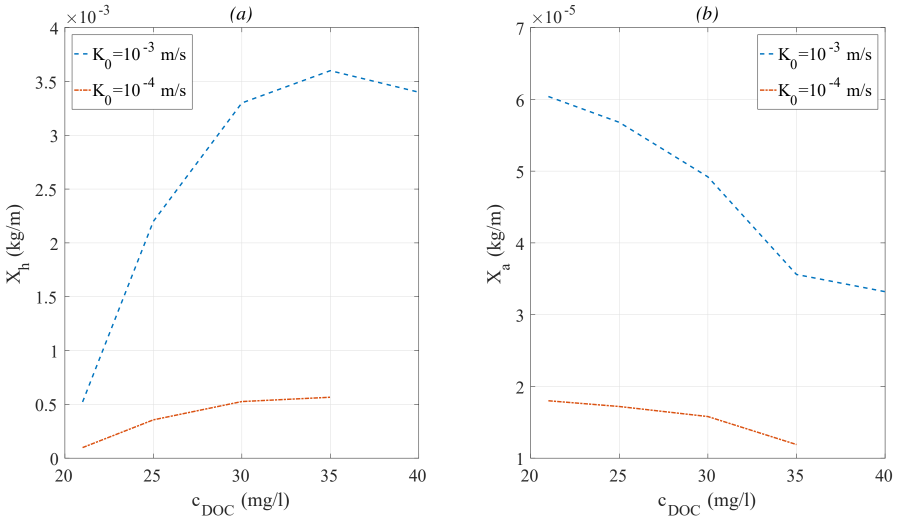

Fig. 4.13 Spatial integration values over the whole domain of (a) heterotrophic and (b) autotrophic biomass for systems with $K_0 = 10^{-3}$ m/s (blue line) and $K_0 = 10^{-4}$ m/s (red line) at the steady state.

a growth of heterotrophic biomass and a decrease of autotrophic biomass for increasing values of DOC concentration. However, the system shows lower values of biomass concentration (and reaction rates) compared to the system composed by coarser sediments. This can be explained considering that a reduction in hydraulic conductivity limits the magnitude of the exchange flux: a slower flow rate (see Figure 4.14) entails a reduction of nutrient supply and, consequently, the biomass growth decreases compared to coarser sediments.

Figure 4.15 shows the comparison of the distributions of solutes and heterotrophic biomass among the systems with different hydraulic conductivity. We considered the case with $c_{DOC} = 30$ Kg/m^3 (Cases 3 and 13). The reduction of K entails that the solute flux and the biomass are confined to a thinner region close to the water-sediment interface. The depth of the fronts is reduced but the fronts are sharper since the concentration gradients increase. Reduction of hydraulic conductivity mainly impact the dominant species (heterotrophic bacteria) since most of the pore space is occupied by these microorganisms, whose behavior is therefore more influenced by variations in sediment properties. Therefore, the results underline a marked effect of the permeability on biomass spatial distributions, with less steep and deeper fronts corresponding to higher values of permeability.

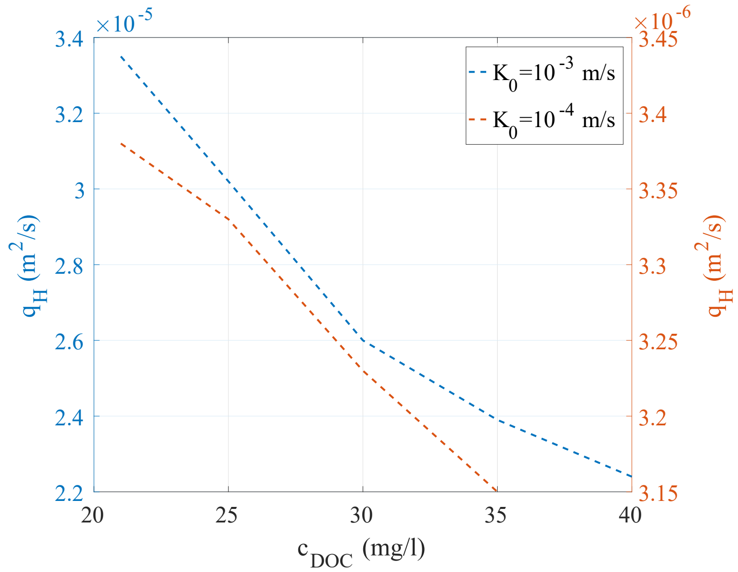

Fig. 4.14 Total hyporheic exchange flux as a function of stream DOC concentration for systems with $K_0 = 10^{-3}$ m/s (blue line) and $K_0 = 10^{-4}$ m/s (red line) at the steady state.

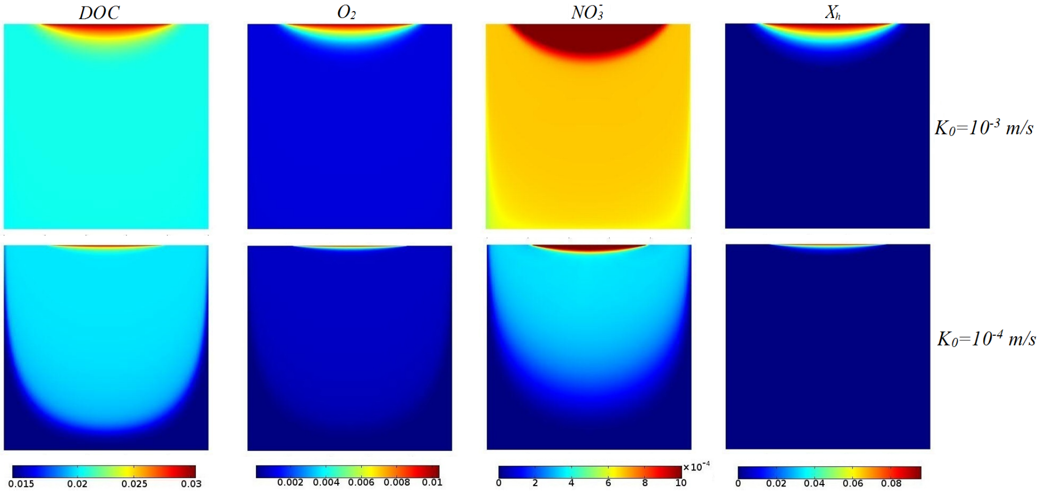

Fig. 4.15 Solute spatial distributions for $K_0 = 10^{-3}$ m/s and $K_0 = 10^{-4}$ m/s at the steady state with $c_{DOC} = 30$ Kg/m^3 (comparison between case 3 and case 13). All concentrations are expressed in Kg/m^3.

4.4 Concluding Remarks

Streambeds are biogeochemical hotspots for several reactions that influence the fate of nutrients in streams and groundwater and that are performed by microorganisms attached to the hyporheic sediments in the form of biofilms. Microbial growth and filling of hyporheic pore spaces is expected to be a generally important control on exchange flow and metabolism within the hyporheic zone. In fact, microbes exert feedbacks on water flow and nutrient transport through the process of bioclogging, i.e. the reduction of water-filled pore volume and sediment permeability caused by biofilm growth and gas production. The hydro-biogeochemical model here presented allowed us to better investigate the dynamics of bioclogging, analyzing the coupling between water fluxes, nutrient reactions, and permeability variations due to microbial growth and shading light on the impact of microbial metabolic activity on nitrogen metabolism.

Our findings show that biofilm-induced bioclogging strongly regulates physical and biogeochemical processes in the hyporheic zone since it limits both exchange flux and biogeochemical transformation rates, and controls the distribution of different types of microorganisms in many streams and rivers. Therefore, the coupling between hyporheic flow exchange, microbial growth and nutrient transport is an important process that has to be better understood in order to correctly evaluate nutrient transformation rates in the hyporheic zone and the role of streambeds in nutrient cycling. The results are interesting for the microbial ecology of biofilms, biogeochemistry of natural aquatic systems and treatment of biofilms for engineering purposes and can give a significant contribution in the fields of environmental physics.

Rivers are subject to additional, larger-scale complexities that will modulate the processes demonstrated here. In particular, hyporheic bioclogging should be compared with siltation-induced clogging and the frequency of sediment remobilization and invertebrate grazing, both of which disrupt biofilms, in order to evaluate in more detail the dynamics of hyporheic permeability, flow, and biogeochemistry in rivers.

In conclusion, the contribution of this work is to demonstrate the surprisingly large effects of physical-chemical-biological coupling processes on rates and patterns of hyporheic flow, microbial growth, and nitrogen transformation. Observations from the field are not obtained at a breadth or spatial resolution to capture these effects. This has lead to the coupling processes demonstrated here being omitted from current models for hyporheic nitrogen dynamics in rivers. Our results clearly show, based on best-available understanding of the underlying physical, chemical, and microbial processes, that coupling induced by microbial growth in hyporheic pore space strongly regulates both rates and patterns of microbial metabolism and nitrogen transformations. Prior studies have represented coupling between porewater flow and biogeochemical transformations on a stoichiometric basis, but have omitted the physical and biological consequences of the microbial growth associated with this metabolism. Our work indicates that microbial growth and resulting bioclogging are essential processes that must be included in hyporheic biogeochemical models. We expect that our results will motivate new field work to characterize co-varation in microbial biomass, metabolism, biogeochemical transformations, permeability, and porewater flow - which are not measured jointly today - and also be adopted in upscaled models for hyporheic flow and biogeochemcial dynamics in rivers.

Chapter 5

Conclusions

This conclusive chapter is structured as follows: the keys issues and the main aims addressed in the present thesis are recalled, together with the main results obtained from our analysis. Future developments and relevant limitations are then mentioned and discussed. The chapter is finally concluded with a summary table.

Conclusions and future developments. The research activity described in the present thesis deals with different aspects concerning the interactions between river water and groundwater, with particular attention to the processes occurring within the hyporheic zone. The first part of this study (Chapter 2 and Chapter 3) was devoted to investigate the impact of the regional groundwater flow system on river-groundwater interactions, in order to better understand how the water and nutrient exchange at small (i.e., of individual bedforms) scale is affected by the complexity characterizing the river-aquifer system at large (i.e., watershed) scale. Specifically, we have firstly examined how the complex geometrical shape of the water table at watershed scale impacts the spatial patterns of groundwater inflow fluxes in a river network (Chapter 2). These groundwater fluxes, in turn, influence the hyporheic exchange since the size of the hyporheic zone is significantly constrained by the upwelling of groundwater. Therefore, the aim was to provide a deeper understanding of how hyporheic processes are influenced by the ambient groundwater flow, examining the impact of groundwater structure at basin scale on the hyporheic fluxes. Subsequently, we have investigated the main controls of groundwater discharge patterns developing a numerical model of surface-groundwater interactions (Chapter 3). The aim was to identify the hydrogeological and topographic characteristics more influential in determining the alternation of gaining and losing conditions along the river network in order to improve the prediction of groundwater-river exchange fluxes.

Results have shown that the topographic complexity of a watershed induces a strong spatial variability of groundwater fluxes along a river network at watershed scale and, consequently, on hyporheic exchange at local scale. Initially, this result has been obtained considering a homogeneous and isotropic aquifer with a topography controlled groundwater table (Chapter 2): the analysis of a case study showed how, even in a (theoretical) simplified aquifer, the complex topographic structure is a direct cause of a substantial spatial variability of hyporheic exchange at basin scale. The importance of faithfully describing the topography of a basin has been confirmed through a refined numerical model developed in Chapter 3. In fact, it has been shown that the geological characteristics of the aquifer have the major impact on controlling of river-aquifer exchange flux patterns, followed by the topographic factors of the catchment, while the influence of other hydrological and hydraulic factors has been demonstrated to be lower. The understanding of the factors that mostly influence the spatial patterns of groundwater discharge and recharge over the river network is an important result for the development of a model able to correctly predict the intensity of groundwater fluxes along the river corridor. In fact, estimating the variability of these fluxes is essential in order to evaluate how stream-groundwater interactions affect the removal of nutrients and pollutants in fluvial sediments. Coupling the prediction of groundwater discharge along a river network with a watershed-scale framework of hyporheic exchange and nutrient transport will be a future step of the work developed in this part of the thesis in order to evaluate the influence of groundwater discharge on nutrient removal.

In the second part of my work (Chapter 4), the focus has been placed on small-scale biogeochemical processes occurring within the hyporheic zone and, more in detail, on bioclogging effects on nutrient dynamics. In order to provide an improved understanding of this effect, a two-dimensional hydrobiogeochemical model has been developed. In the present thesis, bioclogging effects have thus been investigated theoretically through numerical simulations carried out for systems with different in-stream nutrient concentrations and different permeability of streambed sediments. The model has considered two communities of microorganisms (heterotrophs and autotrophs), analyzing the competition for pore space and oxygen consumption among them. Results have shown how the bioclogging process is able to induce a strong spatial stratification of the riverbed sediments in terms of sediment permeability, nutrient supply and microorganisms abundance. The occupancy of the pore space due to biomass growth generates an occlusion effect, which prevents the supply of nutrients and substrates to the deeper zone of the riverbed sediments, causing the biomass to die off. Moreover, results have shown that the bioclogging process is primarily induced by the growth of heterotrophic bacteria within pore space, which win the competition for pore space and oxygen consumption against autotrophic bacteria, confining them to a thin upper layer near the riverbed interface. This result differs from the results obtained in previous works (i.e., [161]), where the clogging mechanism has not been included. Therefore, the distribution of nitrifying/denitrifying microorganisms within the hyporheic zone has been shown to be strongly affected by the coupling between bioclogging and reactive processes. This model makes possible to obtain predictive results on the limitation of exchange flux and biogeochemical transformation rates within hyporheic zone induced by bioclogging and this is important considering the lack of field data. A more detailed characterization of real riverbed sediments (i.e., the inclusion of a spatial variation of grain size and pore space) could shed light on additional zonation effects due to the existence of preferential flow pathways.

Main contributions. The main steps forward made through this work in the understanding of GW-SW interactions and the main conclusions can be summarized as follows:

- the effect of the upwelling component of regional groundwater flow was considered in a more detailed way respect to other similar studies, including spatial variations of groundwater discharge along the river corridor (Chapter 2). In other works, in fact, the potential impact of the ambient groundwater flow on hyporheic exchange was investigated adopting a simplified model to evaluate the across-valley hydraulic head gradient and considering a constant value of groundwater discharge in space [22, 85, 4];

- it was demonstrated that the geometrical complexity of the topographic structure is alone the cause of a fragmentation of the hyporeic corridor induced by groundwater discharge at the basin scale. Moreover, the lack of autocorrelation of the vertical exchange velocity along the river was evidenced (Chapter 2);

- the groundwater in the upper reaches of the watershed seems to be only indirectly connected to the main stem of the river network through surface water and this result indicates that pollution issues associated with groundwater may be addressed at the surface before connecting with downstream waters (Chapter 2);

- a similarity between the structure of groundwater discharge patterns under different hydrogeological conditions has been evidenced, showing that a detailed description of some hydrological factors has a marginal effect on the structure of subsurface flow patterns (Chapter 3). Specifically, a detailed description of the watershed geology has been proven to be essential to correctly model GW-SW exchange patterns along the river corridor. Differently, the spatial resolution of the landscape DEM has moderate influence on GW discharge essentially because it determines the spatial structure of the river network. Finally, spatial variations in precipitation (and, consequently, in GW recharge) and in river characteristics (width, depth) have a minor influence on GW discharge patterns.

- new awareness of the effects of bioclogging on coupled microbial metabolism and nitrogen transformations in hyporheic exchange was achieved and the lack about coupled physical clogging and reactive processes was, at least partially, filled. In fact, the analysis of the biomass growth in filling pore space and of the feedback on rates and patterns of hyporheic exchange flow was coupled with the effects of hyporheic exchange flow in stimulating microbial metabolism and biogeochemical processes (Chapter 4). While prior studies have focused on capturing the influence of GW-SW exchange on the main microbial transformations of nutrients [6, 218], examining nitrogen redox patterns that occur during hyporheic exchange, no prior studies have examined the full coupling between hyporheic flow, metabolism (aerobic and anaerobic), nitrogen transformation, and bioclogging. This type of coupling is known to be extremely important in natural streams and rivers, but it is almost completely unexplored because prior experimental, theoretical, and numerical studies have primarily focused on flow-reaction coupling from the biogeochemistry perspective.

Limitations. The present modeling-based study is limited by the poor amount of calibration data. Concerning the groundwater models (Chapter 2 and Chapter 3), a through calibration would require to know the groundwater head in some points of the basin, in order to verify the correctness of the estimated phreatic surface. Lack of proper site characterization may result in a model calibrated to a set of conditions that are not representative of actual field conditions. However, the sensitivity analysis shown in Chapter 3 is based on a comparison between different models implemented under the same general conditions and, thus, the lack of calibration data does not affect the main results of the analysis. This comparison evidences a stability in exchange flux patterns, indicating the non-dependence of these patterns by some factors. Moreover, most of the presented results are related to the structure of the patterns of exchange fluxes and not to the specific quantitative values. Therefore, it is plausible to assume that these patterns would not suddenly change due to some inaccuracies in the estimation of the water table. Concerning the biogeochemical model (Chapter 4), no detailed *in situ* data are available on spatial distributions of biofilm biomass at the pore scale in the hyporheic zone, making the modeling necessary. The lack of data entails that there is little direct support to this fairly general parameterization of the mechanism employed for porosity reduction with biofilm growth. For this reason, a simplified modeling is adopted, similarly to what is done for filtration problems. Our model is, in fact, based on a relatively simple mechanism to model bacteria growth and permeability reduction caused by bioclogging in porous media. However, we have constructed the best possible parsimonious model based on state-of-the-art information on biofilm growth models, bioclogging models, and hyporheic reactive transport models. Each model component is parameterized based on best-available data from the fields of biofilm microbiology, clogging of porous media, and hyporheic exchange studies.

An additional uncontrolled and neglected factor is the temporal variability of the groundwater level, that could be analyzed considering a temporal variable pattern of the groundwater recharge. In fact, dry-wet years and seasons supposedly show a different behavior regarding to groundwater-surface water interactions. A rapid change in river stage in response to common environmental influences (e.g., storm, rain, wind, evapotranspiration) can result in a temporary reversal of vertical hydraulic gradient and, consequently, flow direction. Temporal changes in regional groundwater flow pathways over long time scales may have a significant impact on the location of upwelling and downwelling areas; at short timescales, diurnal fluctuations in hydraulic heads due to evapotranspiration processes can emerge. A temporal extension of the groundwater model study could be very useful in order to characterize the temporal variability and to identify the resulting effects on geochemical and biological processes at different time scales.

In this work, the estimation of hyporheic exchange flux is based on the bedform-induced pumping model proposed by Elliott and Brooks [63, 62], both in Chapter 2 and in Chapter 4. This model considers a single bedform (dune or ripple) and assumes a sinusoidal head distribution based on empirical observations [65] and resulting from velocity interactions with the bedforms. This spatially explicit physically based approach had the advantage of allowing predictions from a priori parameters [181]. Conversely, this approach only includes one scale of topography, while natural topographies tend to be fractal, and does not allow for variations within the system, or three-dimensional variations in the induced velocity fields. This means the estimated hyporheic exchange fluxes does not integrate the three dimensional exchange induced by larger-scale topography such as bars and meanders. Moreover, Stonedahl *et al.* [183] demonstrated that the volume of water exchanged and the distributions of hyporheic residence times resulting from various scales of topographic features are close to, but not linearly additive, and bedforms typically contributed more to hyporheic exchange than larger features. Therefore, it is assumable that the preponderant contribution to exchange rate is here estimated. However, future work should certainly be oriented toward including a spectral scaling approach for a more generalized analysis of topography-induced stream-aquifer exchange.

Summary. A summary table showing the main points of each chapter has been include as epilogue of the present work.

Summary

	Originality	Achievements	Limits	Future research
Chapter 2	This work goes beyond the traditional approach to quantify hyporheic fluxes where the ambient GW field is omitted or included in a simplified manner - often as a spatially constant prescribed boundary condition to the small scale model - and the effects of the regional fluxes are simply described as gaining, neutral or losing conditions. An improved description, where the ambient GW flow field is spatially varying based on the regional topography and geological conditions, was introduced.	High spatial heterogeneity in groundwater discharge to rivers induced by topography structure has been evidenced, together with no meaningful spatial correlation between vertical velocities. As a result, it is not possible to predict the scale of variation for groundwater recharge and discharge, which could be modeled stochastically.	Methodology applicable only for some typologies of basins. Strong hydrogeological simplifications.	Inclusion of hyporheic exchange fluxes induced by other fluvial morphological features (i.e., bars, meanders, riffle and pools, etc.).
Chapter 3	Previous work did not consider x, y and z components that this work (also the model in Chapter 2) included. Moreover, magnitudes, directions and spatial distributions of river-aquifer exchange fluxes were modeled including some complexity factors neglected in previous studies (and in our previous study).	A sensitivity analysis illustrated the primary characteristics that drive variations in GW exchanges resulting in gaining and losing conditions. Spatial variation in subsurface conductivity and the resolution of heterogeneity of topography resulted the two most important factors affecting the magnitude and distribution of river network gains and losses.	Stationary system. Insufficient calibration data.	Introduction of temporal variability of phreatic surface and, consequently, of exchange fluxes. Integration of the GW model with a watershed-scale framework of nutrient transport. Inclusion of heterogeneity in streambed material as part of the sensitivity study.
Chapter 4	Physical-chemical-biological coupling between microbial metabolism with hyporheic porewater flow and biogeochemistry (such as the effects of spatial patterns of microbial growth driving bioclogging, and feedbacks on patterns of metabolism and redox conditions) was not quantitatively evaluated in prior studies, which focused on flow-reaction coupling from the biogeochemistry perspective.	Hyporheic flow and microbial transformation rates resulted strongly limited due to bioclogging of streambed. The extent of penetration of oxygen, nutrients, and labile carbon from the stream proved to be controlled by distribution of metabolic activity within biofilms.	Lack of field data and applicable lab methodology. Homogeneous riverbed.	More detailed and updated characterization of real sediments (heterogeneity). Introducing cooperation processes between microbial species.

References

[1] P. Ala-aho, P. M. Rossi, E. Isokangas, and B. Kløve. Fully integrated surface–subsurface flow modelling of groundwater–lake interaction in an esker aquifer: Model verification with stable isotopes and airborne thermal imaging. *Journal of Hydrology*, 522:391–406, 2015.

[2] J. K. Anderson, S. M. Wondzell, M. N. Gooseff, and R. Haggerty. Patterns in stream longitudinal profiles and implications for hyporheic exchange flow at the HJ Andrews Experimental Forest, Oregon, usa. *Hydrological Processes*, 19(15):2931–2949, 2005.

[3] E. Angelier. *Recherches écologiques et biogéographiques sur la faune des sables submergés.* PhD thesis, Centre national de la Recherche Scientifique, 1953.

[4] M. Azizian, F. Boano, P. L. Cook, R. L. Detwiler, M. A. Rippy, and S. B. Grant. Ambient groundwater flow diminishes nitrate processing in the hyporheic zone of streams. *Water Resources Research*, 53(5):3941–3967, 2017.

[5] L. Bardini. *Impact of hyporheic zones on nutrient dynamics.* PhD thesis, Politecnico di Torino, 2013.

[6] L. Bardini, F. Boano, M. Cardenas, R. Revelli, and L. Ridolfi. Nutrient cycling in bedform induced hyporheic zones. *Geochimica et Cosmochimica Acta*, 84:47–61, 2012.

[7] L. Bardini, F. Boano, M. Cardenas, A. Sawyer, R. Revelli, and L. Ridolfi. Small-scale permeability heterogeneity has negligible effects on nutrient cycling in streambeds. *Geophysical Research Letters*, 40(6):1118–1122, 2013.

[8] R. Barthel and S. Banzhaf. Groundwater and surface water interaction at the regional-scale–a review with focus on regional integrated models. *Water Resources Management*, 30(1):1–32, 2016.

[9] S. Bartsch, S. Frei, M. Ruidisch, C. L. Shope, S. Peiffer, B. Kim, and J. H. Fleckenstein. River-aquifer exchange fluxes under monsoonal climate conditions. *Journal of Hydrology*, 509:601–614, 2014.

[10] O. Batelaan, F. De Smedt, and L. Triest. Regional groundwater discharge: phreatophyte mapping, groundwater modelling and impact analysis of land-use change. *Journal of Hydrology*, 275(1):86–108, 2003.

[11] T. J. Battin, K. Besemer, M. M. Bengtsson, A. M. Romani, and A. I. Packmann. The ecology and biogeochemistry of stream biofilms. *Nature Reviews Microbiology*, 14(4):251–263, 2016.

[12] T. J. Battin, L. A. Kaplan, S. Findlay, C. S. Hopkinson, E. Marti, A. I. Packman, J. D. Newbold, and F. Sabater. Biophysical controls on organic carbon fluxes in fluvial networks. *Nature Geoscience*, 1(2):95–100, 2008.

[13] P. Baveye, P. Vandevivere, B. L. Hoyle, P. C. DeLeo, and D. S. de Lozada. Environmental impact and mechanisms of the biological clogging of saturated soils and aquifer materials. *Critical reviews in environmental science and technology*, 28(2):123–191, 1998.

[14] J. Bear. *Dynamics of fluids in porous media.* Dover, New York, 1988.

[15] J. Bear and A.-D. Cheng. *Modeling groundwater flow and contaminant transport*, volume 23. Springer Science & Business Media, 2010.

[16] J. Bear and A. Verruijt. *Modeling groundwater flow and pollution.* D. Reidel Publishing Company, 1992.

[17] K. E. Bencala. Interactions of solutes and streambed sediment: 2. a dynamic analysis of coupled hydrologic and chemical processes that determine solute transport. *Water Resources Research*, 20(12):1804–1814, 1984.

[18] K. E. Bencala and R. A. Walters. Simulation of solute transport in a mountain pool-and-riffle stream: A transient storage model. *Water Resources Research*, 19(3):718–724, 1983.

[19] F. Boano, A. Demaria, R. Revelli, and L. Ridolfi. Biogeochemical zonation due to intrameander hyporheic flow. *Water resources research*, 46(2), 2010.

[20] F. Boano, J. W. Harvey, A. Marion, A. I. Packman, R. Revelli, L. Ridolfi, and A. Wörman. Hyporheic flow and transport processes: Mechanisms, models, and biogeochemical implications. *Reviews of Geophysics*, 52(4):603–679, 2014.

[21] F. Boano, R. Revelli, and L. Ridolfi. Bedform-induced hyporheic exchange with unsteady flows. *Advances in water resources*, 30(1):148–156, 2007.

[22] F. Boano, R. Revelli, and L. Ridolfi. Reduction of the hyporheic zone volume due to the stream-aquifer interaction. *Geophysical Research Letters*, 35(9), 2008.

[23] F. Boano, R. Revelli, and L. Ridolfi. Quantifying the impact of groundwater discharge on the surface–subsurface exchange. *Hydrological processes*, 23(15):2108–2116, 2009.

[24] BoM. Annual climate summary. Technical report, Australian Government - Bureau of Meteorology, 2010.

[25] A. J. Boulton, S. Findlay, P. Marmonier, E. H. Stanley, and H. M. Valett. The functional significance of the hyporheic zone in streams and rivers. *Annual Review of Ecology and Systematics*, pages 59–81, 1998.

[26] H. Bouwer and T. Maddock III. Making sense of the interactions between groundwater and streamflow: Lessons for water masters and adjudicators. *Rivers*, 6(1):19–31, 1997.

[27] M. A. Briggs, L. K. Lautz, and D. K. Hare. Residence time control on hot moments of net nitrate production and uptake in the hyporheic zone. *Hydrological processes*, 28(11):3741–3751, 2014.

[28] M. A. Briggs, L. K. Lautz, J. M. McKenzie, R. P. Gordon, and D. K. Hare. Using high-resolution distributed temperature sensing to quantify spatial and temporal variability in vertical hyporheic flux. *Water Resources Research*, 48(2), 2012.

[29] A. Brovelli, F. Malaguerra, and D. Barry. Bioclogging in porous media: Model development and sensitivity to initial conditions. *Environmental Modelling & Software*, 24(5):611–626, 2009.

[30] M. Brunke and T. Gonser. The ecological significance of exchange processes between rivers and groundwater. *Freshwater biology*, 37(1):1–33, 1997.

[31] P. Brunner, C. T. Simmons, P. G. Cook, and R. Therrien. Modeling surface water-groundwater interaction with modflow: some considerations. *Groundwater*, 48(2):174–180, 2010.

[32] S. Buss, Z. Cai, B. Cardenas, J. Fleckenstein, D. Hannah, K. Heppell, P. Hulme, T. Ibrahim, D. Kaeser, S. Krause, et al. *The hyporheic handbook: a handbook on the groundwater-surfacewater interface and hyporheic zone for environmental managers.* Environment Agency, 2009.

[33] M. B. Cardenas. Potential contribution of topography-driven regional groundwater flow to fractal stream chemistry: Residence time distribution analysis of Tóth flow. *Geophysical Research Letters*, 34(5), 2007.

[34] M. B. Cardenas. Surface water-groundwater interface geomorphology leads to scaling of residence times. *Geophysical Research Letters*, 35(8), 2008.

[35] M. B. Cardenas. Stream-aquifer interactions and hyporheic exchange in gaining and losing sinuous streams. *Water Resources Research*, 45(6), 2009.

[36] M. B. Cardenas and J. Wilson. The influence of ambient groundwater discharge on exchange zones induced by current–bedform interactions. *Journal of Hydrology*, 331(1):103–109, 2006.

[37] M. B. Cardenas and J. L. Wilson. Dunes, turbulent eddies, and interfacial exchange with permeable sediments. *Water Resources Research*, 43(8), 2007.

[38] M. B. Cardenas and J. L. Wilson. Exchange across a sediment–water interface with ambient groundwater discharge. *Journal of Hydrology*, 346(3):69–80, 2007.

[39] A. Caruso, F. Boano, L. Ridolfi, D. L. Chopp, and A. Packman. Biofilm-induced bioclogging produces sharp interfaces in hyporheic flow, redox conditions, andmicrobial community structure. *GEOPHYSICAL RESEARCH LETTERS*, 44(10):4917–4925, 2017.

[40] A. Caruso, L. Ridolfi, and F. Boano. Impact of watershed topography on hyporheic exchange. *Advances in Water Resources*, 94:400–411, 2016.

[41] F. Chapelle. *Ground-water microbiology and geochemistry.* John Wiley & Sons, 2001.

[42] P. A. Chappuis. *Eine neue methode zur Untersuchung der Grundwasserfauna.* Universitas Francisco-Josephina, 1942.

[43] C. Chen, B. L. Lau, J.-F. Gaillard, and A. I. Packman. Temporal evolution of pore geometry, fluid flow, and solute transport resulting from colloid deposition. *Water resources research*, 45(6), 2009.

[44] C. Chen, A. I. Packman, and J.-F. Gaillard. Pore-scale analysis of permeability reduction resulting from colloid deposition. *Geophysical Research Letters*, 35(7), 2008.

[45] C. Chen, A. I. Packman, D. Zhang, and J.-F. Gaillard. A multi-scale investigation of interfacial transport, pore fluid flow, and fine particle deposition in a sediment bed. *Water Resources Research*, 46(11):W11560, 2010.

[46] T. Clement, B. Hooker, and R. Skeen. Macroscopic models for predicting changes in saturated porous media properties caused by microbial growth. *Ground Water*, 34(5):934–942, 1996.

[47] A. COMSOL. Comsol multiphysics user's guide, version 4.2. *COMSOL AB: Burlington, MA*, 2008.

[48] A. Costa. Permeability-porosity relationship: A reexamination of the kozeny-carman equation based on a fractal pore-space geometry assumption. *Geophysical research letters*, 33(2), 2006.

[49] K. Z. Coyte, H. Tabuteau, E. A. Gaffney, K. R. Foster, and W. M. Durham. Microbial competition in porous environments can select against rapid biofilm growth. *Proceedings of the National Academy of Sciences*, 114(2):E161–E170, 2017.

[50] M. Cuthbert, R. Mackay, V. Durand, M.-F. Aller, R. Greswell, and M. Rivett. Impacts of river bed gas on the hydraulic and thermal dynamics of the hyporheic zone. *Advances in Water Resources*, 33(11):1347–1358, 2010.

[51] P. Dahlhaus, D. Heislers, D. Brewin, J. Leonard, P. Dyson, and D. Cherry. Port phillip and westernport groundwater flow systems. *Port Phillip and Westernport Catchment Management Authority, Melbourne, Victoria*, 2004.

[52] C. N. Dahm, N. B. Grimm, P. Marmonier, H. M. Valett, and P. Vervier. Nutrient dynamics at the interface between surface waters and groundwaters. *Freshwater Biology*, 40(3):427–451, 1998.

[53] D. de Beer and P. Stoodley. Relation between the structure of an aerobic biofilm and transport phenomena. *Water Science and Technology*, 32(8):11–18, 1995.

[54] DES. Models of the catchment analysis tool (cat1d version 22). Technical manual, Victorian Government Department of Sustainability and Environment Melbourne, 2007.

[55] DES. Pump test database project. Technical report, Victorian Government Department of Sustainability and Environment Melbourne, 2011.

[56] DES. Safe dataset compilation – method report. Method report, Victorian Government Department of Sustainability and Environment Melbourne, 2012.

[57] DES. Victorian aquifer framework: Updates for seamless mapping of aquifer surfaces. Report, Victorian Government Department of Sustainability and Environment Melbourne, 2012.

[58] S. L. Desilets, T. Ferré, and P. A. Troch. Effects of stream-aquifer disconnection on local flow patterns. *Water Resources Research*, 44(9), 2008.

[59] J. Duff, B. Toner, A. Jackman, R. Avanzino, and F. Triska. Determination of groundwater discharge into a sand and gravel bottom river: A comparison of chloride dilution and seepage meter techniques. *PROCEEDINGS-INTERNATIONAL ASSOCIATION OF THEORETICAL AND APPLIED LIMNOLOGY*, 27(1):406–411, 2000.

[60] EarthTech. Maribyrnong river environmental flow determination – site paper. Report for Melbourne Water, EarthTech, 2005.

[61] J. M. Ebeling, M. B. Timmons, and J. Bisogni. Engineering analysis of the stoichiometry of photoautotrophic, autotrophic, and heterotrophic removal of ammonia–nitrogen in aquaculture systems. *Aquaculture*, 257(1):346–358, 2006.

[62] A. H. Elliott and N. H. Brooks. Transfer of nonsorbing solutes to a streambed with bed forms: Laboratory experiments. *Water Resources Research*, 33(1):137–151, 1997.

[63] A. H. Elliott and N. H. Brooks. Transfer of nonsorbing solutes to a streambed with bed forms: Theory. *Water Resources Research*, 33(1):123–136, 1997.

[64] P. A. Ellis, R. Mackay, and M. O. Rivett. Quantifying urban river–aquifer fluid exchange processes: a multi-scale problem. *Journal of contaminant hydrology*, 91(1):58–80, 2007.

[65] H. M. Fehlman. *Resistance components and velocity distributions of open channel flows over bedforms*. PhD thesis, Colorado State University, 1985.

[66] A. Fernald, V. Tidwell, J. Rivera, S. Rodríguez, S. Guldan, C. Steele, C. Ochoa, B. Hurd, M. Ortiz, K. Boykin, et al. Modeling sustainability of water, environment, livelihood, and culture in traditional irrigation communities and their linked watersheds. *Sustainability*, 4(11):2998–3022, 2012.

[67] S. Findlay. Importance of surface-subsurface exchange in stream ecosystems: The hyporheic zone. *Limnology and oceanography*, 40(1):159–164, 1995.

[68] J. H. Fleckenstein, S. Krause, D. M. Hannah, and F. Boano. Groundwater-surface water interactions: New methods and models to improve understanding of processes and dynamics. *Advances in Water Resources*, 33(11):1291–1295, 2010.

[69] H.-C. Flemming, J. Wingender, U. Szewzyk, P. Steinberg, S. A. Rice, and S. Kjelleberg. Biofilms: an emergent form of bacterial life. *Nature Reviews Microbiology*, 14(9):563–575, 2016.

[70] N. Flipo, A. Mouhri, B. Labarthe, S. Biancamaria, A. Rivière, and P. Weill. Continental hydrosystem modelling: the concept of nested stream–aquifer interfaces. *Hydrology and Earth System Sciences*, 18(8):3121–3149, 2014.

[71] A. Fox, F. Boano, and S. Arnon. Impact of losing and gaining streamflow conditions on hyporheic exchange fluxes induced by dune-shaped bed forms. *Water Resources Research*, 50(3):1895–1907, 2014.

[72] G. Fox. Improving modflow's river package for unsaturated stream/aquifer flow. *Proc. 23 rd AGU Hydrol. Days, 31 March 31 2 April*, pages 56–67, 2003.

[73] R. A. Freeze. Three-dimensional, transient, saturated-unsaturated flow in a groundwater basin. *Water Resources Research*, 7(2):347–366, 1971.

[74] R. A. Freeze and P. Witherspoon. Theoretical analysis of regional groundwater flow: 2. effect of water-table configuration and subsurface permeability variation. *Water Resources Research*, 3(2):623–634, 1967.

[75] R. A. Freeze and P. Witherspoon. Theoretical analysis of regional ground water flow: 3. quantitative interpretations. *Water Resources Research*, 4(3):581–590, 1968.

[76] R. A. Freeze and P. A. Witherspoon. Theoretical analysis of regional groundwater flow: 1. analytical and numerical solutions to the mathematical model. *Water Resources Research*, 2(4):641–656, 1966.

[77] C. C. Fuller and J. W. Harvey. Reactive uptake of trace metals in the hyporheic zone of a mining-contaminated stream, pinal creek, arizona. *Environmental Science & Technology*, 34(7):1150–1155, 2000.

[78] C. Gandy, J. Smith, and A. Jarvis. Attenuation of mining-derived pollutants in the hyporheic zone: A review. *Science of the Total Environment*, 373(2):435–446, 2007.

[79] F. P. Gariglio, D. Tonina, and C. H. Luce. Spatiotemporal variability of hyporheic exchange through a pool-riffle-pool sequence. *Water Resources Research*, 49(11):7185–7204, 2013.

[80] GHD. Port phillip cma groundwater model: Transient model development report. Technical report, Victorian Government Department of Sustainability and Environment Melbourne, 2010.

[81] B. Giambastiani, A. McCallum, M. Andersen, B. Kelly, and R. Acworth. Understanding groundwater processes by representing aquifer heterogeneity in the maules creek catchment, namoi valley (new south wales, australia). *Hydrogeology Journal*, 20(6):1027–1044, 2012.

[82] T. Gleeson, L. Marklund, L. Smith, and A. H. Manning. Classifying the water table at regional to continental scales. *Geophysical Research Letters*, 38(5), 2011.

[83] P. Goderniaux, P. Davy, E. Bresciani, J.-R. Dreuzy, and T. Borgne. Partitioning a regional groundwater flow system into shallow local and deep regional flow compartments. *Water Resources Research*, 49(4):2274–2286, 2013.

[84] J. D. Gomez-Velez and J. W. Harvey. A hydrogeomorphic river network model predicts where and why hyporheic exchange is important in large basins. *Geophysical Research Letters*, 41(18):6403–6412, 2014.

[85] J. D. Gomez-Velez, J. W. Harvey, M. B. Cardenas, and B. Kiel. Denitrification in the mississippi river network controlled by flow through river bedforms. *Nature Geoscience*, 8(12):941, 2015.

[86] R. González-Pinzón, A. S. Ward, C. E. Hatch, A. N. Wlostowski, K. Singha, M. N. Gooseff, R. Haggerty, J. W. Harvey, O. A. Cirpka, and J. T. Brock. A field comparison of multiple techniques to quantify groundwater–surface-water interactions. *Freshwater Science*, 34(1):139–160, 2015.

[87] S. B. Grant, K. Stolzenbach, M. Azizian, M. J. Stewardson, F. Boano, and L. Bardini. First-order contaminant removal in the hyporheic zone of streams: physical insights from a simple analytical model. *Environmental science & technology*, 48(19):11369–11378, 2014.

[88] P. Grathwohl, H. Rügner, T. Wöhling, K. Osenbrück, M. Schwientek, S. Gayler, U. Wollschläger, B. Selle, M. Pause, J.-O. Delfs, et al. Catchments as reactors: A comprehensive approach for water fluxes and solute turnover. *Environmental Earth Sciences*, 69(2):317–333, 2013.

[89] N. B. Grimm and S. G. Fisher. Exchange between interstitial and surface water: implications for stream metabolism and nutrient cycling. *Hydrobiologia*, 111(3):219–228, 1984.

[90] J. Ha, M. Eigenraam, J. Chua, and W. Lewis. A programmer's guide for biosym - the biophysical modelling toolbox of ensym. Technical manual, Victorian Government Department of Sustainability and Environment Melbourne, 2010.

[91] R. Haggerty, S. M. Wondzell, and M. A. Johnson. Power-law residence time distribution in the hyporheic zone of a 2nd-order mountain stream. *Geophysical Research Letters*, 29(13), 2002.

[92] H. Haitjema. On the residence time distribution in idealized groundwatersheds. *Journal of Hydrology*, 172(1):127–146, 1995.

[93] H. M. Haitjema and S. Mitchell-Bruker. Are water tables a subdued replica of the topography? *Ground Water*, 43(6):781–786, 2005.

[94] P. J. Hancock, A. J. Boulton, and W. F. Humphreys. Aquifers and hyporheic zones: towards an ecological understanding of groundwater. *Hydrogeology Journal*, 13(1):98–111, 2005.

[95] A. W. Harbaugh. *MODFLOW-2005, the US Geological Survey modular ground-water model: the ground-water flow process.* US Department of the Interior, US Geological Survey Reston, VA, USA, 2005.

[96] J. W. Harvey. Quantifying hydrologic interactions between streams and their subsurface hyporheic zones. *Streams and groundwaters*, pages 4–44, 2000.

[97] J. W. Harvey and K. E. Bencala. The effect of streambed topography on surface-subsurface water exchange in mountain catchments. *Water Resources Research*, 29(1):89–98, 1993.

[98] J. W. Harvey, J. K. Böhlke, M. A. Voytek, D. Scott, and C. R. Tobias. Hyporheic zone denitrification: Controls on effective reaction depth and contribution to whole-stream mass balance. *Water Resources Research*, 49(10):6298–6316, 2013.

[99] J. W. Harvey and C. C. Fuller. Effect of enhanced manganese oxidation in the hyporheic zone on basin-scale geochemical mass balance. *Water Resources Research*, 34(4):623–636, 1998.

[100] J. W. Harvey, B. J. Wagner, and K. E. Bencala. Evaluating the reliability of the stream tracer approach to characterize stream-subsurface water exchange. *Water resources research*, 32(8):2441–2451, 1996.

[101] C. E. Hatch, A. T. Fisher, J. S. Revenaugh, J. Constantz, and C. Ruehl. Quantifying surface water–groundwater interactions using time series analysis of streambed thermal records: Method development. *Water Resources Research*, 42(10), 2006.

[102] C. E. Hatch, A. T. Fisher, C. R. Ruehl, and G. Stemler. Spatial and temporal variations in streambed hydraulic conductivity quantified with time-series thermal methods. *Journal of Hydrology*, 389(3):276–288, 2010.

[103] F. R. Hauer and G. A. Lamberti. *Methods in stream ecology.* Academic Press, 2011.

[104] M. Hayashi and D. O. Rosenberry. Effects of ground water exchange on the hydrology and ecology of surface water. *Groundwater*, 40(3):309–316, 2002.

[105] R. Heath. Basic ground-water hydrology: Us geological survey water-supply paper 2220, 84 p. 1984. *Ground-water regions of the United States: US Geological Survey Water-Supply Paper*, 2242:78, 1983.

[106] A. R. Hill. Ground water flow paths in relation to nitrogen chemistry in the near-stream zone. *Hydrobiologia*, 206(1):39–52, 1990.

[107] A. R. Hill. Nitrate removal in stream riparian zones. *Journal of environmental quality*, 25(4):743–755, 1996.

[108] L. Hu, Z. Xu, and W. Huang. Development of a river-groundwater interaction model and its application to a catchment in northwestern china. *Journal of Hydrology*, 543:483–500, 2016.

[109] K. S. Hunter, Y. Wang, and P. Van Cappellen. Kinetic modeling of microbially-driven redox chemistry of subsurface environments: coupling transport, microbial metabolism and geochemistry. *Journal of hydrology*, 209(1):53–80, 1998.

[110] D. J. Irvine, P. Brunner, H.-J. H. Franssen, and C. T. Simmons. Heterogeneous or homogeneous? implications of simplifying heterogeneous streambeds in models of losing streams. *Journal of hydrology*, 424:16–23, 2012.

[111] P. Jaffe, P. Milly, and S. Taylor. Biofilm growth and the related changes in the physical properties of a porous medium. 2. permeability. *Water Resources Research WRERAQ,*, 26(9), 1990.

[112] X.-W. Jiang, L. Wan, M. B. Cardenas, S. Ge, and X.-S. Wang. Simultaneous rejuvenation and aging of groundwater in basins due to depth-decaying hydraulic conductivity and porosity. *Geophysical Research Letters*, 37(5), 2010.

[113] J. B. Jones and R. M. Holmes. Surface-subsurface interactions in stream ecosystems. *Trends in Ecology & Evolution*, 11(6):239–242, 1996.

[114] J. B. Jones and P. J. Mulholland. *Streams and ground waters*. Academic Press, 2000.

[115] P. Y. Julien and G. J. Klaassen. Sand-dune geometry of large rivers during floods. *Journal of Hydraulic Engineering*, 121(9):657–663, 1995.

[116] T. Kasahara and S. M. Wondzell. Geomorphic controls on hyporheic exchange flow in mountain streams. *Water Resources Research*, 39(1):SBH–3, 2003.

[117] G. J. Kauffman. Economic value of nature and ecosystems in the delaware river basin. *Journal of Contemporary Water Research & Education*, 158(1):98–119, 2016.

[118] J. Keery, A. Binley, N. Crook, and J. W. Smith. Temporal and spatial variability of groundwater–surface water fluxes: development and application of an analytical method using temperature time series. *Journal of Hydrology*, 336(1):1–16, 2007.

[119] J. W. Kirchner, X. Feng, and C. Neal. Fractal stream chemistry and its implications for contaminant transport in catchments. *Nature*, 403(6769):524–527, 2000.

[120] S. Krause, F. Boano, M. O. Cuthbert, J. H. Fleckenstein, and J. Lewandowski. Understanding process dynamics at aquifer-surface water interfaces: An introduction to the special section on new modeling approaches and novel experimental technologies. *Water Resources Research*, 50(2):1847–1855, 2014.

[121] S. Krause and A. Bronstert. The impact of groundwater–surface water interactions on the water balance of a mesoscale lowland river catchment in northeastern Germany. *Hydrological Processes*, 21(2):169–184, 2007.

[122] S. Krause, A. Bronstert, and E. Zehe. Groundwater-surface water interactions in a North German lowland floodplain–implications for the river discharge dynamics and riparian water balance. *Journal of Hydrology*, 347(3):404–417, 2007.

[123] S. Krause, L. Heathwaite, A. Binley, and P. Keenan. Nitrate concentration changes at the groundwater-surface water interface of a small Cumbrian river. *Hydrological Processes*, 23(15):2195–2211, 2009.

[124] K. Lansdown, C. Heppell, M. Trimmer, A. Binley, A. Heathwaite, P. Byrne, and H. Zhang. The interplay between transport and reaction rates as controls on nitrate attenuation in permeable, streambed sediments. *Journal of Geophysical Research: Biogeosciences*, 120(6):1093–1109, 2015.

[125] Y. Liu, S.-F. Yang, and J.-H. Tay. Improved stability of aerobic granules by selecting slow-growing nitrifying bacteria. *Journal of Biotechnology*, 108(2):161–169, 2004.

[126] G. P. Malanson. *Riparian landscapes*. Cambridge University Press, 1993.

[127] F. Malard, K. Tockner, M.-J. Dole-Oliver, and J. Ward. A landscape perspective of surface–subsurface hydrological exchanges in river corridors. *Freshwater Biology*, 47(4):621–640, 2002.

[128] J. Mallard, B. McGlynn, and T. Covino. Lateral inflows, stream-groundwater exchange, and network geometry influence stream water composition. *Water Resources Research*, 50(6):4603–4623, 2014.

[129] A. Marion and M. Zaramella. A residence time model for stream-subsurface exchange of contaminants. *Acta Geophysica Polonica*, 53(4):527, 2005.

[130] L. Marklund and A. Wörman. The use of spectral analysis-based exact solutions to characterize topography-controlled groundwater flow. *Hydrogeology Journal*, 19(8):1531–1543, 2011.

[131] A. Marzadri, D. Tonina, and A. Bellin. A semianalytical three-dimensional process-based model for hyporheic nitrogen dynamics in gravel bed rivers. *Water Resources Research*, 47(11), 2011.

[132] A. Marzadri, D. Tonina, A. Bellin, G. Vignoli, and M. Tubino. Semianalytical analysis of hyporheic flow induced by alternate bars. *Water Resources Research*, 46(7), 2010.

[133] A. M. McCallum, M. S. Andersen, B. Giambastiani, B. F. Kelly, and R. Ian Acworth. River–aquifer interactions in a semi-arid environment stressed by groundwater abstraction. *Hydrological Processes*, 27(7):1072–1085, 2013.

[134] P. L. Mccarty. Energetics and kinetics of anaerobic treatment. ACS Publications, 1971.

[135] M. G. McDonald and A. W. Harbaugh. A modular three-dimensional finite-difference ground-water flow model. 1988.

[136] B. V. Merkey, B. E. Rittmann, and D. L. Chopp. Modeling how soluble microbial products (smp) support heterotrophic bacteria in autotroph-based biofilms. *Journal of theoretical biology*, 259(4):670–683, 2009.

[137] E. Mohamed and R. Worden. Groundwater compartmentalisation: a water table height and geochemical analysis of the structural controls on the subdivision of a major aquifer, the sherwood sandstone, merseyside, uk. *Hydrology and Earth System Sciences Discussions*, 10(1):49–64, 2006.

[138] D. R. Montgomery and E. Foufoula-Georgiou. Channel network source representation using digital elevation models. *Water Resources Research*, 29(12):3925–3934, 1993.

[139] P. J. Mulholland, A. M. Helton, G. C. Poole, R. O. Hall, S. K. Hamilton, B. J. Peterson, J. L. Tank, L. R. Ashkenas, L. W. Cooper, C. N. Dahm, et al. Stream denitrification across biomes and its response to anthropogenic nitrate loading. *Nature*, 452(7184):202–205, 2008.

[140] P. J. Mulholland, E. R. Marzolf, J. R. Webster, D. R. Hart, and S. P. Hendricks. Evidence that hyporheic zones increase heterotrophic metabolism and phosphorus uptake in forest streams. *Limnology and Oceanography*, 42(3):443–451, 1997.

[141] J. D. Newbold, J. W. Elwood, R. V. O'Neill, and W. V. Winkle. Measuring nutrient spiralling in streams. *Canadian Journal of Fisheries and Aquatic Sciences*, 38(7):860–863, 1981.

[142] M. E. Newcomer, S. S. Hubbard, J. H. Fleckenstein, U. Maier, C. Schmidt, M. Thullner, C. Ulrich, N. Flipo, and Y. Rubin. Simulating bioclogging effects on dynamic riverbed permeability and infiltration. *Water Resources Research*, 52(4):2883–2900, 2016.

[143] B. L. O'Connor, M. Hondzo, and J. W. Harvey. Predictive modeling of transient storage and nutrient uptake: Implications for stream restoration. *Journal of Hydraulic Engineering*, 136(12):1018–1032, 2009.

[144] T. Oga, S. Suthersan, and J. Ganczarczyk. Some properties of aerobic biofilms. *Environmental technology*, 12(5):431–440, 1991.

[145] D. Ophori and J. Toth. Characterization of ground-water flow by field mapping and numerical simulation, ross creek basin, alberta, canada. *Groundwater*, 27(2):193–201, 1989.

[146] T. Orghidan. Ein neuer lebensraum des unterirdischen wassers: der hyporheische biotop. *Arch. Hydrobiol*, 55(5):392–414, 1959.

[147] T. Orghidan. A new habitat of subsurface waters: the hyporheic biotope. *Fundamental and applied limnology*, 176(4):291, 2010.

[148] Y. Z. Osman and M. P. Bruen. Modelling stream–aquifer seepage in an alluvial aquifer: an improved loosing-stream package for modflow. *Journal of Hydrology*, 264(1):69–86, 2002.

[149] A. I. Packman, M. Salehin, and M. Zaramella. Hyporheic exchange with gravel beds: basic hydrodynamic interactions and bedform-induced advective flows. *Journal of Hydraulic Engineering*, 130(7):647–656, 2004.

[150] M. Peszynska, A. Trykozko, G. Iltis, S. Schlueter, and D. Wildenschild. Biofilm growth in porous media: experiments, computational modeling at the porescale, and upscaling. *Advances in Water Resources*, 95:288–301, 2016.

[151] D. W. Pollock. *User's Guide for MODPATH/MODPATH-PLOT, Version 3: A Particle Tracking Post-processing Package for MODFLOW, the US: Geological Survey Finite-difference Ground-water Flow Model.* US Department of Interior, 1994.

[152] G. Poole, S. O'daniel, K. Jones, W. Woessner, E. Bernhardt, A. Helton, J. Stanford, B. Boer, and T. Beechie. Hydrologic spiralling: the role of multiple interactive flow paths in stream ecosystems. *River Research and Applications*, 24(7):1018–1031, 2008.

[153] G. C. Poole, J. A. Stanford, S. W. Running, and C. A. Frissell. Multiscale geomorphic drivers of groundwater flow paths: subsurface hydrologic dynamics and hyporheic habitat diversity. *Journal of the North American Benthological Society*, 25(2):288–303, 2006.

[154] F. T. Portmann, S. Siebert, and P. Döll. MIRCA2000–Global monthly irrigated and rainfed crop areas around the year 2000: A new high-resolution data set for agricultural and hydrological modeling. *Global Biogeochemical Cycles*, 24(1), 2010.

[155] D. Postma and R. Jakobsen. Redox zonation: equilibrium constraints on the Fe (III)/$s_{o}^{4}-$ reduction interface. *Geochimica et Cosmochimica Acta*, 60(17):3169–3175, 1996.

[156] D. E. Prudic. Documentation of a computer program to simulate stream-aquifer relations using a modular, finite-difference, ground-water flow model. 1989.

[157] L. J. Puckett, C. Zamora, H. Essaid, J. T. Wilson, H. M. Johnson, M. J. Brayton, and J. R. Vogel. Transport and fate of nitrate at the ground-water/surface-water interface. *Journal of environmental quality*, 37(3):1034–1050, 2008.

[158] C.-Z. Qin and S. M. Hassanizadeh. Pore-network modeling of solute transport and biofilm growth in porous media. *Transport in Porous Media*, 110(3):345–367, 2015.

[159] B. Rittmann. Comparative performance of biofilm reactor types. *Biotechnology and bioengineering*, 24(6):1341–1370, 1982.

[160] B. Rittmann and P. McCarty. *Environmental Biotechnology: Principles and Applications*. McGraw-Hill series in water resources and environmental engineering. Tata McGraw Hill Education Private Limited, 2012.

[161] B. E. Rittmann and J. A. Manem. Development and experimental evaluation of a steady-state, multispecies biofilm model. *Biotechnology and bioengineering*, 39(9):914–922, 1992.

[162] B. E. Rittmann and P. L. McCarty. Model of steady-state-biofilm kinetics. *Biotechnology and Bioengineering*, 22(11):2343–2357, 1980.

[163] I. Rodríguez-Iturbe, A. Rinaldo, R. Rigon, R. L. Bras, A. Marani, and E. Ijjász-Vásquez. Energy dissipation, runoff production, and the three-dimensional structure of river basins. *Water Resources Research*, 28(4):1095–1103, 1992.

[164] D. O. Rosenberry, P. Z. Klos, and A. Neal. In situ quantification of spatial and temporal variability of hyporheic exchange in static and mobile gravel-bed rivers. *Hydrological Processes*, 26(4):604–612, 2012.

[165] K. Rushton. Representation in regional models of saturated river–aquifer interaction for gaining/losing rivers. *Journal of Hydrology*, 334(1):262–281, 2007.

[166] M. Salehin, A. I. Packman, and M. Paradis. Hyporheic exchange with heterogeneous streambeds: Laboratory experiments and modeling. *Water Resources Research*, 40(11), 2004.

[167] S. A. Savant, D. D. Reible, and L. J. Thibodeaux. Convective transport within stable river sediments. *Water Resources Research*, 23(9):1763–1768, 1987.

[168] A. Sawyer. Enhanced removal of groundwater-borne nitrate in heterogeneous aquatic sediments. *Geophysical Research Letters*, 42(2):403–410, 2015.

[169] A. H. Sawyer, M. Bayani Cardenas, and J. Buttles. Hyporheic exchange due to channel-spanning logs. *Water Resources Research*, 47(8), 2011.

[170] C. Schmidt, M. Bayer-Raich, and M. Schirmer. Characterization of spatial heterogeneity of groundwater-stream water interactions using multiple depth streambed temperature measurements at the reach scale. *Hydrology and Earth System Sciences Discussions*, 3(4):1419–1446, 2006.

[171] C. W. Shelton. *An Analytical and Numerical Investigation of Stream/aquifer Interaction Methodologies.* PhD thesis, Washington State University, 2011.

[172] H. W. Shen, H. M. Fehlman, and C. Mendoza. Bed form resistances in open channel flows. *Journal of Hydraulic Engineering*, 116(6):799–815, 1990.

[173] S. K. Singh, G. C. Mishra, P. K. Swamee, and C. S. P. Ojha. Aquifer diffusivity and stream resistance from varying stream stage. *Journal of irrigation and drainage engineering*, 128(1):57–61, 2002.

[174] J. Smith, B. W. Surridge, T. Haxton, and D. Lerner. Pollutant attenuation at the groundwater–surface water interface: A classification scheme and statistical analysis using national-scale nitrate data. *Journal of hydrology*, 369(3):392–402, 2009.

[175] J. W. N. Smith. Groundwater - surface water interactions in the hyporheic zone. Science report, Environment Agency, Bristol, UK, 2005.

[176] R. L. Smith, B. L. Howes, and J. H. Duff. Denitrification in nitrate-contaminated groundwater: occurrence in steep vertical geochemical gradients. *Geochimica et Cosmochimica Acta*, 55(7):1815–1825, 1991.

[177] M. Sophocleous. Interactions between groundwater and surface water: the state of the science. *Hydrogeology journal*, 10(1):52–67, 2002.

[178] J. Stanford. *Landscapes and riverscapes.* Elsevier: Amsterdam, 2006.

[179] J. Stanford and J. Ward. *The hyporheic habitat of river ecosystems.* Nature Publishing Group, 1988.

[180] J. A. Stanford and J. Ward. An ecosystem perspective of alluvial rivers: connectivity and the hyporheic corridor. *Journal of the North American Benthological Society*, pages 48–60, 1993.

[181] S. H. Stonedahl. *Investigation of the Effect Multiple Scales of Topography on Hyporheic Exchange.* Susa Stonedahl, 2011.

[182] S. H. Stonedahl, J. W. Harvey, J. Detty, A. Aubeneau, and A. I. Packman. Physical controls and predictability of stream hyporheic flow evaluated with a multiscale model. *Water Resources Research*, 48(10), 2012.

[183] S. H. Stonedahl, J. W. Harvey, and A. I. Packman. Interactions between hyporheic flow produced by stream meanders, bars, and dunes. *Water Resources Research*, 49(9):5450–5461, 2013.

[184] S. H. Stonedahl, J. W. Harvey, A. Wörman, M. Salehin, and A. I. Packman. A multiscale model for integrating hyporheic exchange from ripples to meanders. *Water Resources Research*, 46(12), 2010.

[185] B. J. Suchomel, B. M. Chen, and M. B. Allen. Macroscale properties of porous media from a network model of biofilm processes. *Transport in porous media*, 31(1):39–66, 1998.

[186] M. A. Sutton, C. M. Howard, J. W. Erisman, G. Billen, A. Bleeker, P. Grennfelt, H. Van Grinsven, and B. Grizzetti. *The European nitrogen assessment: sources, effects and policy perspectives.* Cambridge University Press, 2011.

[187] L. J. Thibodeaux and J. D. Boyle. Bedform-generated convective transport in bottom sediment. *Nature*, 325(6102):341–343, 1987.

[188] M. Thullner and P. Baveye. Computational pore network modeling of the influence of biofilm permeability on bioclogging in porous media. *Biotechnology and Bioengineering*, 99(6):1337–1351, 2008.

[189] M. Thullner, M. H. Schroth, J. Zeyer, and W. Kinzelbach. Modeling of a microbial growth experiment with bioclogging in a two-dimensional saturated porous media flow field. *Journal of contaminant hydrology*, 70(1):37–62, 2004.

[190] M. Thullner, J. Zeyer, and W. Kinzelbach. Influence of microbial growth on hydraulic properties of pore networks. *Transport in porous media*, 49(1):99–122, 2002.

[191] M. C. Thullner. *Experimental and numerical investigations of bioclogging in porous media using two-dimensional flow fields.* PhD thesis, 2001.

[192] D. Tonina and J. M. Buffington. Hyporheic exchange in mountain rivers i: Mechanics and environmental effects. *Geography Compass*, 3(3):1063–1086, 2009.

[193] D. Tonina and J. M. Buffington. Effects of stream discharge, alluvial depth and bar amplitude on hyporheic flow in pool-riffle channels. *Water resources research*, 47(8), 2011.

[194] T. Tosco and R. Sethi. Transport of non-newtonian suspensions of highly concentrated micro-and nanoscale iron particles in porous media: a modeling approach. *Environmental science & technology*, 44(23):9062–9068, 2010.

[195] J. Tóth. A theory of groundwater motion in small drainage basins in central alberta, canada. *Journal of Geophysical Research*, 67(11):4375–4388, 1962.

[196] J. Tóth. A theoretical analysis of groundwater flow in small drainage basins. *Journal of Geophysical Research*, 68(16):4795–4812, 1963.

[197] K. Townsend, C. Kellar, K. Hassell, and V. Pettigrove. A review of aquatic ecosystem health in the upper Jacksons Creek catchment. Technical report, Centre for Aquatic Pollution Identification and Management, 2015.

[198] N. Trauth, C. Schmidt, U. Maier, M. Vieweg, and J. H. Fleckenstein. Coupled 3-D stream flow and hyporheic flow model under varying stream and ambient groundwater flow conditions in a pool-riffle system. *Water Resources Research*, 49(9):5834–5850, 2013.

[199] N. Trauth, C. Schmidt, M. Vieweg, U. Maier, and J. H. Fleckenstein. Hyporheic transport and biogeochemical reactions in pool-riffle systems under varying ambient groundwater flow conditions. *Journal of Geophysical Research: Biogeosciences*, 119(5):910–928, 2014.

[200] F. J. Triska, J. H. Duff, and R. J. Avanzino. The role of water exchange between a stream channel and its hyporheic zone in nitrogen cycling at the terrestrial-aquatic interface. *Hydrobiologia*, 251(1):167–184, 1993.

[201] F. J. Triska, V. C. Kennedy, R. J. Avanzino, G. W. Zellweger, and K. E. Bencala. Retention and transport of nutrients in a third-order stream in northwestern california: Hyporheic processes. *Ecology*, 70(6):1893–1905, 1989.

[202] N. P. Unland, I. Cartwright, D. I. Cendón, and R. Chisari. Residence times and mixing of water in river banks: implications for recharge and groundwater-surface water exchange. *Hydrology and Earth System Sciences*, 18(12):5109, 2014.

[203] N. Vittal, K. Ranga Raju, and R. Garde. Resistance of two dimensional triangular roughness. *Journal of Hydraulic Research*, 15(1):19–36, 1977.

[204] C. J. Vörösmarty, P. B. McIntyre, M. O. Gessner, D. Dudgeon, A. Prusevich, P. Green, S. Glidden, S. E. Bunn, C. A. Sullivan, C. Reidy Liermann, et al. Global threats to human water security and river biodiversity. *nature*, 467(7315):555, 2010.

[205] B. J. Wagner and J. W. Harvey. Experimental design for estimating parameters of rate-limited mass transfer: Analysis of stream tracer studies. *Water Resources Research*, 33(7):1731–1741, 1997.

[206] O. Wanner and W. Gujer. A multispecies biofilm model. *Biotechnology and bioengineering*, 28(3):314–328, 1986.

[207] M. Water. Maribyrnong basin current and unimpacted daily flows – updating maribyrnong river realm models and deriving daily streamflows. Report for Melbourne Water, 2005.

[208] M. Water. Healthy waterways strategy 2013/14–2017/18: Chapter 5: Catchments and systems. Report for Melbourne Water, Melbourne Water, 2013.

[209] T. C. Winter. *Ground water and surface water: a single resource*, volume 1139. DIANE Publishing Inc., 1998.

[210] W. W. Woessner. Stream and fluvial plain ground water interactions: rescaling hydrogeologic thought. *Groundwater*, 38(3):423–429, 2000.

[211] D. M. Wolock and C. V. Price. Effects of digital elevation model map scale and data resolution. *Water Resources Research*, 30(11):3041–3052, 1994.

[212] S. S. Workshop. Concepts and methods for assessing solute dynamics in stream ecosystems. *Journal of the North American Benthological Society*, 9(2):95–119, 1990.

[213] A. Wörman, A. I. Packman, L. Marklund, J. W. Harvey, and S. H. Stone. Exact three-dimensional spectral solution to surface-groundwater interactions with arbitrary surface topography. *Geophysical Research Letters*, 33(7), 2006.

[214] A. Wörman, A. I. Packman, L. Marklund, J. W. Harvey, and S. H. Stone. Fractal topography and subsurface water flows from fluvial bedforms to the continental shield. *Geophysical Research Letters*, 34(7), 2007.

[215] G. J. Wroblicky, M. E. Campana, H. M. Valett, and C. N. Dahm. Seasonal variation in surface-subsurface water exchange and lateral hyporheic area of two stream-aquifer systems. *Water Resources Research*, 34(3):317–328, 1998.

[216] M. S. Yalin and E. Karahan. Steepness of sedimentary dunes. *Journal of the Hydraulics Division*, 105(4):381–392, 1979.

[217] J. P. Zarnetske, R. Haggerty, S. M. Wondzell, and M. A. Baker. Labile dissolved organic carbon supply limits hyporheic denitrification. *Journal of Geophysical Research: Biogeosciences*, 116(G4), 2011.

[218] J. P. Zarnetske, R. Haggerty, S. M. Wondzell, V. A. Bokil, and R. González-Pinzón. Coupled transport and reaction kinetics control the nitrate source-sink function of hyporheic zones. *Water Resources Research*, 48(11), 2012.

[219] Y. Zhou and W. Li. A review of regional groundwater flow modeling. *Geoscience frontiers*, 2(2):205–214, 2011.

[220] W. Zijl. Scale aspects of groundwater flow and transport systems. *Hydrogeology Journal*, 7(1):139–150, 1999.

Appendix A

River bedform inception by flow unsteadiness

During my PhD, I had the opportunity to carry on the work undertaken in my master's thesis. This work has led to a research article published in a peer-reviewed international journal [1] and it is here described as appendix, even if the topic is different from the main issue of this thesis (the related reference list as well is enclosed at the end of this part). However, as it is part of my work and experience during my declaration studies, I think that it is appropriate to include it in the present dissertation.

The work is related to the fluvial morphodynamics, that deals with the study of the spatio-temporal dynamics of river geomorphology. Morphodynamics is the branch of fluid mechanics devoted to study the interaction between a stream and its flow-influenced boundary. Specifically, my study is focused on small-scale fluvial morphologies, such as ripples, dunes and antidunes, and on the instability of the interface bed-stream. River bedforms, in fact, arise as a result of the interaction between a turbulent free-surface flow and its erodible boundary.

Dunes and antidunes constitute the most typical patterns, and their occurrence and dynamics are relevant for a number of engineering and environmental applications. Although flow variability is a typical feature of all rivers, the bedform-triggering morphological instabilities have generally been studied under the assumption of a constant flow rate. In order to partially address this shortcoming, the influence of (periodic) flow unsteadiness on bedform inception is here discussed. To this end, the recent one-dimensional validated model coupling Dressler's equations with a refined mechanistic sediment transport formulation is adopted, and both the asymptotic and transient dynamics are investigated by modal and nonmodal analyses.

Introduction

River bedforms are widespread morphological patterns which arise as a result of an unstable interaction between a turbulent free-surface flow and an erodible bottom. Research interest about these morphologies derives from their relevance in hydraulic engineering and environmental applications. River bedforms not only interfere with river navigation [2, 3] and human infrastructure [4, 5], they also induce differential pressure gradients that modify the flow field and consequently the overall hydraulic resistance, induce hyporheic fluxes [6, 7] and affect underground flows through preferential patterns within ancient sedimentary deposits [8, 9]. The present work focuses on dunes and antidunes (see Fig. A.1), that are micro-scale patterns generated under subcritical (Froude number, $F_0 < 1$) and supercritical ($F_0 > 1$) streams, respectively. Whereas dunes propagate in the downstream direction, antidunes are characterized by a periodic pattern that migrates upstream and causes the free surface to be in-phase with the bottom.

Dunes exhibit different shapes, depending on the amount of available erodible sediments and on the width-to-depth ratio of the river. In this work, we focus on two-dimensional transverse dunes and antidunes, which arise perpendicularly to the flow direction in narrow rivers. However, it is worth recalling that transverse dunes can decay into a chain of crescent-shaped barchans and display a ”sea-wave-like” shape with meandering. The formation of barchan dunes is very common and widely studied in an aeolian environment, as demonstrated by a vast body of literature [10–12], but has also been detected in subaqueous conditions both in laboratory experiments [13] and in real rivers [14].

Traditionally, the stability analysis of the sediment-fluid interface has largely been studied using two important simplifications: (i) the use of classical linear

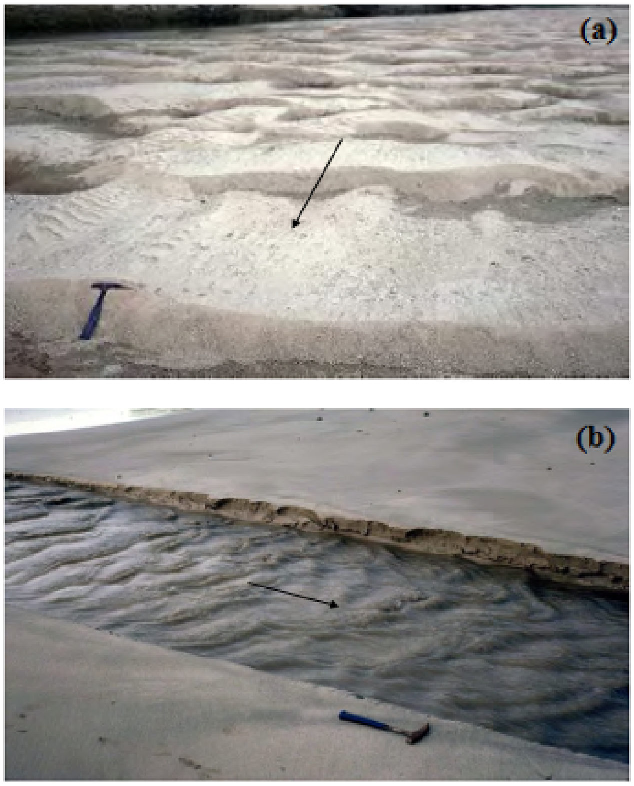

Fig. A.1 Examples of morphologies relevant for the evolution of the river bottom: (a) river dunes after a flood event and (b) active antidunes [15]. The arrows indicate the stream direction. Bedform wavelength and amplitude are about $0.5 - 1$ m and $10 - 20$ cm, respectively.

stability theory based on normal modes and (ii) the hypothesis of steady base conditions, *i.e.*, no discharge variations [16–21]. The modal (or normal) approach constitutes a powerful mathematical tool in stability theory and has been extensively used in fluid mechanics for more than a century. By means of this analysis, the dispersion relationship that relates the growth rate of the disturbance to its wave number vector is obtained. A zero-growth rate condition allows one to obtain the neutral (marginal) stability condition as a function of the governing parameters and to delineate stability and instability regions in parameter space. The main goal of such an approach is to establish the asymptotic temporal fate of the disturbances (i.e., for $t \to \infty$), since focus is on the least stable eigenvalue. In this manner, one determines whether disturbances tend to zero or infinity as time tends to infinity and, accordingly, classifies the base state as asymptotically stable or unstable. However, no information is gained on the disturbance behavior over finite time horizons; in particular, the stability of the system is determined, regardless of the way in which the disturbance tends to zero.

In order to understand the importance of studying the system behavior over finite times as well, three emblematic qualitative temporal evolutions of perturbations are represented in Fig. A.2(a). The analysis of asymptotic behavior by means of eigenvalues allows the asymptotically stable cases A and B (the perturbation decays to zero for $t \to \infty$) to be distinguished from the unstable case C, where the disturbance grows exponentially. However, curves A and B exhibit very different behavior for finite times: the perturbation in system A decays monotonically to zero, whereas it shows transient amplification in system B. The mathematical reason of this non-monotonic behavior lies in the nonnormality of the differential (or algebraic) operator which governs the temporal evolution of perturbations. This aspect is illustrated in Fig. A.2(b) for a simple two-dimensional algebraic problem. The non-orthogonality of the eigenvector set implies that their superposition exhibits transient growth, even though both associated eigenvalues are negative and *individual* eigenvectors decay monotonically in time. As disturbances can be written as linear combinations of eigenvectors, non-orthogonality causes disturbances to experience transient growth similar to case B of Fig. A.2(a), and the stronger the nonnormality, the more pronounced the transient amplification. This short-term

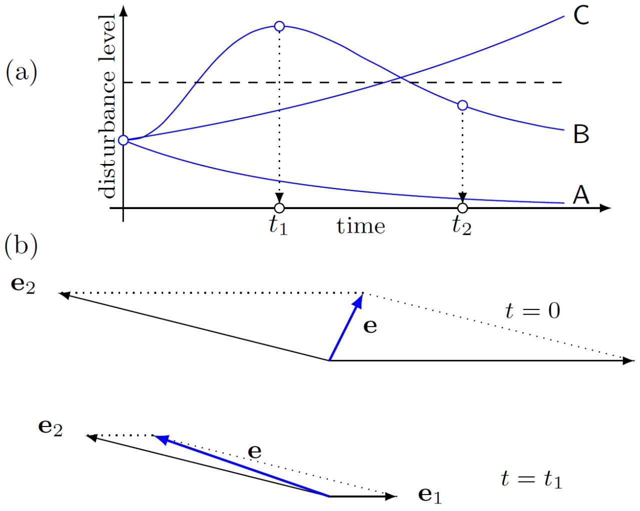

Fig. A.2 Three possible linear evolutions of an initial, infinitesimal perturbation are reported in subfigure (a): monotonic asymptotic decay (A), transient growth before asymptotic decay (B), and monotonic indefinite growth (C). The dashed line indicates a schematic possible threshold of the perturbation amplitude beyond which nonlinear terms start to be non-negligible. Subfigure (b) illustrates the concept of transient amplification on a two-dimensional system, where the non-orthogonality of the two eigenvectors $\mathbf{e}_{1,2}$ gives rise to transient growth: even though both eigenvectors, $\mathbf{e}_1$ and $\mathbf{e}_2$, individually decay in time, their non-orthogonal superposition causes the norm (length) of the resulting vector $\mathbf{e}$ to exceed its initial value before ultimately decaying to zero. Figures are qualitative and adapted from [22].

growth of the initial disturbance can be observed and investigated within a linear framework; no nonlinear mechanism needs to be invoked.

The distinction between monotonic and non-monotonic temporal perturbation dynamics is not a mere mathematical detail, but is fundamental for several reasons. First, transient growth may trigger nonlinear instabilities. Thus, although the problem would be asymptotically stable according to a normal-mode analysis, it could trigger transient instabilities which amplify (linearly) to such an extent that they render nonlinear terms significant (e.g., the dashed line in Fig. A.2 is exceeded). This process – referred to as by-pass transition [23, 24] – has been suggested as a critical factor in shear-flow transition to account for discrepancies between experimental findings and analytical forecasts based on normal modes [25]. The second key point is that transient growth can occur on time scales that are comparable to those of the studied process. As a result, the system appears unstable, even though disturbances decay over far longer time scales. Third, the characteristics of transient growth (time scales, local growth rate, etc.) may strongly depend on the physical parameters as well as the characteristics of the disturbances. It is altogether conceivable that, over the first stages of evolution, perturbations that are most amplified differ in shape and wavelengths from the characteristics of the asymptotically most amplified solutions.

Nonmodal analysis of nonnormal operators has a long tradition in fluid mechanics, providing insight into hydrodynamic instabilities for a variety of shear flows [26, 25, 27]. This approach has elucidated the role played by linear mechanisms in the triggering of instabilities in simple shear flows [e.g. 28–30]. In contrast, in a morphodynamic context this approach has only recently been applied, where it demonstrated the potential for transient growth for one-dimensional bed waves [31], river dunes [32] and bars [33]. Moreover, the transient dynamics of river patterns has not been investigated in the presence of flow variations. Even though unsteadiness is prevalent in any fluvial system, there are only a few studies on the effect of base-flow unsteadiness on the formation of morphodynamic instabilities [34–36], and an analysis of the interplay between unsteadiness and nonnormality in the formation of river patterns is still missing.

The main aim of this study is to investigate the role that unsteady discharges play in the inception and subsequent development of river bed forms. To this end, we perform both modal and nonmodal analyses and study the stability of the system at short and long times. The classical stability analysis (by normal modes) is complemented by a nonmodal analysis. This allows us to uncover the existence of transient, short-time growth that is not predicted by the classic modal analysis. Therefore, the stability of the system is investigated across all inherent time-scales. We use a depth-averaged model proposed by three of the authors [37]. This model was obtained by coupling one-dimensional shallow-water (Dressler's) equations to a mechanistic sediment-transport formulation; it was validated with experimental data. The analysis will be limited to the case of temporally periodic variations of the flow discharge. In this way – and despite the simplicity of the underlying model – we will shed new light on river morphodynamics by addressing the mutual interaction between unsteadiness and nonnormality.

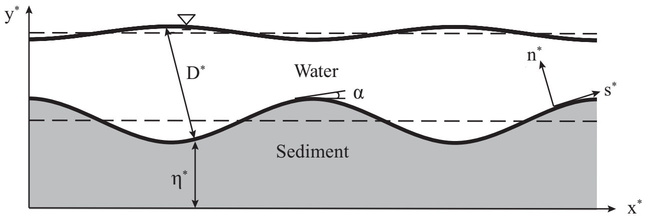

Fig. A.3 Scheme of a channel with river bedforms. The dotted and continuous lines refer to unperturbed and perturbed conditions, respectively. Note that the free-surface elevation is given by $H^* - D^*(1-\gamma)$.

Problem formulation and governing equations

Let us consider a free-surface turbulent water stream flowing in a rectangular channel of width B_0^* and slope J (asterisked variables refer to dimensional quantities). The bed is composed of granular material with a mean grain diameter d_s^*. We define a local reference frame $\{s^*, n^*\}$ and a global Cartesian system $\{x^*, y^*\}$, linked by the relation $\partial/\partial s = \gamma \partial/\partial x$, with $\gamma = \cos\alpha$ and α denoting the local slope of the bed. The variables η^* and H^* indicate the local bed elevation and the free-surface elevation, respectively, while $D^* = H^* - \eta^*$ represents the local stream depth (see Fig. A.3).

The base flow (unperturbed condition) is assumed unsteady with water depth $D_0^*(t)$ and longitudinal velocity $U_0^*(t)$. The following analysis considers the case of periodic time variations of the flow discharge in the form $Q^*(s^*, t^*) = \bar{Q}_0^* + \delta^* \sin(\omega^* t^* + \phi)$, where $\bar{Q}_0^*$ stands for the mean value, δ^* represents the amplitude of the harmonic variation, ω^* denotes the angular velocity, and ϕ refers to the phase. The period of oscillation is given as $T^* = 2\pi/\omega^*$.

We consider the one-dimensional model proposed by Vesipa et al. [37], which allows analytical tractability of the full stability analysis. Two-dimensional approaches, where the dependence of the flow field on the vertical coordinate direction is maintained, require sophisticated numerical methods [38] and analytical techniques are precluded. The herein adopted one-dimensional depth-averaged flow model is based on two key elements which play a crucial role in the one-dimensional modeling of river-bed instabilities. The first element is the non-hydrostatic pressure induced by the curvature of the bottom. This pressure plays a pivotal role in correctly selecting the dominant wavelength of antidunes [37]. In fact, neglecting the bed curvature-induced non-hydrostatic pressure component still results in the prediction of an instability, the most unstable wavelength, however, is misrepresented. The second key element is the non-equilibrium modeling of the sediment transport. For this, we remove the hypothesis of uniform equilibrium conditions (i.e., the particle deposition rate equals the erosion rate in any point of the bed) on which many empirical formulas derived from experiments are based (e.g., the Fernandez-Luque and Van-Beek formula). Conversely, a more refined mechanistic approach based on the momentum exchange between the fluid and the sediment and on the (space- and time-dependent) balance of the forces acting on the sediment particles [39, 40] is adopted. This approach allows us to describe the unstable conditions more realistically, as the stream-bed system is far from a local equilibrium.

Let us briefly recall the main ingredients of the modeling approach, where the averaged values of depth and velocity, defined as $\bar{D}_0^* = \int_0^{T^*} D_0^*(t)dt/T^*$ and $\bar{U}_0^* = \int_0^{T^*} U_0^*(t)dt/T^*$, respectively, will be used to scale the governing quantities. Time is made dimensionless by the hydrodynamic temporal scale, namely $t = t^*\bar{U}_0^*/\bar{D}_0^*$ and $\omega = \omega^*\bar{D}_0^*/\bar{U}_0^*$, where ω stands for the dimensionless angular velocity. The hydrodynamics are described by the one-dimensional Dressler formulation [41] that generalizes the classical Saint-Venant equations to the case of a non-hydrostatic pressure distribution, therefore allowing us to also consider the profile of normal velocity. The continuity equation and the longitudinal momentum equation are given as

$$\frac{\partial D}{\partial t} + \frac{U}{\mathcal{N}^2}\frac{\partial D}{\partial s} - V = 0, \tag{A.1}$$

$$\frac{\partial U}{\partial t} + \frac{U}{\mathcal{N}^2}\frac{\partial U}{\partial s} + \frac{\sin\alpha}{F_0^2} + \frac{\tau_B}{D(1-\kappa D/2)} + \left.\frac{\partial \mathcal{P}}{\partial s}\right|_{n=0} = 0, \tag{A.2}$$

where $\mathcal{N} = 1 - \kappa D$, with κ as the local bed curvature, D as the dimensionless depth measured perpendicular to the channel bed, and V as the dimensionless normal velocity evaluated at $n = D$. Eq. (A.2) accounts for the effects of flow acceleration (first two terms), gravity (third term), and the drag induced by bed roughness (fourth term). The shear stress at the bottom, τ_B, is evaluated using the Chezy formula $\tau_B = CU^2$, where C is the friction coefficient, which is a function of the relative roughness d_s and the dimensionless depth, following a closure relation provided by [42]. We note that the dimensional flow shear velocity of the basic state can be obtained as $u_{0*} = U_0^* \sqrt{C}$. The last term in (A.2) reads

$$\left.\frac{\partial \mathcal{P}}{\partial s}\right|_{n=0} = \left(\frac{\gamma}{F_0^2} + \frac{\kappa U^2}{\mathcal{N}^3}\right)\frac{\partial D}{\partial s} - \left(\frac{\kappa \sin\alpha}{F_0^2} - \frac{U^2}{\mathcal{N}^3}\frac{\partial \kappa}{\partial s}\right) D, \tag{A.3}$$

where $\mathcal{P}(s, n, t)$ is the vertical profile of the dimensionless pressure. Accordingly, the Froude number, defined as $F_0 = U_0^*/(gD_0^*)^{1/2}$ (with g as the gravitational acceleration), is periodically dependent on time. A morphodynamic model which accounts for the morphological evolution of the river bed is coupled to the shallow-water formulation of hydrodynamics. Through a mechanistic approach, sediment deposition and erosion rates are not balanced, because the flow is non-uniform; he dimensionless sediment transport rate, q, is given by $q = \xi v$, where $v(s, t)$ denotes an ensemble average of the particle velocity and $\xi(s, t)$ represents the area-based particle concentration.

The competition between the local entrainment and deposition of particles provides the longitudinal gradient of the sediment transport, according to the following balance equation for the sediment mass

$$\frac{1}{Q_h}\frac{\partial \xi}{\partial t} + \frac{\partial q}{\partial x} = \Theta(\mathcal{E} - \mathcal{D}), \tag{A.4}$$

where $\Theta = (Rd_s^3)^{1/2}/(1-p)F_0 = \mathcal{O}(10^{-3}-10^{-4})$, p denotes the porosity, $R = \rho_s/\rho - 1$ is the submerged sediment density, and ρ_s and ρ are the sediment and fluid densities, respectively. We select $p = 0.4$ and $R = 1.65$, which are typical values for silicate sediments [31, 18], but the choice of other reasonable values would not greatly modify the picture that emerges. Q_h stands for the ratio between the scale of sediment discharge and the flow rate discharge. The sediment erosion rate $\mathcal{E}$ and the sediment deposition rate $\mathcal{D}$ can be accounted for via the relations proposed by [40]

$$\mathcal{E} = \frac{r_e A_e}{d_s}\left(\theta_f - \theta_c\right)^{3/2}, \quad \mathcal{D} = (1-p)\frac{r_s A_s}{d_s^2}\theta_s^{1/2}\xi, \tag{$A.5a, b$}$$

where $A_e = 0.028$, $A_s = 0.068$. The coefficients r_e and r_s are correction coefficients to account for gravity and are given by the following expressions

$$r_e=[1+(1-r_\mu r_{dc})K_0]^{-3/2}, \qquad r_s=(r_\mu r_{dc})^{-1/2}, \tag{A.6}$$

where

$$r_\mu = 1 + \frac{\tan\alpha}{\mu} - \frac{\tan\alpha}{\mu_{d0}}, \qquad r_{dc} = \cos\alpha\left(1+\frac{\tan\alpha}{\mu_d}\right), \tag{A.7}$$

with $K_0 = (\mu_{do}A_e/A_s)^{2/3}$, $\mu_{d0} = 0.3$ and $\mu = 0.6$. As far as the total shear stress exerted on the bottom of the bed-load layer is concerned, two components have to be considered: the (dimensionless) stress exerted by the sediment, τ_s, and the stress exerted by the fluid, τ_f, where $\tau_s + \tau_f \sim \tau_B$ and $\theta = F_0^2\tau/Rd_s$ is the Shields stress.

By expressing the stress exerted by the sediment as a quadratic function of the relative velocity of the particle with respect to the fluid, and imposing a standard velocity distribution near the bottom, the relationship between the different components of stress is as follows

$$\theta_f = \theta_B - T_\mu\xi\left(\frac{f}{F_0}\sqrt{Rd_s\theta_B} - v\right)^2, \tag{A.8}$$

with $f=11.5$ and T_μ as a parameter of the mechanistic transport model that accounts for gravity effects. The expression for T_μ is given by

$$T_\mu = T_0\frac{r_\mu}{r_\lambda^2}, \tag{A.9}$$

where T_0 is a parameter for flat-bed conditions given by

$$T_0 = \frac{F_0^2\mu_{d0}(1-p)}{\lambda^2\theta_{ch}f^2d_s^2R}, \tag{A.10}$$

with $R = 1.65$, $\mu_{d0} = 0.3$, $\lambda = 0.7$, $\theta_{ch} = 0.047$, and $p = 0.4$. Finally,

$$r_\lambda = \left(\frac{r_{sc}}{r_{dc}}\right)^{1/2}, \tag{A.11}$$

with

$$r_{sc} = \cos\alpha\left(1+\frac{\tan\alpha}{\mu}\right). \tag{A.12}$$

It has been established that gravity effects play a secondary role in triggering river-bed instabilities when compared to the stream-induced forces [37]. However, gravitational effects influencing transport thresholds are nonetheless maintained for a more rigorous treatment.

The longitudinal gradient of the sediment transport is responsible for the evolution of the bed elevation as established by the Exner equation, namely, by a kinematic condition for the bottom boundary which reads

$$\frac{\partial \eta}{\partial t} + \frac{\partial (v\xi)}{\partial x} = 0. \tag{A.13}$$

Finally, the particle velocity v is evaluated using a dynamical balance of all forces acting on the sediment grain

$$I^* = F^* - A^* - G^*_{\parallel}, \tag{A.14}$$

where F^* is the drag force (proportional to $[f\sqrt{\theta_B} - q]^2$, as in (A.8)); $A^* = \mu_d G^*_{\perp}$ is the resistive force due to friction (μ_d is the dynamic friction coefficient, see Appendix); $\{G^*_{\perp}, G^*_{\parallel}\} = G^*\{\cos\alpha, \sin\alpha\}$ are the components of the submerged particle weight, respectively measured normal and parallel to the bottom, and I^* is the particle inertia. In dimensionless form, we obtain

$$\frac{\partial v}{\partial t} + v\frac{\partial v}{\partial x} + R_\mu - S_\mu \left(\frac{f}{F_0}\sqrt{Rd_s\theta_B} - v \right)^2 = 0. \tag{A.15}$$

The coefficients R_μ and S_μ are parameters of the mechanistic transport model that accounts for gravity effects and are given by

$$R_\mu = R_0 r_\mu r_{dc}, \qquad S_\mu = S_0 \frac{r_\mu}{r_\lambda^2}, \tag{A.16}$$

where R_0 and S_0 are the parameters for flat bed conditions given by

$$R_0 = \frac{R\mu_{d0}}{F_0^2(R+1)}, \qquad S_0 = \frac{4\mu_{d0}(3\lambda^2\theta_{ch}f^2)^{-1}}{c_s d_s (R+1)}. \tag{A.17}$$

In summary, the five partial differential equations (A.1), (A.2), (A.4), (A.13), and (A.15) constitute our hydro-morphodynamic model where the unknowns are $\mathbf{X} = \{U, H, \eta, v, \xi\}$, recalling that $D = H - \eta$.

In setting up a linear stability analysis, we perturb the unsteady base state with an infinitesimal periodic perturbation following the ansatz

$$\mathbf{X} = \{U_0(t), H_0(t), \eta_0, v_0(t), \xi_0(t)\} + \varepsilon \mathbf{X}_1 \mathrm{e}^{ik\mathrm{x}} \tag{A.18}$$

where $\mathbf{X}_1 = \{u_1(t), h_1(t), \eta_1(t), v_1(t), \xi_1(t)\}$ contains the amplitudes of the wave-like perturbations, k denotes the longitudinal wave number, and $\varepsilon \ll 1$ is the amplitude of the bed perturbation. After substituting (A.18) into our model equations and expanding in ε, we can solve for the unperturbed basic state, obtaining analytical expressions for $\bar{U}_0$, $\bar{H}_0$, $\bar{v}_0$, and $\bar{\xi}_0$ as well as relations between the Froude number and the discharge. The first-order terms in the expansion, $\mathcal{O}(\varepsilon)$, yield a governing system of linear differential equations of the form

$$\frac{d}{dt}\mathbf{X}_1(t) = \mathbf{A}(t)\mathbf{X}_1(t), \tag{A.19}$$

where $\mathbf{A}(t) = \mathbf{A}(t+T)$ is a 5×5 time-periodic matrix with period $T = 2\pi/\omega$, that depends on the base-state variables and on the sediment and stream characteristics of the problem.

Modal analysis

A modal analysis aims at the assessment of the asymptotic, long-term fate of infinitesimal perturbations superimposed on the base state. Using this framework, the stability of the periodic solution for long times can be investigated by Floquet theory, a technique which permits the analysis of linear systems with time periodic basic state. Accordingly, the system is classified as asymptotically stable if all infinitesimal perturbation decays in time as $t \to \infty$; otherwise, the base system is unstable. Floquet stability analysis supplies the natural modes of the perturbation behavior and hence the general stability properties of the system's equilibrium. According to Floquet theory, the fundamental solution operator associated with (A.19) is introduced as the matrix $\Psi(t)$ which is computed by advancing a 5×5 identity matrix over one temporal period (from $t = 0$ to $t = T$) according to (A.19). Each column of $\Psi(t)$ is a linearly independent solution of the system. The asymptotic stability of the problem is inferred from the eigenvalues ν_j (Floquet multipliers) of the monodromy matrix

$\mathcal{B}$, defined as $\mathcal{B} = \Psi^{-1}(0)\Psi(T)$. The flow is deemed asymptotically stable, if all eigenvalues of $\mathcal{B}$ fall inside the unit disk, suggesting a contractive map over a full period; otherwise, the flow is asymptotically unstable.

Nonmodal analysis

Nonmodal analysis addresses the transient evolution of disturbances over finite times, taking into account the nonnormality of the governing operator. In this analysis, a key point is to find a suitable metric for the perturbation magnitude. Following the temporal evolution of the total fluctuation energy can be physically motivated and is commonplace in studies of transient behavior and nonnormality [29, 27]. For the present problem, the dimensionless energy is composed of a kinetic component $K = K_u + K_v$, where K_u and K_v are the contributions from fluctuations of flow and particle velocities, as well as a potential component $P = P_s + P_b$, where P_s and P_η account for the free-surface and bed fluctuations. The flow's kinetic energy is easily obtained as $K_u = |u_1|^2/2$, while the kinetic energy of the solid particles, K_v, can be assumed to be proportional to the velocity $(\xi v/h_s)^2$, where h_s is the bedload layer thickness, considered equal to $2.5d_s$ [39]. The product ξv is the volumetric solid discharge per unit width which, when divided by h_s, provides a particle velocity averaged over a moving volume. After expanding in Fourier series and integrating in x over one wavelength, we obtain

$$K_v = \frac{K(\xi_0^2|v_1|^2 + v_0^2|\xi_1|^2)}{2} + 2Kv_0\xi_0(v_1\xi_1^H + v_1\xi_1^H), \tag{A.20}$$

with $K = 0.4\rho_s(1-p)^2/(2\rho d_s)$. The superscript ^{H} refers to the complex conjugate. The contributions P_s and P_η coincide with those reported in [31] neglecting the capillary forces (which is reasonable in a turbulent flow) and setting the null potential at the undisturbed surface and are equal to

$$P_s = F_0^{-1}\frac{|h_1|^2}{2}, \quad P_\eta = rF_0^{-1}\frac{|\eta_1|^2}{2}, \tag{$A.21a, b$}$$

with $r = (1-p)R$. The last term of (A.20) causes the energy weight to be not positive definite, thus not complying with the definition of a norm. We must realize that the choice of an appropriate disturbance measure does not only stem from physical arguments but also must satisfy mathematical constraints. In order to arrive at a positive definite energy weight, while capturing a maximum of physical effects, we choose to neglect the last term of (A.20).

As the primary goal of this work is to analyze the morphological instabilities, our focus is on the behavior of the bed response. More specifically, we aim at determining initial conditions that maximize the transient growth of bed disturbances rather than maximize the global energy of the system at given times. This class of initial conditions can easily be identified by adding weight coefficients to the energy density such that the bed response is emphasized while the remaining components of energy are penalized – a technique that has previously been employed in [31, 32]. The thus weighted energy is defined as follows:

$$E = cK_u + cP_s + P_\eta + cK_v, \tag{A.22}$$

where c is a coefficient much less than unit (we take $c = 10^{-6}$; other values give similar results, provided that $c \ll 1$). In this way, we consider a new kind of energy that formally uses all the components of the governing system (thus avoiding the issues of a semi-norm [43]) but primarily consists of the bed potential energy. Provided that the vector $\mathbf{q}$ is defined as

$$\mathbf{q} = \frac{\sqrt{2c}}{2}\left\{u_1, \frac{h_1}{\sqrt{F_0}}, \eta_1\frac{\sqrt{r}}{\sqrt{cF_0}}, K\sqrt{\xi_0}v_1, K\sqrt{v_0}\xi_1\right\}, \tag{A.23}$$

the energy becomes simply $E = \|\mathbf{q}\|^2$, where $\|\cdot\|$ indicates the common l_2 norm. For this reason, equation (A.19) can be recast in terms of the disturbance energy, rather than the disturbance amplitude, as

$$\frac{d}{dt}\mathbf{q}(t) = \mathbf{L}(t)\mathbf{q}(t). \tag{A.24}$$

The nonmodal behavior of system (A.24) is investigated through the analysis of the growth function, which is defined as the maximum amplification of initial energy optimized over all admissible initial conditions [25], namely

$$\hat{G}(t) = \max_{\mathbf{q}_0} G(t) = \max_{\mathbf{q}_0} \frac{\|\mathbf{q}(t)\|^2}{\|\mathbf{q}_0\|^2}, \tag{A.25}$$

where $\mathbf{q}_0$ represents the initial disturbance, and $\| \cdot \|$ denotes the standard Euclidean 2-norm. Transient energy amplification occurs when $\hat{G} > 1$.

For a time-dependent system matrix $\mathbf{L}(t)$, the problem can be solved by applying an optimization technique known as the direct-adjoint method [22, 27], which determines the maximum amplification of initial energy that occurs over a specified time horizon. It involves maximizing a user-supplied cost functional and imposing constraints from the governing equations via Lagrange multipliers (or adjoint variables). The augmented cost functional is defined as

$$\begin{aligned}\mathcal{L}(\mathbf{q}, \tilde{\mathbf{q}}, \mathbf{q}_0, \tilde{\mathbf{q}}_0) =& \frac{\|\mathbf{q}(T)\|^2}{\|\mathbf{q}_0\|^2} - \int_0^T \left\langle \tilde{\mathbf{q}}, \left[\frac{d}{dt} - \mathbf{L}\right]\mathbf{q} \right\rangle dt \\ & - \langle \tilde{\mathbf{q}}_0, (\mathbf{q}(0) - \mathbf{q}_0) \rangle,\end{aligned} \tag{A.26}$$

where tildes indicate the Lagrange multipliers or adjoint variables. The first term on the righthand side of (A.26) is the cost functional, while the second and third terms impose the constraints related to the governing equations and the initial conditions, respectively.

Seeking a maximum of the cost functional, the first variations of $\mathcal{L}$ with respect to its independent variables $\mathbf{q}$, $\tilde{\mathbf{q}}$, $\mathbf{q}_0$, $\tilde{\mathbf{q}}_0$ have to be set to zero, thus yielding the following set of equations

$$\left[\frac{d}{dt} - \mathbf{L}\right]\mathbf{q} = 0, \qquad \left[\frac{d}{dt} + \mathbf{L}^H\right]\tilde{\mathbf{q}} = 0, \tag{$A.27a, b$}$$

$$\tilde{\mathbf{q}}_0 = \frac{2}{\|\mathbf{q}_0\|^2}\mathbf{q}(T), \qquad \mathbf{q}_0 = \frac{\|\mathbf{q}_0\|^4}{2\|\mathbf{q}(T)\|^2}\tilde{\mathbf{q}}(0). \tag{$A.28a, b$}$$

Equations (A.27a) and (A.27b) represent the direct and adjoint problem, respectively, while equations (A.28a) and (A.28b) give the optimality conditions. An iterative solution procedure is applied to solve this set of equations. During each cycle of this procedure, a given initial condition is used to integrate the direct equation (A.27a) over the chosen time interval from $t = 0$ to $t = T$ (forward). The output of this integration at time $t = T$ is $\mathbf{q}(T)$. This integration provides also a terminal condition $\tilde{\mathbf{q}}(T)$ for the adjoint equation (A.27b) which is subsequently integrated from $t = T$ to $t = 0$ (backward) to produce $\tilde{\mathbf{q}}(0)$. From $\tilde{\mathbf{q}}(0)$ a new initial condition $\mathbf{q}(0) = \tilde{\mathbf{q}}(0)$ for the direct problem is determined [27]. The iterative process terminates when an appropriate convergence criterion

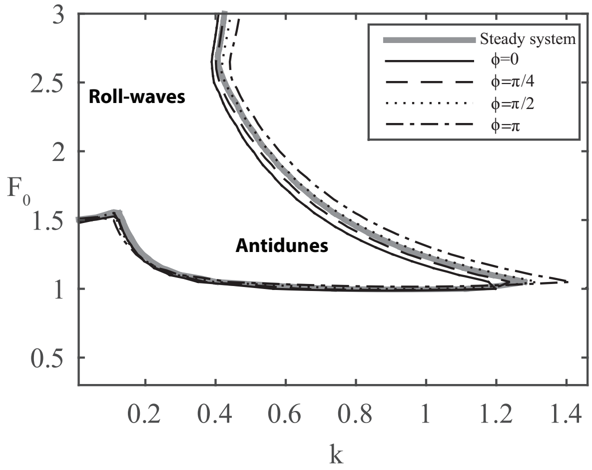

Fig. A.4 The marginal stability curve ($\nu_j = 1$) is displayed for the steady (thick line) and the unsteady cases in the F_0-k-plane. The unsteady curves are obtained for $\omega = 1$ and different values of ϕ.

is satisfied (i.e., the relative error of the growth function at the end of each iteration is less than 10^{-3}).

For time-independent system matrices ($\delta = 0$), there is a more straightforward technique: the singular value decomposition (SVD). It evaluates the growth function as $\hat{G}(t) = s^2[\mathbf{V}\exp(t\mathbf{\Lambda}(\mathbf{L}))\mathbf{V}^{-1}]$, where $s[\cdot]$ denotes the maximum singular value of its matrix argument, $\mathbf{V}$ is the matrix whose columns are the eigenvectors of $\mathbf{L}$, and $\mathbf{\Lambda}$ is the diagonal matrix containing the eigenvalues of $\mathbf{L}$.

Results

The problem under investigation is characterized by three hydraulic parameters (F_0, J, d_s), the wavenumber k, and three parameters describing the flow unsteadiness (ω, δ, ϕ). For simplicity, the domain of existence of morphodynamic instabilities is evaluated in the F_0-k-plane for fixed values of the remaining parameters. The dimensionless wavenumber ranges in the interval $[0,\ 1.5]$, since higher values run counter to the shallow water hypothesis. The parameter F_0 is taken in the range $[0.3,\ 3]$ which covers both the dunes ($F_0 < 1$) and antidunes ($F_0 > 1$) regime. We also set $d_s = 0.001$, $J = 0.005$, and $\delta = Q_0/4$ other choices of $d_s \in [10^{-3}, 10^{-2}]$; $J \in [10^{-3}, 10^{-2}]$; $\delta \in [0.1, 0.9]Q_0$ would influence the results quantitatively but not qualitatively). Finally, the frequency ω and the phase ϕ will be varied in order to explore their influence on the system behavior.

We first investigate the role played by the flow unsteadiness on the asymptotic stability of the bed-stream system. To this end, periodic changes occurring on a time scale typical of sediment transport (daily or monthly variations) are considered. Figure A.4 shows the marginal stability curve (corresponding to $\nu_j = 1$), that divides the asymptotically stable and unstable regions, under steady and unsteady conditions and for different values of the phase ϕ in the F_0-k-plane. The Floquet multipliers do not dependent on the frequency ω, as also pointed out by [36] for bar instabilities. On the other hand, a weak dependence on the phase can be observed: the instability region enlarges with an increase in ϕ. However, it is evident that the unsteadiness does not significantly affect the asymptotic fate of disturbances, and the instability regions are nearly unaltered when compared to the steady case. We remark that the instability region corresponds to an amalgam of two different modal processes: based on antidunes and roll-waves. The latter prevail at low wavenumbers and high Froude numbers (see figure) and arise mathematically, provided the temporal derivatives of Eqs. (A.1) and (A.2) are retained. In contrast, a third mode of instability (stemming from dune formation) is not detected asymptotically by this model, as highlighted in [37].

We now proceed to the transient growth analysis, focusing on intermediate time horizons. For time-independent base-flow conditions ($\delta = 0$), the optimal energy growth can be evaluated by the singular value decomposition (SVD) and is reported in Fig. A.5. Maximum amplification of initial energy is significant throughout the entire parameter space — an indication of substantial nonnormality of the operator $\mathbf{L}$. This finding also occurs in regions of asymptotic stability corresponding to dune formation and establishes the possibility of total energy growth by several orders of magnitude before exponential decay ultimately sets in. Noticeable transient growth of asymptotically stable modes is therefore expected during the early stages of bed form inception. This result also illustrates that the present one-dimensional model is capable of predicting dune inception, albeit via transient effects.

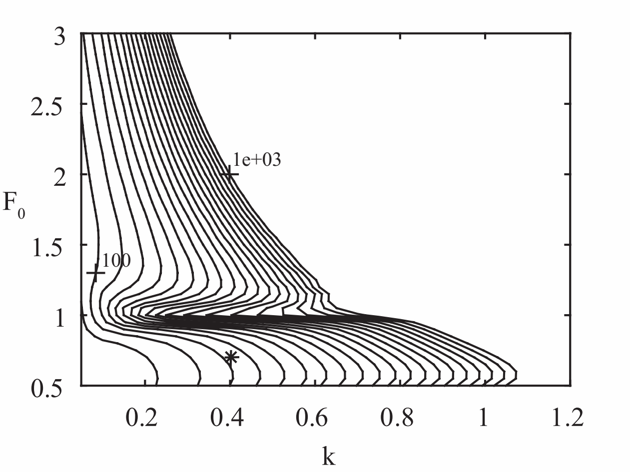

Fig. A.5 Contour plot of optimal energy growth evaluated by the singular value decomposition (SVD) for $\delta = 0$ (steady case) in the F_0-k-plane. The line spacing is $\Delta\hat{G} = 50$. The asterisk symbol marks the conditions chosen for the subsequent analysis.

By the nonmodal analysis, we have shown that river bedform dynamics exhibits remarkable transient growth, even for asymptotically stable wavenumbers. The application of a nonmodal approach is critical in order to predict the inception of short-time instabilities not captured by the classical modal analysis. Another interesting point is the dominant bedform wavelength that is predicted by a nonmodal analysis. Figs. A.6(a) and A.7(a) depict the dependence of the growth function $\hat{G}$ on the wavenumber k for fixed optimization times for a dune and antidune case, respectively. The value of the wavenumber corresponding to the highest growth rate, k_{max}, is reported in Figs. A.6(b) and A.7(b) as a function of time in conjunction with the corresponding values of the growth function, $\hat{G}_{max}$. The wavenumber displaying the highest growth rate decreases with increasing time; this decay is more pronounced in the dune case (where the wavenumber drops from $k \simeq 1.5$ for $t = 500$ to $k \simeq 0.2$ for $t = 1.5 \cdot 10^4$) than in the antidune case (where the range of variation is rather limited, from $k \simeq 0.88$ for $t = 500$ to $k \simeq 0.77$ for $t = 1.5 \cdot 10^4$).

These results confirm a marked difference in behavior between the dunes and the antidunes. In the dune case, the wavenumber undergoes a significant decrease, i.e., the selected wavelength evolves in time, as already discussed in theoretical studies [32] and shown in experimental work [44]. Therefore, the dynamical system shows (at least in its linear behavior) different dominant

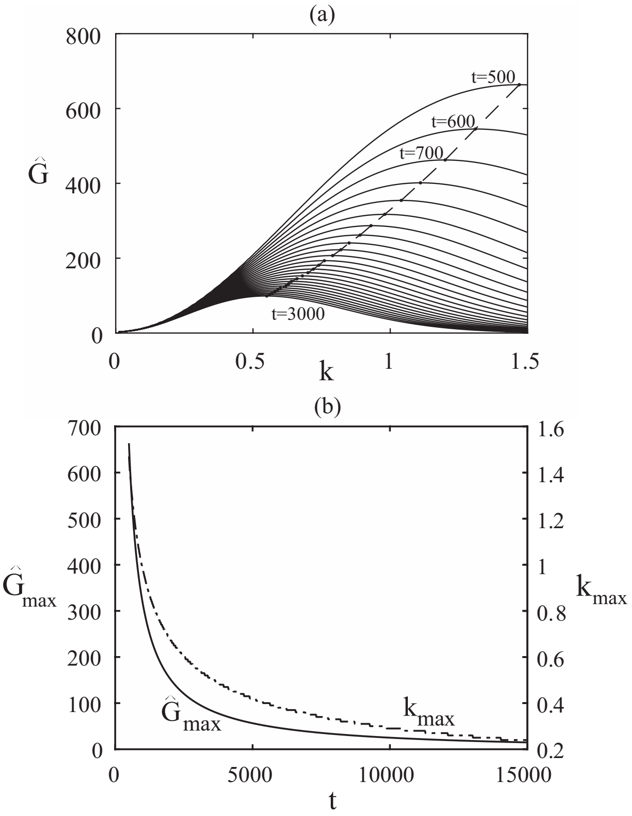

Fig. A.6 Dune case ($Fr = 0.7$): (a) behavior of $\hat{G}$ as a function of the wavenumber k for fixed times. The dashed line indicates the most unstable wavenumber for each time. The line spacing is $\Delta t = 100$. (b) Evolution of the most unstable wavenumber over time in conjunction with the corresponding value of the growth function.

wavenumbers at different times: the wavelengths corresponding to transient growth will arise first, but will gradually disappear (the wavelength increases, but the amplitude decreases in time) since they are stable in the long term. What we discussed until now suggests the possibility of a linear scale selection mechanism for the dunes driven by nonmodal effects [32]. A distinct rise of a characteristic wavelength is not observable in the antidune case. These river bedforms are, in fact, selected by purely linear mechanisms, and the correct formation of these pattern can be predicted asymptotically. This entails that the asymptotic wavelength is selected immediately. Therefore, the dynamical system displays a characteristic wavelength that is selected at short times and approximately maintained for subsequent times; in other words, asymptotically unstable wavenumbers already dominate the dynamics in the early stages. Finally, the results depicted in Figs. A.6 and A.7 show that the wavelengths favored and selected by the transient dynamics are attributable to typical wavelengths of dunes and antidunes (e.g., 1–50 m). For this reason, it can be stated that the bedforms which are transiently observed representcharacteristic pattern of a river environment.

So far, the transient growth of bedforms has been investigated under the hypothesis of a constant flow velocity. Since the system has demonstrated the potential for remarkable transient growth under these steady conditions, it is interesting to next explore the effect of flow unsteadiness. To this end, the nonmodal analysis is extended to time-dependent flow discharge. The introduction of this temporal dependence requires the application of a variational approach based on adjoint techniques.

For addressing the influence of unsteady conditions, a representative point is chosen in the parameter region of dune formation ($F_0 = 0.7$ and $k = 0.4$). For a first analysis, the frequency of the oscillating base flow is changed, but the phase relation between the unsteady forcing and the response in the perturbation of the unforced system is held constant ($\phi = 0$). Figure A.8 shows the growth function versus time for the steady case and for different values of ω for the unsteady case. In accordance with previous work on morphological pattern instabilities [31, 32], the temporal evolution of $\hat{G}(t)$ shows an oscillatory structure. This is linked to the imaginary part of the least stable eigenvalue. The period of this oscillatory structure, $T_f = 38$, is in fact an intrinsic property of the system; it is the inverse of its natural frequency ω_f. As mentioned in the

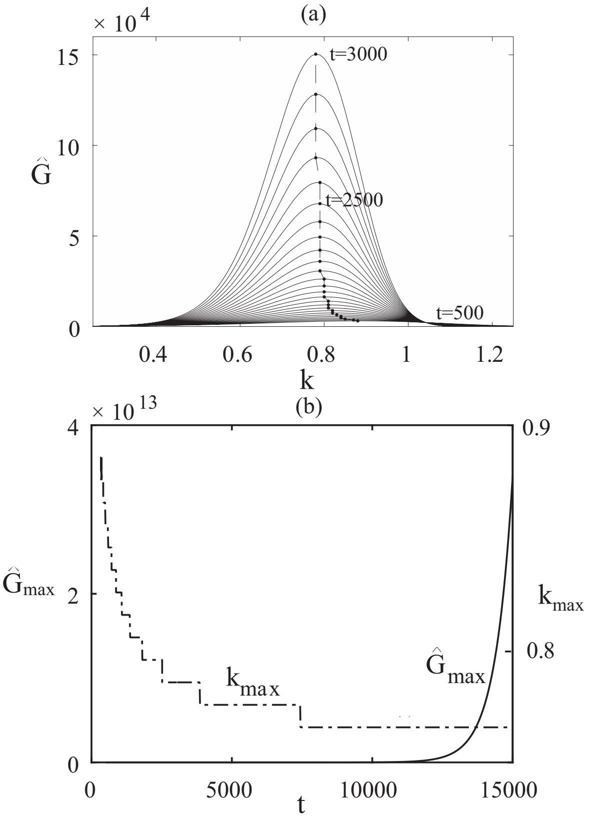

Fig. A.7 Antidune case ($Fr = 1.2$): (a) behavior of $\hat{G}$ as a function of the wavenumber k. The dashed line indicates the most unstable wavenumber for each time. The line spacing is $\Delta t = 100$. (b) Evolution of the most unstable wavenumber over time in conjunction with the corresponding value of the growth function.

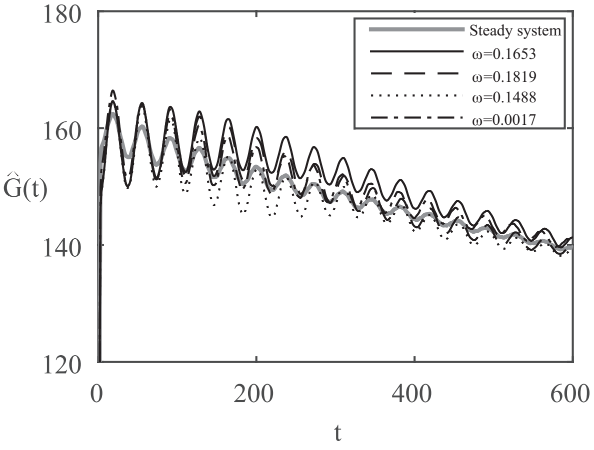

Fig. A.8 Growth function versus time, evaluated at the point $\{k, F_0\} = \{0.4, 0.7\}$ for the steady system and for different values of the frequency ω ($\phi = 0$).

model section, the time scale emerging from the scaling is the hydrodynamic one, thus the dimensionless frequency is given by $\omega = \omega^* \bar{D}_0^*/\bar{U}_0^*$.

The evaluation of the growth function by the direct-adjoint procedure for a wide range of time horizons is computationally demanding and usually unnecessary. All unsteady curves are instead obtained by the following simplified procedure [45]: (i) the growth function $\hat{G}(t)$ is computed by the more efficient SVD-method for the corresponding steady problem; (ii) the time t_{max} at which $\hat{G}(t)$ reaches a maximum is identified; (iii) the iterative direct-adjoint technique is applied for $t = t_{max}$ to determine the optimal initial condition $\mathbf{q}_0$; (iv) the direct problem (A.27a) is integrated in time starting from the optimal initial condition and the growth function is evaluated.

Our focus is on the role of the frequency ω in triggering a parametric resonance. Resonance occurs, when the system is subjected to a periodic forcing with a frequency close to the natural oscillation of the system ($\omega_f = 2\pi/T_f \simeq 0.165$). The curve obtained for $\omega = \omega_f = 0.165$ (solid black line) shows a larger energy amplification than the steady case. Higher and lower values ($\omega = 1.1\ \omega_f = 0.182$ and $\omega = 0.9\ \omega_f = 0.149$) result in an initial amplification followed by a smaller response for larger times.

According to the adopted scaling, the dimensionless time is given by $t = t^* \bar{U}_0^*/\bar{D}_0^*$. As the ratio $\bar{U}_0^*/\bar{D}_0^*$ is generally $\simeq 1$, we obtain $t \simeq t^*$ seconds. It is interesting to observe the behavior of the system, when the period of the

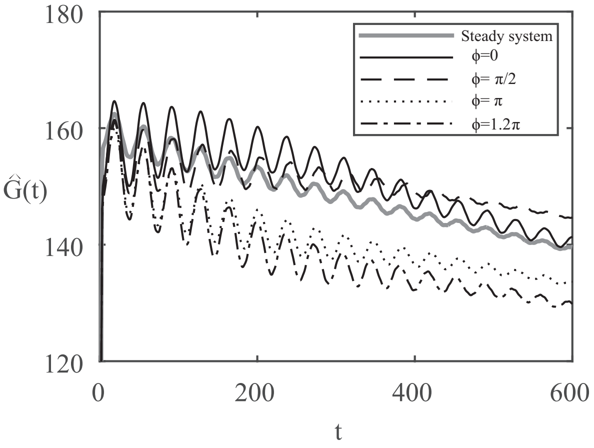

Fig. A.9 Growth function versus time evaluated at the point $\{k, F_0\} = \{0.4, 0.7\}$ for the steady system and for different values of the phase ϕ ($\omega = 0.1653$).

unsteadiness is similar to the characteristic time of river bed-form formation – so as to probe the geomorphological relevance of our results. The dashed-dotted curve in Fig. A.8 is obtained for $\omega = \omega_f/100 = 0.0017$, from which we determine $T^* \simeq 1$ h, and with an optimal condition computed at $t = t_{max}$. It can be observed that the previous results are confirmed, even when periodic forcing with more physically significant frequencies, corresponding to longer times, are considered ($\omega = 0.0017$). Another remarkable result is related to the time necessary for the growth function to decay below unity (when the system returns to the base state). Extrapolating from the plot, the decay time appears to be $\simeq 2 \cdot 10^4$ s $\simeq 6$ h, which is comparable to typical morphodynamic times and hence physically significant [46].

Finally, Fig. A.9 depicts the effect of the phase lag ϕ. The different curves are obtained for a constant value of the frequency ($\omega = 0.1653$) and for phase values increasing from $\phi = 0$ to $\phi = 1.2\pi$. We notice that an increase in ϕ produces a decrease of the maximum amplification of the system energy.

The obtained results demonstrate that the mutual interaction between flow unsteadiness and nonnormality plays an important role in the stability of river bedforms. First, the nonmodal analysis of a one-dimensional model allowed us to demonstrate that bed perturbation can be transiently amplified by subcritical unsteady flows. Therefore, one of the mechanisms that contributes on the inception of dunes is linked to the transient amplification of disturbances. This result is beyond the reach of classical modal analysis, which focuses on the asymptotic disturbance behaviour of the system only. Secondly, we have shown that flow unsteadiness can amplify, to a great extent, the transient growth of these perturbations when compared to equivalent steady conditions. Critical parameters governing this amplification effect are the frequency and the phase of the periodic forcing.

Conclusions

In the present work, we have addressed the interplay between unsteadiness and nonnormality as it relates to the inception of river bedforms. Specifically, modal and nonmodal stability analyses have been carried out to investigate the river-bed instability and to assess the occurrence of transient growth. Both analyses have been performed while retaining all time dependencies of the system's governing equations. River bedform dynamics exhibit a significant amount of nonnormality over a large part of parameter space. Consequently, substantial transient growth, despite asymptotically stable modes, is possible during the early stages of bed instabilities. It has been observed that the characteristic wavelength of the river bedform decreases with time; furthermore, it is correctly selected also for short time. The phase and frequency of the base-flow discharge have been recognized to play a key role in defining the magnitude of the transient energy amplifications. Importantly, the time scales of bedform transient growth are comparable to typical fluvial morphological and hydrological time scales, suggesting the development of bedforms by transient processes in real rivers. Finally, we have shown that our one-dimensional antidune model is capable of capturing, modeling and predicting the transient formation of river dunes.

Nonmodal analysis for unsteady conditions has revealed important results for the stability of subaqueous dunes. In view of this, it could be useful to apply a similar analysis for other morphological instabilities in which flow unsteadiness plays an important role, such as aeolian dunes [11]. As the barchan shape transition in the aeolian dune environment is very relevant, a nonmodal analysis could be used for improving existing studies on this transversal instability. The investigation of a transient-growth potential in this field is in fact lacking.

References

[1] A. Caruso, R. Vesipa, C. Camporeale, L. Ridolfi, and P. J. Schmid. River bedform inception by flow unsteadiness: A modal and nonmodal analysis. *Physical Review E*, 93(5):053110, 2016.

[2] J. W. Lillycrop, J. D. Rosati, and D. D. McGehee. A study on sand waves in the panama city, florida, entrance channel. Technical Report CERC-TR-89-7, US Army Engineer and Development Center, 1989.

[3] D. J. Harbor. Dynamics of bedforms in the lower mississippi river. *J. Sedim. Res.*, 68(5), 1998.

[4] P. Y. Julien and G. J. Klaassen. Sand-dune geometry of large rivers during floods. *J. Hydr. Eng.*, 121(9):657–663, 1995.

[5] J. Best. The fluid dynamics of river dunes: A review and some future research directions. *J. Geophys. Res.: Earth Surface (2003–2012)*, 110(F4), 2005.

[6] A. I. Packman and N. H. Brooks. Hyporheic exchange of solutes and colloids with moving bed forms. *Water Resour. Res.*, 37(10):2591–2605, 2001.

[7] F. Boano, J. W. Harvey, A. Marion, A. I. Packman, R. Revelli, L. Ridolfi, and A. Wörman. Hyporheic flow and transport processes: Mechanisms, models, and biogeochemical implications. *Rev. Geophys.*, 52(4):603–679, 2014.

[8] A. Blom, J. S. Ribberink, and H. J. de Vriend. Vertical sorting in bed forms: Flume experiments with a natural and a trimodal sediment mixture. *Water Resour. Res.*, 39(2), 2003.

[9] M.G. Kleinhans. Sorting in grain flows at the lee side of dunes. *Earth Sci. Rev.*, 65(1):75–102, 2004.

[10] H. Niiya, A. Awazu, and H. Nishimori. Bifurcation analysis of the transition of dune shapes under a unidirectional wind. *Physical review letters*, 108(15):158001, 2012.

[11] H. P.M. Melo, E. J.R. Parteli, J. Andrade, and H. J. Herrmann. Linear stability analysis of transverse dunes. *Physica A: Statistical Mechanics and its Applications*, 391(20):4606–4614, 2012.

[12] L. Guignier, H. Niiya, H. Nishimori, D. Lague, and A. Valance. Sand dunes as migrating strings. *Physical Review E*, 87(5):052206, 2013.

[13] N. Endo, K. Taniguchi, and A. Katsuki. Observation of the whole process of interaction between barchans by flume experiments. *Geophysical Research Letters*, 31(12), 2004.

[14] D.S. McCulloch and R.J. Janda. Subaqueous river channel barchan dunes. *Journal of Sedimentary Research*, 34(3), 1964.

[15] R. Vesipa. *River antidunes and bars: new models and nonmodal analysis.* PhD thesis, Politecnico di Torino, 2013.

[16] F. Engelund. Instability of erodible beds. *J. Fluid Mech.*, 42(02):225–244, 1970.

[17] K.J. Richards. The formation of ripples and dunes on an erodible bed. *J. Fluid Mech.*, 99(03):597–618, 1980.

[18] C. DiCristo, M. Iervolino, and A. Vacca. Linear stability analysis of a $1-$d model with dynamical description of bed-load transport. *J. Hydr. Res.*, 44:480–487, 2006.

[19] M. Colombini. Revisiting the linear theory of sand dune formation. *J. Fluid Mech.*, 502:1–16, 2004.

[20] M. Colombini and A. Stocchino. Three-dimensional river bed forms. *J. Fluid Mech.*, 695:63–80, 2012.

[21] B. Andreotti, P. Claudin, O. Devauchelle, O.Durán, and A. Fourrière. Bedforms in a turbulent stream: ripples, chevrons and antidunes. *J. Fluid Mech.*, 690:94–128, 2012.

[22] P. J. Schmid and D. S. Henningson. *Stability and Transition in Shear Flows*. Springer Verlag, first edition, 2001.

[23] D. Rempfer. Low-dimensional modeling and numerical simulation of transition in simple shear flows. *Annu. Rev. Fluid Mech.*, 35(1):229–265, 2003.

[24] C.B. Lee and J.Z. Wu. Transition in wall-bounded flows. *Appl. Mech. Rev.*, 61(3):030802, 2008.

[25] L. N. Trefethen, A. E. Trefethen, S. C. Reddy, and T. A. Driscoll. Hydrodynamic stability without eigenvalues. *Science*, 261:578 – 584, 1993.

[26] K. M. Butler and B. F. Farrell. Three-dimensional optimal perturbations in viscous shear flow. *Phys. Fluids A: Fluid Dynam. (1989-1993)*, 4(8):1637–1650, 1992.

[27] P. J. Schmid. Nonmodal stability theory. *Annu. Rev. Fluid Mech.*, 39:129–162, 2007.

[28] S. C. Reddy and D. S. Henningson. Energy growth in viscous channel flows. *J. Fluid Mech.*, 252:209–238, 1993.

[29] P. J Olsson and D. S. Henningson. Optimal disturbance growth in watertable flow. *Studies in Appl. Math.*, 94(2):183–210, 1995.

[30] S. V. Malik and A. P. Hooper. Three-dimensional disturbances in channel flows. *Phys. Fluids (1994-present)*, 19(5):052102, 2007.

[31] C. Camporeale, and L. Ridolfi. Nonnormality and transient behavior of the de saint-venant-exner equations. *Water Resour. Res.*, 45:W08418, 2009.

[32] C. Camporeale, and L. Ridolfi. Modal versus nonmodal linear stability analysis of river dunes. *Phys. Fluids*, 23:104102, 2011.

[33] R. Vesipa, C. Camporeale, and L. Ridolfi. Transient growths of stable modes in riverbed dynamics. *EPL (Europhys. Lett.)*, 100(6):64002, 2012.

[34] M. Tubino, R. Repetto, and G. Zolezzi. Free bars in rivers. *J. Hydraul. Res.*, 37(6):759–775, 1999.

[35] F. Visconti, C. Camporeale, and L. Ridolfi. Role of discharge variability on pseudomeandering channel morphodynamics: Results from laboratory experiments. *J. Geoph. Res.*, page doi: 10.1029/2010JF001742, 2010.

[36] P. Hall. Alternating bar instabilities in unsteady channel flows over erodible beds. *J. Fluid Mech.*, 499:49–73, 2004.

[37] R. Vesipa, L. Ridolfi, and C. Camporeale. A shallow-water theory of river bedforms in supercritical conditions. *Phys. Fluids*, 24, 2012.

[38] C. Camporeale, C. Canuto, and L. Ridolfi. A spectral approach for the stability analysis of turbulent open-channel flows over granular beds. *Theor. Computa. Fluid Dynam.*, 26(1-4):51–80, 2012.

[39] G. Seminara, L. Solari, and G. Parker. Bed load at low shields stress on arbitrarily sloping beds: Failure of the bagnold hypothesis. *Water Resour. Res.*, 38(11):31–1, 2002.

[40] G. Parker, G. Seminara, and L. Solari. Bed load at low shields stress on arbitrarily sloping beds: Alternative entrainment formulation. *Water Resour. Res.*, 39(7):1183, 2003.

[41] R. F. Dressler. New nonlinear shallow-flow equations with curvature. *J. Hydraul. Res.*, 16(3):205–222, 1978.

[42] S. Wright and G. Parker. Flow resistance and suspended load in sand-bed rivers: simplified stratification model. *J. Hydraul. Eng.*, 130(8):796–805, 2004.

[43] D. P. G. Foures, C. P. Caulfield, and P. J. Schmid. Variational framework for flow optimization using seminorm constraints. *Phys. Rev. E*, 86:026306, 2012.

[44] S. E. Coleman and B. W. Melville. Initiation of bed forms on a flat sand bed. *J. Hydraul. Eng.*, 122(6):301–310, 1996.

[45] C. Camporeale and P. J. Schmid. Parametric resonance in unsteady watertable flow. *J. Fluid Mech.*, 768:524–548, 2015.

[46] P. Ph. Jansen, L. V. Bendegom, J. Van den Berg, M. De Vries, and A. Zanen. *Principles of river engineering: the non-tidal alluvial river*. Delftse Uitgevers Maatschappij, 1994.